

Advanced Manufacture and Characterisation of Thick Tungsten Coatings for Nuclear Fusion Applications



Benjamin Evans

St Edmund Hall

University of Oxford

A thesis submitted for the degree of

Doctor of Philosophy

Supervised by Professor David Armstrong and Professor Patrick Grant

Trinity Term 2023

Abstract

Nuclear fusion is a promising technology for the production of sustainable, clean energy, but its successful implementation is dependent on a number of practical aspects. One important factor is the performance of plasma-facing components (PFCs), such as the divertor or first wall (FW) of a tokamak. W is currently the leading candidate to withstand the extreme environment, but establishing a replicable means of manufacture of W components that is faster than the currently-employed diffusion bonding method is essential to achieve commercial viability. It is predicted that 300,000 divertor tiles will be initially required for the International Thermonuclear Experimental Reactor (ITER) alone.

Bonding W to structural materials such as steel and Cu is challenging; the large difference in coefficient of thermal expansion (CTE) results in coating delamination during thermal excursions. Several manufacturing technologies are being actively investigated to improve the production and performance of W coatings.

This thesis focuses on two techniques: vacuum plasma spraying (VPS) and the field-assisted sintering technique (FAST). Optimisation of the VPS process using Taguchi analysis resulted in the production of thick (4 mm) W coatings on steel substrates, exceeding previous best efforts. Finite element modelling (FEM) was used to investigate the residual strains and stresses due to the CTE difference following FAST manufacture, and the effect of substrate texturing on crack propagation.

Thermal stability in fusion-relevant conditions is a key performance indicator of candidate PFCs. Three investigations are reported in this thesis: thermal ageing (up to a week and up to 1000 °C), to observe and analyse any diffusional effects that occur at reactor temperatures; steady-state thermal cycling in HIVE[1] (300–800 °C) and UPP[2] (150–550 °C), to observe crack development and test long-term coating survival; and transient thermal cycling in UPP (up to 800 °C base temperature with an additional 300–800 °C due to transient pulsing), to observe localised high heat flux effects that are common to 'off-normal' tokamak events such as edge-localised modes (ELMs). The results obtained led to the following conclusions: oxides and carbides formed through diffusion, which embrittled the coatings; flat steel substrates led to coating delamination, whereas samples with W substrates were only damaged locally by transient heating pulses; texturing of steel substrates improved thermal performance (better conductivity and no coating delamination) of samples during thermal cycling; and thicker coatings (on steel substrates) exhibited fewer, but larger, cracks than thinner coatings.

Following these investigative tests, thermally-cycled samples had an additional 1 mm layer of W applied using the FAST, to assess the viability of this technique to repair damaged coatings. Results were encouraging: pre-existing vertical cracking in the original coating of steel substrate samples caused crack initiation and propagation in the new repair coatings, whereas in W substrate samples no dam-

[1] **H**eating by **I**nduction to **V**erify **E**xtremes
[2] **U**pgraded **P**ilot-**P**SI

age was observed; repair coatings were thinner than original coatings and higher concentrations of C had diffused in. Subsequently, samples with repaired coatings were retested in HIVE, whereupon some steel substrate samples either severely cracked or delaminated, whilst W substrate samples remained undamaged.

Overall, alternative production routes for W coatings yielded some promising results that warrant further investigation and development, most notably the potential for in-situ repair of W plasma-facing components (PFCs).

COVID-19 Impact Statement

The outbreak of the COVID-19 pandemic in early 2020 had profound and unprecedented effects on research activities worldwide. This impact statement outlines the disruptions and challenges encountered during the course of this project, which significantly contributed to delays in project milestones and necessitated adjustments to the research plan.

Laboratory Access Disruption

On 24$^{\text{th}}$ March 2020, the Oxford Materials department implemented a complete lockdown in response to concerns about the safety of on-site work. It was not until 6$^{\text{th}}$ October 2020, that I was able to resume on-site work, marking a hiatus of seven months.

My research relied heavily on experimental work, particularly utilising the Advanced Processing Lab (APL) in Begbroke. Unfortunately the APL was one of the last facilities to reopen, further extending the period without access to essential laboratory resources. As the sole user of a large industrial machine (VPS), I was responsible for its upkeep and repair (and I was only able to call out external technicians when there were faults that could not be understood, due to the high call-out cost). This machine was only restored to full functionality on 18$^{\text{th}}$ February 2021, resulting in an additional 4.5 month delay to my experimental work. In total, this period accounted for an 11.5 month interruption in my primary research activities.

Computational Modelling Challenges

Recognising the need to diversify my research activities as a results of the lock-down, I began computational modelling work. However, limited support and the absence of face-to-face interactions hindered my progress. The necessity to train to use several different modelling software packages proved time-consuming and reduced my working efficiency significantly during this period. As a Fusion CDT student, the first nine months of my project were interspersed with taught lecture courses and associated coursework: consequently during the early stages of the pandemic my productivity was impacted because I had limited experimental data for analysis.

Revised Research Plan

In late December 2020, I acquired samples from previous researchers for further investigation. These provided some limited research opportunities, though insufficient to compensate for the lack of primary sample production. Additionally, I began utilising a secondary production machine (FAST) in early January 2021 to facilitate some sample production and study.

In light of the prolonged delays and uncertainties posed by the pandemic, my supervisors and I made the decision to exclude the mechanical testing aspect of my original project due to the extended timescale that would have been required. Furthermore, I actively sought and established collaborations with the Culham Centre for Fusion Energy (CCFE) and the Dutch Institute for Fundamental Energy

Research (DIFFER), with the aim of completing external experimental testing by May 2022. However, knock-on effects from the pandemic (and the Russian invasion of Ukraine) meant that this work was only completed at the beginning of September 2022, and required subsequent data analysis.

Conclusion

The COVID-19 pandemic undeniably had a substantial impact on the progress of my DPhil research. Delays in laboratory access and resultant equipment failure, challenges in computational modelling and the need to rescope my research plan all extended the timeline for completing my work. While I had initially aimed to conclude all research activities by April 2022, these unforeseeable pandemic-related setbacks rendered this goal unattainable. Nevertheless, I remained committed to the successful completion of my research, and I was grateful for the extension funding granted by the COVID-19 Scholarship Extension Fund (CSEF) and the Oxford Materials Continuation Bursary in recognition of these exceptional circumstances.

Acknowledgements

I should like to express my gratitude to all those who have supported and encouraged me during the course of this research project. My specific thanks go to:

My supervisors, Professor David Armstrong and Professor Patrick Grant, for their continued guidance and contributions throughout my project. Your patience and encouragement have been invaluable during times of equipment failure and through a global pandemic.

The Engineering and Physical Sciences Research Council [EP/L01663X/1] and the Oxford Materials department: without their sponsorship this work would not have been possible.

The administrative teams of the Materials department and the Fusion CDT, particularly to Dr. Adrian Taylor and Mrs. Rebecca Bradford.

My collaborators at UKAEA and DIFFER, for use of their facilities, HIVE and UPP, and their expertise. Special thanks to Mr. Stephen Cosser, Mr. James Paterson, Mr. Josh Whitley and the rest of the HIVE team for their time and patience with my long sample exposures; to Dr. David Bowden for his support and advice; and to Professor Thomas Morgan, Mr. Jordy Vernimmen, Mr. Remco Timmer, Miss Maria Morbey, Mr. Ameya Ranade and Mr. Richard Al for their technical guidance and assistance.

Mr. Robin Vincent and Mr. Gideon Ring for their skill and assistance when repeatedly fixing the VPS; to Dr. Colin Johnston, Mr. Greg Cook and the rest of the OMCS team for their help at Begbroke; and to Dr. Phani Karamched and the rest of the DCCEM team for their training and help with equipment challenges.

My time in Oxford would not have been the same without the fantastic friends I have made along the way. Special mentions go to Brad, Keivan, Pedr, Rob, Robin and the rest of the corner office for your help and for keeping me sane; to Joe, Dhaval, Tak, Siân and Ollie for being there whenever I needed a boost or a break; and to George and Issy (and Bertie and Anna) for reminding me that there's life outside the labs.

To Mum, Dad and Seb, thank you for all your love and support, for knowing when I need distracting with cricket, D&D or food, and for always believing in me.

And lastly to Eva: meeting and getting to know you has been the best part of my time here. Thank you for everything you do.

Contents

Abstract **i**

COVID-19 Impact Statement **iv**

Acknowledgements **vii**

1 Introduction **1**

1.1 Project Aims and Objectives 6

2 Literature Review **7**

2.1 Problems for the first wall and divertor 8

2.1.1 Materials selection 9

2.1.2 Current status 11

2.1.3 Manufacturing 15

2.2 Manufacture of tungsten coatings 18

2.2.1 Diffusion bonding 18

2.2.2 Chemical vapour deposition 21

2.2.3 Physical vapour deposition 23
2.2.4 Spark plasma sintering 25
2.2.5 Cold spray 28
2.2.6 Atmospheric plasma spraying 30
2.2.7 Vacuum plasma spraying 35
2.2.8 Summary of Manufacturing Processes 43
2.3 Fusion-relevant thermal testing 48
2.3.1 Why do we need fusion-relevant testing? 48
2.3.2 Steady-state heat load testing 50
2.3.3 Transient heat load testing 52
2.3.4 Summary of fusion-relevant testing 67
2.4 Future developments 68
2.5 Summary 70

3 Optimisation of Vacuum Plasma Spraying 71
3.1 Introduction 71
3.2 Methodology 77
3.2.1 Materials and preparation 77
3.2.2 Equipment and VPS set up 81
3.2.3 Powder mass flow rate 82
3.2.4 Plasma optimisation using Taguchi analysis 83
3.2.5 Further optimisation 86
3.3 Results and Discussion 89
3.3.1 Powder mass flow rate 90
3.3.2 Plasma optimisation via Taguchi analysis 91

3.3.3 Further optimisation . . . 103
3.4 Summary . . . 110

4 Modelling of Substrate Texturing 111

4.1 Introduction . . . 111
4.2 Methodology . . . 116
4.2.1 Model validation and mesh refinement analysis . . . 117
4.2.2 Crack path analysis . . . 118
4.2.3 Comparison of experiments with modelled predictions . . . 122
4.3 Results and Discussion . . . 126
4.3.1 Model validation and mesh refinement analysis . . . 126
4.3.2 Crack path analysis . . . 131
4.3.3 Comparison of experiments with modelled predictions . . . 168
4.4 Summary . . . 171

5 Effects of Thermal Ageing and Cycling 173

5.1 Introduction . . . 173
5.2 Methodology . . . 179
5.2.1 Sample Preparation . . . 179
5.2.2 Thermal Ageing . . . 180
5.2.3 Thermal Cycling: HIVE . . . 183
5.2.4 Thermal Cycling: UPP . . . 186
5.3 Results and Discussion . . . 189
5.3.1 Thermal Ageing . . . 189
5.3.2 Thermal Cycling: HIVE . . . 215
5.3.3 Thermal Cycling: UPP . . . 232

5.4 Summary 247

6 Repair of Plasma Facing Components 249

6.1 Introduction 249

6.2 Methodology 252

6.2.1 Initial Damage: UPP 254

6.2.2 Sample Repair 256

6.2.3 Further Damage 257

6.3 Results and Discussion 258

6.3.1 Initial Damage: UPP 258

6.3.2 Sample Repair 304

6.3.3 Further Damage 323

6.4 Summary 345

7 Conclusions and further work 347

7.1 Conclusions 347

7.2 Further work 355

1 Introduction

Since the 1950s, nuclear fusion reactors have been heralded as the energy source of the future. With a promise of clean, reliable energy, many people believe that nuclear fusion may be one of the answers to the current energy crisis. By fusing the nuclei of light elements, vast amounts of energy can be released in a process similar to the one that fuels the stars. However, containing a 'Sun in a box' presents major physics and engineering challenges that must be overcome in order for a nuclear fusion reactor plant to become an economically-viable way of producing useful energy.

Meeting the world's ever-increasing demand for energy with current production methods contributes over 80% of global carbon emissions [1] — it is clear that radical change is required in our energy generation and usage habits to make any meaningful progress in meeting the goals of the 2015 Paris Climate Accords.

Although large corporations such as Shell [2] and BP [3] have committed to net-zero carbon emissions by 2050; to achieve this on a wider scale, sufficient to have the necessary global impact, utilisation of other, more sustainable, forms of energy generation (such as renewable and nuclear sources) is urgently needed.

Nuclear fusion has long been considered a potentially more environmentally-friendly approach to energy generation [4] in comparison with fossil fuels and nuclear fission, due to its predicted reduction of waste products, lower emissions and excellent availability of necessary resources [5–7].

The proton-proton nuclear fusion process that occurs in the Sun is a result the extreme gravitational pressure at the core (23 quadrillion Pa [8]) which forces together the H nucleii. This is relatively inefficient and unachievable on Earth, so a modified version of the reaction is employed by using different isotopes of H. The deuterium-tritium (DT) reaction, shown in Figure 1.1, has been selected as the most commercially-viable option due to the high energy release per collision [9] and higher reactivity at lower temperatures than other potential reactions, as seen in Figure 1.2. The DT reaction releases 17.6 MeV (carried kinetically mostly by the high-speed neutron, but also by the resulting He nucleus) whereas a deuterium-deuterium (DD) reaction only releases 3.7 MeV (and no high-speed neutron) [10]. Higher reactivity means there is a higher chance of a fusion event occurring when two ions collide. This is vital for commercial fusion reactors as, even with the more efficient DT reaction, a temperature ten times hotter than the Sun is required to produce electricity effectively [11, 12].

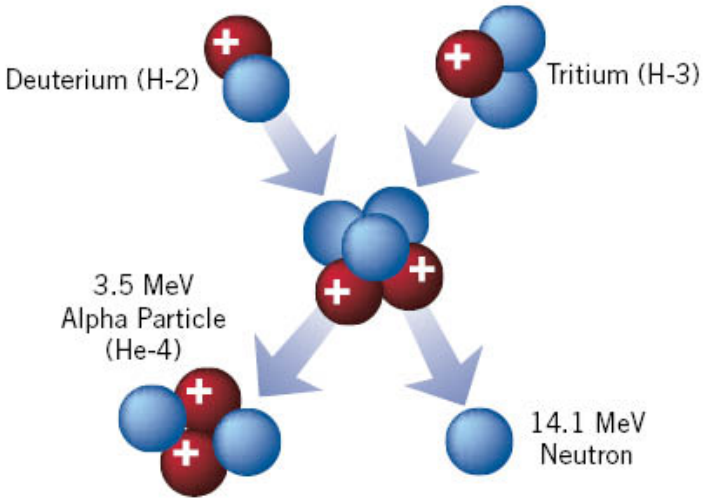


Figure 1.1: Schematic diagram showing the DT fusion reaction [13][1].

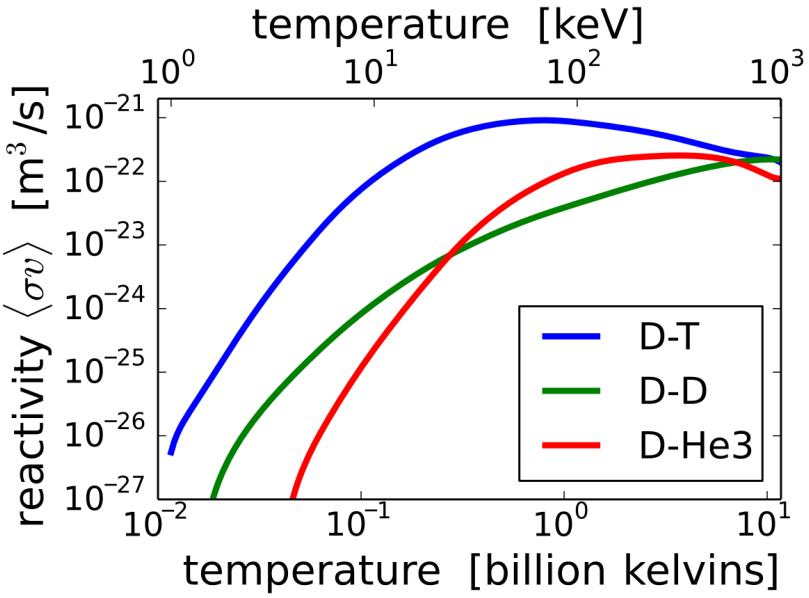


Figure 1.2: A comparison of reactivity as a function of temperature for different fusion reactions: deuterium-tritium, deuterium-deuterium and deuterium-Helium-3 [14][2].

[1]Credit:©American Nuclear Society

[2]https://commons.wikimedia.org/wiki/File:Fusion_rxnrate.svg, Author: Dstrozzi, CC by 2.5

Commercial realisation of nuclear fusion is currently held back by significant scientific and technical challenges [5]. These can be split into two categories: materials challenges and physics challenges. Most of the major problems preventing the development of nuclear fusion have become materials-related, such as identifying materials which are capable of withstanding the high heat flux from the plasma [15, 16] as well as providing sufficient stability and longevity under the intense neutron flux [15, 17, 18]. These issues could be mitigated by improving the confinement of the plasma in order to reduce the number of plasma-wall interactions such as plasma disruptions, edge-localised modes (ELMs) and vertical displacement events (VDEs) [19].

W is the only material capable of withstanding the high heat fluxes that plasma-facing components (PFCs) are exposed to in a fusion device. Currently diffusion bonding is deployed to adhere W coatings onto structural materials to produce PFCs, however significant surface preparation is required in order to achieve the required bond strength. Millions of W coated tiles will be required for commercial fusion, meaning that diffusion bonding may not be appropriate at such a scale. This project investigated two manufacturing techniques — vacuum plasma spraying (VPS) and the field-assisted sintering technique (FAST) — as potential alternatives for producing thick W coatings for PFCs on an industrial scale.

Careful optimisation of the many VPS processing parameters was undertaken in order to achieve dense coatings of an appropriate thickness for use in a fusion reactor.

Previous work on W coatings produced via FAST highlighted vertical segmentation that occurs within the W coatings, however this was not fully understood. Finite element models (FEM) were produced in order to understand the origin and propagation behaviour of cracks and the associated relationship with residual strain and stress following manufacture, due to the difference in coefficient of thermal expansion (CTE) between substrate and coating.

The suitability of these coatings for use in a fusion environment was assessed by means of thermal ageing stability tests and two types of thermal cycling tests using induction and plasma heating. The variety of these tests give an indication of performance across the lifetime of a reactor, and act as a filter to reject less-promising samples.

Finally, transient plasma disruptions were experimentally simulated in order to generate the type of surface damage which is anticipated in the first wall. Damaged coatings had an additional W layer applied via the FAST in an attempt to demonstrate proof-of-concept of in-situ repair of erosion damage — something that has not been previously explored. These samples were then subjected to further thermal cycling tests to investigate the survival of the repaired coating.

1.1 Project Aims and Objectives

1. Produce an optimised, repeatable VPS recipe for spraying dense W coatings.

2. Develop FE models of W coatings manufactured using the FAST, with the aim of understanding substrate texture and why it helps (or not) retain thick tungsten coatings.

3. Understand and identify any compositional changes that occur at the W-steel interface of manufactured (FAST & VPS) samples.

4. Quantify the effect of substrate texture, material, and coating thickness on survival and crack response during steady-state thermal cycling of W coatings produced by FAST.

5. Investigate the impact of substrate texture and material on coating survival and crack response during transient thermal cycling of W coatings produced by FAST.

6. Investigate the feasibility of repairing W coatings using the FAST.

7. Quantify the quality of repair, how this is affected by pre-existing damage and how this affects FAST-repaired coating survival.

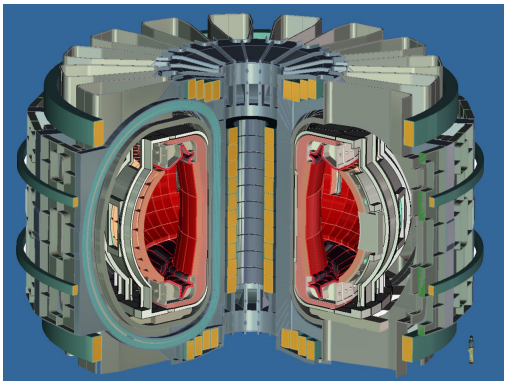
2

Literature Review

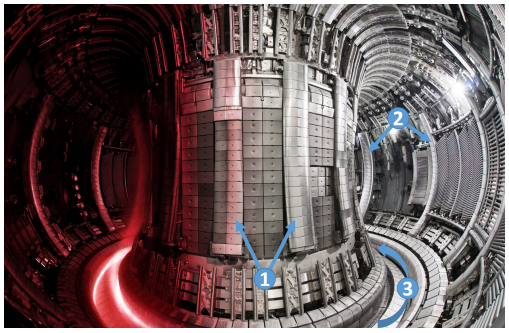
This literature review focuses on the materials requirements for a fusion reactor first wall and divertor — key plasma facing components without which a reactor cannot function. Particular focus will be given to W coatings, the front-runner in suitability for the hostile reactor environment, and the various manufacturing processes for plasma facing components (PFCs) that are being investigated. Substrate texturing and functionally graded materials (FGMs), and their impact on adhesion (and therefore lifetime) and coating thickness, are described along with key mechanical properties. Fusion-relevant thermal testing facilities are also explored and classified into three categories. Thermal ageing provides a better understanding of diffusion effects over a component's lifetime, while steady-state and transient thermal cycling accurately replicate the heat loads and plasma interactions experienced by materials during operation. An outlook on some near-future developments is also presented.

2.1 Problems for the first wall and divertor

It is estimated that in a commercially sized reactor — such as ITER (International Thermonuclear Experimental Reactor, diagram shown in Figure 2.1) — the divertor target will be subject to a heat flux in the region of 10–20 $MW \cdot m^{-2}$ in steady-state operation and even higher fluences (up to 1 $MJ \cdot m^{-2}$ over 1 ms [20]) for transient events [21, 22], such as when the plasma is 'dumped' on the divertor as a safety precaution [23]. These values are similar to the calculated levels of heat flux in inertially confined fusion (ICF) reactor designs [24]. It is therefore of paramount importance that the first wall (FW) armour, and also the divertor in magnetically confined fusion (MCF) reactors, can survive these extreme conditions for several years to allow for commercial operation.



(a) Cross-section of ITER [25][1]. The internal walls and divertor are shown in red. A person is shown in the bottom right corner for an idea of scale.



(b) A labelled photo of the interior of the Joint European Torus (JET) with superimposed plasma[2]. ① is the inner wall guard limiters, ② is the outer poloidal limiters and ③ is the divertor.

Figure 2.1: The first wall and divertor of (a) ITER and (b) JET.

[1] Credit:© ITER Organization, http://www.iter.org/

[2] Credit:© UKAEA, courtesy of EUROfusion

Figure 2.2 shows a prototype of an inboard subsection of the divertor to be installed in ITER. The inset image is a schematic showing how the subsection fits together with the rest of the divertor section. There are 1104 W monoblocks (small tiles) on this component; approximately 300,000 individual monoblocks will be required for the ITER divertor alone [26]. It is imperative that the manufacture of these blocks is eventually fast and scalable for commercial realisation of this technology.

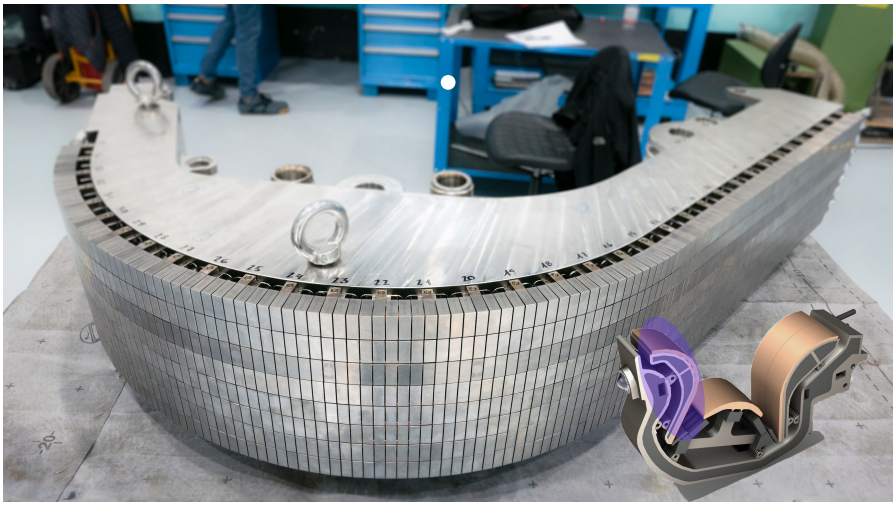


Figure 2.2: A photograph of a prototype inner vertical target for ITER with an inset image showing its location within the divertor section [26][3].

2.1.1 Materials selection

There are five major requirements to consider when selecting the material for the FW and divertor:

- High melting temperature — to survive the high operational temperature (1000 °C for first wall [27] and up to 2200 °C for divertor [28]) of the inner reactor

[3]Credit:© ITER Organization, http://www.iter.org/

- High thermal conductivity — to increase energy harnessed from the reactor by ensuring efficient heat transfer from the inner reactor to the coolant
- Short time for nuclear decay to low activity — to meet the fusion community's aim of having only low level waste (LLW) remaining, within 100 years of the decommissioning of a fusion power plant [29]
- Low tritium retention — to increase reactor efficiency (by not absorbing unburnt fuel) and to ensure that the radioactivity inventory limit is not prematurely reached
- Acceptable cost — to ensure that components can be manufactured on an industrial scale, materials should be available at practical cost

These requirements are overlaid onto the periodic table in Figure 2.3.

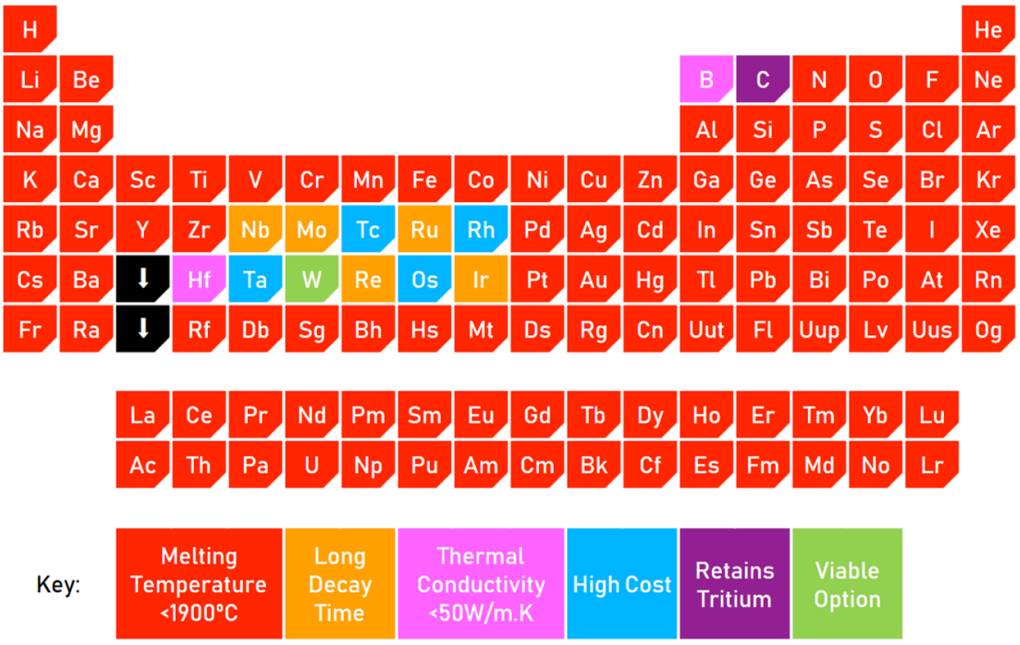


Figure 2.3: Periodic table colour-coded by the major restricting factors of each element for use in the divertor or FW of a nuclear fusion reactor.

2.1.2 Current status

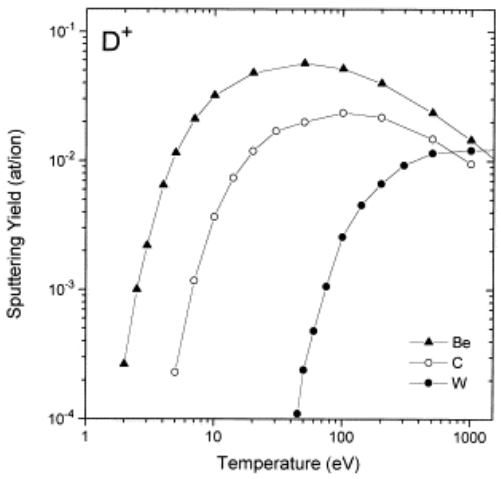
Few elements or compounds meet the fusion reactor environment requirements, and for PFCs reduce to: Be, Mo, W, graphite and silicon carbide (SiC).

Be is often discounted due to its relatively low melting point in comparison with other candidate materials (shown in Table 2.1) and its poor erosion properties, displayed in Figure 2.4 (a). Be is used in JET to investigate the potential knock-on effects of Be erosion and transport for use in ITER [30], for components in lower temperature areas (top and inboard sides of the reactor). Low-Z impurities, such as Be, in the plasma due to reactor component erosion contribute lower radiative power losses from the plasma than high-Z impurities (such as W). The maximum impurity concentration before plasma ignition is prevented due to radiative loss is $\sim$0.01% for W (Z=74) [31, 32] and $\sim$10% for C (Z=6) [32, 33]. There is evidence that other low-Z impurities (such as C, N and O) can deposit on the surface of the Be, forming an impurity layer which acts as a shield to the Be, suppressing its erosion [32].

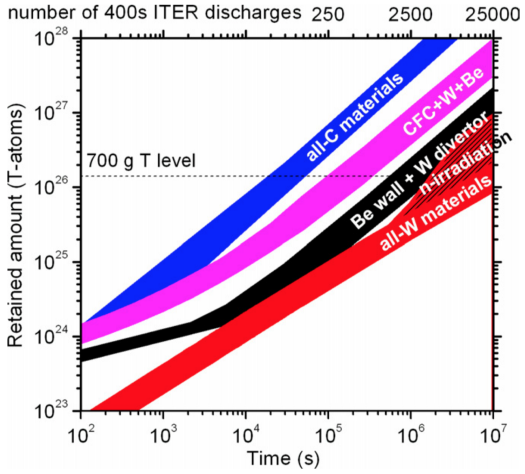
Be toxicity is also a major concern as inhalation can cause acute or chronic berylliosis, which can be fatal [34]. Be is already in use in fission and fusion applications as a neutron barrier and multiplier due to its (n,2n) cross-section, so health research (for identifying symptoms of berylliosis and applying fast, effective treatment) and engineering design (remote maintenance and handling) efforts are ongoing to mitigate Be risks [35, 36]. However, it has been proposed that the Be be replaced with W for the ITER FW [37] due to these health concerns.

Element	Melting Point (K)	Thermal Conductivity ($W \cdot m^{-1} \cdot K^{-1}$)
C	3825*	140
W	3695	170
SiC	3003 [38]	120–170 [38]
Mo	2896	139
Be	1560	190

Table 2.1: The melting points and thermal conductivities of candidate materials for PFC applications [39]
(*Diamond melting point — graphite has a similar sublimation temperature [40]).



(a) The sputtering yield of candidate materials at varying temperature [41][4]. Sputtering yield is an important measurement for determining the rate of erosion due to plasma-wall interactions.



(b) Simulated retention of tritium in various PFC choices in ITER as a function of time exposed to plasma [42][5].

Figure 2.4: Comparison of erosion properties and tritium retention between candidate materials Be, C and W.

Graphite is an attractive option for FW applications, however it retains an unacceptable amount of tritium as shown in Figure 2.4 (b). Nonetheless, graphite tiles are frequently used in non-DT fusion experiments as they meet the design criteria in all other aspects including a low-Z [32, 33]. SiC is also attractive in terms of high melting point but only avoids tritium retention problems when vapour deposited as a very thin (100 µm) layer [43].

Of the other metallic, high-Z elements, Mo is close to W in terms of erosion resistant behaviour and low tritium retention, but it has an extremely long decay time (>1000 years) to LLW after irradiation [44]. Mo would likely be high level waste (HLW) for a significant amount of time after decommissioning, which requires expensive long term management as HLW is capable of dangerous self-heating due to its radioactivity [45]. Figure 2.5 shows that Mo is considered 4.5 orders of magnitude worse in terms of exceeding waste disposal limits than W.

[4]Reprinted from Fusion Engineering and Design, Volume 37 Issue 4, Joachim Roth et al., Erosion of Be as plasma-facing material, 465-480, © copyright (1997), with permission from Elsevier.

[5]Reprinted from Plasma Physics and Controlled Fusion, Volume 50 Issue 10, Joachim Roth et al., Tritium inventory in ITER plasma-facing materials and tritium removal procedures, 103001, Copyright (2008), © IOP Publishing. Reproduced with permission. All rights reserved.

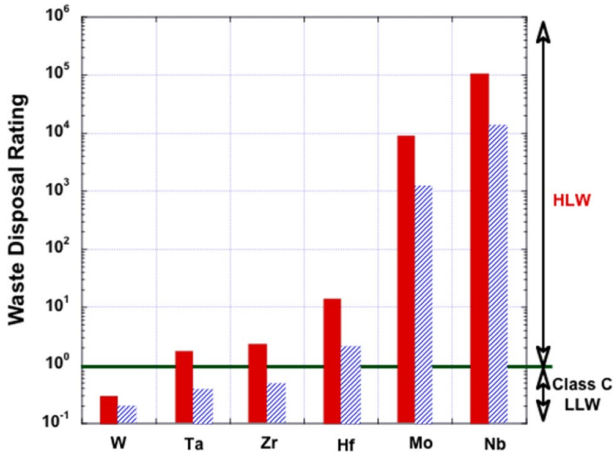


Figure 2.5: Comparison of waste disposal rating based on the activation of elements after irradiation. Waste disposal rating is a ratio between radioactivity 100 years after decommissioning and the radioactivity limit — a rating higher than unity denotes HLW. Red bars denote armour only, hatched bars show armour combined into the divertor structure (lower due to volume averaging) [46][6].

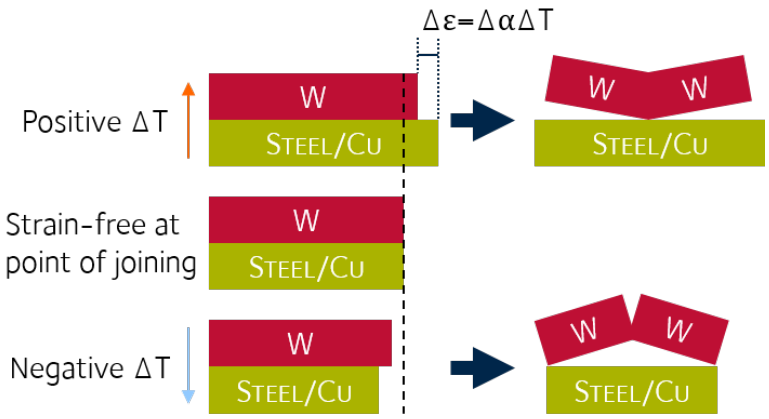
Although W is high-Z and highly radiative and thus potentially plasma quenching as an impurity, it is hard to erode or sputter and tends to be redeposited once eroded rather than penetrating deep into the plasma. Other challenges include: He embrittlement, microstructural changes, transmutations and neutron damage (and their impact on material properties) [47]. Nonetheless, when combined with its high melting point, high thermal conductivity and low tritium retention, W is the best metallic element for solid PFCs.

[6]Reprinted from Nuclear Fusion, Volume 55 Issue 4, Jeffrey Brooks et al., Plasma-facing material alternatives to tungsten, 043002, © copyright (2015), with permission from the IAEA.

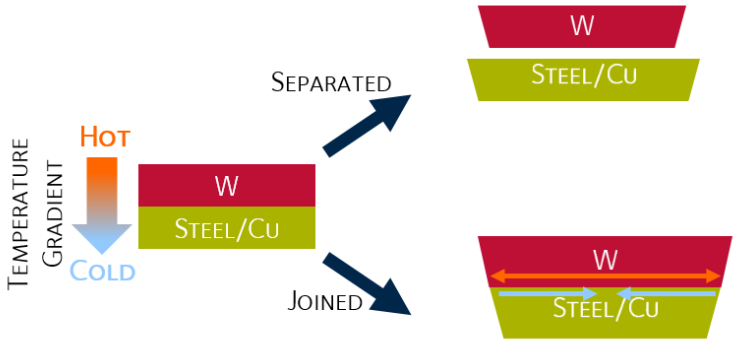
2.1.3 Manufacturing

Arguably, the positive attributes of W such as its high melting point also make manufacture of large-scale engineering components difficult. Casting is the most flexible process for complex shapes and used widely for many metals [48], but is unavailable for W due to its very high melting point (3695 K). Instead, powder metallurgy routes, usually direct from chemically-refined W ore are needed, with assembly making use of sintering and solid-state thermomechanical processes, such as forging, extrusion and drawing (as used to make a W light-bulb filament). However, all these processes require high temperatures to avoid cracking due to the inherent brittleness of W at low and intermediate temperatures due to its comparatively high ductile-to-brittle-transition-temperature (DBTT) of 500–700 K [49, 50]. The high DBTT arises due to the body-centred cubic (BCC) crystal structure of W. BCC materials are not close packed and have a higher activation energy to overcome the Peierls stress for dislocations to glide during deformation than face-centred cubic (FCC) and hexagonal close-packed (HCP) systems [51]. Rieth et al. [52] investigated the possibility of a full-W divertor (i.e. using W as the structural material as well as the plasma-facing armour). It was found that without shifting the DBTT, this technology would be unfeasible — further investigation into this design ceased around 2015. Therefore, joining W to a structural material, such as steel or Cu, is necessary. This, however, comes with its own complications.

The very low coefficient of thermal expansion (CTE) of W (α=4.3 $\times 10^{-6}$ K^{-1}) for a metallic element make W difficult to join to other metallic structural materials such as Cu (α=16.6 $\times 10^{-6}$ K^{-1}) and steel (α=10–17 $\times 10^{-6}$ K^{-1}) [53]. Differences in the CTE lead to materials expanding or contracting by different amounts for a given temperature change. When these different materials are joined — as is frequently required in system designs — the mismatch in CTE means that both materials are subject to compressive or tensile strains ($\Delta\epsilon$) during temperature excursions (ΔT) from the initial strain-free point of joining. These strains lead to thermal stresses (often termed 'residual stress') in both materials. The stored strain energy associated with this strain is then available to drive strain-relieving mechanisms, most typically de-bonding/delamination and cracking along the interface between the two materials (although cracks can also be propagated through one or both of the materials in some instances). Figure 2.6 (a) shows schematically how thermal strains arise and how strain energy release drives different modes of interfacial failure. Figure 2.6 (b) highlights how a thermal gradient can lead to high interfacial strains and stresses between two materials with a high CTE mismatch. In practice, calculating the stresses and strains in such a situation is particularly complicated. Common joining approaches such as screws, rivets and other physical joints are difficult due to the low fracture toughness of W (K_Q = $\sim$5 MPa$\cdot\sqrt{\text{m}}$ at room temperature) [54] and the high melting point makes welding W practically impossible.



(a) Schematic showing the evolution of negative and positive residual strains in a W-steel/Cu joined system during thermal excursions, and failure of the W and/or the interface.



(b) Schematic showing the strain effects due to an imposed thermal gradient, such as an incident heat flux on the W coating surface, as would be seen during operation in a nuclear fusion reactor.

Figure 2.6: Two illustrations highlighting the challenges faced when joining two materials with very different thermal expansion coefficients.

In summary, the fusion plasma reactor presents a uniquely hostile environment for which only a few elements are suitable (such as Be, C and W), and all have some limitations and restrictions. Currently, W is favoured for the PFC environment but its manufacturability into practical engineering components of many kilograms,

significant area and with reasonable geometrical complexity associated with PFC designs remains a challenge. To avoid some of the mechanical challenges that come with bulk W components, W coatings have been the principle focus of research and development and are now the focus of this review.

2.2 Manufacture of tungsten coatings

The current industry standard technique for producing W PFCs is diffusion bonding. Other processes also investigated are: physical and chemical vapour deposition (PVD and CVD); spark plasma sintering (SPS); and various thermal spray techniques including cold spraying, atmospheric plasma spraying (APS) and vacuum plasma spraying (VPS).

2.2.1 Diffusion bonding

Diffusion bonding is generally considered a joining process rather than a coating process, but can be used readily to join thin layers to a bulk substrate to form a coating. Diffusion bonding is a solid-state joining process that works via the diffusion of atoms across an interface between two materials. Relatively high temperatures (50–90 % of melting point [55]) are required for the diffusion to take place within a reasonable time scale. The surfaces of the joined materials must be as clean and smooth as possible to ensure adhesion, and most usually a uniaxial force is applied to ensure continuous intimate contact at the interface. When joining dissimilar materials, an interface layer of a third material with intermediate properties (such as CTE or melting temperature) can be used to improve the bond quality and to speed up joining.

Basuki et al. observed the effect of two different interlayers (Nb and V) on bond strength between W and EUROFER-97 (a steel produced specifically for nuclear fusion applications). A W thickness of 16 mm was used with a 1 mm interlayer with bond parameters of 900–1050 °C, 10–20 MPa and 0.5–2 hrs. Using scanning electron microscopy (SEM) and Auger electron spectroscopy (AES) the thickness of diffusion layers was 7–8 µm between steel and Nb and 1–2 µm between W and Nb. Nb_2C and Nb_6C_5 formed between steel and Nb, whereas there was no significant fraction of new phases at the W-Nb diffusion layer [56]. Similarly, there was a 0.8–1.4 µm VC rich diffusion layer at the V-steel interface [57]; carbide formation led to local decarburisation of the EUROFER-97.

Guided by finite element modelling (FEM), Cai et al. [58] successfully bonded W (13 mm thick) and steel using “composite interlayers". Samples with V/Cu and V/Ni bilayers (assembly ordered by ductility and CTE) had the highest joint strengths. This progressive transition in properties reduced the residual stresses with CTE matching between V and W, and plastic deformation occurring in the Cu/Ni layer. Joint strength increased from 272 MPa with a single Nb interface (the highest strength cited in the literature for this arrangement) to 402 MPa with the V/Cu composite interface. Micrographs of the joints are shown in Figure 2.7.

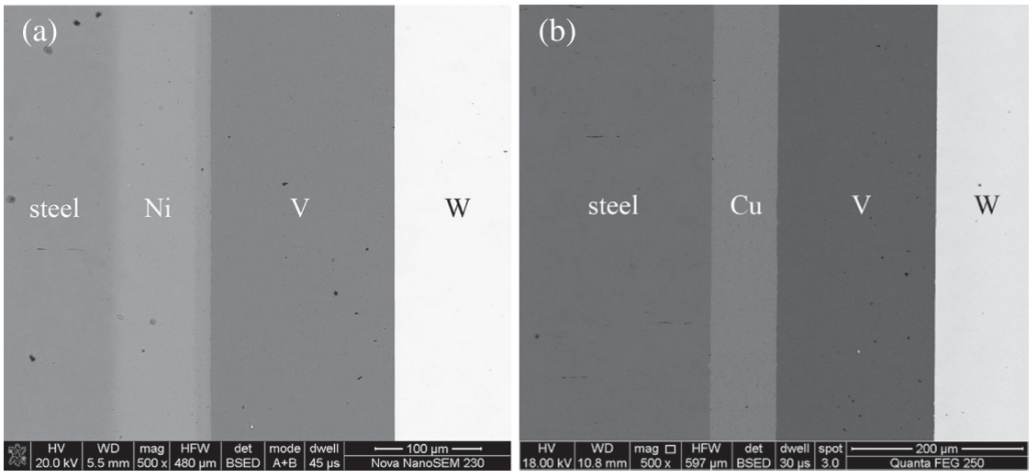


Figure 2.7: SEM image of the two V/Cu and V/Ni composite interlayer samples produced by Cai et al. [58][7].

Surface preparation (cleanliness and flatness) of the materials is vital to ensure there is no porosity, and adds time and cost to the overall process. Currently a three step process is required to join W and CuCrZr as both materials are coated with different coatings prior to joining the two sections [59, 60]. Optimum temperature and pressure are sensitive and require high levels of control to ensure good joining [61].

[7]Reprinted from International Journal of Refractory Metals and Hard Materials, Volume 70, Qingshan Cai et al., Rational design of composite interlayer for diffusion bonding of tungsten–steel joints, 155-161, © copyright (2018), with permission from Elsevier.

2.2.2 Chemical vapour deposition

Chemical vapour deposition (CVD) uses gaseous precursors that flow across and react at the surface of a substrate to form a coating. This process has many sub-categories and often occurs at reduced pressure. CVD is traditionally used to produce coatings <10 µm thick, and relies on suitable chemical reactions being available to form the required coating.

W coatings were deposited at atmospheric pressure on Cu substrates by Lian et al. with thicknesses ranging between 1.2–3.3 mm, using WF_6 and H_2 precursors at 500–560 °C. The substrate was then chemically dissolved and the free-standing coatings annealed at 1000 °C for 2 hrs to remove residual stresses. Coatings were characterised and exposed to an electron beam to simulate a thermal shock similar to ELM reactor events. Single pulse disruption-like loading was compared with repetitive (100 pulses) ELM-like loading; the power density at which cracking occurred at room temperature was significantly lower in the ELM-like case (0.16 GW·m^{-2}, 0.22–0.28 GW·m^{-2} for single pulse) due to the effect of thermal fatigue. As-deposited (relatively rough) and polished (relatively smooth) coatings were compared. As-deposited coatings cracked at lower power density exposure; when polished, crack formation was almost suppressed at elevated temperatures [62].

A summary of CVD W research at Southwestern Institute of Physics and Xiamen Tungsten Co., Ltd. by Chen et al. reported a variety of W thicknesses on a variety of substrates all produced through atmospheric pressure CVD [63]. Cu and Cu-based alloys were the most common substrates used. One sample highlighted was a 2 mm thick W coating on a CuCrZr substrate with a Cu/W functionally-graded

material (FGM) interlayer (fabricated by liquid phase sintering) produced by Lian et al. [64]. The sample survived 1000 cycles under a 11.7 $MW \cdot m^{-2}$ scanning electron beam with a 15 s pulse (15 s unloaded, alternately). Figure 2.8 shows a cross-section of the FGM. When using W (ODS[8]-W) alloys as a substrate, a W coating thickness greater than 5 mm was achieved [63] — this is currently the minimum thickness forecast to be required to survive the erosion between maintenance periods in order for a reactor to be commercially viable. CVD W and hot rolled W were exposed to a D plasma to investigate their irradiation resistance. There were fewer blisters on the exposed CVD W surface than the uniformly-blistered rolled W. Some limited mechanical testing was undertaken. Uniaxial tensile tests at 200 °C and 400 °C revealed a ultimate tensile strength (UTS) of ∼175 MPa and ∼200 MPa respectively, and an elongation of >10% at 400 °C (brittle failure occurred at 200 °C) [63].

[8] **O**xide **D**ispersion **S**trengthened

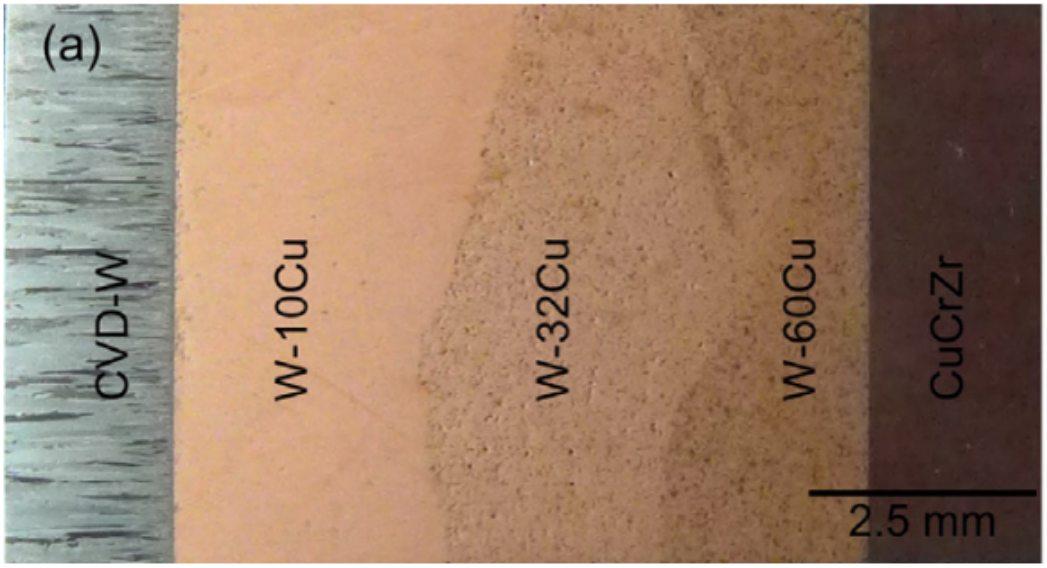


Figure 2.8: Optical micrograph of the cross-section of the FGM sample produced by Lian et al. [64][9].

2.2.3 Physical vapour deposition

Similar to CVD, physical vapour deposition (PVD) creates a coating from a vapour, in this case from a vapourised source that condenses on the substrate surface. PVD is used industrially to produce hard coatings and thin films (<10 µm) in semiconductor applications, however, thicker films can be produced by running the process for longer, although this is often uneconomic. Typical deposition rates are of the order 10–100 Å/s [65] — a 5 mm coating would take almost a week to produce with uninterrupted operation at the higher end of this range.

[9]Reprinted from Fusion Engineering and Design, Volume 88 Issue 9-10, Youyun Lian et al., Preparation and properties of CVD-W coated W/Cu FGM mock-ups, 1694-1698, © copyright (2013), with permission from Elsevier.

García-Rosales et al. [66] fabricated PVD W coatings up 100 µm thick on a graphite substrate using a 10 µm Re interlayer to improve adhesion and prevent carbon diffusion, followed by heat treatment for 4 hrs at 1000 °C, with densities >99%. Coatings were investigated at the JUDITH electron beam facility and cyclic fatigue tests at the MARION hydrogen ion beam facility. Electron beam testing progressively increased power load and pulse duration in steps up to 16 MW·m^{-2} for 2 s. There was crack formation in the W at a power density of 15.3 MW·m^{-2}. Ion beam testing consisted of 1000 cycles with a power load of up to 10 MW·m^{-2} (depending on position within the reactor) and a pulse length of 2 s. There was crack formation in thinner (20 µm) W coatings after 261 cycles, because of the high thermal load. The 100 µm coating survived 1000 cycles with a load of 7.9 MW·m^{-2} with no damage. W cracking was suggested to occur in part because of rapid carbide formation at the W/Re interface due to localised heating, which was exacerbated in the thinner coatings, and because of the strain energy due to the difference in thermal expansion between the graphite substrate and the W coating. It was suggested that residual pores may have contributed to crack arrest. Through thickness crack propagation was likely also promoted by the anisotropic columnar grain structure typical of PVD coatings.

PVD FGM coatings were investigated by Weber [67] as interlayers for joining W and EUROFER-97. W and EUROFER-97 targets were first magnetron sputtered at the same time to produce a grading of 33–44–60–75–84–86 at.% W with a total thickness of 1 mm. The graded interlayer was dense, although grading range was restricted to 33 to 86 at.%, rather than the target range of 0 to 100 at.% with graduations of 20 at.%. It was noted that inclining the targets differently during

sputtering might yield a better graduation range. The assembly was then diffusion bonded onto EUROFER-97 at 800 °C. There was some vertical (perpendicular to the substrate) cracking and cracking along the bonded interface after thermal cycling between room temperature and 650 °C (10 cycles). Overall there was a lack of compelling data on the use of graded interlayers to make a significant difference to cycling life, although interlayers did facilitate improved joining.

2.2.4 Spark plasma sintering

Spark plasma sintering (SPS) or the field-assisted sintering technique (FAST) works in a similar manner to hot pressing, but applies a low voltage (∼10 V) and high current (∼10 kA) through the graphite punches and die during consolidation. This current flow leads to significant Joule heating effects. For an electrically conductive powder, a proportion of the applied current flows through the powder particles and generates high temperatures at contact points between particles that drives rapid sintering. The main advantage of SPS processing is the ability to reduce sintering times from up to 10 hrs [68] to 5 mins [69] whilst retaining full densification. As well as cost and time savings, microstructural coarsening may also be avoided by the reduced high temperature exposure [70]. SPS/FAST is not generally considered for coating manufacture, as it is currently a batch process and yet to be proven scalable, but there are some studies on bulk W consolidation.

Matějíček et al. [71] studied the effect of carbon diffusion from the graphite die into W during sintering. Temperatures ranging between 1700–2000 °C were used with a variety of sintering times and foil types (graphite or tungsten foil). Sintering occurred under He atmosphere at 60 Pa to reduce oxidation. Carbon appeared

to have a reducing effect on W-based oxides on the surface of the powder. The longer sinter time and higher temperature allowed the carbon to diffuse further, resulting in fewer residual oxide particles. There were small (at the equipment detection limit) oxide particles at grain boundary junctions on fracture surfaces. Carbon foil was more effective in promoting consolidation, leading to a reduced level of porosity (∼4%) in comparison to the W foil (∼11%). As expected, there was a linear correlation between bending strength and porosity, the highest flexural strength measured was 1550 MPa. Thermal diffusivity showed ∼93% and ∼88% of ITER-qualified W at room temperature and 400 °C respectively.

Going a step further, Novak et al. [72] sintered bulk W with additional WC powder in order to reduce oxygen content further. At least 5 vol% WC was required to reduce oxides on the W powder at 1900 °C, 60 MPa and 5 minutes. In some samples there were small WO_2 inclusions on grain boundaries, which led to intergranular fracture. In comparable, conventionally-sintered W, transgranular fracture occurred because there were pores within the grains. Increasing the WC fraction decreased the number of WO_2 particles and there were no inclusions at 10 or 25 vol% WC. Density also increased with WC fraction, reaching >99% density. Flexural strength increased up to 10 vol% WC to ∼1200 MPa. Ageing at 1600 °C for 24 hrs significantly degraded strength. Thermal conductivity was reduced by WO_2 inclusions and lower density. Sample thickness was not explicitly stated, though three point bend specimens were 2 mm thick.

Matějíček et al. [73] produced 1.5 mm graded (25 vol% graduations) W/steel interlayers on steel substrates via SPS, and 1–5 µm thick Fe_7W_6 formed at the interface. They suggested that the electrical current aided the diffusion across the interfaces of the graded layers. The graded layers were manufactured by first sintering W only powder at 1600 °C, and then progressively adding layers in 25 vol% steps at 1000 °C. A comparable 50/50 powder mix interlayer was also produced at 1000 °C. Unfortunately, little further information was presented, other than noting that intermetallic phases began to form at 1000 °C. Micrographs are shown in Figure 2.9.

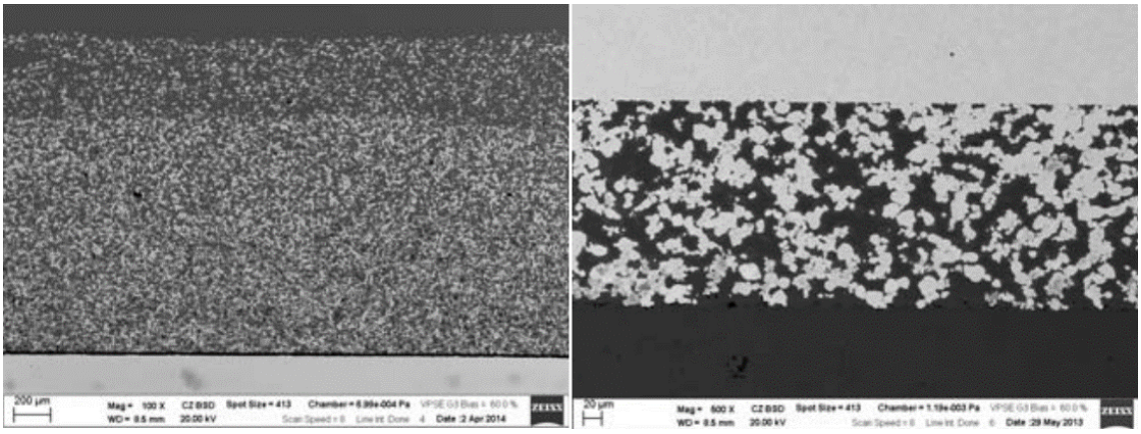


Figure 2.9: Cross-sectional micrographs of: (LHS) an FGM interlayer; (RHS) mixed powder (50/50) interlayer produced by Matějíček et al. to bond steel and W [73][10].

[10]Reprinted from Nukleonika, Volume 60 Issue 2, Jiří Matějíček et al., Overview of processing technologies for tungsten-steel composites and FGMs for fusion applications, 267-273, © copyright (2015), under CC by 4.0.

Cui et al. [74] produced W coatings up to 2 mm thick on steel substrates that had been electro-discharge-machined (EDM) to produce a 'hatched' texture in order to produce vertical segmentation cracks. Their coatings were sintered at 1000 °C at 50 MPa for 10 mins. Samples were thermally cycled 50 times between 300–800 °C; surface cracking was observed on the thinner (1 & 1.5 mm) coatings and a significant proportion of the 2 mm W coating delaminated during testing.

2.2.5 Cold spray

Thermal spray processes are where the projection of a powder feedstock onto a prepared substrate progressively forms a coating from the superposition of many particles. In almost all cases, the powder is heated into the liquid state and deposits as droplets on the substrate. Different techniques have varying heat sources (combustion, plasma, etc.), particle velocities (10–1200 $m{\cdot}s^{-1}$), particle sizes (1–500 µm), and environments (air, inert, vacuum, etc.) which means that not every technique is appropriate for every material. Oxidation of W at high temperatures means special considerations are required for operation in normal atmospheric conditions.

Cold spray is a relatively new variant, in which the powder is heated only to approximately 80% of its melting point in an attempt to suppress surface oxidation, but particles are propelled at particularly high speed (300–1200 $m{\cdot}s^{-1}$ [75]), to undergo rapid deformation on deposition. The high-speed deformation generates high temperature and the particle spreads over the substrate and may yield a strong diffusion/mechanical bond.

Cold spray works best with easily deformed FCC elements. As W is BCC and hard to deform (high modulus, high yield strength, and low toughness) it is not a likely candidate for cold spray deposition. However, Hall et al. [76] hypothesised that coating W powder particles with Cu might facilitate processing. Three powder batches were produced with 10, 15 and 20 wt% Cu and sprayed at 300–400 °C and gas pressure 2.2 MPa to produce coatings ∼250 µm thick. However, the coatings contained less W than the feedstock powder because of separation of W and Cu during spraying. It was noted that better optimisation of spraying parameters was required to minimise particle separation.

Petrovskiy et al. [77] attempted to produce W-Cu cold spray coatings with a variety of compositions, ranging from Cu only to W only on Al substrates at 450 °C. Deposition was successful for all powders except W, with a deposition efficiency close to zero. Even in the more successful composite coatings, the local W composition was significantly lower than targeted. Overall, coating deposition efficiency decreased with increasing W fraction. Unsurprisingly, thermal conductivity decreased with increasing W fraction, whereas microhardness increased (∼200 $W{\cdot}m^{-1}{\cdot}K^{-1}$ and ∼180 HV, respectively for 95 wt% W coatings). The thermal conductivity of deposited Cu was 20% lower than bulk Cu due to defects (such as oxides) on splat boundaries.

Kang et al. [78] produced spherically agglomerated a 75W-25Cu wt% powder through ball-milling and spray-drying. The powder was then cold sprayed at 470 °C to fabricate 600 µm thick coatings on mild steel substrates. There was a segregated microstructure, with some porosity in the W-rich zones. Segregation

was caused by the high velocity impact which separated the constituent parts of the powder. In comparison to the Cu, the W failed to adhere as well due to reduced plastic deformation — this led to void formation in the W regions where particles bounced off.

Cizek et al. [79] cold sprayed four types of powder: pure W, W-10Cr, W-5Ti & W-10–12Cr-5Ti (wt%) onto a variety of substrates (steels and Al 6060 alloy) at 1100 °C and 5 MPa. A 78 µm thick pure W coating was fabricated on the Al alloy, with particles well embedded into the soft substrate. Particles closer to the free surface had less plastic deformation which led to a decrease in deposition efficiency. A similar effect occurred in the W-Cr powders with cracks spanning several particles in a 200 µm thick coating. Ti was added to reduce the extent of cracking; a crack-free coating was produced with W-5Ti powder. The W-10–12Cr-5Ti coating was 450–1100 µm thick. Mechanical alloying improved the mixing of Cr and Ti through the W. The lower processing temperature of cold spray resulted in low oxygen content; oxidation testing showed that Cr had a significant positive impact on oxidation resistance. Further investigation is required to study the thermal response of these W alloys, as it is well-known that increasing alloying content will reduce the operational temperature of the W.

2.2.6 Atmospheric plasma spraying

Plasma spraying involves the injection of a feedstock powder into a hot gas plasma to melt and propel the resulting droplets at high velocity towards a substrate to form a coating. Atmospheric plasma spraying (APS) is the most common form of plasma spraying, as it is very flexible because the plasma allows melting and

deposition of practically any metal, polymer or ceramic material. The process operates in a sound- and light-proof "booth" but does not involve any protective ambient atmosphere, unlike vacuum plasma spraying (VPS). The plasma is usually a collimated Ar-H_2 mixture.

Wang et al. [80] sprayed submicron W powder to produce a 1 mm thick coating on a Cu substrate. Some coatings were annealed under vacuum at 910 °C. As-sprayed coatings had a density of ∼84%; after annealing, the density increased to 89%. Oxygen concentration reduced after annealing from 0.49 wt% to 0.36 wt%. Note that despite use of a Ar-H_2 plasma, significant W oxidation could not be avoided. As-sprayed microhardness was 250–320 HV; after annealing this increased by nearly 150 HV due to the increased density. Thermal conductivity also increased from 30–42 $W{\cdot}m^{-1}{\cdot}K^{-1}$ to 60–80 $W{\cdot}m^{-1}{\cdot}K^{-1}$ across a temperature range between 30 °C and 600 °C following annealing.

Matějíček et al. [81] manufactured graded (25 wt%) W-Cu coatings by APS on Cu and W substrates. The coating thicknesses ranged between 0.41–0.73 mm. There was intimate mixing of the powder in the coatings, however there was significant (unquantified) porosity. Porosity might be reduced by further optimisation of the spray parameters, but little detail was given.

In a different paper by Matějíček et al. [82], different patterns formed by laser texturing of the substrates were investigated to increase adhesive strength. After some preliminary testing on designs, five different textures (some examples are shown in Figure 2.10) were applied to W and steel substrates before APS of W powder to form coatings ∼0.8 mm thick. In an attempt to prevent in-flight oxidation, Matějíček used a mixture of W and WC powders — all WC was completely

converted to W during flight. However, when mechanically tested, no clear trend due to texturing was observed. Steel substrates all failed within the W coating (cohesive failure) between 25–45 MPa in a shear stress test. All but one of the W substrate coatings failed at the substrate-coating interface (adhesive failure) between 10–25 MPa (the exception failed in a mixed adhesive-cohesive manner at approximately 33 MPa — however the same substrate pattern was one of the worst performing steel substrates). Most coatings on textured substrates had higher adhesive strengths than those where the substrates were only grit-blasted. It was proposed that localised melting of the steel substrate led to intermixing of the substrate and coating which formed a stronger, more cohesive interface.

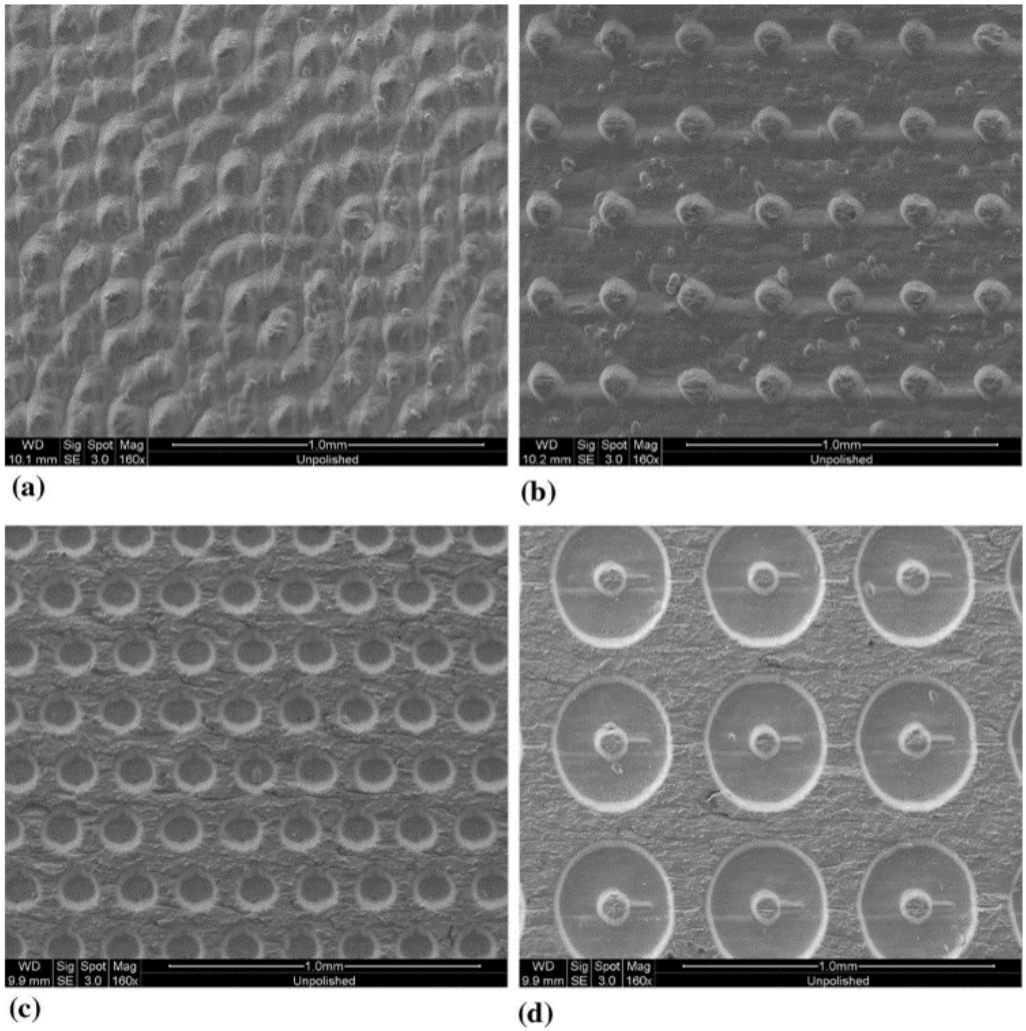


Figure 2.10: Laser textured substrates used by Matějíček et al.: (a) randomly placed grooves; (b) columns; (c) holes; and (d) donut-shaped holes [82][11].

[11]Reprinted from Journal of Thermal Spray Technology, Volume 28 Issue 7, Jiří Matějíček et al., The Role of Laser Texturing in Improving the Adhesion of Plasma Sprayed Tungsten Coatings, 1346-1362, © copyright (2019). Reproduced with permission from Springer Nature.

Heuer et al. [83] sprayed mixed W/steel powders onto steel substrates with different volume fractions (steps of 25%). A FGM was then fabricated by progressively 'stacking' these graduations during spraying. Again, the W powder feedstock contained WC to prevent oxidation in-flight (by preferentially forming CO). Exact thickness of coatings was not stated, but sections suggested ∼2 mm. Micrographs showed reasonable mixing with each coating graduation. When substrates were preheated to 900 °C intermetallic phases formed along the W-steel interface. The highest porosity was 5.5 vol%; oxygen concentration decreased from 6.6 at% to 0.3 at% with increasing W content. Energy dispersive X-ray spectroscopy (EDX) confirmed that the majority of oxides contained Fe and Cr. In comparison to bulk reference W, sprayed W had a higher CTE ($\sim 7.5\times10^{-6}$ K^{-1}) and a lower thermal conductivity ($\sim$42 $W{\cdot}m^{-1}{\cdot}K^{-1}$); sprayed steel had a CTE ($\sim 13\times10^{-6}$ K^{-1}) similar to bulk and a lower thermal conductivity ($\sim$24 $W{\cdot}m^{-1}{\cdot}K^{-1}$). The reduction in thermal conductivity for steel was due to oxide formation, and the poor performance of sprayed W was suggested to have arisen from low interfacial cohesion between W droplet splats. Young's modulus measurements were calculated in-plane and perpendicular to the substrate surface. The ratio of these values was used as an indicator for intersplat bonding (the ratio for an isotropic material would be 1) — this ratio increased from 1.03 for steel-only to 1.18 for W-only, showing poorer interfacial bonding between W splats in comparison with steel. Yield strength and ultimate bending strength were relatively high in sprayed steel (665–813 MPa and 757–863 MPa respectively) in comparison with the bulk (365–450 MPa and

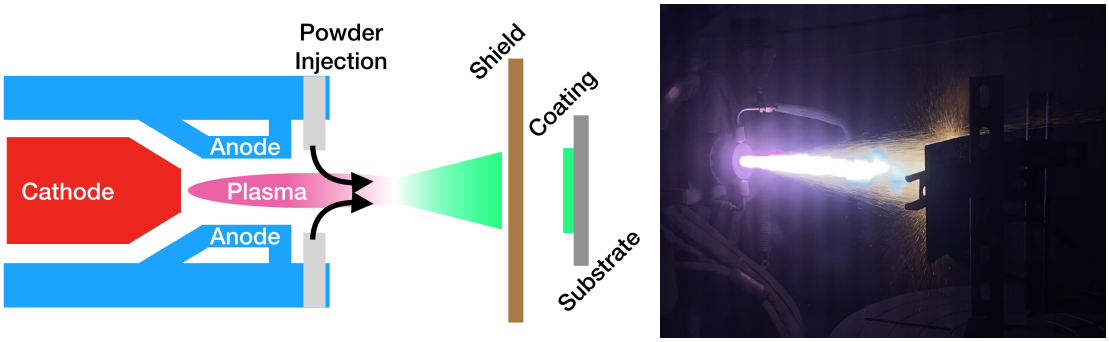
>650 MPa respectively), presumed to be from the residual stresses and small grain size from rapid cooling. Sprayed W (σ_y=557–731 MPa and UTS=629–894 MPa) was weaker than the bulk (σ_y=1050–1360 MPa and UTS=1070–1360 MPa) — this was again attributed to poor interfacial cohesion between splats.

Hu et al. [84] compared APS with VPS — only APS coatings will be discussed here while VPS W coatings are discussed in Section 2.2.7. Graded, ∼80 µm thick Cu/W interfaces were used to secure 1 mm thick coatings on Cu substrates. There were microcracks on the surface of APS coatings with an average grain size of 0.34 µm. Porosity was 10.2% (determined by image analysis) and oxygen concentration was 0.21 wt%. Microhardness was 69% (2.44 GPa) of bulk W, due to oxidation, porosity and other defects. Bonding strength of the APS coating was 22.7 MPa; fracture surfaces revealed that failure occurred at the Cu/W graded interfaces due to Cu and W oxides. Thermal conductivity was 32.2 $W{\cdot}m^{-1}{\cdot}K^{-1}$, and surface temperature at 7.5 $MW{\cdot}m^{-2}$ of thermal loading was 1290 °C, and with significant microcracks on subsequent cooling to room temperature.

2.2.7 Vacuum plasma spraying

Unlike APS, vacuum plasma spraying (VPS) occurs in a sealed chamber which is evacuated and then backfilled with Ar, making it suitable for reactive and O-sensitive metals. Spraying takes place at 20–400 mbar — 'vacuum' is used to distinguish it from APS. In industry, VPS is used to deposit oxidation resistant

CoNiCrAlY 200 µm thick bond coats on Ni superalloy gas turbine components [85] and synthetic bone hydroxyapatite coatings on Ti femur implants [86]. Figure 2.11 (a) displays the schematic operation of the VPS 'torch' that creates the Ar-H_2 plasma, and 2.11 (b) shows the VPS unit in Oxford in operation.



(a) Schematic diagram of the VPS set up.

(b) Plasma (and particles) emitting from the plasma 'gun' during spraying.

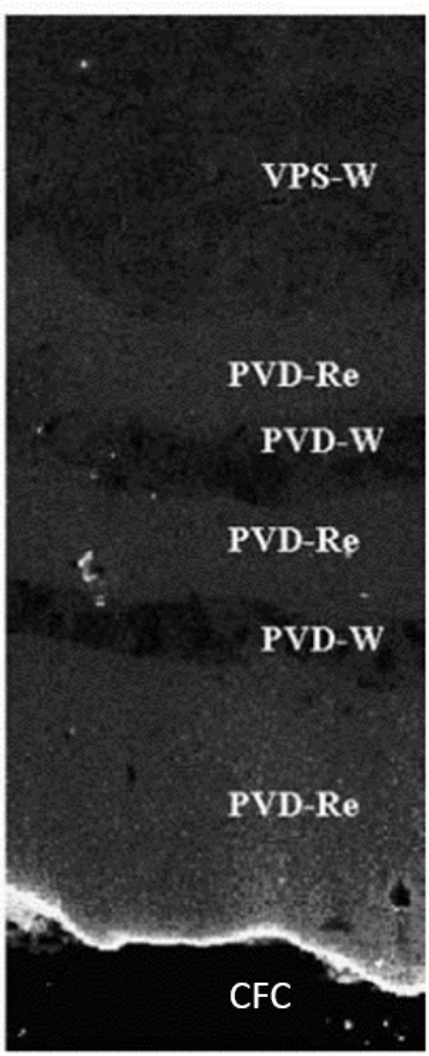
Figure 2.11: VPS schematic and photograph.

Using a similar set-up to produce APS coatings, Hu et al. [84] fabricated 1 mm thick VPS W coatings on Cu substrates with an 80 µm graded Cu/W interface. These coatings were noticeably higher quality: porosity was 2.1% (via image analysis; APS was 10.2%); oxygen concentration was 0.07 wt% (0.21 wt% in APS); and microcracking was not apparent from initial microscopy, which was attributed to the reduced pressure, inert atmosphere leading to higher energy impacts and droplet deformation. Grain size was larger in VPS (0.78 µm) than in APS (0.34 µm) — due to the slower convective cooling rate in the reduced pressure VPS. Microhardness was 2.71 GPa (77% of bulk W) and the bonding strength was 44.8 MPa — almost double that achieved in APS. Fractography showed that failure occurred at the Cu/interlayer interface, rather than within the graded interlayer.

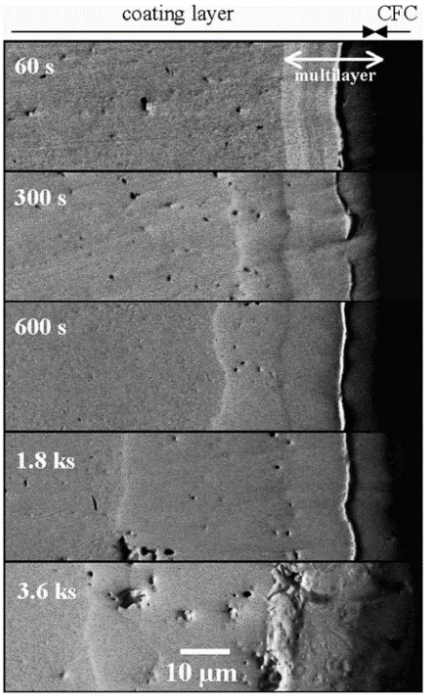
Thermal conductivity of 59.3 $W \cdot m^{-1} \cdot K^{-1}$ was also much higher than that achieved in APS (32.2 $W \cdot m^{-1} \cdot K^{-1}$). The larger grain size (fewer grain boundaries) and lack of oxides were suggested to be the causes of the improved thermal conductivity. High thermal conductivity had a positive effect on thermal loading performance: at 10.75 $MW \cdot m^{-2}$ the surface temperature was 1160 °C whereas with a lower 7.5 $MW \cdot m^{-2}$ thermal load the APS surface temperature was 1290 °C. Furthermore, microcracks that formed on cooling in the APS coatings did not occur in the VPS coatings.

García-Rosales et al. [66] compared W coatings by VPS with PVD on graphite substrates with Re interlayers to prevent carbide formation. VPS coatings were heat treated for 1 hr at 1400 °C. VPS coatings were substantially thicker (550 µm) than the PVD coatings (100 µm). They also tolerated a higher electron beam power density of 15.8 $MW \cdot m^{-2}$ with 2 s pulses, rather than 15.3 $MW \cdot m^{-2}$ with 1 s pulses for the PVD coating. However, VPS porosity was higher (8–9%) than PVD (<1%). It was suggested that this porosity acted as a crack arresting mechanism during thermal cycling experiments: the 20 µm PVD sample failed after 261 cycles, whereas at the same power density (10 $MW \cdot m^{-2}$), the VPS sample did not fail after 1000 cycles. Other possible explanations for the improved toughness could be: the finer grain size observed in the VPS sample; the thicker coating, which may have provided better protection from the imposed heat flux; or the heat treatment, which may have caused diffusion to occur, resulting in improved coating adhesion. The Re interlayer was a successful diffusion barrier to carbon once initial WC and W_2C layers formed during heat treatment.

Following a similar idea to García-Rosales et al., Tamura et al. [87] fabricated 0.5 mm thick VPS W coatings on a carbon fibre composite (CFC) with multiple interlayers of W and Re applied by PVD, shown in Figure 2.12 (a), in an attempt to prevent carbon diffusion, which leads to carbide formation. This sample was then heat treated at 1300 °C (duration not stated). The average density of the W coating was 85%. A variety of annealing conditions were then tested, with temperature ranging between 1400–2000 °C and annealing time between 60–3600 s. The PVD "multi-layer" was still visible after 3600 s at 1400 °C — however, at (and beyond) 1600 °C for 300 s, the multi-layer was changed and carbide layers began to form, shown in Figure 2.12 (b). X-ray diffraction (XRD) showed the formation of ReW, WC and W_2C in a layer. Formation rates of carbides at different temperatures were observed; there was a diffusion barrier that slowed carbide formation below 1800 °C.



(a) Cross-section of multiple PVD interlayers after annealing at 1400 °C for 3.6 ks.



(b) A series of backscattered SEM images showing the evolution of the W-Re multi-layer at 1600 °C for various annealing times.

Figure 2.12: Two SEM images of similar multi-layer material, highlighting the diffusion of C through the multi-layer at temperatures above 1600 °C [87][12].

[12]Reprinted from Journal of Nuclear Materials, Volume 329, Satoshi Tamura et al., High-temperature properties of joint interface of VPS-tungsten coated CFC, 711-716, © copyright (2004), with permission from Elsevier.

Thomas et al. [88] investigated sprayed FGMs and surface texturing separately for VPS coatings on steel substrates to reduce residual stresses. FEM was used to lead investigations into both areas, predicting stress distributions in the different coatings. Several types of FGM were investigated including a 5-layer (composition steps of 25%) W/steel FGM with a 100 µm sprayed pure W coating at the surface shown in Figure 2.13. Porosity was not stated but a small fraction apparent in the micrograph is highlighted by yellow circles — the difference in contrast makes it difficult to observe any porosity in the mixed layers. It was noted that complete mixing of the W and steel powders was not achieved within each layer and likely derived from separate W and steel streams of particles in the plasma itself (as they were injected from different powder hoppers). Beyond microstructural analysis, there was no further physical testing of the FGMs.

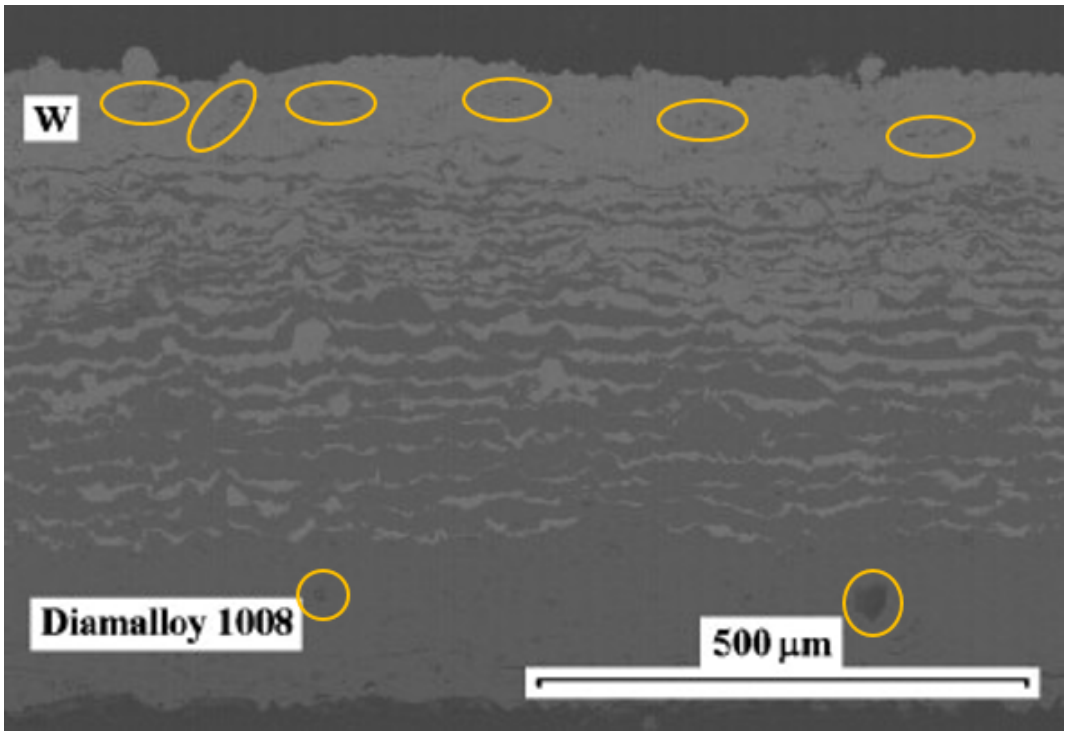


Figure 2.13: Cross-sectional SEM image of the FGM sprayed by Thomas [88][13].

Four types of textured substrates were produced via "Surfi-Sculpt", a localised melting process controlled by a focussed electron beam, and are shown in Figure 2.14. The stress concentration around geometric features was calculated to be between 1.2–1.6 GPa for all geometries. Only one Surfi-Sculpt geometry led to thick (1–1.5 mm) coatings that were integral after manufacture with good cohesion (shown in the bottom right of Figure 2.14). It was suggested that as well as promoting mechanical adhesion of the W, the 'sculptured' surface also induced regular micro-cracking of the W as a means to reduce the inevitable build up of stored strain energy due to CTE mismatch during thermal excursions. The effect of microcracking was to avoid uncontrolled cracking along a conventional planar W-steel interface, and to create a micro-cracked, ultra-low-modulus coating that could not develop any significant residual strain in the future.

[13]Reprinted from Materials Science and Engineering: A, Volume 447 Issue 1-2, Gareth Thomas et al., Interface topography and residual stress distributions in W coatings for fusion armour applications, 35-42, © copyright (2008), with permission from Elsevier.

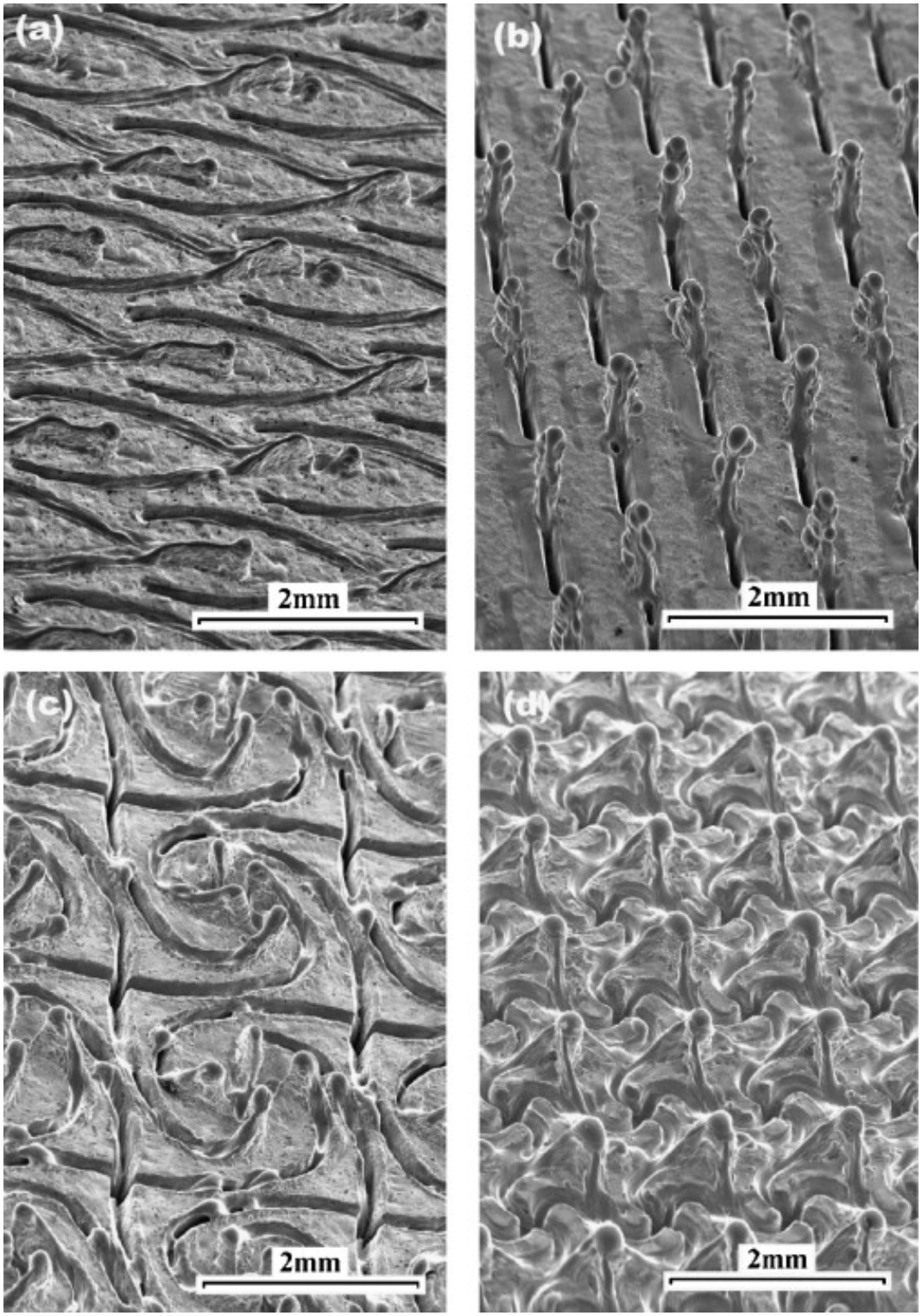


Figure 2.14: SEM images of the Surfi-Sculpt substrates used by Thomas [88][14].

2.2.8 Summary of Manufacturing Processes

Some of the range of manufacturing processes, coating arrangements and material properties are summarised in Table 2.2 and shown graphically in Figure 2.15.

With the exception of diffusion bonding and CVD, W coating thicknesses are currently too low (4 mm minimum requirement) for use in a reactor. Diffusion bonding is the current industry standard, however it requires significant preparation, which means it is relatively expensive and not very fast. While effective, CVD faces challenges in terms of the time required to build up sufficient coating thickness and scalability, which is dependent on chamber size. Thermal spraying techniques have the potential to produce thick coatings at an industrial level, and thermal spray use is mature in other industries. VPS is a leading candidate for achieving higher quality (more dense with fewer impurities) coatings. Conversely, research on SPS, especially in the context of W coatings, remains relatively limited and warrants further investigation, due to the short processing times compared with diffusion bonding.

[14]Reprinted from Materials Science and Engineering: A, Volume 447 Issue 1-2, Gareth Thomas et al., Interface topography and residual stress distributions in W coatings for fusion armour applications, 35-42, © copyright (2008), with permission from Elsevier.

Table 2.2: Summary table listing reported processes and properties of W coatings.

Lead Author	**Process**	**Substrate**	**Interlayer**	**Thickness**	**Density**	**Other Properties**
Basuki [56]	Diffusion Bonding	EUROFER-97	Nb	16 mm	N/A	-
Basuki [57]	Diffusion Bonding	EUROFER-97	V	16 mm	N/A	-
Cai [58]	Diffusion Bonding	Steel	V/Cu & V/Ni	13 mm	N/A	402 MPa (joint strength for V/Cu)
Lian [62]	CVD	Cu	-	1.2–3.3 mm	-	160 $MW{\cdot}m^{-2}$ (cyclic thermal loading)
Chen [63]	CVD	CuCrZr	FGM	2 mm	-	11 $MW{\cdot}m^{-2}$ (cyclic thermal loading)
García-Rosales [66]	PVD	Graphite	Re	100 µm	99%	7.9 $MW{\cdot}m^{-2}$ (cyclic thermal loading)
Weber [67]	PVD	EUROFER-97	FGM	1 mm	-	Cracking with 10 thermal cycles
Matějíček [71]	SPS	N/A	N/A	2–3 mm	-	1550 MPa (flexural strength) ∼90% ITER Thermal Conductivity (TC)

Continued on next page

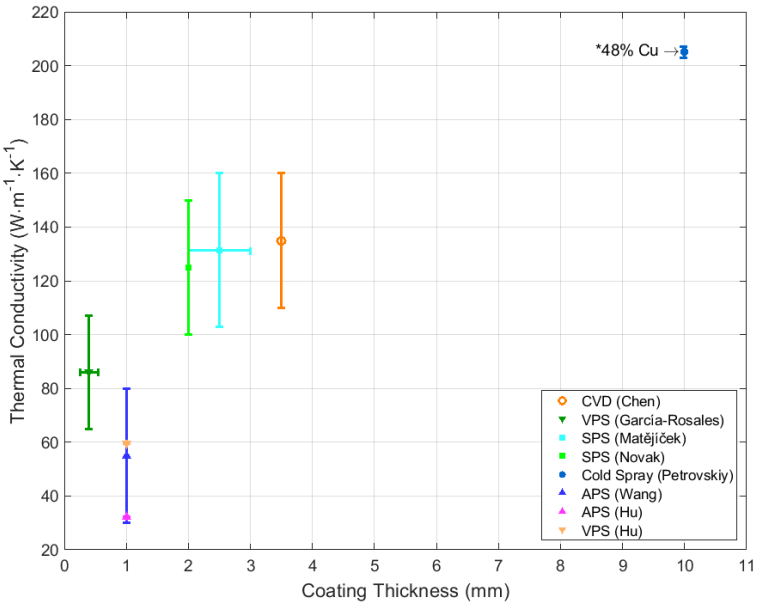
Table 2.2: Summary table listing reported processes and properties of W coatings. (Continued)

Lead Author	**Process**	**Substrate**	**Interlayer**	**Thickness**	**Density**	**Other Properties**
Novak [72]	SPS	N/A	N/A	2 mm	99%	1200 MPa (flexural strength) ∼80% ITER TC
Matějíček [73]	SPS	Steel	FGM	1.5 mm	-	Fe_7W_6 forms above 1000 °C
Cui [74]	SPS	Steel	-	1–2 mm	-	50 cycles between 300–800 °C 2 mm coating delaminated
Hall [76]	Cold Spray	-	-	0.26 mm	-	Mixed W/Cu Powder
Petroviskiy [77]	Cold Spray	Al	-	>10 mm	-	Mixed W/Cu Powder ∼180 HV (microhardness) ∼200 $W{\cdot}m^{-1}{\cdot}K^{-1}$ (TC)
Kang [78]	Cold Spray	Steel	-	0.6 mm	-	Mixed W/Cu Powder
Cizek [79]	Cold Spray	Steel	-	1.1 mm	-	Mixed W/Cr/Ti Powder
Wang [80]	APS	Cu	-	1 mm	89%	∼470 HV (microhardness) 60–80 $W{\cdot}m^{-1}{\cdot}K^{-1}$ (TC)
Matějíček [81]	APS	Cu & W	FGM	0.9 mm	-	-

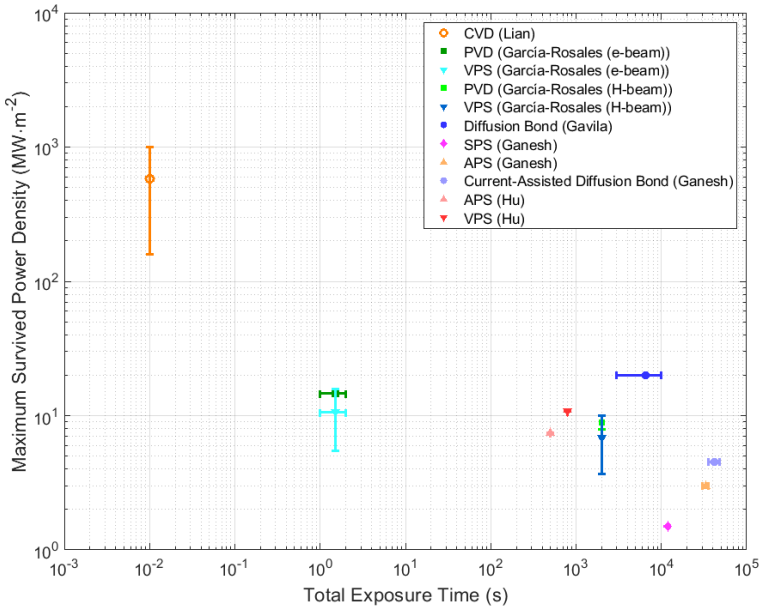
Continued on next page

Table 2.2: Summary table listing reported processes and properties of W coatings. (Continued)

Lead Author	**Process**	**Substrate**	**Interlayer**	**Thickness**	**Density**	**Other Properties**
Matějíček [82]	APS	Steel & W	-	0.8 mm	-	Laser Texturing 25–45 MPa (shear)
Heuer [83]	APS	Steel	FGM	2 mm	94–98%	600–900 MPa (UTS for pure W)
Hu [84]	APS	Cu	Cu/W FGM	1 mm	90%	2.4 GPa (microhardness) 22.7 MPa (bond strength) 32.2 $W \cdot m^{-1} \cdot K^{-1}$ (TC)
Hu [84]	VPS	Cu	Cu/W FGM	1 mm	98%	2.7 GPa (microhardness) 44.8 MPa (bond strength) 59.3 $W \cdot m^{-1} \cdot K^{-1}$ (TC)
García-Rosales [66]	VPS	Graphite	Re	550 µm	91–92%	10 $MW \cdot m^{-2}$ (cyclic thermal loading)
Tamura [87]	VPS	CFC	W & Re	0.5 mm	85%	PVD multilayer works up to 1600 °C
Thomas [88]	VPS	Steel	-	∼0.8–1.5 mm	-	FGM & Substrate Texturing



(a) Graphical representation of range of coating thicknesses and thermal conductivities across various manufacturing techniques.



(b) Graphical representation of the highest power density and total exposure times that samples survived for various manufacturing techniques.

Figure 2.15: Two summary graphs comparing the reported manufacturing techniques discussed in Table 2.2.

2.3 Fusion-relevant thermal testing

2.3.1 Why do we need fusion-relevant testing?

With the wide variety of proposed manufacturing techniques and the harsh environments that the W PFCs are required to withstand, it is of paramount importance that materials are thoroughly validated prior to installation and use in a fusion reactor. However, the unique neutron energy spectrum produced during fusion and the predicted lifetime dosage for the materials used in the reactor makes it nearly impossible to test effectively in the 'real' fusion environment. Fission reactors can be utilised to an extent; however, the high energy 14 MeV neutrons produced in fusion cannot be replicated. Figure 2.16 shows the comparison of neutron flux profiles for the DEMO fusion reactor (predicted) and three types of fission reactor [89].

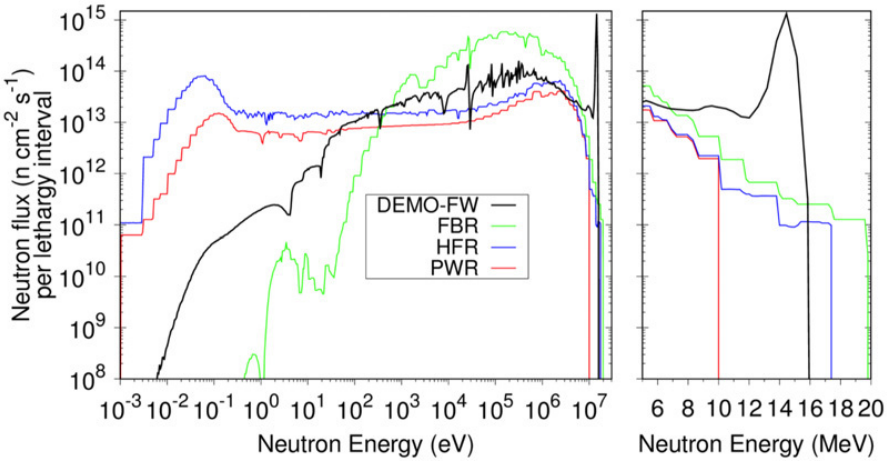


Figure 2.16: Neutron flux spectra for different nuclear reactor types (fusion, fast breeder, high flux and pressurised water) [89][15].

[15]Reprinted from EPJ Web of Conferences, Volume 146, Jean-Christophe Sublet et al., From cutting-edge pointwise cross-section to groupwise reaction rate: A primer, 02003, © copyright (2017), under CC by 4.0.

Other fusion-relevant testing methods are therefore required to build confidence in the proposed materials to be used. At such close proximity to the fusion reaction, the PFCs are largely transparent to the high-energy neutrons, with only ∼10% of the incident neutron energy deposited in the FW [90]. Consequently, the priority of PFCs is to stop/absorb thermal energy and other particles emanating from the plasma, with the underlying breeder blanket used to capture and convert neutrons to tritium.

The expected heat loads can be split into two categories: stationary heat loads from standard operation (most likely pulsed), and transient 'off-normal' events, such as edge-localised modes (ELMs), that occur during operation. ELMs occur with a frequency in the order of a few Hz. Figure 2.17 shows a schematic of the heat loads [91].

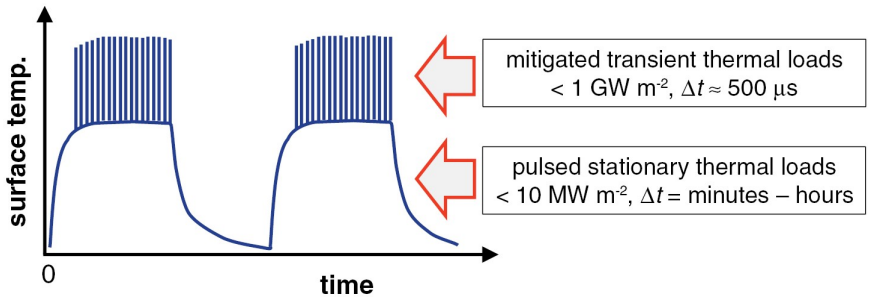


Figure 2.17: Schematic of PFC surface temperature in a fusion device during operation, showing the two types of applied heat load: pulsed steady-state thermal loading with fast transient ELM-loads which increase the temperature further during H-mode operation [91][16].

[16]Reprinted from Nuclear Fusion, Volume 57 Issue 9, Christian Linsmeier et al., Material testing facilities and programs for plasma-facing component testing, 092012, © copyright (2017), under CC by 3.0.

2.3.2 Steady-state heat load testing

Survival of PFC materials at sustained elevated temperatures throughout the lifetime of the component is the most important property, and potentially the easiest to verify. As tokamak design and control continue to develop, it is anticipated that the pulse length will increase until eventually operation is continuous, such as in a stellarator [92]. Moreover, if a liquid metal breeder blanket is used, then the reactor will need to be kept above the melting temperature of the liquid metal, even outside of operation (180 °C for Li and 230–245 °C for PbLi).

Thermal ageing of samples is an effective initial assessment technique for evaluating prospective PFC materials before performing more complex testing. Thermal ageing studies can reveal diffusion-related effects, such as the formation of new phases (e.g. at interfaces) and microstructural changes, which are key to understanding how a material will perform over an extended period within a fusion reactor. Reisner et al. investigated the interdiffusion between a magnetron-sputtered 1 µm W coating on an Fe substrate for different annealing time and temperatures. Above 1000 K a Fe_2W phase formed with a growth rate coefficient of 1.0×10^{-18} $m^2 \cdot s^{-1}$ at 1050 K, and 2.8×10^{-18} $m^2 \cdot s^{-1}$ at 1100 K [93]. Heuer et al. investigated constituent parts of a functionally-graded (25 vol% steps) W-Fe composite to determine their feasibility for use in a fusion reactor. High W fraction (50 & 75 vol%) components were aged for up to 72 hrs at a range of temperatures (300–800 °C). A combination of pure-W, pure-Fe, solid solution ($Fe_{0.95}W_{0.05}$) and Fe_7W_6 phases was observed, but no Fe_2W after ageing. Notched microcantilevers were produced at the W-Fe interfaces using a focussed ion beam (FIB) and a fracture toughness of $\sim$1.85 MPa$\cdot\sqrt{\text{m}}$ was measured (approximately 3$\times$ more brittle

than pure W) [94]. Wang et al. varied Ni-Si-B interlayer thickness to study the affect on the shear strength of W-steel joints. As interlayer thickness increased, so did joint strength up to 5.3 µm (363.5 MPa), because more diffusion occurred between the interlayer and the steel and W. Beyond this limit, shear strength decreased as the thicker interlayers formed joints with an increasing number of voids. No reference sample was tested to provide a comparison [95].

The Heating by Induction to Verify Extremes (HIVE) facility at Culham Centre for Fusion Energy (CCFE) was specifically built for thermal cycling testing of prospective fusion materials. Cui et al. manufactured W coatings up to 2 mm thick on patterned steel substrates using the FAST. The samples showed visible surface cracking (deliberately induced to facilitate a low modulus) following manufacture and were then cycled between 300–800 °C for 50 cycles. Thinner coatings (1–1.5 mm) survived cycling, but a significant proportion of the 2 mm coating delaminated [74]. Pearl et al. cycled a 5 mm thick W-6 wt%Ta coating produced by laser powder bed additive manufacture (the top 3 mm being a lattice structure) that was brazed onto a copper heat sink. 507 of the 606 total recorded pulses delivered heat fluxes between 8-10 $MW{\cdot}m^{-2}$, which corresponded to a maximum temperature of ∼3000 °C, measured by an infra-red (IR) camera. Visual inspection following testing identified some cracking on the surface between lattice pores and a larger crack on one side of the structure, where the lattice structure transitioned into solid W-Ta alloy. The area around the larger crack took longer to cool as the thermal conductivity was reduced locally [96].

2.3.3 Transient heat load testing

Since reactors will experience intermittent bursts of high-energy plasma, transient heat load testing is important to ensure that PFCs will survive the elevated heat fluxes. Several methods are employed to simulate transient heat loads, including ion irradiation [97–99], electron-beam irradiation [100–104], and plasma irradiation by means of linear plasma devices [69, 105–109]. The parameters used for ion and plasma irradiation can be adapted to provide a constant heat flux, and can therefore also facilitate steady-state testing. Some studies have combined and compared these techniques to an extent [110, 111], and a suggested framework [112] has been produced to compare the variety of facilities better.

Ion irradiation

Ion irradiation facilities, such as GLADIS[17] [97] and MARION[18] [98, 99], work by accelerating charged ions to high energies towards the surface of the tested material, simulating the effects of particle bombardment as experienced in fusion reactor environments.

Nemati et al. compared steady-state heating (in a furnace) with transient thermal cycling using a neutral H beam in GLADIS, both at 1500 °C and 2100 °C for comparable times. After 1500 °C testing, W monoblock 'mock-ups' had recrystallised and were comparable between both heating techniques. However, after annealing at 2100 °C, they were significantly less hard, whereas by comparison, cycled monoblocks had a minimal reduction in hardness. Annealed W monoblocks had a relatively uniform grain size following heat treatment, whereas significant grain

[17] **G**arching **LA**rge **DI**vertor **S**ample test facility
[18] **MA**terial **R**esearch **ION** beam test stand

growth was observed at the surface when cycled. The overall grain size in the cycled sample was smaller than in the annealed, and higher dislocation densities were observed in the large surface grains — both of these factors resulted in the higher measured hardness in comparison to the equivalent annealed sample [113]. Neu et al. produced 2 mm thick, cold-sprayed W-Ta coatings on steel substrates which were then tested using an H beam in GLADIS. There was no coating deterioration during initial screening pulses up to 800 °C. Components were then exposed to a heat flux of 40 $MW \cdot m^{-2}$ for 200 ms, which resulted in surface temperatures of 1400 °C and delamination within the coatings (near the interface) [114].

Parish et al. irradiated high-purity W at 1130 °C with He ions in the Multicharged Ion Research Facility (MIRF) at Oak Ridge National Laboratory (ORNL). Four surface morphology changes were identified which were dependent on crystal orientation: pyramidal ({001}), smooth ({103}), wavy and stepped/terraced ({114}–{112}). An unirradiated, but otherwise identical sample was compared: grain growth and texture were similar but there were no surface morphology changes. Figure 2.18 shows a selection of micrographs that highlight the different surface morphology types [115].

[19] Reprinted from Acta Materialia, Volume 62, Chad Parish et al., Effect of tungsten crystallographic orientation on He-ion-induced surface morphology changes, 173-181, © copyright (2014), with permission from Elsevier.

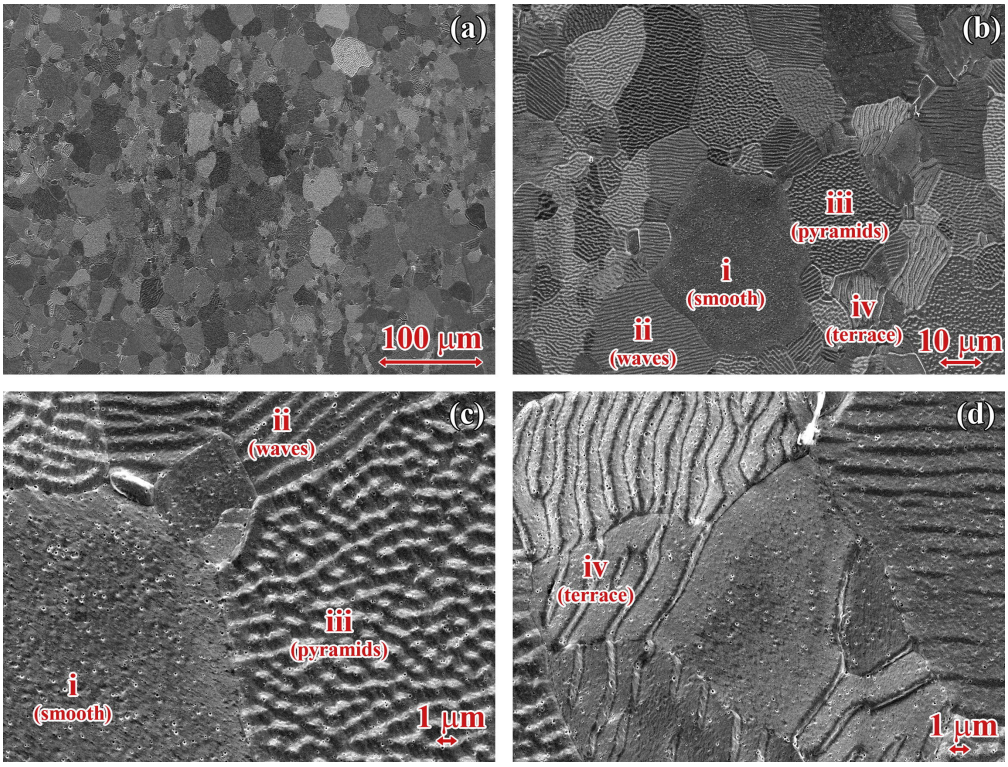


Figure 2.18: SEM images of the different surface morphologies of W produced by He irradiation observed by Parish et al. [115][19].

Electron beam irradiation

Electron beam facilities, such as JUDITH[20] 1 & 2 [100, 101], JEBIS[21] [102] and EMS-60[23] [103], generate intense transient heat loads by accelerating high-energy electrons at a material's surface.

Ganesh et al. compared different W-steel FGMs manufactured using APS (with a diffusion-bonded V interlayer to a bulk W surface coating) and SPS with diffusion-bonded W coatings on steel substrates (including one with a thick V interlayer). The W-steel composites were brazed onto a copper heat sink and were tested in JUDITH 2 for 1600 cycles (increasing the incident heat flux from 1.0 $MW{\cdot}m^{-2}$ by 0.5 $MW{\cdot}m^{-2}$ every 200 cycles up to 4.5 $MW{\cdot}m^{-2}$). The reference diffusion-bonded W with no interlayer performed best, with failure occurring during cycles at 4.0-4.5 $MW{\cdot}m^{-2}$ due to delamination occurring at the edge of the coating. The APS FGM failed during the 3.5 $MW{\cdot}m^{-2}$ cycles at the top of the FGM and between the V interlayer and the W coating. The reference diffusion-bonded W with V interlayer composite failed at the beginning of the 3.5 $MW{\cdot}m^{-2}$ cycling due to delamination between the V and W. The FGM SPS composite failed at the beginning of the 2 $MW{\cdot}m^{-2}$ cycles because of delamination between the top FGM layer and the W surface coating. The APS FGM with V interlayer had a lower thermal conductivity (20 $W{\cdot}m^{-1}K^{-1}$) than V (31 $W{\cdot}m^{-1}K^{-1}$), which resulted in higher surface temperatures for the same incident heat flux. The SPS FGM had a higher theoretical thermal conductivity (45 $W{\cdot}m^{-1}K^{-1}$), but due to the high defect density in the interlayer it had the highest surface temperature of all.

[20] **Jü**lich **Di**vertor **T**est Facility in **H**ot Cells
[21] **J**AERI[22] **E**lectron **B**eam **I**rradiation **S**ystem
[22] **J**apan **A**tomic **E**nergy **R**esearch **I**nstitute
[23] **E**lectron-beam **M**aterial-test **S**cenario

Nakamura et al. studied thermal shock at room temperature and at 1000 °C for four types of tungsten: CVD, monocrystal, powder sintered and brush. Brush W comprises fine bundles of W fibres (0.2 mm diameter fibres in this study) often held together with Cu melted to the base to facilitate further diffusion bonding. The W samples were exposed to a single electron beam pulse in JEBIS. Pulses lasted 2 ms, with a peak heat flux of 1000–2400 $MW \cdot m^{-2}$. Damage was exhibited for all types of W at room temperature; mostly cracking perpendicular to the surface. No observable damage was found when preheated, however mass loss was increased. Significant grain growth was visible at the surface of all samples [102].

Lian et al. used the EMS-60 facility to test CVD W (removed from a copper substrate) compared with hot-rolled commercially pure W. Two tests were performed to simulate disruptions and ELMs. Disruption-like tests were 5 ms single shots at 0.16–1.0 $GW \cdot m^{-2}$, whereas ELM-like tests consisted of 100 pulses at the same heat flux for 1 ms with a 5 s cool-down window. Base temperature was varied between room temperature and 600 °C. CVD W out-performed the hot-rolled W at room temperature, with cracking occurring between 0.28–0.33 $GW \cdot m^{-2}$ in comparison to <0.22 $GW \cdot m^{-2}$. At 200 °C the CVD W did not crack, whereas the hot-rolled W had discontinuous cracking at 400–600 °C. Similarly, for ELM-like tests, cracking occurred up to 400 °C for the hot-rolled W, but only up to 200 °C for the CVD. The heat flux threshold was 0.16–0.22 $GW \cdot m^{-2}$ for both types of W at room temperature. It was suggested that survival was more likely for the CVD W as grains were columnar in comparison to equiaxed grains observed in the hot-rolled W [103].

Pure W and W-1 wt%La_2O_3 manufactured using the FAST and reference bulk (Plansee) W were tested by Kanpara et al. using an electron beam in the High Heat Flux Test Facility (HHFTF). Samples were exposed for 500 pulses with an energy density of 1.0–3.14 MJ·m^{-2} for 20 ms and a cool-down time of 1 s. Significant cracking was observed following testing in the W-La_2O_3 which was attributed to the difference in CTE between W and La_2O_3. Cracking appeared to have occurred following FAST manufacture for both pure W and W-La_2O_3 prior to testing, but was not reported [104].

Linear plasma devices

Linear plasma devices, such as PLM (I & II) [106, 107], SNU-HLT[24] [69, 108] and Magnum-PSI [105], are experimental devices designed to produce a controlled flow of plasma towards the material being tested. This setup allows researchers to simulate the plasma-surface interactions (PSI) that occur in fusion reactors during operation. While linear plasma devices often operate in a steady-state mode, some have the capability of applying transient conditions on top of this steady state, using methods such as capacitor bank discharge [116] or a high-power laser beam.

When exposed to a high-energy helium plasma, W surfaces form a 'fuzz'. This fuzzy layer consists of fine, hair-like structures and originates from the coalescence of helium bubbles within the W. As helium ions bombard the surface, they become trapped within the material and cluster to form the distinctive fuzzy structures. Fuzz growth condition and rate are relatively well understood, but deposition effects are of interest as the fuzz protrudes from the W surface and can easily break off and form a dust which enters and cools the plasma and can cause arcing. The thermal conductivity of fuzzy samples has also been shown to be two orders of magnitude lower than bulk W [117–119].

Budaev et al. studied ITER mock-ups brazed onto CuCrZr. They were first thermally cycled at 40 $MW{\cdot}m^{-2}$ (1 s heating and cooling for 100 cycles, surface temperature was 1000–1400 °C) in the electron beam facility, AELTK-12–244, before being exposed to a steady-state (0.5–1.0 $MW{\cdot}m^{-2}$) He plasma for up to 200 mins in the PLM plasma device. Cycled testing resulted in cracking, and fuzz formation on the surface occurred during plasma irradiation. Further testing

[24] **S**eoul **N**ational **U**niversity Thermal Loading Test Facility

of W samples produced a fuzz layer 1.6 µm thick, with fuzz fibre diameters in the range of 20–50 nm. The fuzzy surface was subjected to an electron beam with heat fluxes up to 49 $MW{\cdot}m^{-2}$, which only slightly melted the fuzz fibre edges. Average surface temperature was estimated to be 900–1400 °C, however the fine microstructure of the fuzz will have resulted in highly-localised heating [120]. Budaev et al. further studied W fuzz layers in a He plasma with a high-powered (2.1×10^{13} $W{\cdot}m^{-2}$) Nd:YAG (neodymium-doped yttrium aluminium garnet) laser. The laser was pulsed (10 ns) in order to "ignite" arcing between the negatively-biased sample and the near-wall plasma; the resulting damage can be seen in Figure 2.19. Fuzz fibres were melted and micron-scale craters produced, as well as localised cracking [121].

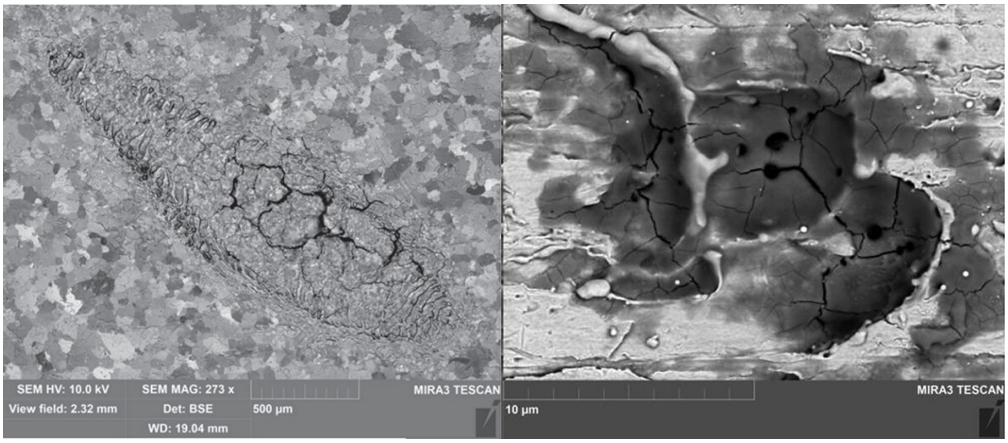


Figure 2.19: SEM images of surface of W fuzz following laser arc ignition by Budaev et al. [121][25].

[25]Reprinted from Fusion Science and Technology, Volume 79 Issue 4, Viacheslav Budaev et al., Erosion of Fuzz Layers Formed in Steady-State Plasma Discharge, 407-412, © copyright (2023), by permission of Informa UK Limited, trading as Taylor & Taylor & Francis Group, http://www.tandfonline.com.

Kim et al. produced APS W coatings on a graphite substrate with a Mo interlayer and compared it with cold-worked bulk W. Bulk W samples were plasma-irradiated in the SNU-HLT facility with a heat flux of 5–7 $MW{\cdot}m^{-2}$, which resulted in surface temperatures higher than 1750 °C. Whilst plasma gas composition was not explicitly stated, a figure suggested that an Ar/N_2 mixture (unstated ratio) was used. Grains recrystallised and grew, which resulted in surface roughening. The longer that samples were exposed, the thicker the recrystallisation layer was. FIB cross-sections showed that bubbles and cracks also occurred towards the surface. APS samples were irradiated with a lower heat flux (4.3–4.7 $MW{\cdot}m^{-2}$) but had higher surface temperatures (2190–2479 °C) than the bulk W. Cross-sectional SEM images showed that heating "destroyed" the interlayer between splats as they merged vertically. It was concluded that because heat loads annealed the APS W coatings, they would be better than bulk W for long pulse durations. However, APS W would be worse for shorter pulses because the interlayer between splats acted as a thermal barrier which reduced thermal shock resistance [108]. Choi et al. produced high density SPS W (>99.9 %) with a two-step (heat to 1700 °C and hold for 5 mins at 1400 °C) sintering process and by reducing the O content on the W powder by annealing it for 1 hr at 1100 °C in a 100% H_2 atmosphere prior to sintering. This sample was exposed to a 4 $MW{\cdot}m^{-2}$, N_2 plasma in SNU-HLT for 300 s, along with a W mono-block sample for comparison. Surface temperatures were approximately 2300 °C. There was grain growth in both samples, however this effect was significantly larger in the commercial W; SPS W average grain size

increased from 4.4 to 6.4 µm, whereas commercial W increased from 4.2 to 35.3 µm. Changes in measured sample hardness were also observed: monoblock W hardness decreased from 389 to 303 HV, whereas SPS W softened from 370 to 340 HV [69].

Yin et al. irradiated pure W and three W alloys (W-5–10 wt%V, W-0.5 wt%Y_2O_3 and W-0.5 wt%ZrC) with a deuterium (D) plasma in the Simulator for Tokamak Edge Plasma facility. Exposure time and heat flux were not stated; however, the flux and fluence for each sample type stated are shown in Table 2.3 along with exposure times calculated from these values. Surface temperatures were ∼180 °C. Surface blistering decreased with increasing V content, and with the addition of oxides and carbides. It was suggested that oxide and carbide additions had a similar effect microstructurally, by strengthening the grain boundaries. This then prevented large blisters from covering several grains. It was also suggested that the D concentration was reduced in the W and suppressed the onset of blistering as the V preferentially dissolved it [109].

Sample type	Fluence (m^{-2})	Flux ($m^{-2}{\cdot}s^{-1}$)	Calculated Exposure Time
Pure W	5.6×10^{25}	4.6×10^{21}	3 hrs 20 mins
W-V	5.6×10^{25}	4.6×10^{21}	3 hrs 20 mins
W-Y_2O_3	1.3×10^{26}	1.2×10^{22}	3 hrs
W-ZrC	7.0×10^{25}	5.0×10^{21}	3 hrs 50 mins

Table 2.3: Applied fluences and fluxes on samples tested by Yin et al. [109] and calculated exposure times.

Li et al. also studied the effect of Y_2O_3 and TiC additions in W. W-1 wt%TiC and W-2 wt%Y_2O_3 alloys manufactured by powder-injection moulding and were compared with pure hot-rolled W. These samples were exposed to a H_2 plasma in Magnum-PSI for 1000–5000 transient pulses (1 Hz and 5 Hz respectively) that were superimposed on the steady-state plasma (base temperatures 1500 & 2000 °C, heat flux 3.75 & 13.3 MW·m^{-2} respectively) using a multi-pulse ELM replication system (peak temperature excursions 225 & 50 °C, heat flux 600 & 460 MW·m^{-2} respectively) [122]. The replication system is a modular capacitor bank consisting of 28 identical sections that can be independently charged (to 3000V) and discharged sequentially to apply transient pulses up to 100 Hz [123]. Figure 2.20 shows the microstructure for each exposure. Increasing pulse repetition rate resulted in higher levels of damage in the pure hot-rolled W. Oxide and carbide inclusions produced a high density of microcracks that formed at grain boundaries. Increasing the number of pulses had little effect on the cracking behaviour, but increasing the base temperature caused a single large crack to develop across each surface. Grain growth was also observed for W alloys. It was suggested that more cracking occurred in the alloys because the ceramic particles suppressed plasticity at the grain boundaries. These cracks relieved transient thermal stress but intensified the steady-state thermal stress, which promoted crack propagation [122].

[26]Reprinted from Nuclear Fusion, Volume 60 Issue 4, Yu Li et al., Fracture behavior of tungsten-based composites exposed to steady-state/transient hydrogen plasma, 046029, © copyright (2020), with permission from the IAEA.

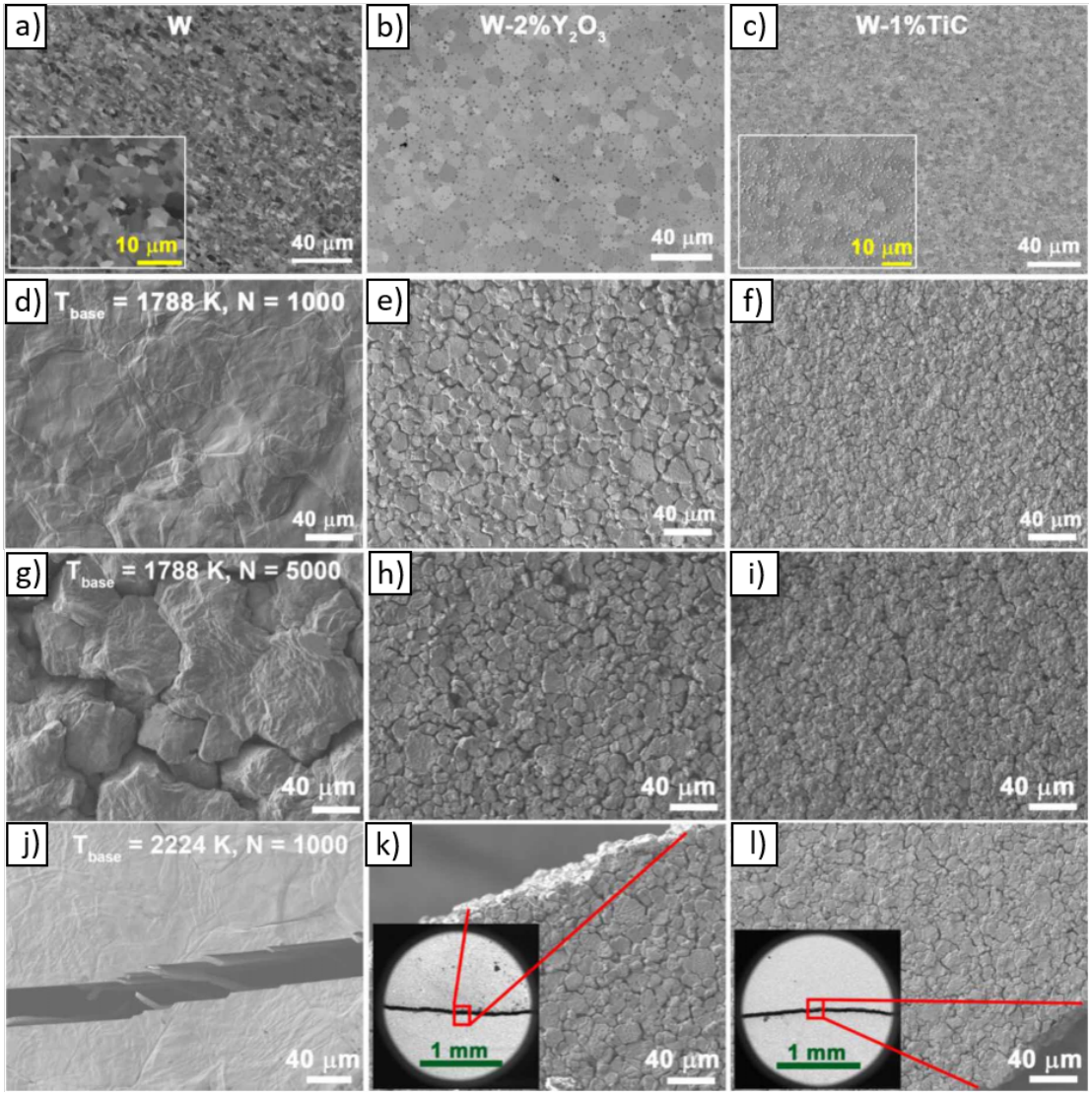


Figure 2.20: SEM images of surface of W and W alloys tested in Magnum-PSI by Li et al. [122][26]. Each row represents a different testing condition as stated in left-most image (the top row is before testing). Each column corresponds to the three materials studied.

Li et al. also tested pure polycrystalline W in Magnum-PSI with a 1064 nm Nd:YAG laser firing 1 ms pulses at 10 Hz to apply transient heat loads while an Ar plasma was maintained in steady state. The W surface in Figure 2.21 was first exposed to a H plasma to induce surface blistering (∼6% area density). Pre-existing blisters had a significant impact on the amount of cracking, as average crack length increased from 117 to 265 µm and crack density increased from 14 to 24 μm^{-1} when compared with a slightly porous sample tested under the same plasma conditions (without the initial H plasma exposure). It was suggested that the sharp corners of the cavities located underneath the blisters were susceptible to stress concentration and therefore initiated cracks [124].

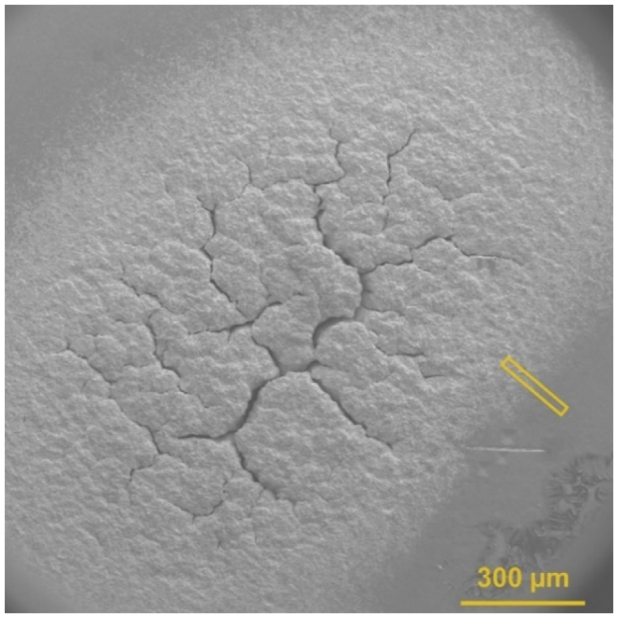


Figure 2.21: SEM image of sample surfaces after testing in Magnum-PSI from Li et al. [124][27]. Base temperature was ∼300 °C and ΔT=280 °C for 10^5 pulses at 10 Hz.

[27]Reprinted from Nuclear Fusion, Volume 62 Issue 7, Yu Li et al., Influence of porosity and blistering on the thermal fatigue behavior of tungsten, 076039, © copyright (2022), with permission from the IAEA.

Morgan et al. utilised a H plasma and the high-powered Nd:YAG laser (1 ms pulse, 10–80 Hz) in Magnum-PSI to investigate the effect of base temperature with transient pulse number and heat flux. Samples were W monoblock mock-ups that were bonded to a CuCrZr pipe with a Cu interlayer. The base temperature was varied between 750–1500 °C and the power density from the laser was between 80–410 MW·m^{-2}. Figure 2.22 shows that transient temperature excursion and base temperature had the largest effect on the level of cracking. It was suggested that grain boundaries were more pronounced at 1500 °C because of recrystallisation which led to more cracking [125].

[28]Reprinted from Nuclear Fusion, Volume 61 Issue 11, Thomas Morgan et al., Combined high fluence and high cycle number transient loading of ITER-like monoblocks in Magnum-PSI, 116045, © copyright (2021), with permission from the IAEA.

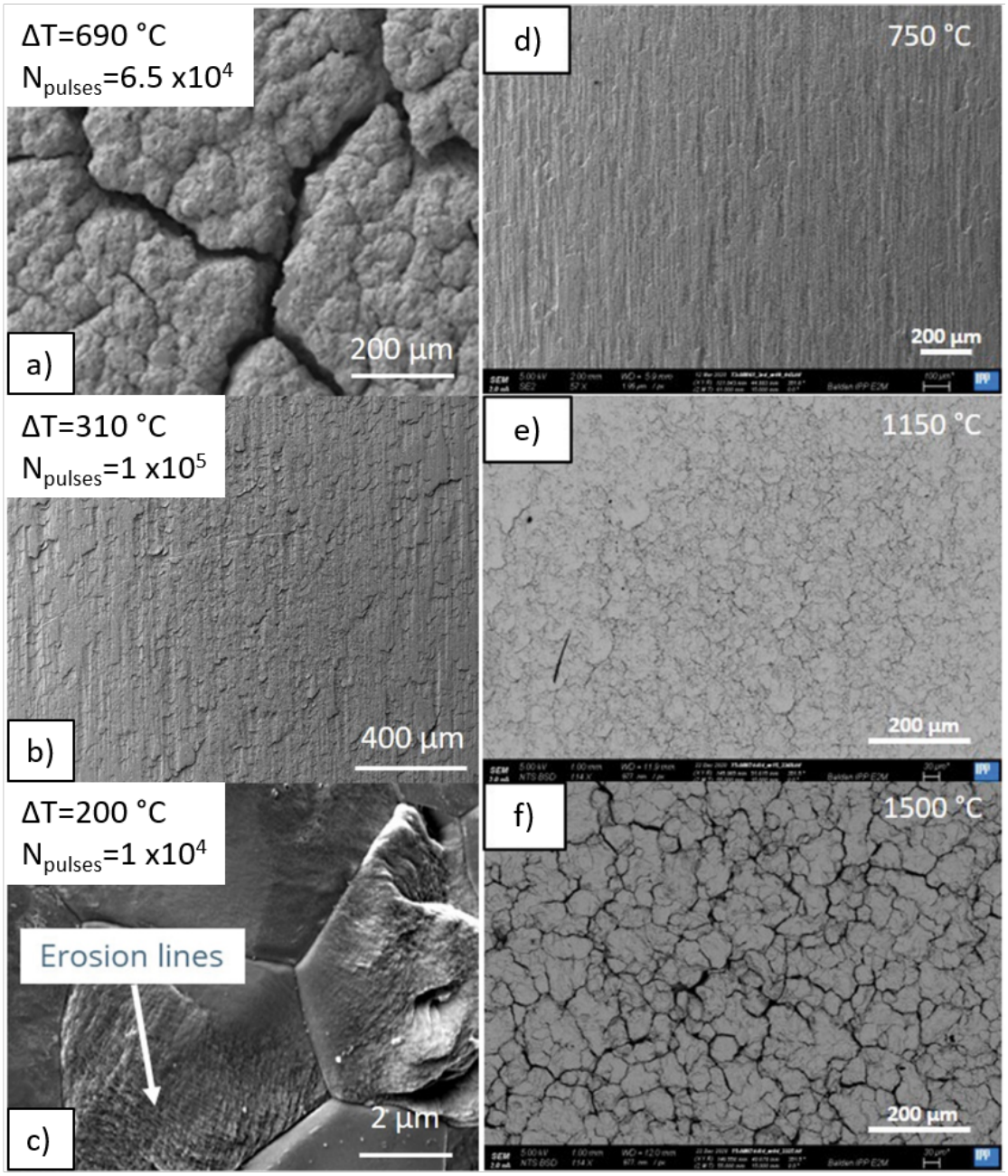


Figure 2.22: SEM images of surfaces of samples tested in Magnum-PSI from Morgan et al. [125][28]. The left column shows the effect of transient temperature change (ΔT) and number of pulses (all base temperatures were 750 °C). The right column shows the effect of base temperature (all surfaces were exposed to 4 $\times 10^5$ pulses with ΔT=310 °C).

2.3.4 Summary of fusion-relevant testing

Fusion-relevant thermal testing can be split into three categories of equal importance: thermal ageing, steady-state thermal cycling, and transient thermal cycling.

Thermal ageing is a crucial preliminary step for components with bonded materials to ensure that undesirable new phases do not form through diffusion over the material's lifetime. Accelerating diffusion through elevated temperatures allows for relatively quick and resource-efficient testing.

Steady-state thermal cycling is essential for comprehending the thermomechanical response of components over the reactor's operational life. Thermal strains and stresses resulting from such cycling can lead to issues like cracking and delamination, which severly degrade the thermal properties of W coatings.

Transient thermal cycling becomes particularly relevant for tokamaks where regular plasma disruptions are expected. Shock testing 'cold' components inadequately simulates the conditions within a fusion reactor. More representative results are likely to be obtained from linear plasma devices, where transient pulses can be applied either externally, such as through a high-powered laser, or integrated into the plasma via a capacitor bank to increase the incident heat flux. Depending on the base temperature and number of transient pulses, significant amounts of surface modification and cracking can occur.

2.4 Future developments

This section discusses upcoming prospects in the fields of plasma-facing materials and thermal testing facilities. It focuses on two developments with the potential to influence the future of fusion technology.

The General Atomics Modular BLanket (GAMBL) is a dual-cooled fusion blanket design that uses SiC as the main structural material. It is a fully modular design that integrates the PFCs with the breeder blanket. As W and SiC have very similar coefficients of thermal expansion (CTEs), 4.3×10^{-6} and 4.0×10^{-6} respectively, it is anticipated that there will be little thermal strain mismatch and therefore stresses from manufacture and thermal excursions should be minimal. The proposed fabrication method is a FGM of SiC and W which has recently been demonstrated using PVD [126]. SiC also has a higher operating temperature than steels (>1000 °C as opposed to 500-600 °C), which would allow the reactor to be more efficient (>60%) as the coolant leaving the reactor can be hotter. The GAMBL design uses high pressure He to cool the FW, and self-cooled liquid PbLi in the breeder containers. Further development of SiC and this design are required to ensure structural validity, but initial results appear promising [126].

The Combined Heating and Magnetic Research Apparatus (CHIMERA) test facility is currently under construction. The first-of-its-kind device will facilitate the combination of several areas of testing research (heat flux testing, cooling, magnet systems, high volume components) for in-situ operation. The first phase of operation will encompass water cooling with high, pulsed, magnetic fields (5 $\pm$0.25 T), large surface heating up to 0.5 MW$\cdot$m^{-2}, as well as volumetric heating in either high vacuum or inert gas environments. Phase two will introduce high heat flux

testing up to 200 $MW \cdot m^{-2}$ from a continuous-wave laser and a liquid metal (PbLi) loop. Magneto-hydrodynamics of liquid metal coolant loops are recognised as a potential issue for operation in a reactor where further research is required. A large part of the CHIMERA design is focussed on systems simulation technology, where virtual representations of the system and components are used to construct a model which can be split into subsections to decrease computational time and cost. There is significant scope for expansion in this area, with the development of 'digital twins' (where a virtual model is mapped to and synchronised with a real-world sample) and advances in non-destructive, in-situ testing. Feedback from the physical system can be provided to the simulation to develop prediction algorithms for servicing or replacements of components. CHIMERA can enable these techniques to be benchmarked for deployment in future fusion reactors [127].

2.5 Summary

Several areas were highlighted in this literature review as requiring further investigation and are thus subsequently investigated in this thesis.

In terms of manufacturing, many research papers failed to mention enough processing information, and many others failed to provide any physical measurements of W coatings. The thorough nature of the analysis shown by Wang [80], Heuer [83] & Hu [84] is unfortunately rare.

Basic mechanical and thermal properties are required in order to judge the initial suitability of W coatings for use in a nuclear fusion reactor. For example, density measurements are essential for powder-manufactured coatings to quantify the quality of processing parameters and to indicate whether components are likely to perform as anticipated.

A wide range of thermal testing facilities are available and have been employed to validate candidate fusion materials and to gain a better understanding of irradiation mechanisms, and a useful framework for W coating research was suggested [112]. Thermal ageing, cyclic testing and plasma irradiation are the most valuable for assessing the feasibility of W coatings as PFCs.

Because the issue of thermally induced residual stress and strain are fundamental to W coated systems, finite element modelling (FEM) or other similar approaches are also crucial for helping to explain the physical response of W-coated systems.

3 Optimisation of Vacuum Plasma Spraying

3.1 Introduction

Production of reproducible and high performing W coatings at an industrial scale would be a major stride towards practical implementation of nuclear fusion. Currently, W coatings are typically manufactured by joining a high purity, oxygen-free, high thermal conductivity (OFHC) Cu interlayer (brazed onto the W coating) with a precipitation-hardened CuCrZr alloy (with an electrodeposited 5 µm Ni coating interlayer) via hot radial pressing (HRP) at 600 °C and at a pressure of 50 MPa for 2 hrs [59, 60]. A high quality surface finish is also required to successfully bond the W-Cu coating and Ni-CuCrZr substrate. Furthermore, the small temperature window afforded by the CuCrZr (before mechanical property degradation occurs) adds an additional constraint on process operation [61]. Finding an alternative means of manufacturing W coatings at lower cost and larger volumes is highly desirable.

Although alternative processes exist, as discussed in Chapter 2, reproducibly achieving sufficient thickness to be useful in a fully operational reactor is difficult, and most methods have produced a maximum thickness of 1 mm [66, 67, 76, 78, 80–82, 84, 87].

Previous vacuum plasma spraying (VPS) studies by Thomas et al. [88] produced thick W coatings (up to 2 mm and >97% dense) on bespoke textured steel substrates. Unpublished research also showed that hatched substrate texturing, produced by electro-discharge machining (EDM), gave similar results.

In this project, the VPS process is explored to produce W coatings of fusion-relevant thickness on hatched substrates. This chapter describes the use of Taguchi analysis for optimisation of complex, inter-related VPS parameters in order to produce thick, dense W coatings.

Taguchi analysis is a technique that can be used to reduce the time and cost of finding optimised (or near-optimised) parameters that produce a desired outcome for complex systems such as materials processes, including thermal spray, where there are many operating variables [128–131]. Taguchi experimental design uses orthogonal arrays of parameters under user control to assess their relative effect on final coating characteristics of interest. The approach assumes that the parameter-characteristic relationship is linear, and that parameters are independent. Though these assumptions (especially the latter) may sometimes be false, the technique can nonetheless accelerate the process of identifying promising parameter combinations when compared with standard optimisation approaches [132]. The analysis works best when the number of level settings for any parameter is as high as practical [133], although of course more settings require more experiments. Table 3.1 shows

Experiment No.	Parameter Setting			
	a	b	c	d
1	L1	L1	L1	L1
2	L1	L2	L2	L2
3	L1	L3	L3	L3
4	L2	L1	L2	L3
5	L2	L2	L3	L1
6	L2	L3	L1	L2
7	L3	L1	L3	L2
8	L3	L2	L1	L3
9	L3	L3	L2	L1

Table 3.1: An example of an L9 Taguchi orthogonal array for four variables a–d and three settings L1, L2 and L3.

a typical Taguchi orthogonal array design for parameters a–d each with three settings/levels (low - 1, medium - 2 and high - 3). By using this type of array, a signal-to-noise (SN) ratio can be calculated for each level of each parameter using Equations 3.1 and 3.2 for the 'smaller-the-better' case (SN_S) — for example in the case of porosity and surface roughness — and the 'larger-the-better' case (SN_L) — for example coating thickness [134]. For both Equations 3.1 and 3.2, the larger the SN obtained in an experiment, the better the match to the target values of zero for porosity and surface roughness, and of ∞ for deposition efficiency and coating thickness [134].

$$SN_S = -10log(\frac{1}{n}\sum_{i=1}^{n} y_i^2) \tag{3.1}$$

$$SN_L = -10log(\frac{1}{n}\sum_{i=1}^{n}\frac{1}{y_i^2}) \tag{3.2}$$

where y_i is the measurement of the characteristic of a coating from experiment (e.g. thickness), and n is the number of measurements of that characteristic.

Once SN ratios have been calculated for every experiment, the effect of each individual parameter level is then analysed by averaging the SN ratios obtained from those experiments where that particular parameter level was selected. For example, in Table 3.1 the SN ratio for parameter 'b' level '1' would be obtained from the average of experiments one, four and seven. Plotting these then shows which level is best for each parameter. For example, Figure 3.1 shows an optimisation outcome for APS of a yttria stabilised zirconia (YSZ) coating [135], where the maximum SN value was the best optimised setting of each variable.

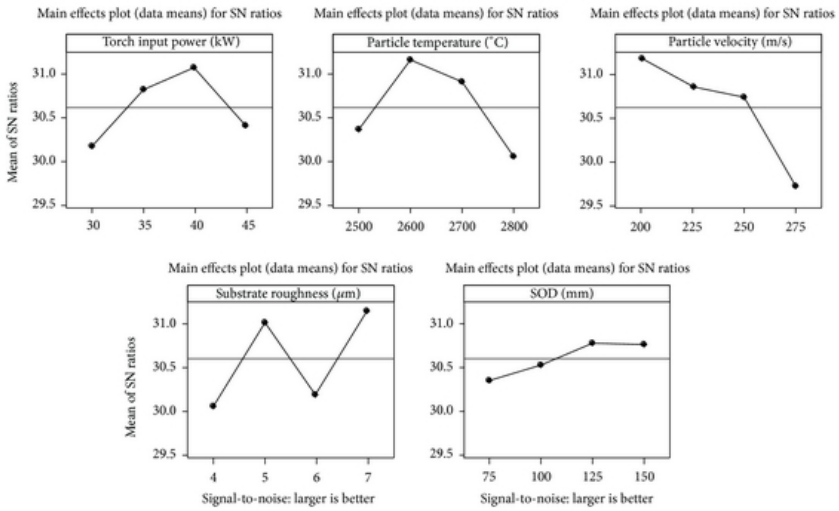


Figure 3.1: Optimisation of YSZ APS parameters, where the highest signal-to-noise ratio indicated the optimisation value [135][1].

Coating porosity and density are critical coating attributes and can be calculated in two ways, bulk and apparent. Bulk density includes surface porosity, that can be removed by post-production surface polishing. Apparent density only accounts for internal porosity which is impossible to remove following manufacture. Using the Archimedes' principle, both types of density and porosity can be calculated from mass measurements of samples when dry (M_D), submerged (M_S) and wet (M_W) and the densities of water and air (ρ_{Water} and ρ_{Air}, respectively) according to Equations 3.3–3.11 (where ρ_{Theory} is the theoretical density of the measured material).

$$\text{Closed Volume: } V_C = \frac{M_D - M_S}{\rho_{Water} - \rho_{Air}} \tag{3.3}$$

$$\text{Percentage Apparent Density: } \%_{App} = \frac{\rho_{App}}{\rho_{Theory}} \times 100\% = \frac{M_D \div V_C}{\rho_{Theory}} \times 100\% \tag{3.4}$$

$$\text{Volume of Enclosed Voids: } V_E = \frac{(V_C \times \rho_{Theory}) - M_D}{\rho_{Theory}} \tag{3.5}$$

$$\text{Volume of Surface Pores: } V_S = \frac{M_W - M_D}{\rho_{Water} - \rho_{Air}} \tag{3.6}$$

[1]Reprinted from The Scientific World Journal, https://doi.org/10.1155/2013/527491, Sisir Mantry et al., Parametric Appraisal of Process Parameters for Adhesion of Plasma Sprayed Nanostructured YSZ Coatings Using Taguchi Experimental Design, © copyright (2013), under CC by 3.0.

$$\begin{aligned}\text{Percentage Bulk Density: } \%_{Bulk} &= \frac{\rho_{Bulk}}{\rho_{Theory}} \times 100\% \\ &= \frac{M_D \div (V_C + V_S)}{M_D \div (V_C - V_E)} \times 100\% \\ &= \frac{V_C - V_E}{V_C + V_S} \times 100\%\end{aligned} \tag{3.7}$$

$$\text{Open Porosity: } \phi_O = \frac{V_S}{V_C + V_S} \times 100\% \tag{3.8}$$

$$\text{Bulk Closed Porosity: } \phi_{C_{Bulk}} = \frac{V_E}{V_C + V_S} \times 100\% \tag{3.9}$$

$$\text{Apparent Closed Porosity: } \phi_{C_{App}} = \frac{V_E}{V_C} \times 100\% \tag{3.10}$$

$$\text{Total Porosity: } \phi_T = \phi_O + \phi_{C_{Bulk}} \tag{3.11}$$

3.2 Methodology

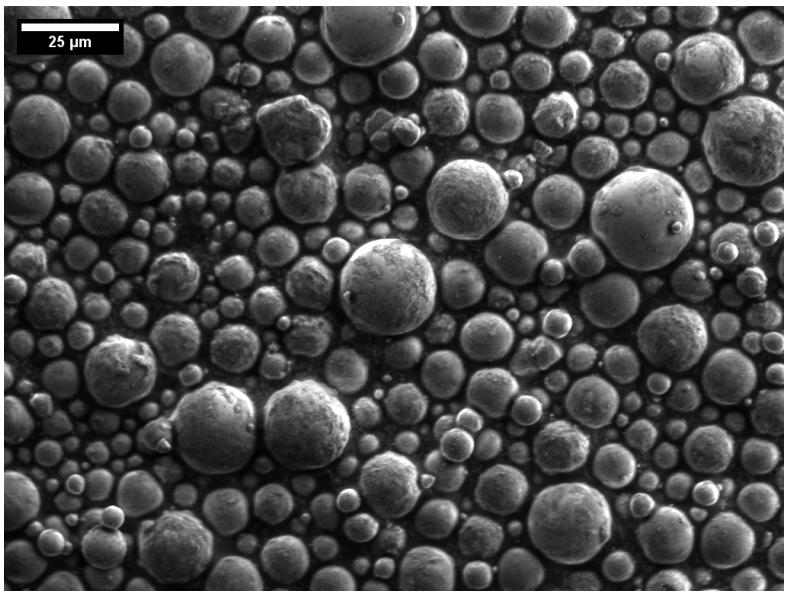
3.2.1 Materials and preparation

Spherodised 5–25 µm W powder (>99.9 % purity) supplied by Carpenter Additive Ltd. (formerly LPW) was used in all VPS experiments. SEM images of the powder were taken using a ZEISS EVO with EDX capabilities (Oxford Instruments X-act) in both secondary electron (SE) and backscattered electron (BSE) modes. A Malvern Instruments Mastersizer 2000 particle size analyser with large volume sample dispersion unit (Hydro 200MU) was used to measure the size and distribution of the powder particles. Images and results are shown in Figure 3.2.

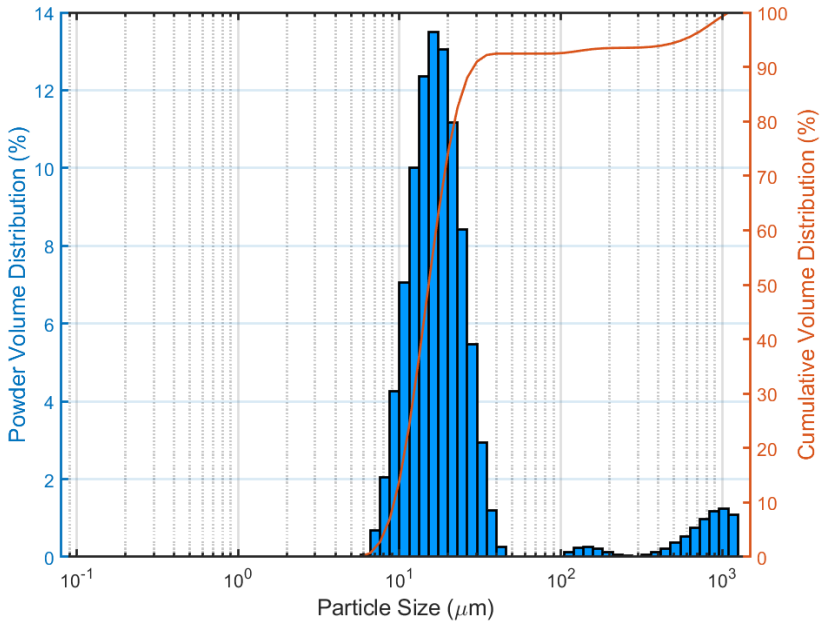
All substrates were 28 mm diameter with 5 mm thickness. Substrates for wipe tests to assess W melting were D2 tool steel supplied by Acton Bright Steel (composition shown in Table 3.2) and were prepared using progressively smoother sandpaper up to 1200 grit. Substrates were submerged in iso-2-propanol in an ultrasonic bath for two minutes and wiped clean with methanol.

Element	**Fe**	**Al**	**C**	**Cr**	**Mn**
F91	Balance	0.01	0.105	8.62	0.42
BD2	Balance	-	1.40–1.60	11.5–12.5	≤0.60
Element	**Mo**	**N**	**Nb**	**Ni**	**P**
F91	0.92	0.0485	0.07	0.25	0.017
BD2	0.70–1.20	-	-	-	≤0.035
Element	**S**	**Si**	**Ti**	**V**	**Zr**
F91	0.002	0.37	0.002	0.212	0.005
BD2	≤0.035	≤0.60	-	0.25–1.00	-

Table 3.2: Chemical compositions (wt%) of ASTM A182-16a F91 and BD2 tool steel substrates.



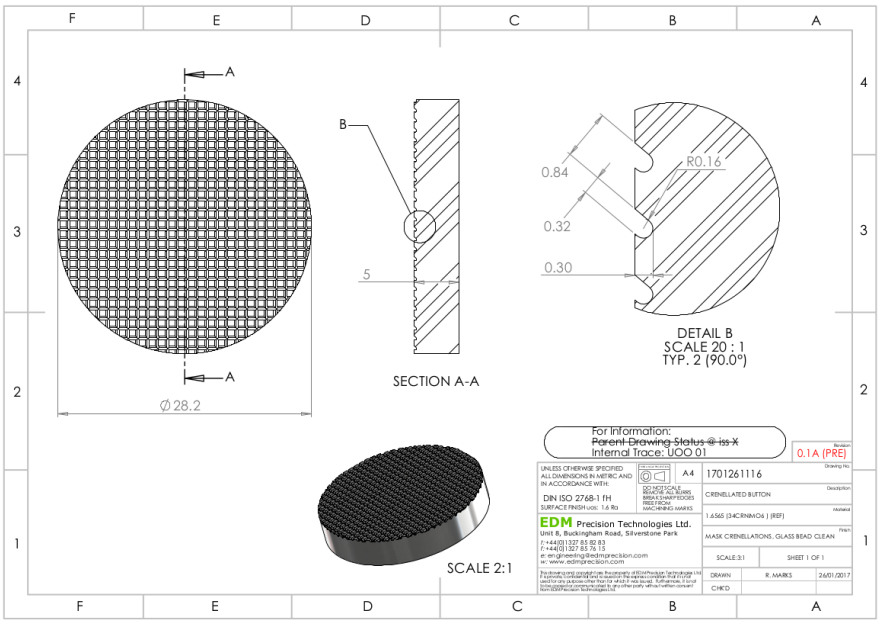
(a) SEM image of W powder used in VPS experiments.



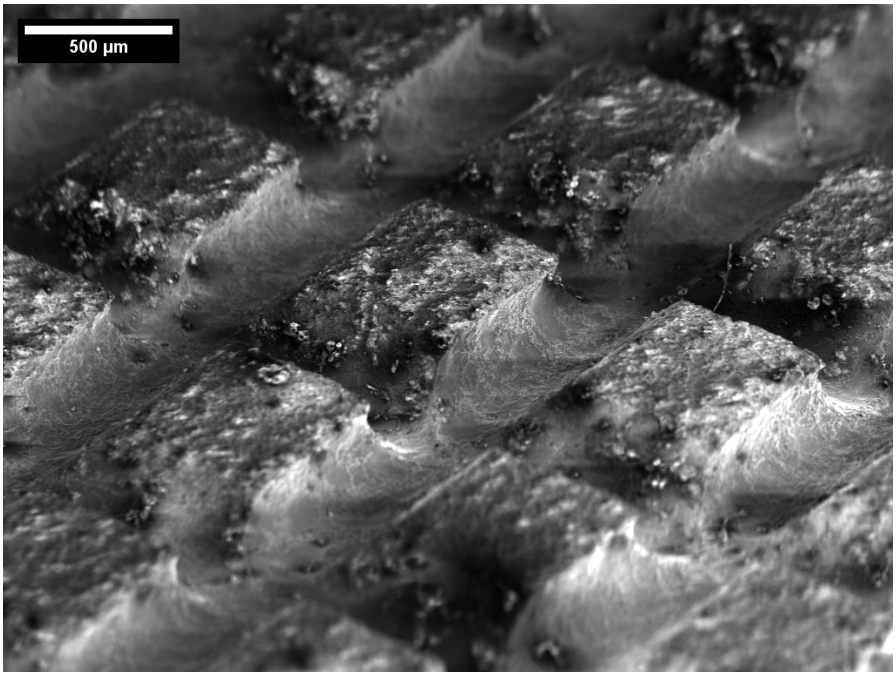
(b) Particle size distribution of W powder supplied by Carpenter Additive. There was a small fraction of large powder particles >300 µm that occurred due to agglomeration.

Figure 3.2: (a) SEM image and (b) particle size distribution of W powder supplied by Carpenter Additive used in VPS experiments.

Substrates for all other experiments were F91 steel supplied by Abbey Forged Products (composition shown in Table 3.2). Flat samples were grit-blasted with 80/120 Guyson Saftigrain blast media with a working distance in the range of 100–200 mm. Textured (or hatched) substrates were produced by wire erosion by EDM Precision Technologies Ltd. according to Figure 3.3 (a). Figure 3.3 (b) shows an SEM image of a hatched substrate surface. Substrates were sonicated for 90 s in a soap and water mixture before mounting.



(a) Technical drawing of a 'hatched' EDM substrate.



(b) SEM image of the surface of a 'hatched' EDM substrate.

Figure 3.3: Technical drawing and SEM image of 'hatched' EDM substrate used for thick VPS coatings.

The density and porosity of coatings were calculated using Equations 3.3–3.11 from dry, wet, and submerged mass measurements (Luna Precision Balance LPB 423i, Adam Equipment) taken multiple times and averaged.

3.2.2 Equipment and VPS set up

Vacuum plasma spraying was performed using an Oerlikon (formerly Sulzer) Metco MultiCoat™ VPS System operating with a 03CP plasma gun. Substrates were mounted using thermal paste (Heat Sink Compound Plus supplied by RS Components) in Cu holders, covered by a steel shield for protection with a 20 mm diameter aperture aligned with the centre of the substrate. Substrates were wiped clean with IPA spray.

The VPS process has several key parameters that require optimisation in order to promote powder melting and therefore to maximise coating thickness and quality (e.g. low porosity). These parameters were grouped into three categories:

1. Powder mass flow rate calibration: to ensure all powder was successfully entrained from the feedstock hoppers and then injected into the plasma at a known mass flow rate.

2. Plasma optimisation (using Taguchi analysis): to maximise the fraction of molten W particles to maximise adhesion, density and deposition efficiency.

3. Further optimisation: to maximise coating quality and thickness.

Table 3.3 shows the parameter setting previously used for W coatings.

3.2.3 Powder mass flow rate

Carrier gas flow rate and disc speed affect the injection of the powder into the gun. If the injection rate (radial momentum) is too high, then the powder will traverse radially through the hot plasma core, experience limited heating and miss the target (shown in Figure 3.4). If the injection momentum is too low, the powder fails to penetrate the hot plasma core, or worse may fail to reach the gun and cause a powder build-up in the hopper or feed lines.

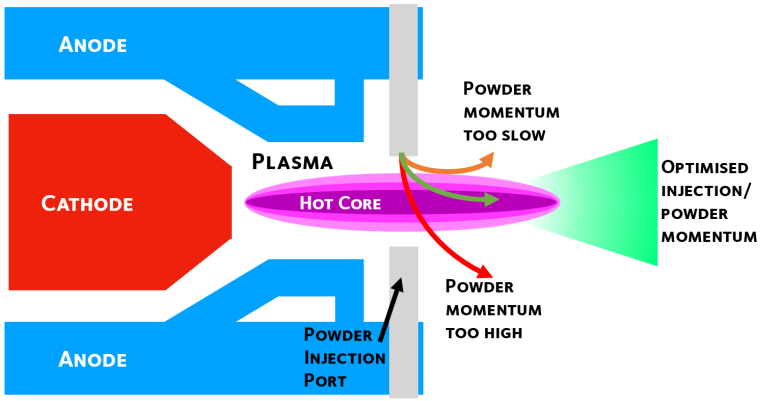


Figure 3.4: Schematic highlighting different powder injection trajectories into the VPS plasma.

Powder mass flow rate was calculated by flowing W powder from the hopper feed system into a plastic bottle (rather than the plasma gun) for 15 s, and measuring the change in mass. Powder feeder disc speed, measured as the percentage of the maximum revolution speed (158 rpm), and Ar carrier gas flow rate were systematically varied. To conserve W powder, for the majority of the optimisation campaign process, a disc speed of 1% of the maximum rpm (158 rpm) was used.

3.2.4 Plasma optimisation using Taguchi analysis

Powder injection is important to ensure that as much powder as possible is entrained, heated beyond melting point and accelerated by the plasma during spraying. High deposition velocities are desirable to increase density and the impact ('splat') area of the powder particle, however a high particle velocity will also reduce the plasma exposure (heating) time for the particles. It is anticipated that an optimum combination of process parameters can be determined that balances these competing requirements.

Current, Ar and H_2 flow rates (which affect plasma voltage), resulting net power (after gun cooling) and chamber pressure all affect the plasma behaviour. A gun current of 1000 A was used for all experiments. 1000 A was the maximum producible current (chosen to increase the likelihood of the ultra-high melting point W particle melting).

Taguchi analysis was initially used to optimise the following parameters affecting the plasma 'flame' and, by extension, powder particle melting: chamber pressure, Ar flow rate and H_2 flow rate, as the gas flow rates also affect the particle velocity. Table 3.4 shows the variable parameters used in the Taguchi optimisation experiments.

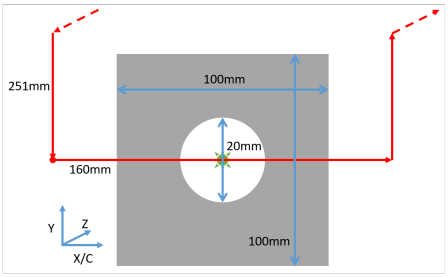
Experiment No.	Chamber Pressure (mbar)	Ar Flow Rate (NLPM)	H_2 Flow Rate (NLPM)
1	80	80	13
2	80	100	15
3	80	120	18
4	120	80	15
5	120	100	18
6	120	120	13
7	160	80	18
8	160	100	13
9	160	120	15

Table 3.4: Array used for Taguchi analysis experiments.

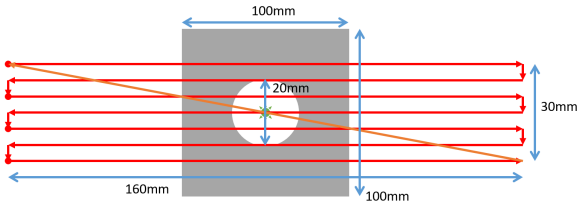
Two experiments were performed as a part of the Taguchi optimisation: wipe tests and cycled spraying.

Wipe tests were a means of investigating deposition efficiency using a single fast pass of the spray lasting approximately 0.17 seconds (effective traverse speed = 950 mm·s^{-1}). A schematic of the gun path is shown in Figure 3.5 (a). Optical micrograph images were then taken of the substrate surface at $\times 5$ magnification using a Leica DM2700 M optical microscope. Each image had a square box with side length 750 μm superimposed at its centre. The number of powder 'splats' located within each box was determined manually, and from this a splat density was calculated. A splat occurs only from a molten droplet, whereas unmelted particles are assumed to bounce away.

Cycled spraying enabled investigation of surface roughness and coating thickness by building up a coating through repetitive passes (or cycles) of the spray. The experiment comprised seven passes of the spray per cycle to try to ensure an even coating. A schematic of the gun path is shown in Figure 3.5 (b). 100 cycles were performed, with a break after 50 cycles to allow the plasma gun to cool (because for high melting point W powder the VPS gun was having to operate at the very limit of its specification). The gun traverse speed over the substrate surface was 200 mm·s^{-1}. Surface roughness measurements were taken using a Veeco DekTak 6M stylus profiler. Coating thicknesses were measured using a micrometre calliper.



(a) Schematic of path taken by VPS gun for wipe tests.



(b) Schematic of path taken by VPS gun for cycled tests. The orange diagonal line shows the resetting of spray path at the end of a cycle.

Figure 3.5: Spray paths for wipe and cycled testing in red, with dimensions in blue.

The Taguchi optimisation process was used to identify parameter settings that would maximise coating thickness (cycled tests) and particle melting (wipe tests) but minimise coating surface roughness (cycled tests). Previous work suggested a strong correlation between surface roughness and porosity, explained by increased particle melting leading to a denser, less rough deposit [134]. Using the Taguchi-

optimised parameter values, a W coating was then sprayed with 100 cycles. The thickness and surface roughness of the optimised sample were compared with the corresponding data from each Taguchi experiment shown in Table 3.4 to verify that the optimisation process was successful.

3.2.5 Further optimisation

Spray distance, gun traverse speed, and substrate temperature all affect the deposition of coating particles on the substrate; ensuring that particles are still molten upon contact with the substrate, whilst not overheating and damaging/contaminating the substrate. A spray distance of 300 mm was initially selected based on experience, so that the substrate was just beyond the tip of the plasma 'flame' as shown in Figure 3.6.

Following Taguchi optimisation of the plasma parameters to maximise particle melting, the following parameters were further investigated to maximise the number of molten particles reaching the substrate: spray distance, powder feed disc speed (powder feed rate) and gun traverse speed over the substrate. Table 3.5 details the parameters used for each set of experiments. Again, coating thickness and surface roughness were measured.

Parameter	Taguchi	Additional
Spray Distance (mm)	300	350
Disc Speed (%)	1	4
Traverse Speed (mm·s^{-1})	200	100

Table 3.5: Parameters further explored following Taguchi optimisation.

Parameter	Original Value
Current (A)	1000
Resulting Net Power (kW)	19.2
Chamber Pressure (mbar)	80
Ar Flow Rate (NLPM)	45
H_2 Flow Rate (NLPM)	6
Carrier Gas Flow Rate (NLPM)	0.4
Disc Speed (%)	1
Spray Distance (mm)	300
Traverse Speed ($mm \cdot s^{-1}$)	60

Table 3.3: VPS parameters used for spraying W coatings prior to optimisation optimisation process.



Figure 3.6: Photograph of the VPS during operation with inset QR code linking to a video hosted on YouTube of the VPS in operation. (*https://youtu.be/0benc2TA_6Y*)

Following optimisation, a relatively thick W coating for microstructural assessment was produced on a hatched steel substrate using 127 cycles with the optimised spray parameters detailed in Table 3.6.

Parameter	Final Value
Current (A)	1000
Resulting Voltage (V)	51.2–52.1
Resulting Net Power (kW)	27.7–31.9
Chamber Pressure (mbar)	80
Ar Flow Rate (NLPM)	120
H_2 Flow Rate (NLPM)	13
Carrier Gas Flow Rate (NLPM)	5.0
Disc Speed (%)	4
Powder Mass Flow Rate ($g \cdot min^{-1}$)	$\sim$60
Spray Distance (mm)	300
Traverse Speed ($mm \cdot s^{-1}$)	100

Table 3.6: Final optimised parameters for vacuum plasma spraying of thick W coatings on steel substrates.

3.3 Results and Discussion

Table 3.7 summarises how the W VPS parameters evolved during the optimisation.

Parameter	Prior work	Injection optimisation	After Taguchi analysis	Final optimisation
Current (A)	1000	N/A	1000	1000
Resulting Net Power (kW)	19.2	N/A	27.7–31.9	27.7–31.9
Chamber Pressure (mbar)	80	N/A	80	80
Ar Flow Rate (NLPM)	45	N/A	120	120
H_2 Flow Rate (NLPM)	6	N/A	13	13
Carrier Gas Flow Rate (NLPM)	0.4	5.0	5.0	5.0
Disc Speed (%)	1	4 (1 for powder conservation)	1	4
Spray Distance (mm)	300	N/A	300	300
Traverse Speed ($mm \cdot s^{-1}$)	60	N/A	950 (wipe), 200 (cycled)	100

Table 3.7: Evolution of VPS parameters throughout optimisation process.

3.3.1 Powder mass flow rate

The first part of the optimisation process was powder mass flow rate (PMFR) calibration. Figure 3.7 shows the effect of carrier gas flow rate (CGFR) and powder-feed disc speed on powder mass flow rate. If the CGFR was too low, the powder began to accumulate at the injection line entrance and was unable to be fluidised and injected subsequently into the plasma. Even if fluidised, if the CGFR was too low, there would be insufficient powder momentum to penetrate the plasma flame and reach the hottest core regions, as shown schematically in Figure 3.4. On the other hand, if the CGFR was too high, the powder can be injected 'through' the hot plasma core and out the other side. A CGFR of 5 NLPM was selected as this fluidised the powder at all disc speeds tested. A 4% powder-feed disc speed corresponding to $\sim$60 g$\cdot$s^{-1} was selected as the highest rate which avoided any W powder accumulation at the fluidising inlet.

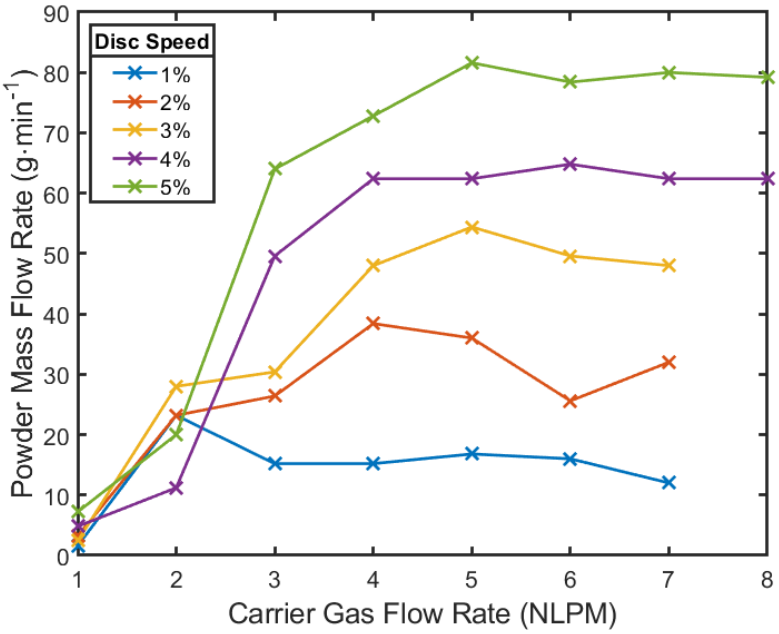
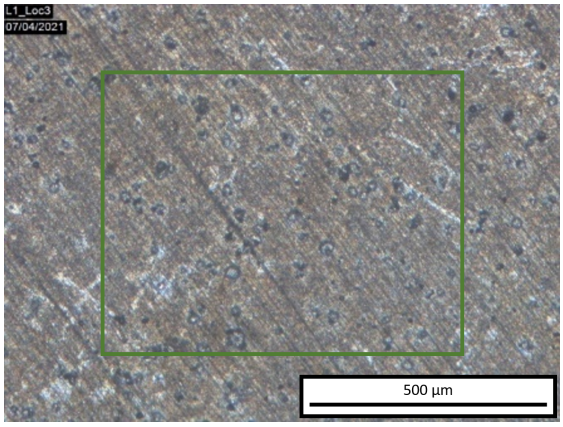


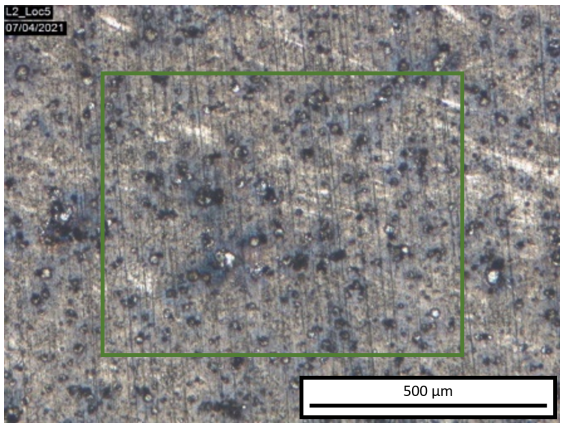
Figure 3.7: Plot showing the effect of carrier gas flow rate and powder feed disc speed on powder mass flow rate. When each respective data set reached a plateau, the minimum carrier gas flow rate was achieved for the corresponding disc speed.

3.3.2 Plasma optimisation via Taguchi analysis

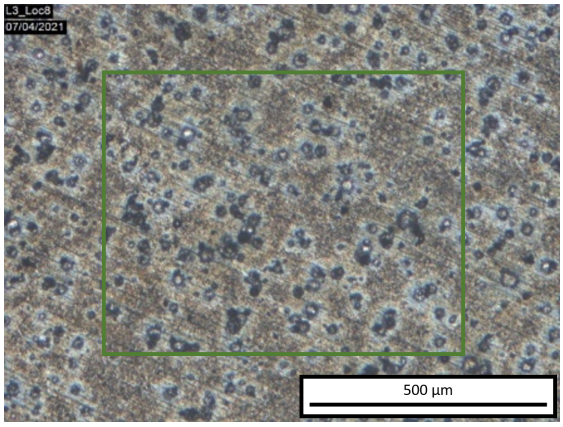
The second part of the optimisation process utilised Taguchi analysis to indicate near-optimum chamber pressure, and Ar and H_2 flow rate. Figure 3.8 shows representative substrate surface images from wipe tests. To assist with results analysis, a square box of side 750 µm (area 0.56 mm^2) was superimposed at the centre of each image, as discussed in Section 3.2.4.



(a) Experiment 1: 80, 80, 13.

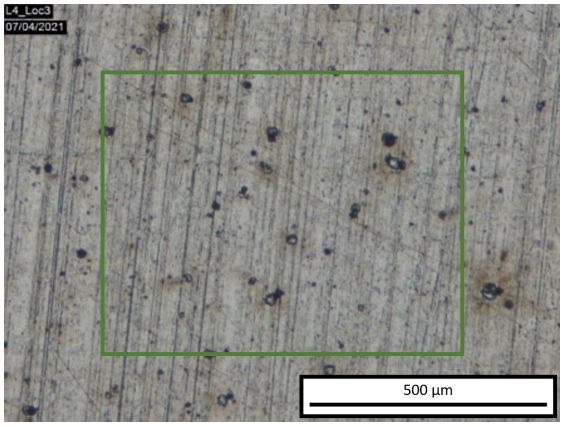


(b) Experiment 2: 80, 100, 15.

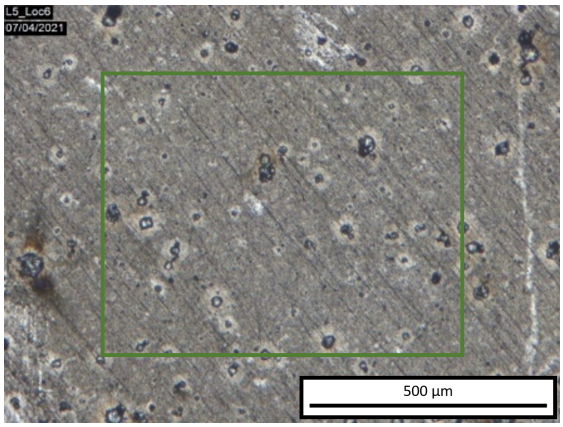


(c) Experiment 3: 80, 120, and 18.

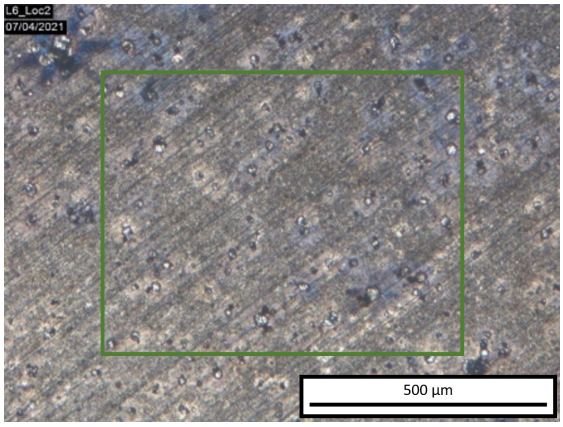
Figure 3.8: Representative examples of each Taguchi wipe test experiment. The chamber pressure (mbar), Ar and H_2 flow rates (NLPM) for each experiment are given in the captions.



(d) Experiment 4: 120, 80, and 15.

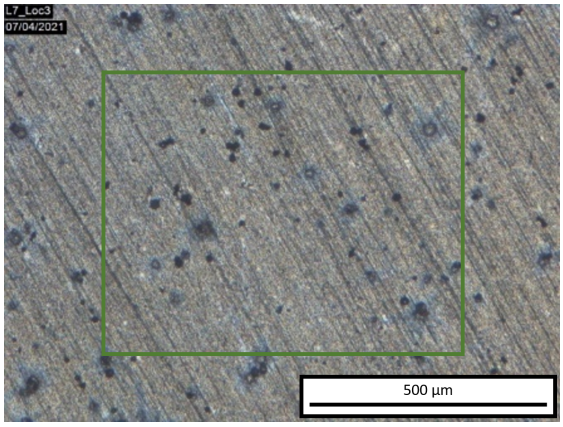


(e) Experiment 5: 120, 100, and 18.

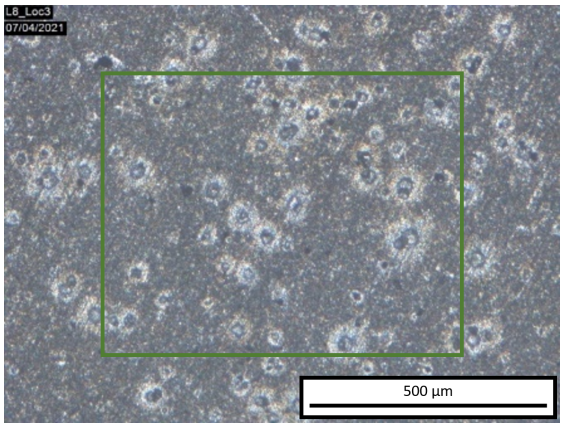


(f) Experiment 6: 120, 120, and 13.

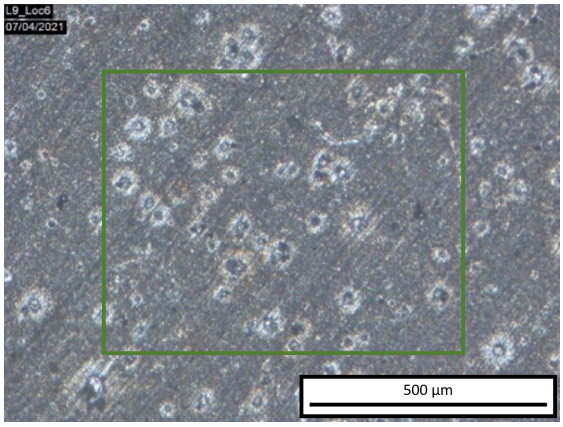
Figure 3.8: Representative examples of each Taguchi wipe test experiment. The chamber pressure (mbar), Ar and H_2 flow rates (NLPM) used for each experiment are given in the captions.



(g) Experiment 7: 160, 80, and 18.



(h) Experiment 8: 160, 100, and 13.

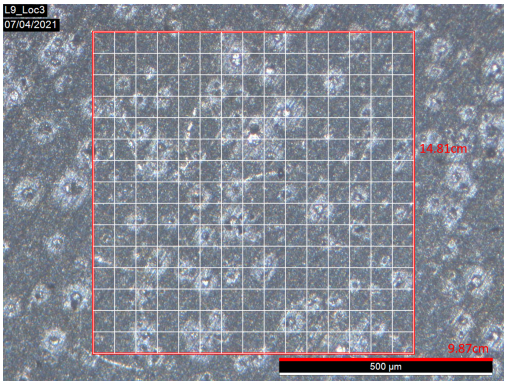


(i) Experiment 9: 160, 120, and 15.

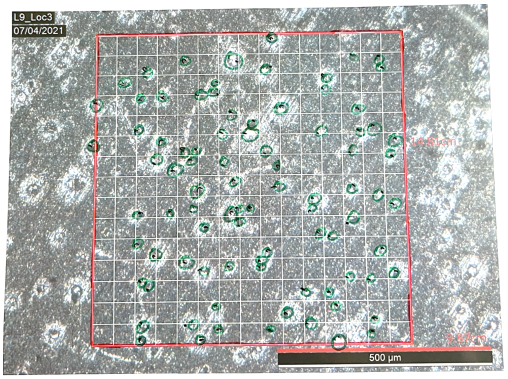
Figure 3.8: Representative examples of each Taguchi wipe test experiment. The chamber pressure (mbar), Ar and H_2 flow rates (NLPM) used for each experiment are given in the captions.

Figures 3.9 (a–b) shows an example of the approach adopted to count the number of splats. Figure 3.9 (c) illustrates schematically how as the optimisation improves (e.g. plasma temperature and powder particle dwell time both increase), the maximum size of the particles that reach the melting point will increase (as will the total number of molten particles).

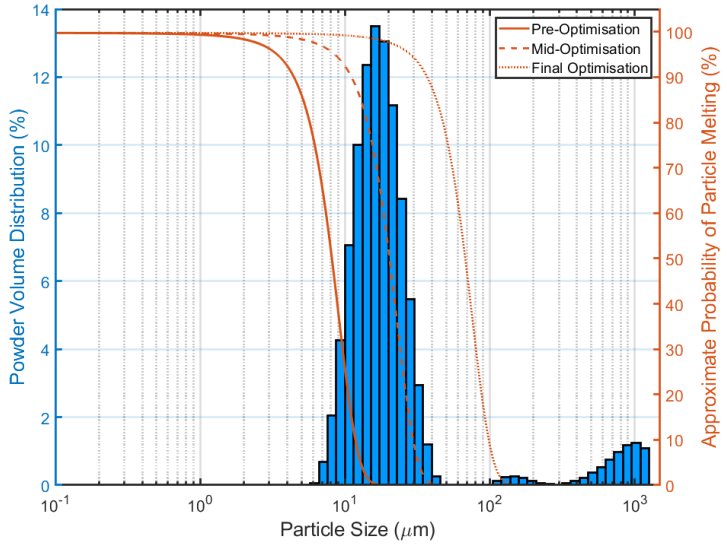
Table 3.8 summarises the average number of splats and the splat density for each experiment. Similarly, Table 3.9 summarises the average W coating thickness and surface roughness (arithmetic mean, R_A) for each cycled spraying experiment. The SN ratios for each experiment (included in the relevant tables) for splat density, coating thickness, and surface roughness were calculated using Equations 3.1–3.2. The range of splat densities was 6.3×10^{-5} to 3.2×10^{-4} µm^{-2}. Thomas [136] attempted a similar experiment with W powder and reported a range of 1.4×10^{-4} to 2.9×10^{-4} µm^{-2} with a 2 s wipe test. This wipe test speed was approximately an order of magnitude slower than the present work, meaning that there would be $\sim \times10$ splats assuming all other variables were constant. At an equivalent wipe test speed, the present work suggested a higher splat density, indicating that the particular powder/plasma combination in the present work was better optimised. This was principally due to the use of a much higher power plasma gun (Thomas used a F4-VB gun capable of reaching 55 kW whereas the 03CP gun has a maximum limit of 130 kW).



(a) Experiment 9 prior to counting number of splats.



(b) Experiment 9 after counting number of splats.



(c) Schematic illustrating the effect of process optimisations on the probability of particle melting (orange) shown against particle size distribution of the supplied W powder shown previously in Figure 3.2 (b).

Figure 3.9: Images of experiment 9 wipe test substrate (a) before and (b) after counting the number of splats, and (c) a schematic showing how an increasing fraction of the powder distribution reaches the melting point as plasma conditions are optimised. The objective of optimisation was to maximise the fraction of molten particles at the point of deposition.

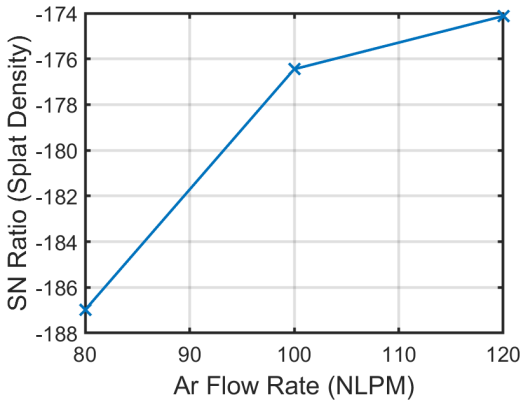
Experiment No.	Average No. of Splats	Average Splat Density (μm^{-2})	SN_L (Splat Density)
1	81.8	1.45×10^{-4}	-177.4
2	179.3	3.19×10^{-4}	-162.1
3	146.9	2.61×10^{-4}	-166.4
4	35.4	6.29×10^{-5}	-194.0
5	54.9	9.75×10^{-5}	-185.4
6	91.4	1.62×10^{-4}	-175.4
7	45.0	7.99×10^{-5}	-189.6
8	64.9	1.15×10^{-4}	-181.8
9	69.8	1.24×10^{-4}	-180.6

Table 3.8: The signal-to-noise values for the Taguchi analysis of VPS W wipe tests.

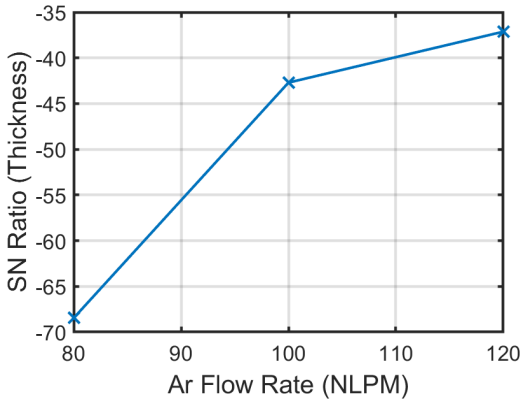
Experiment No.	Average Thickness (µm)	SN_L (Thickness)	Average Surface Roughness (µm)	SN_S (Surface Roughness)
1	218	-30.6	5.17	-217.3
2	230	-29.5	4.98	-216.4
3	287	-25.9	4.95	-216.3
4	69	-61.9	5.90	-219.9
5	100	-46.8	5.84	-219.7
6	146	-43.4	4.48	-214.4
7	5	-112.9	3.00	-206.3
8	79	-51.8	5.89	-219.8
9	137	-42.1	5.56	-218.7

Table 3.9: The signal-to-noise values for the Taguchi analysis of VPS W cycled spraying tests.

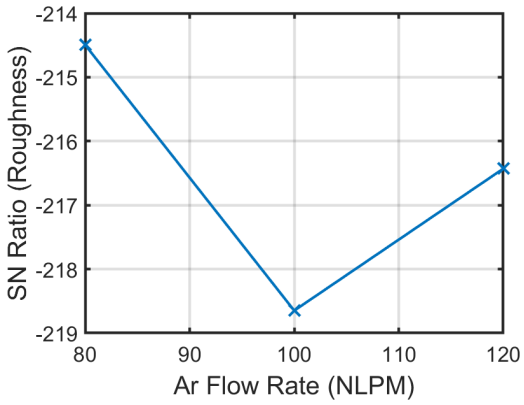
SN ratios were then calculated for each level of each parameter by averaging the three SN ratios for experiments with the same setting. For example, to calculate the SN ratio for chamber pressure of 120 mbar, experiments 4, 5 and 6 (in Table 3.4) were averaged. The plots in Figure 3.10 show the SN ratios for each parameter. Thickness and splat density optimisations agreed well and followed similar trends because they both indicated the extent of powder melting. Using roughness to identify an optimum provided a contradicting set of parameters, although the second highest SN ratio for each parameter agreed with using thickness and splat density.



(d) Ar Flow Rate: Splat Density

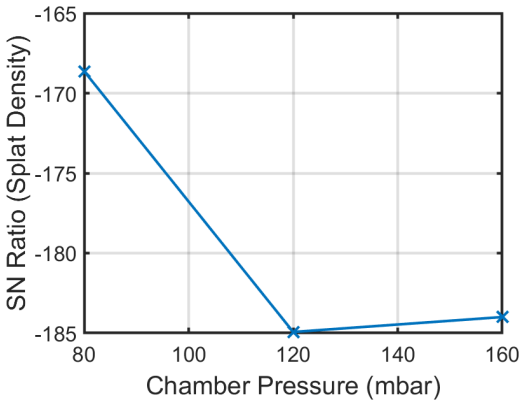


(e) Ar Flow Rate: Thickness

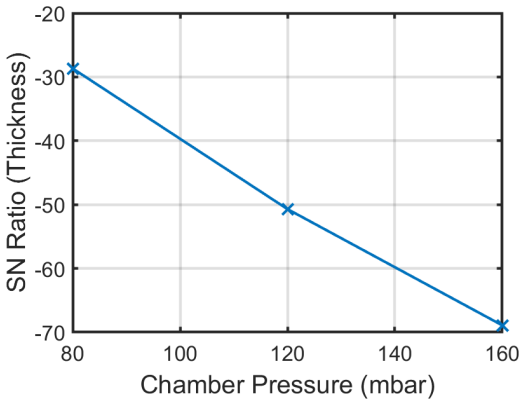


(f) Ar Flow Rate: Roughness

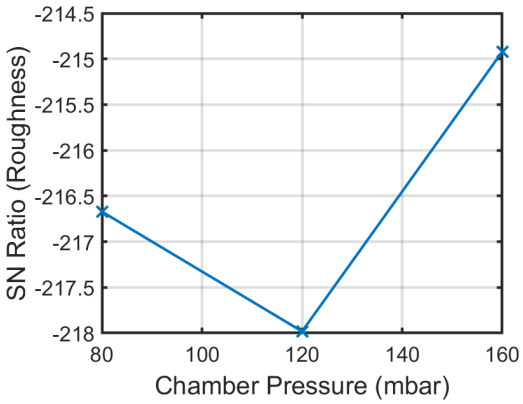
Figure 3.10: Signal-to-noise ratios from the Taguchi analysis of VPS W for each parameter assessed by the three measures: splat density, coating thickness and coating roughness.



(a) Chamber Pressure: Splat Density

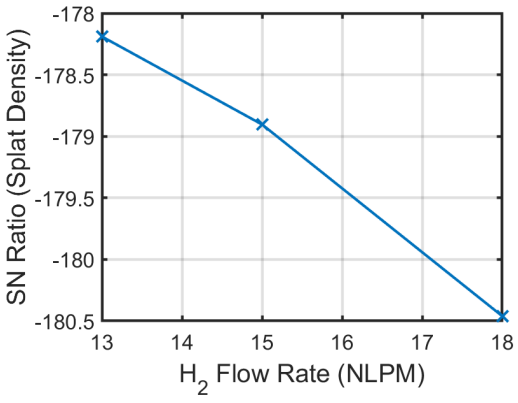


(b) Chamber Pressure: Thickness

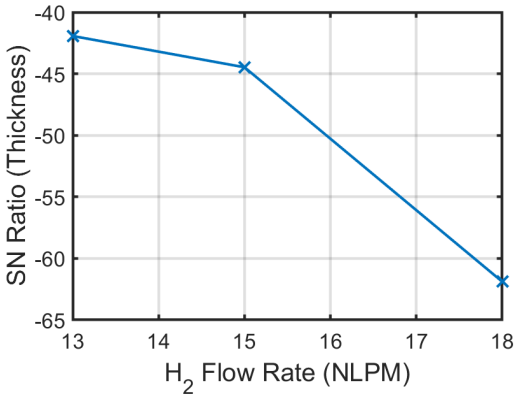


(c) Chamber Pressure: Roughness

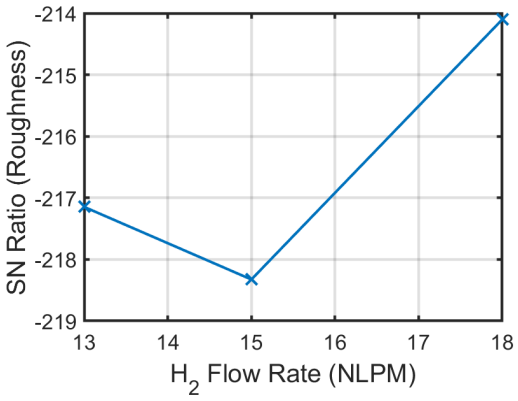
Figure 3.10: Signal-to-noise ratios from the Taguchi analysis of VPS W for each parameter assessed by the three measures: splat density, coating thickness and coating roughness.



(g) H_2 Flow Rate: Splat Density



(h) H_2 Flow Rate: Thickness



(i) H_2 Flow Rate: Roughness

Figure 3.10: Signal-to-noise ratios from the Taguchi analysis of VPS W for each parameter assessed by the three measures: splat density, coating thickness and coating roughness.

The W coating obtained in experiment 7 was particularly thin (5 µm) and had a surface roughness close to the substrate, as shown in Figure 3.11, due to particularly poor particle melting.

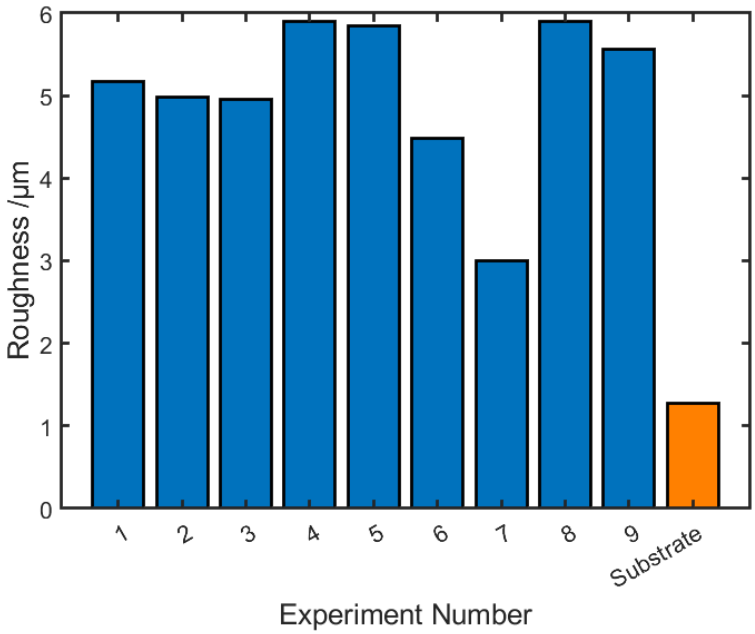


Figure 3.11: The average surface roughness (R_A) for each Taguchi experiment and the substrate surface roughness.

Figure 3.12 shows a comparison of W coating thickness obtained from each experiment and the thickness of coating produced using the optimum suggested parameters derived in Table 3.7. A W coating thicker than that produced by any prior combination of parameters was achieved.

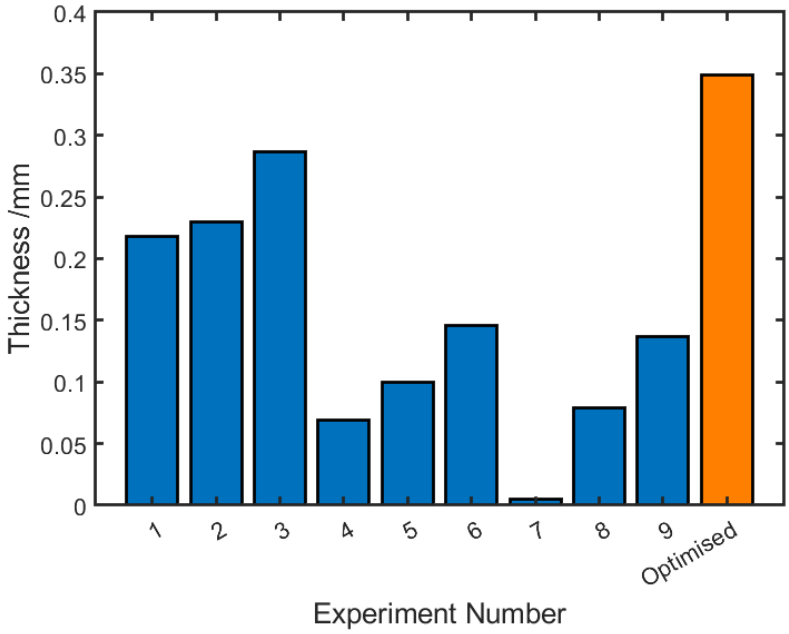
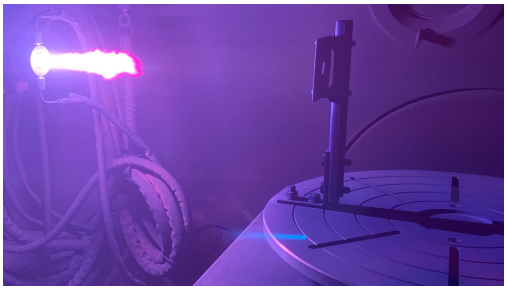


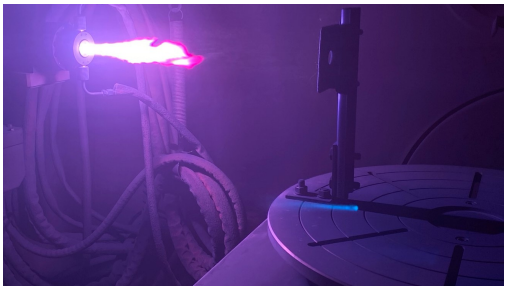
Figure 3.12: W coating thickness for each Taguchi experiment and for the final optimised coating.

3.3.3 Further optimisation

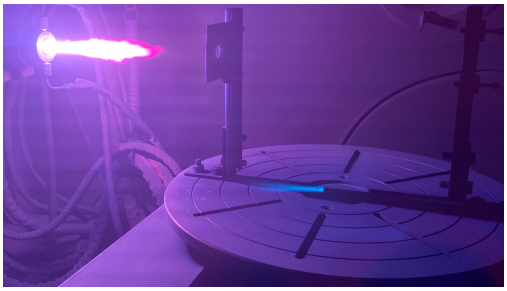
With the Taguchi-optimised parameters, the spray distance was then varied from 600 mm to 300 mm. Figure 3.13 shows photographs of the different arrangements during W spraying.



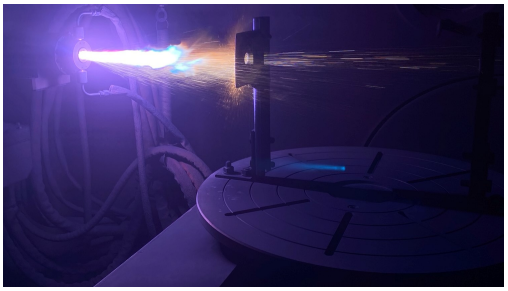
(a) 600 mm spray distance.



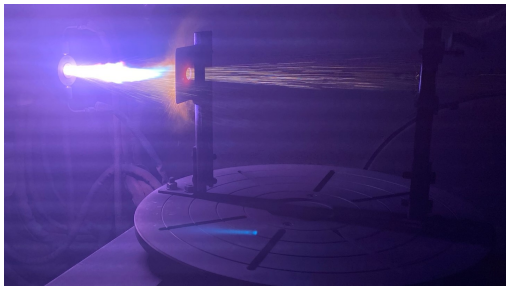
(b) 500 mm spray distance.



(c) 400 mm spray distance.



(d) 350 mm spray distance.



(e) 300 mm spray distance.

Figure 3.13: Photographs of W spraying at different spray distances between the gun and the substrate shield/mask.

Distances of 300 and 350 mm were judged to be the two best candidate distances with the hottest part of the plasma core not quite reaching the substrate mask, meaning that melted powder particles should still be molten when they reached the substrate. Figure 3.14 shows a comparison of coating thickness and roughness, indicating that 300 mm (as used in the Taguchi approach) produced a superior coating.

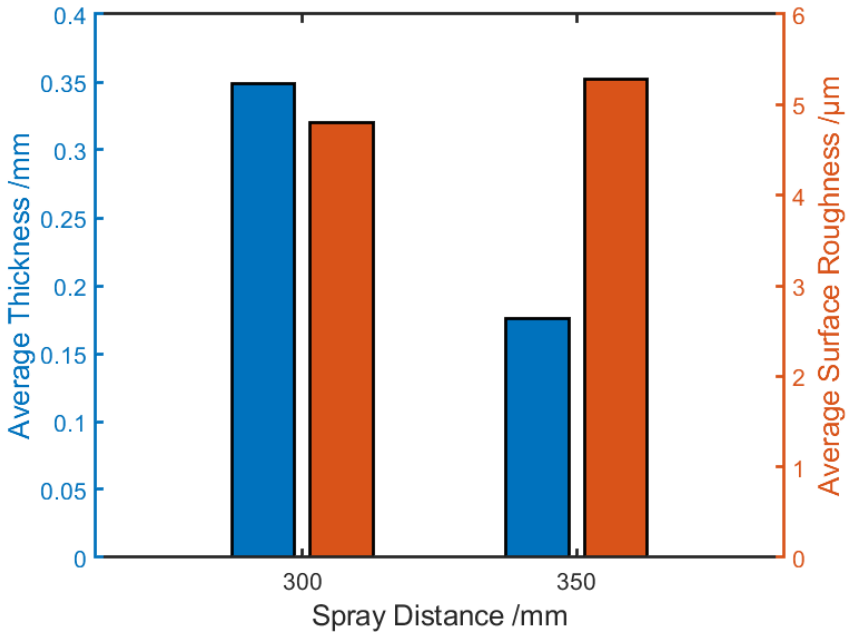


Figure 3.14: W coatings sprayed at spray distances of 300 and 350 mm.

Figure 3.15 shows the effect of the two further optimisations. Increasing powder-feed disc speed and decreasing traverse speed increased mass flux of W powder (per unit time and area) arriving at the substrate, resulting in an increase in coating thickness. Powder-feed disc speed was increased by a factor of four and the resulting thickness was 3.9 times larger than the Taguchi-optimised equivalent. Surface roughness increased with increased powder-feed disc speed, perhaps because too much cold W powder began to quench the plasma. When traverse speed was halved, which effectively doubled the particle flux, the thickness doubled as expected. However, increased powder flux would also increase substrate and pre-deposited W coating heating. It is well known that as temperature increases, powder deformation and flow on deposition increases, helping to reduce porosity and surface roughness [137, 138].

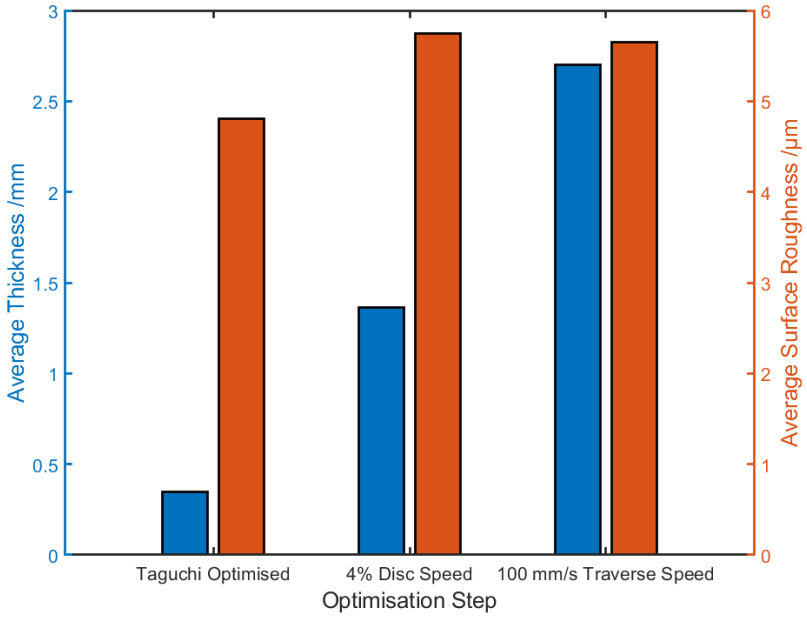
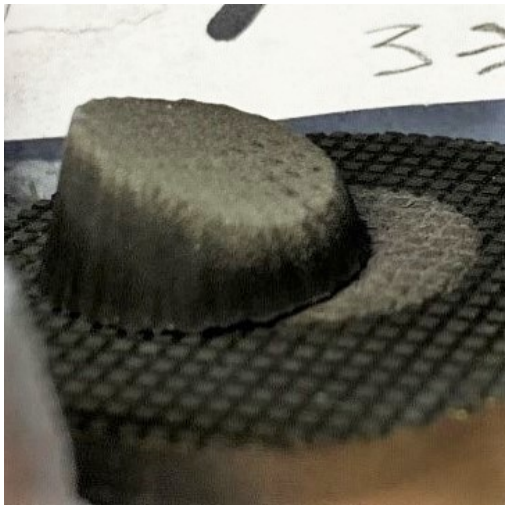


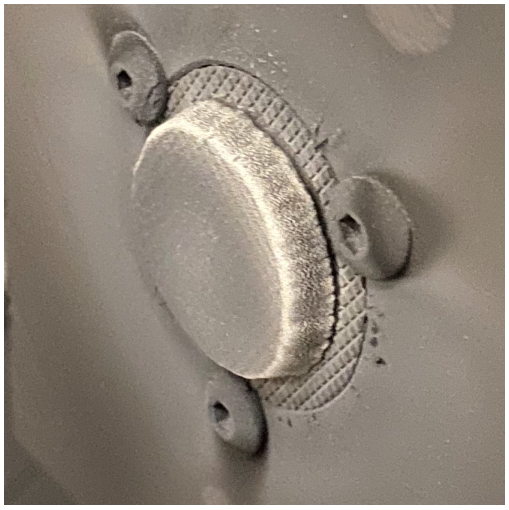
Figure 3.15: W coating thickness and surface roughness of progressive optimisation steps.

Figure 3.16 (a–b) show two 4 mm thick coatings on a hatched substrate using the previous parameters and the final optimised parameters shown in Table 3.7, respectively. Figure 3.16 (a) shows the W coating had delaminated and was deformed. In Figure 3.16 (b), the W coating had begun to delaminate. Upon removal from the Cu mount, the W coating fully delaminated. Figures 3.16 (c–d) show cross-sectional micrographs for the pre-existing plasma conditions and the final optimisation (following delamination). There were pores throughout the non-optimised coating, which was substantially reduced following optimisation. Most

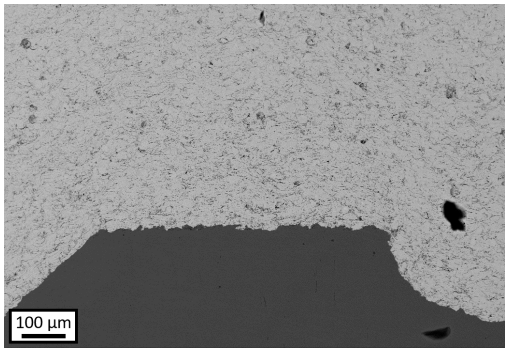
residual porosity resided at the coating-substrate interface around geometric features, such the corners of the hatched design [88]. The optimisation led to thicker, denser, and more homogeneous W coatings, although adhesion on cooling was still problematic.



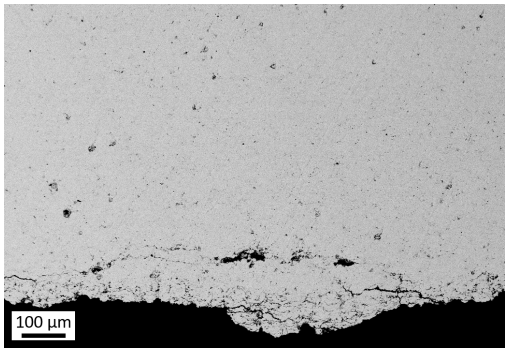
(a) 4 mm coating produced using previous group recipe (unpublished).



(b) 4 mm coating produced using optimised coating.



(c) SEM of cross-section of coating produced using previous group recipe.



(d) SEM of cross-section of coating produced using optimised coating.

Figure 3.16: Photographs and SEM images of W coatings manufactured using the previous parameters and the final optimised parameters shown in Table 3.7.

Table 3.10 highlights the difference in density between the optimised VPS W coating and the FAST W coating produced using the same method as Cui et al. [74]. Apparent density is the most commonly stated value in the literature as it provides a 'best-case-scenario' value which is obtainable by removing any open porosity found at the surface (i.e. via polishing). However, for additively-manufactured components this could be misleading if there is significant porosity. Therefore, it is good practice to investigate and state the open, closed and total porosity as defined in Equations 3.8, 3.9 & 3.11. W produced via FAST had a value of open porosity that exceeded 14% — the statistical threshold for interconnected porosity [139, 140] — which indicated that removal of this porosity would be impractical. On the other hand, the optimised VPS sample had an open porosity value of 6.2%, most likely to be located near the original interface, as seen in Figure 3.16 (d), due to the geometry of the hatched substrate design. If this volume of porosity were to be removed via surface polishing then only the regions of closed porosity would remain. Due to the resulting decrease in sample volume, the percentage of closed porosity would increase to the value of closed apparent porosity (9.3%), which matches the 'best case' apparent density.

	VPS	FAST
Apparent Density ($g \cdot cm^3$)	17.4	17.4
Percentage of Theoretical Density (19.28 $g \cdot cm^3$)	90.7%	90.6%
Open Sample Porosity	6.2%	20.6%
Closed (Bulk) Sample Porosity	8.8%	7.5%
Total Sample Porosity	15.0%	28.1%

Table 3.10: Density and porosity measurements of optimised VPS W and FAST W coatings. FAST coatings were produced using the recipe stated by Cui et al. [74].

3.4 Summary

Correct optimisation of vacuum plasma spraying parameters is important to achieve sufficient coating density, thickness and adhesion. In this work, a three-stage optimisation process was used with the aim of producing 4 mm thick tungsten coatings on textured steel substrates.

Optimisation began by calibrating the W powder feed mass flow rate, to ensure that all powder was successfully injected into the plasma. Following this, parameters relating to the plasma 'flame' were optimised using Taguchi analysis. An orthogonal array consisting of chamber pressure, Ar flow rate and H_2 flow rate was produced; each of these variables had three possible levels, resulting in a total of nine specific combinations. These permutations were applied in both 'wipe' tests and cycled spraying tests. Signal-to-noise ratios were calculated from Equations 3.1–3.2 for each set of experimental variables using the measured deposition efficiency, coating thickness and surface roughness. These ratios enabled the efficacy of the different parameter levels to be assessed in order to produce a set of near-optimum values. Finally, spray distance and gun traverse speed were optimised to increase coating deposition rate.

The final VPS recipe produced a 91% dense, 4 mm thick, W coating on hatched F91 steel substrates. The coating was a significant improvement in comparison to the original group recipe in terms of porosity and homogeneity.

4 Modelling of Substrate Texturing

4.1 Introduction

Thomas was able to achieve a W coating thickness of 2 mm by using highly bespoke and small scale "Surfi-Sculpt" substrates which demonstrated that thick W coatings could remain adhered with the aid of substrate texturing. Finite element modelling (FEM) with geometries based on cross-sectional micrographs provided insights into the geometric stress concentration behaviour and it was suggested that induced micro-cracking relieved stored strain energy due to thermal contraction mismatch during cool-down from manufacture [88].

Cui et al. later utilised hatched substrates produced via EDM to explore W coatings up to 2 mm thick on steel using the field assisted sintering technique (FAST) [74], as shown in Figure 4.1. Some qualitative EDX, EBSD and nanoindentation analysis was undertaken to explore the nature of the W coating, interface reactions and the scale of crack formation. For the first time, sculptured substrates

with ultra-thick W coatings were investigated by thermal cycling, and showed that induced coating segmentation enabled dramatically enhanced thermal cycling response. However, only a simple quantitative analysis of the behaviour was attempted.

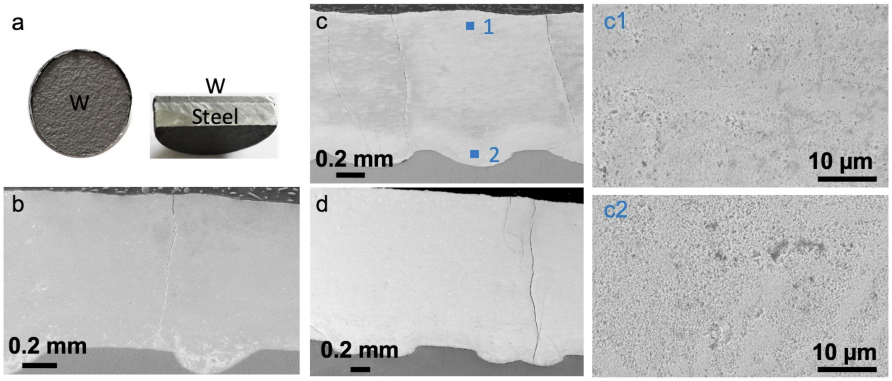


Figure 4.1: Optical and SEM images showing the W coatings on hatched steel substrates investigated by Cui et al. [74][1].

Finite element (FE) based simulations are typically used to estimate the distribution of stress and strain in coated systems. FE-based codes rely on the discretisation of continuous expressions for stress and strain onto a grid of computational nodes and this mesh of nodes often requires careful optimisation/refinement to obtain stable 'grid independent' solutions to these equations, especially where there are sharp geometry changes, such as crack tips or substrate hatching.

[1]Reprinted from Materials and Design, Vol 212, Wen Cui et al., Joining and cycling performance of ultra-thick tungsten coatings on patterned steel substrates for fusion armour applications, 110250, © copyright (2021), under CC by 4.0.

The vertical micro-cracking in thick W on sculpted substrates observed in both Thomas and Cui's work stems from the thermal strain experienced by the W due to the difference in the coefficient of thermal expansion (CTE) between W and steel. This system can be approximated as a bimetallic strip. Timoshenko's analytical work on bimetallic strips in 1925 [141] provides a good starting point to estimate coating/substrate elastic curvature and induced stresses and strains in 2D given by:

$$k = \frac{2(t_1 + t_2)(\alpha_2 - \alpha_1)\Delta T}{(t_1 + t_2)^2 + \frac{1}{3}(E_1 t_1^3 + E_2 t_2^3)(\frac{1}{E_1 t_1} + \frac{1}{E_2 t_2})} \tag{4.1}$$

$$k = \frac{2\delta}{x^2 + \delta^2} \rightarrow \delta = \frac{kx^2}{2}, \text{ when } \delta \ll k \tag{4.2}$$

where k is curvature of a beam -shaped arrangement, x is beam length, δ is beam deflection, ΔT is change in temperature, and for two metals (1) and (2): t_1 & t_2 denote their thicknesses, α_1 & α_2 their coefficients of thermal expansion, and E_1 & E_2 their Young's moduli, respectively. Further,

$$\begin{aligned} \sigma_{max_i} &= \sigma_{axial_i} + \sigma_{bending_i} \\ &= \frac{(\alpha_2 - \alpha_1) \cdot \Delta T \cdot (\frac{2}{ht_i}(E_1 I_1 + E_2 I_2) + \frac{t_i E_i}{2})}{\frac{h}{2} + \frac{2(E_1 I_1 + E_2 I_2)}{h} \cdot (\frac{1}{E_1 t_1} + \frac{1}{E_2 t_2})} \end{aligned} \tag{4.3}$$

$$\epsilon_{misfit} = (\alpha_2 - \alpha_1) \cdot \Delta T \tag{4.4}$$

where σ_{max_i}, σ_{axial_i} and $\sigma_{bending_i}$ are the maximum (which must occur at the interface), axial and bending stresses in either the coating or substrate (denoted by i), ΔT is change in temperature, h is the total thickness of the bimetallic strip, ϵ_{misfit} is the misfit strain between the two components of the bimetallic strip and for two metals (1) and (2) and the analysed coating/substrate (again, denoted by i): t_1, t_2 & t_i denote their thicknesses, I_1 & I_2 their second area moments, α_1 & α_2 their coefficients of thermal expansion, and E_1, E_2 & E_i their Young's moduli, respectively.

Thomas observed that stored strain energy reductions were key to coating survival during cool-down from elevated manufacturing temperatures [88] and therefore modelling stored strain energy release rate (G) could be useful. Crack growth occurs when the energy release rate exceeds a critical value, G_C, for the material:

$$G_C = \frac{K_{IC}^2}{E'} \tag{4.5}$$

where K_{IC} is the fracture toughness of the material in mode-I loading, and E' is the Young's modulus of the material for plane stress conditions.

The mode-I fracture toughness of W is approximately 4–9 MPa$\cdot\sqrt{\text{m}}$ [54, 142–144]. The upper limit of this range corresponds to a critical energy release rate of $\sim$200 J$\cdot$m^{-2}.

The J-integral is one way to determine the amount of energy released per unit area of crack surface increase and is compatible with many FEM software packages [145]. It is only equatable to the stored strain energy release rate when deformation near the crack is elastic and when a crack is growing straight ahead [146].

This chapter uses FEM in an initial attempt to understand the origin and propagation of any cracks that occur due to thermal strains and stresses experienced during manufacture. The models were used as a coarse assessment of the mechanics of bimetallic components with a large difference in CTE. This was achieved by analysing the effect that a crack, propagated by user-selected increases in crack length, would have on stress, strain, stored strain energy density and J-integral. Whilst this FEM was compared with coatings produced using the FAST, the pressures and dynamic cooling regimes experienced in the FAST were not considered and isothermal material properties were used for simplicity, meaning that it would be unsuitable for use outside of this project without development to account for these factors.

4.2 Methodology

Stress analysis of W coatings on steel substrates was undertaken by finite element modelling (FEM) conducted using the COMSOL Multiphysics® (COMSOL Inc.) software. The modelling was in two stages:

1. Simple bimetallic strip/disc FEM simulations for comparison with theory. These simulations were used to build experience in the software, establish boundary conditions and optimise mesh refinement.

2. Investigation of surface texture effects and crack path analysis, leading to comparison with experimental results.

The material parameters used in the models were the W and AISI 4340 steel properties shown in Table 4.1 (with ASTM A182-16a F91 included for reference):

Property	Tungsten	AISI 4340	F91 [147]
Coefficient of Thermal Expansion (K^{-1})	4.5 $\times 10^{-6}$	12.3 $\times 10^{-6}$	10.6-12.7 $\times 10^{-6}$
Heat Capacity ($J \cdot kg^{-1} \cdot K^{-1}$)	132	475	440
Density ($kg \cdot m^{-3}$)	17800	7850	7700
Thermal Conductivity ($W \cdot m^{-1} \cdot K^{-1}$)	175	44.5	26–30
Young's Modulus (GPa)	360	205	218–162
Poisson's Ratio	0.28	0.28	-

Table 4.1: Parameters used for stress analysis and simulation of W coatings on steel substrates. Property data for W and AISI 4340 were available within the COMSOL software.

4.2.1 Model validation and mesh refinement analysis

Using Equations 4.1 and 4.2, the deflection of a bimetallic strip was calculated analytically. FE models were then created in 2D, 3D and axisymmetric 'Space Dimension' modes. The same parameters (material thicknesses, stresses, and expansion coefficients) used in the analytical equation were used in FE analysis and the results compared to verify that the boundary conditions used in the FE models were appropriate.

Substrate surface geometries were then introduced into the model, and an image of the modelled hatched substrate used is shown in Figure 4.2.

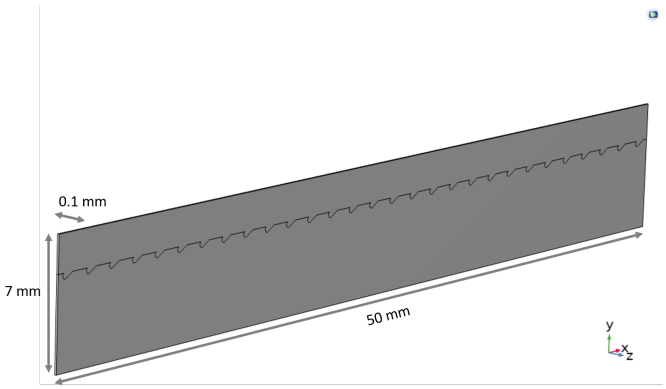


Figure 4.2: 2 mm W coating on 'hatched' substrate modelled using COMSOL to simulate the substrate texturing shown in Figure 3.3.

After appropriate boundary conditions were set, mesh refinement was undertaken. This was split into two parts: overall mesh refinement, to ensure the geometry was fully captured by the model, and crack tip mesh refinement, to ensure that modelling of localised stresses followed the crack tip during propagation.

As the hatched profile was the most complex surface geometry and was expected to lead to the steepest stress/strain gradients, it was chosen to guide the overall mesh refinement. Crack tip mesh refinement was completed for a flat substrate geometry. The objective of the mesh refinement process was to use the coarsest mesh possible, for speed of calculation, while ensuring consistent results with finer, but more computationally demanding, grids. In all cases, mean and median element volume, median stored strain energy density and maximum first principle stress were considered in identifying grid-independent solutions.

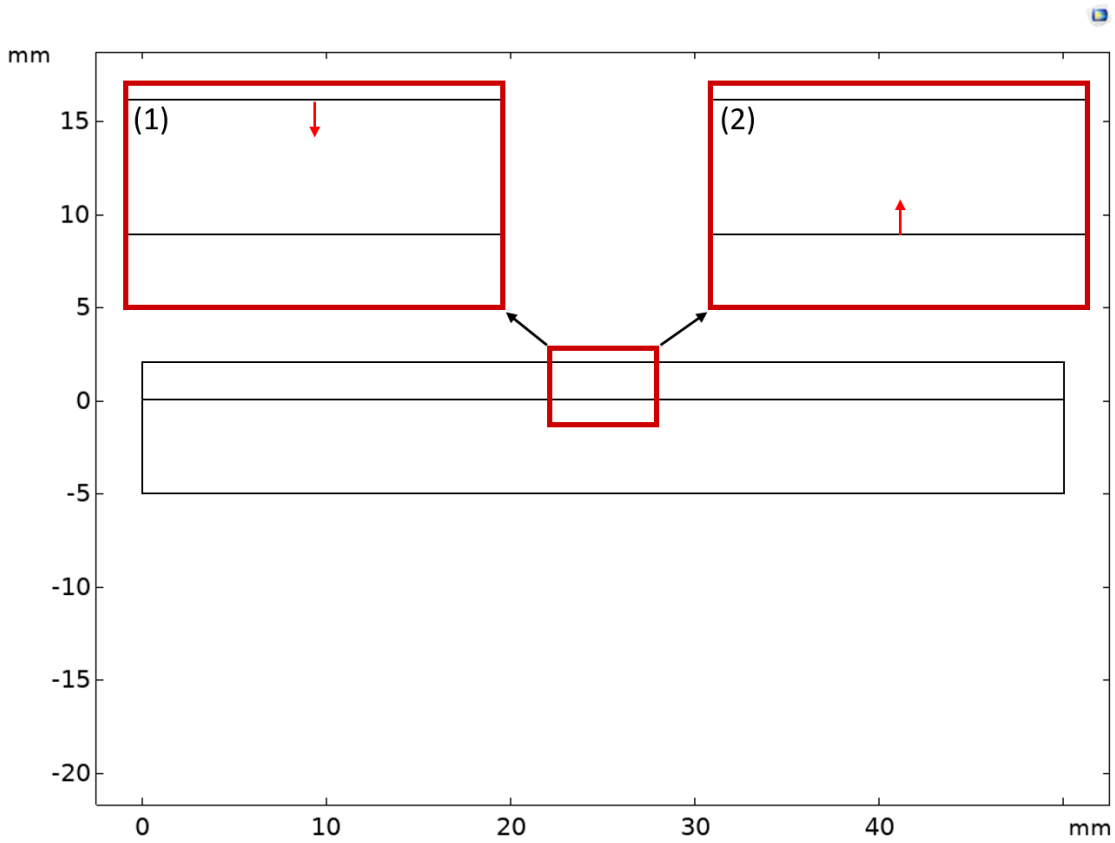
4.2.2 Crack path analysis

Following creation of different surface textures, a simple 2D bimetallic strip was modelled using the determined mesh sizing to compare with models containing pre-selected cracks, located at positions based on microstructural analysis. The deviatoric strains, principal stresses and stored strain energy density distributions were calculated. Then a study was undertaken to investigate the effect that different crack geometries might have on residual strains, stresses and crack growth, driven by the local strain energy release rate around a pre-existing crack tip. Two different crack types were considered and examples are shown in Figure 4.3 (a). These cracks were 'propagated' by user-selected increases in crack length. At each increment of crack length, the deviatoric strains, principal stresses and stored strain energy density were calculated, along with a J-integral calculation of the

energy density released by the crack as it grew. More sophisticated approaches to crack propagation are possible that do not rely on 'user driven' crack assumptions, but required additional software packages that were unavailable. However, overall qualitative insights are likely to be similar.

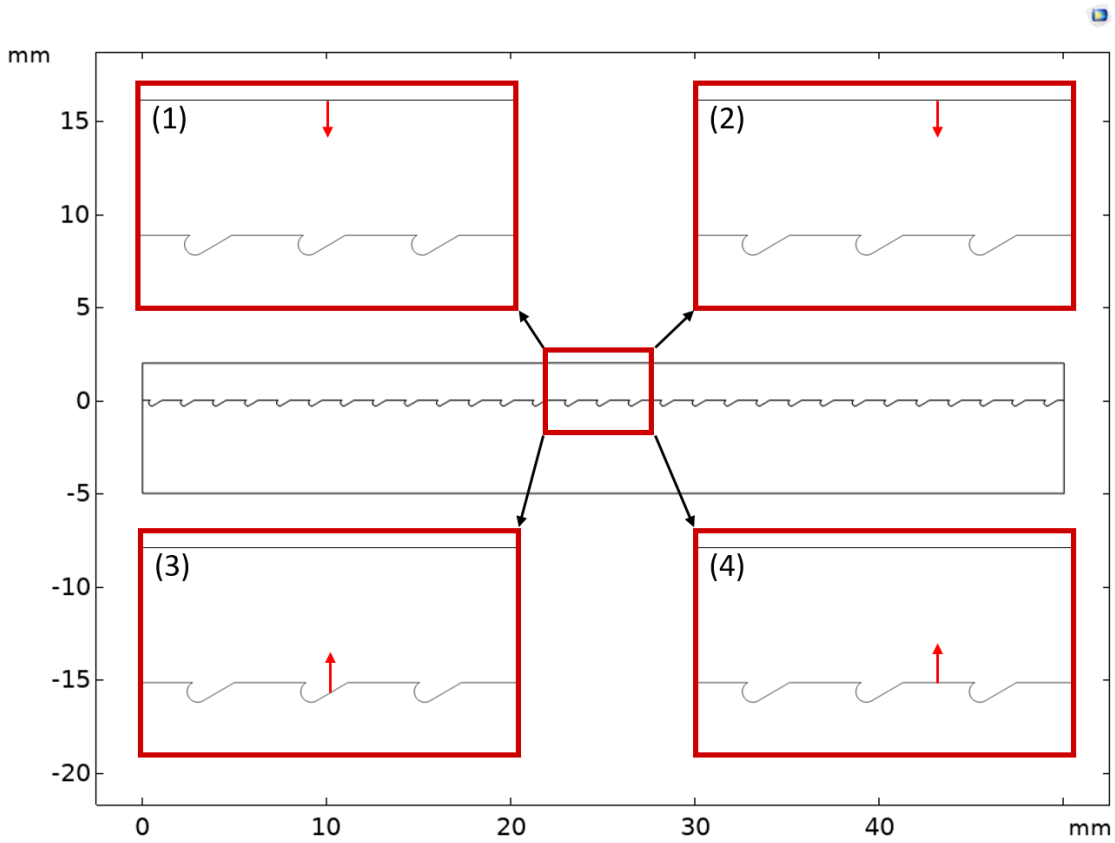
Further models were made using the hatched substrate design and user-selected crack direction, location and growth and are shown in Figure 4.3 (b). At each imposed crack length increment, stress and strain distributions and a J-integral calculation were again computed.

Through-thickness cracks in the W coating have previously been observed to split near the interface with the steel substrate [74], so two models were made with a hatched substrate and an interface crack originating at user-selected locations. The angle of the cracks were then increased by a user-selected amount as shown schematically in Figures 4.3 (c–d). In both models, stress and strain distributions and a J-integral calculation were established for each iteration.



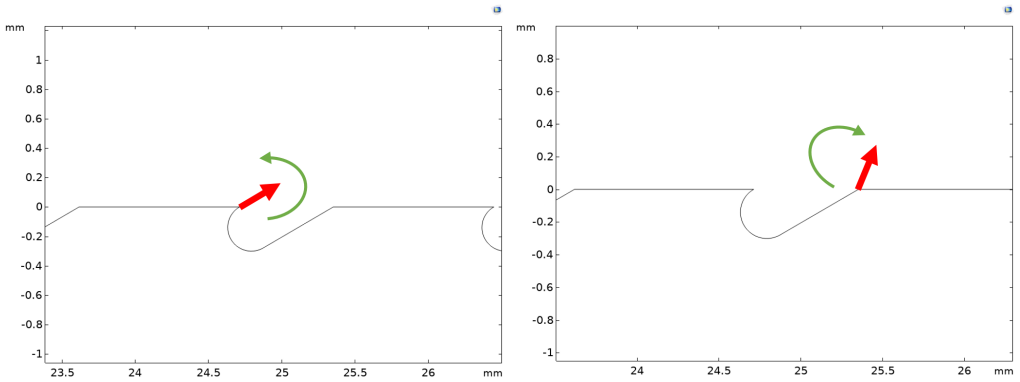
(a) Model set-up for a 2D bimetallic strip with two expanded inset images illustrating the location of a crack in the centre of the strip starting at the surface (1) and interface (2).

Figure 4.3: Examples of user-selected crack locations, directions and splitting in COMSOL simulations for flat and hatched substrates. The red arrows highlight the crack locations and growth directions.



(b) Model set-up for a 2D bimetallic strip with a hatched substrate with four inset expanded images showing: (1) surface crack aligned with the hatching ('in the groove'), (2) surface crack located between crenellations ('out of the groove'), (3) interfacial crack 'in the groove', and (4) interfacial crack 'out of the groove'.

Figure 4.3: Examples of user-selected crack locations, directions and splitting in COMSOL simulations for flat and hatched substrates. The red arrows highlight the crack locations and growth directions.



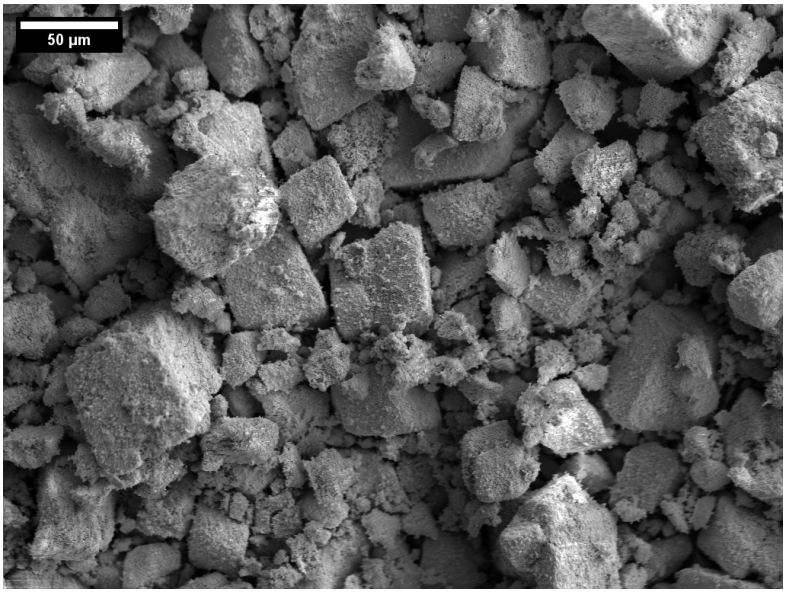
(c) Model set-up for an interfacial crack originating from the overhanging part of the substrate hatching. The green arrow indicates the increasing value of θ.

(d) Model set-up for an interfacial crack originating from the sloped part of the substrate hatching. The green arrow indicates the increasing value of θ.

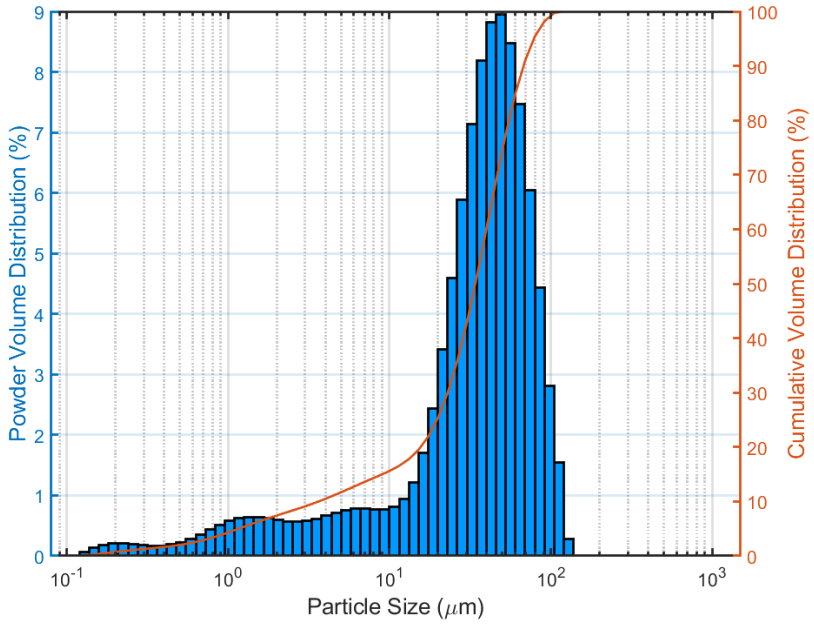
Figure 4.3: Examples of user-selected crack locations, directions and splitting in COMSOL simulations for flat and hatched substrates. The red arrows highlight the crack locations and growth directions.

4.2.3 Comparison of experiments with modelled predictions

Crack formation predictions from these simulations were then compared to experimental micrographs from FAST samples produced on hatched F91 steel substrates. FAST processing used a Dr Fritsch Direct Sinter Press DSP-507 and W nanopowder (purity 99.95%, nominal mean particle size 50 nm) supplied by Buffalo Tungsten Inc., US. An SEM image and powder particle size distribution are shown in Figure 4.4. Figure 4.4 (a) clearly illustrates that the powder formed large agglomerates between 10–50 μm in size. However, Cui et al. used the same powder and obtained a higher-magnification image confirming that particles were nanopowder which, when sintered, produced an average grain size of 227 $\pm$9 nm [74].

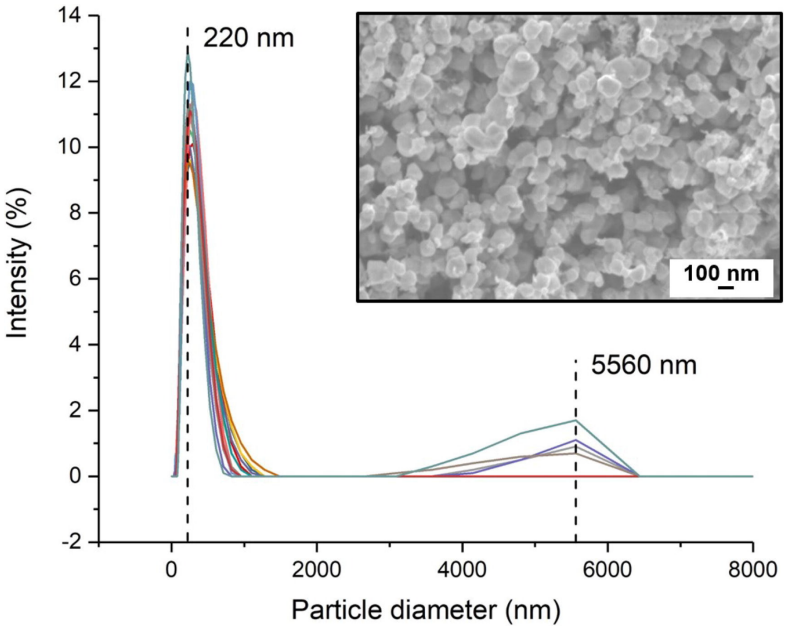


(a) SEM image of W powder used in FAST experiments.



(b) Particle size distribution of W powder supplied by Buffalo Tungsten Inc, US. Particles were significantly more likely to form agglomerates than the powder used for VPS.

Figure 4.4: (a) SEM image and (b) particle size distribution of W powder supplied by Buffalo Tungsten Inc. used in FAST experiments; (c) SEM image and particle size distribution determined by Cui et al. [74] for the same powder.



(c) Particle size distribution of W powder with inset SEM image produced by Cui et al. [74][2].

Figure 4.4: (a) SEM image and (b) particle size distribution of W powder supplied by Buffalo Tungsten Inc. used in FAST experiments; (c) SEM image and particle size distribution determined by Cui et al. [74] for the same powder.

The W powder was first cold-pressed onto the substrate inside a graphite die using a hydraulic press in the glove box before the die assembly was placed in a sealed bag for transfer. Upon opening the bag, the assembly was clad in graphite felt, positioned between the upper and lower electrodes of the FAST with a thermocouple inserted into the side of the die. The chamber was sealed and evacuated to 0.1 mbar as quickly as possible. This procedure was employed in order to min-

[2]Reprinted from Materials and Design, Vol 212, Wen Cui et al., Joining and cycling performance of ultra-thick tungsten coatings on patterned steel substrates for fusion armour applications, 110250, © copyright (2021), under CC by 4.0.

imise sample exposure to atmosphere, however some exposure was inevitable. The program settings used in the FAST 'recipe' are shown in Table 4.2. A pellet of W was made with no substrate using the same method for measurement of W density and compared with the density of VPS W coatings.

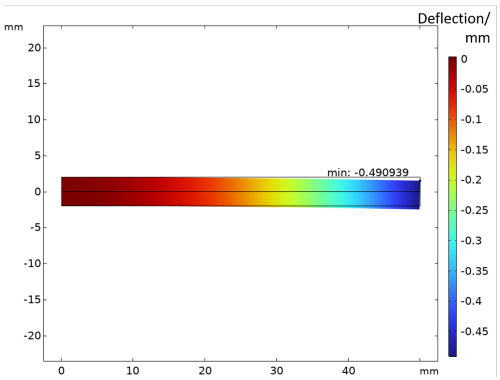
Parameter	Initial	1	2	3	4	5	Units
Pressure	9	9	50*	50	50	9	MPa
Temperature	∼30	600	1000	1000	300	30	°C
Time	-	342	240	600	1400	540	s
Temperature Rate	-	100	100	Hold	-30	-30	°C·min^{-1}

Table 4.2: FAST program sequential segments (*pressure progressively ramped).

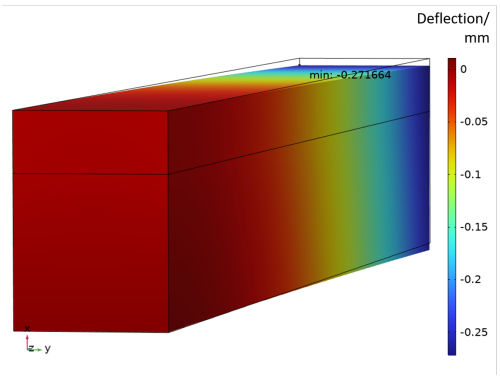
4.3 Results and Discussion

4.3.1 Model validation and mesh refinement analysis

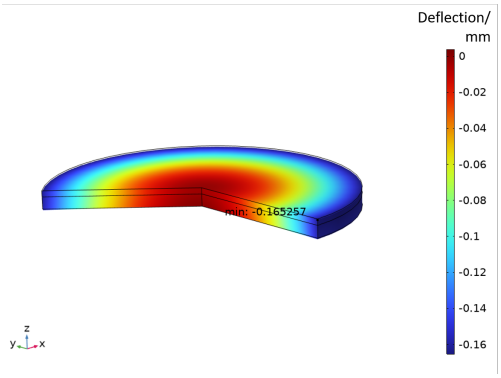
Figure 4.5 (a–c) shows the three finite element models used to explore thermal expansion mismatch effects on residual stresses and strains, and possible crack propagation. The models comprise a simple 2D strip, a 3D beam and an axisymmetric plate geometry for a bimetallic system. The bimetallic strip deflection due to thermal expansion mismatch can be obtained analytically from Equations 4.1–4.2, and is plotted in Figure 4.5 (d) for a W coating on a steel substrate with varying thicknesses of each (shown in the graph legend), all cooling from 200 °C to 20 °C under plane stress conditions. Figure 4.5 (d) also shows the predicted deflection under the identical condition from the three FE models. The calculated deflections using FEM agreed well with the analytical solutions for every geometry case, which gave credibility to the boundary conditions used in the model.



(a) 2D FEM of bimetallic strip deflection during cooling.

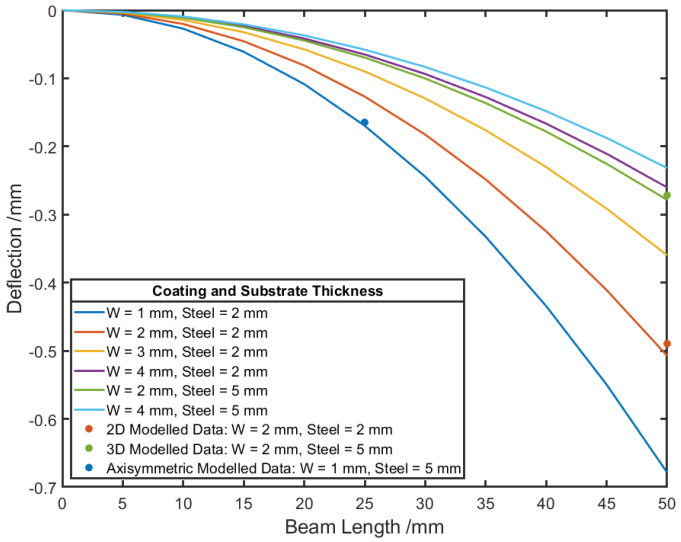


(b) 3D FEM of bimetallic beam deflection during cooling.



(c) Axisymmetric FEM of bimetallic plate (25 mm radius) deflection during cooling.

Figure 4.5: (a–c) 2D, 3D and axisymmetric bimetallic finite element models and (d) analytical and numerical beam deflection solutions as a function of coating (W) and substrate (steel) thicknesses. All models and solutions were calculated using a temperature change from 200 °C to 20 °C.



(d) Analytical solutions (lines) for a bimetallic beam deflection for varying thicknesses using Equations 4.1–4.2 compared with equivalent 2D, 3D and axisymmetric geometries (symbols) shown in Figure 4.5 (a–c).

Figure 4.5: (a–c) 2D, 3D and axisymmetric bimetallic finite element models and (d) analytical and numerical beam deflection solutions as a function of coating (W) and substrate (steel) thicknesses. All models and solutions were calculated using a temperature change from 200 °C to 20 °C.

Another check of the FE simulations was to ensure grid-independent solutions. Figure 4.6 shows the change in grid element median and mean volume, median stored strain energy density and maximum first principle stress for a fixed bimetallic strip with a hatched substrate geometry. As the finite element volume decreased and number of elements increased, the calculated stored strain energy density and first principle stress was stable up to a maximum mesh size of ∼2.5 mm. To avoid approaching this limit, 1.5 mm was chosen as the default grid or mesh size.

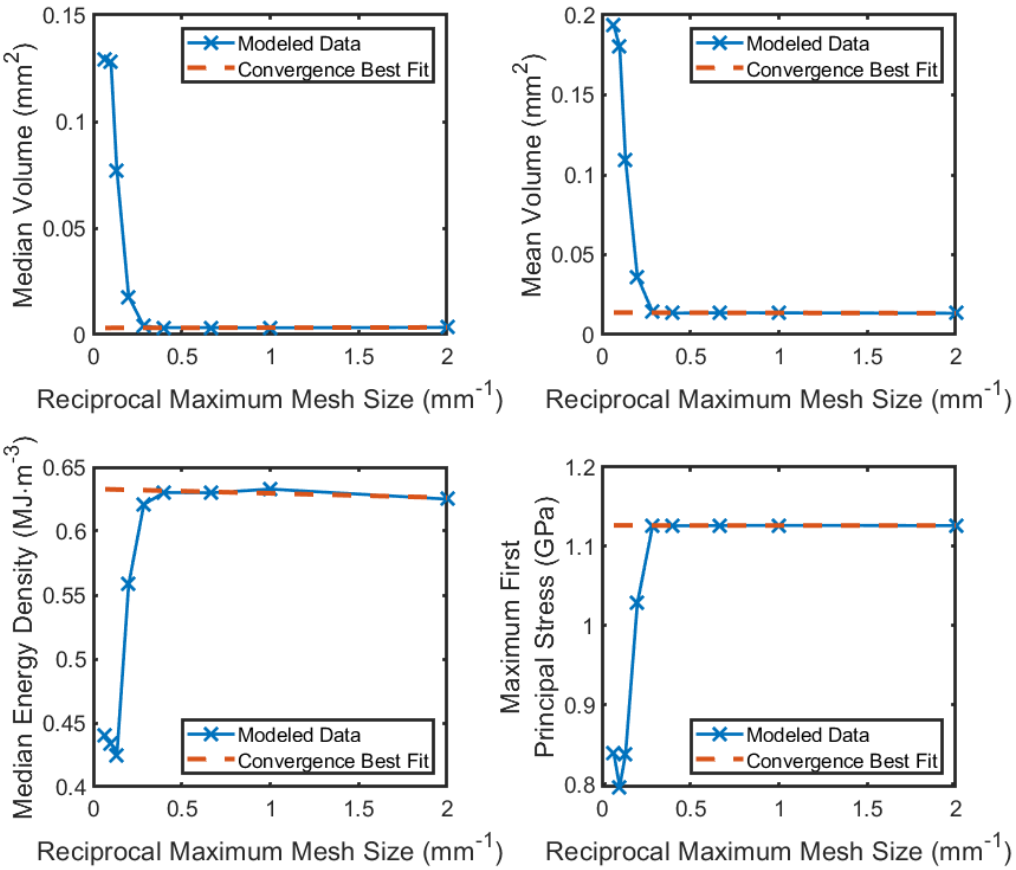


Figure 4.6: Calculated median and mean volume, median stored strain energy density, and maximum first principal stress against the inverse maximum mesh size for a 2D FEM simulation of a bimetallic strip with a hatched substrate.

Figure 4.7 shows a similar analysis for the more demanding case when a crack was introduced to a model (with a flat substrate geometry). The equivalent previous refinement analysis is shown in blue. The grid around the crack tip had to be refined to ∼0.05 µm, to ensure the steep strain and stress fields in this region could

be stably captured by the model. Subsequently median stored strain energy density was replaced by a method to assess the J-integral around the crack. The J-integral estimates the effect of strain energy release rate on possible crack propagation effects.

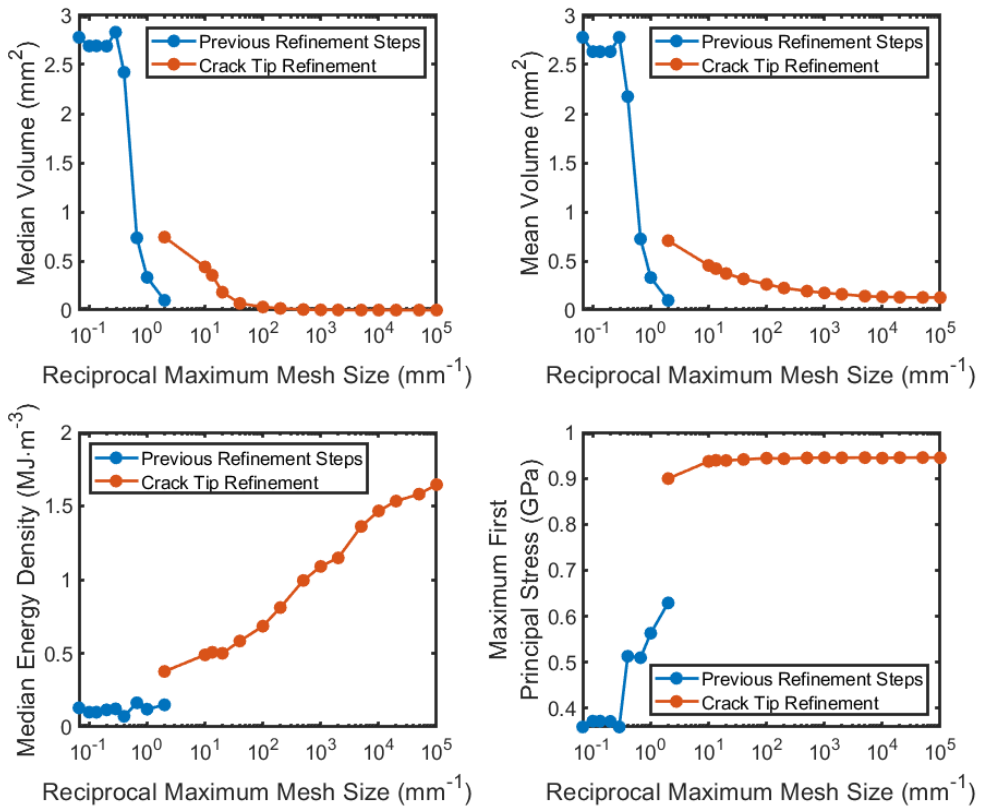


Figure 4.7: Calculated median and mean volume, median stored strain energy density, and maximum first principal stress against the inverse maximum mesh size (around the crack tip) for a 2D FEM simulation of a bimetallic strip (flat interface) with a surface crack introduced. The blue line shows equivalent data from Figure 4.6 for comparison.

4.3.2 Crack path analysis

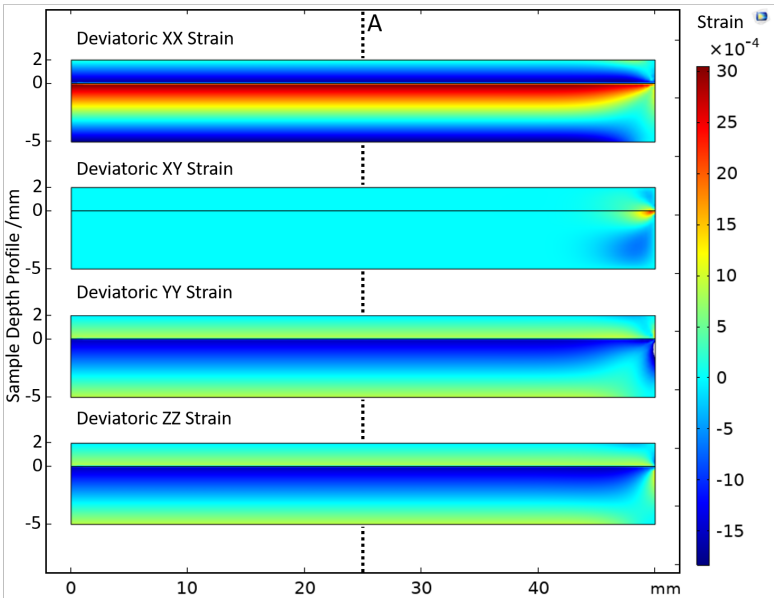
No crack

Selecting the maximum mesh size of 1.5 mm as determined above, a 2D bimetallic strip with a flat substrate cooling from 1020 °C to 20 °C was modelled under plane stress conditions. The system was assumed strain free at the manufacturing temperature of 1020 °C. The calculated distributions of deviatoric strains, principal stresses and stored elastic strain energy density at 20 °C are shown in Figures 4.8–4.10.

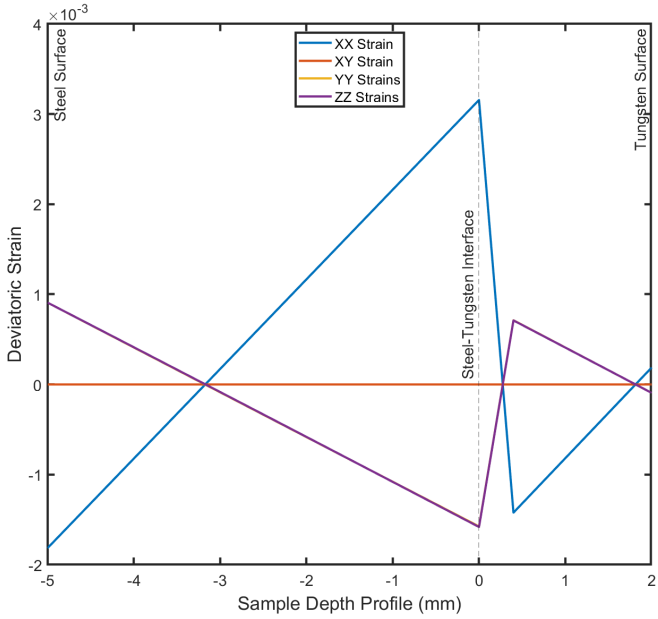
Deviatoric strain shows the strain involved in non-volumetric deformation and therefore shows strain within the coating and substrate more clearly. Figure 4.8 (a) demonstrates the four strain component distributions throughout the bimetallic strip; 0 in the sample depth profile represents the W-steel interface. The through-thickness strains halfway (25 mm) along the beam are shown in Figure 4.8 (b), denoted by the dashed line 'A' in Figure 4.8 (a). Strain distributions were linear from the interface to the free surfaces and there was a steep strain gradient at the interface due to the misfit strain. Away from the end of the beam, YY and ZZ strains were identical and approximately half the magnitude of the XX strain, due to the Poisson effect. The largest strain values (XX strains of 0.032 and -0.014 in the steel and W coating respectively) were found at the interface and at the free surfaces of the bimetallic strip.

Stress was anisotropic and almost entirely contained in the XX component halfway along the beam, as shown in Figure 4.9 (a). There was a small shear in the XY plane, in an opposing direction to stress in the XX plane at the interface; YY stress was negligible. The tensile and compressive regions are shown in the first and third principal stress distributions respectively and were largest at the interface, as shown in Figure 4.9 (b). The majority of the W coating was in compression and consequently the beam deflected downwards. However, the free surface of the W coating was in tension. At the end of the beam, 'local' shear stresses were produced along a distance from the end (approximately the same length as the total height of the strip) [141]. This was seen in all three principal stress distributions in the final 5 mm of the beam in Figure 4.9 (a). The highest stresses in the majority of the strip were again found at the interface (XX stresses of 744 MPa and -683 MPa for the steel and W coating respectively) and at the free surfaces.

The stored (elastic) strain energy density (SSED) distribution is shown in Figure 4.10. As expected, the SSED was highest at the interface (1.41 $MJ \cdot m^{-3}$), where the strains were largest.

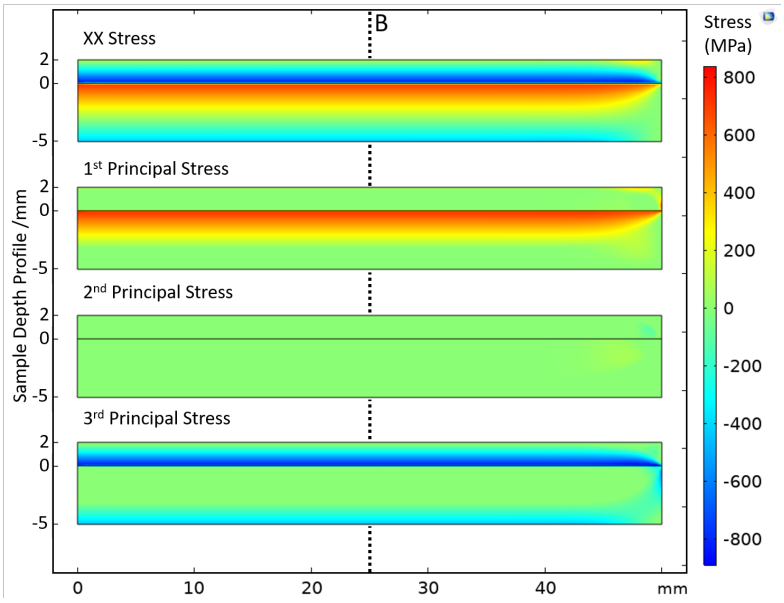


(a) The four deviatoric strain distributions calculated for a 2D FEM of a bimetallic strip following cooling from manufacture.

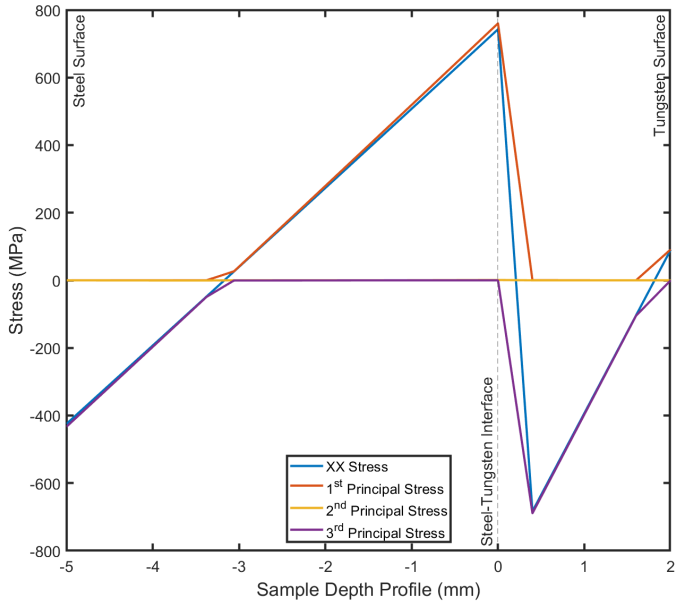


(b) Through-thickness deviatoric strain distributions calculated along dashed line 'A' in Figure 4.8 (a).

Figure 4.8: Deviatoric strain distributions calculated for a 2D FEM of a bimetallic strip cooled by 1000 °C.

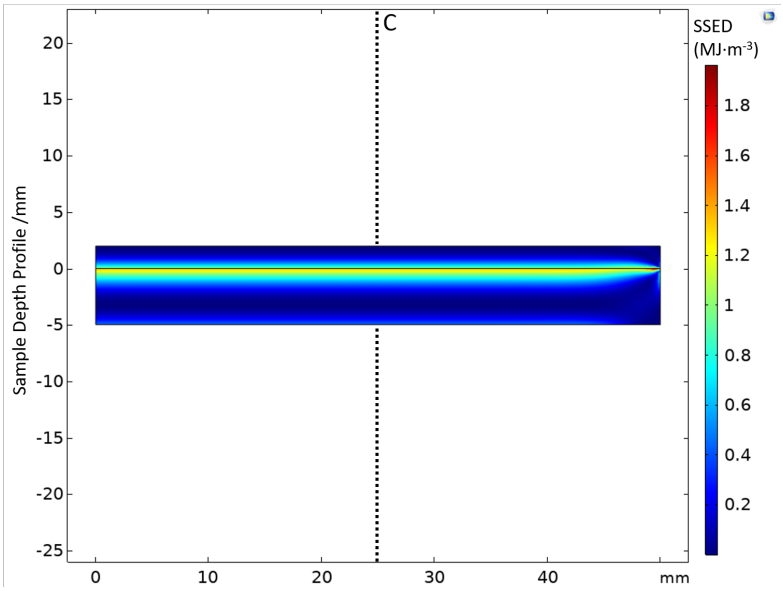


(a) XX and the three principal stress distributions calculated for a 2D FEM of a bimetallic strip following cooling from manufacture.

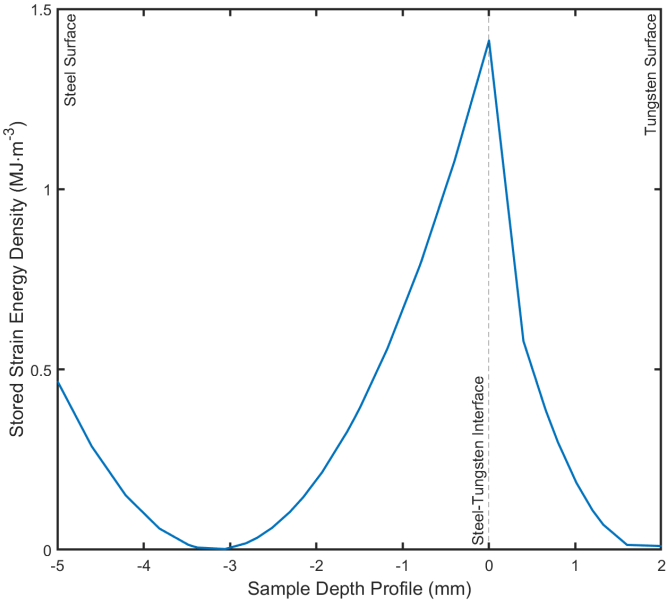


(b) Through-thickness stress distributions calculated along dashed line 'B' in Figure 4.9 (a).

Figure 4.9: Stress distributions calculated for a 2D FEM of a bimetallic strip cooled by 1000 °C.



(a) SSED distribution calculated for a 2D FEM of a bimetallic strip following cooling from manufacture.



(b) Through-thickness SSED distribution calculated along dashed line 'C' in Figure 4.10 (a).

Figure 4.10: Stored strain energy density (SSED) distributions calculated for a 2D FEM of a bimetallic strip cooled by 1000 °C.

Surface cracking

A bimetallic strip with a crack initiated at the surface, halfway along the beam was then modelled.

Figures 4.11–4.13 show the deviatoric strain distributions for a 1 mm long crack and how the deviatoric strains vary through the thickness of the bimetallic strip for user-selected crack lengths. Values calculated for the region directly above the crack tip were ignored as the model cannot take into account that there was no longer any material present. Strain distributions in the surface crack model followed a similar trend to the model with no crack, with the largest strains again at the interface and the free surfaces. However, the largest strain was always at the crack tip for crack lengths longer than ∼0.5 mm. Figure 4.13 (a) indicates that compressive strain in the W increased (in magnitude and the volume over which it occurred) ahead of the crack tip as crack length increased. This was due to progressively less W being subjected to the same compressive force applied by the shrinking steel. Because more of the W coating was in compression as crack length increased, there was a steeper strain gradient to the interface, up to a crack length of 1–1.25 mm and the highest interfacial strain was in the XX plane. Figure 4.11 shows that strain was higher at the interface ahead of the crack for each of the normal directions than at any other point at the interface. For crack lengths greater than 1.25 mm, strain in the XX plane at the interface decreased because the strain field from the crack began to overlap with the strain field from the interface.

A similar effect was observed in the stress distributions (Figures 4.14–4.15) as compressive stress increased and extended further into the W coating as the crack length was increased (seen in Figure 4.16). This was accompanied by a reduction in tensile stress at the interface and less stress at the free surface of the steel substrate as shown in Figures 4.16 (b) and (d) respectively; this was a result of the coating effectively becoming more compliant as the crack length increased.

SSED distributions shown in Figure 4.17 and Figure 4.18 (a) show that through-thickness SSED was similar to the uncracked coating, with the exception of a sharp spike ahead of the crack tip due to the steep strain gradients seen in Figures 4.11–4.13. This peak grew with increasing crack length because the crack tip was located in steadily more compressive regions which meant that the surrounding strains were also larger. Because the stored strain energy ahead of the crack also increased with crack length, more energy was released as the crack grew. Figure 4.18 (b) shows the calculated J-integral as a function of crack length. The shape of the J-integral plot approximately matches the shape of the highest SSED, stresses and strains (located at the crack tip) for each crack length. The critical energy release rate for W (from Section 3.1) is marked by the dot-dashed line in Figure 4.18 (b). The J-integral magnitude exceeded G_C at a crack length of 0.6 mm, inferring that such a crack would propagate freely.

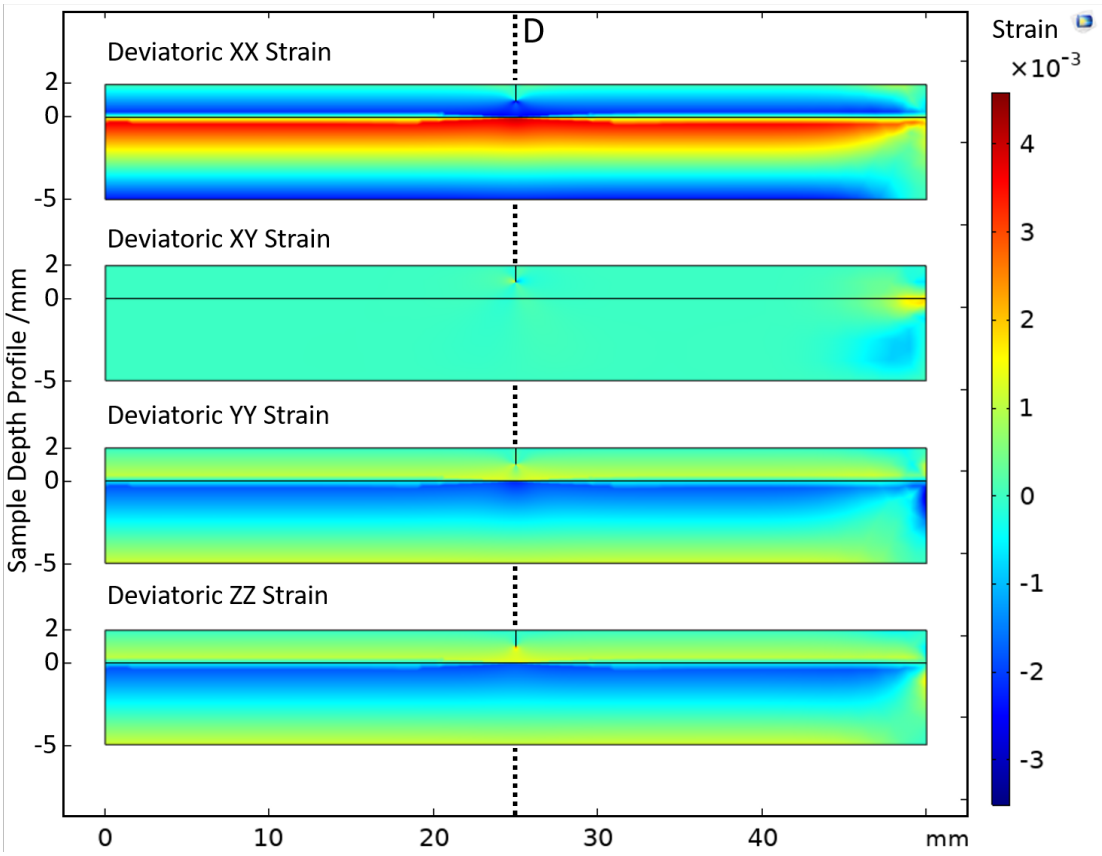
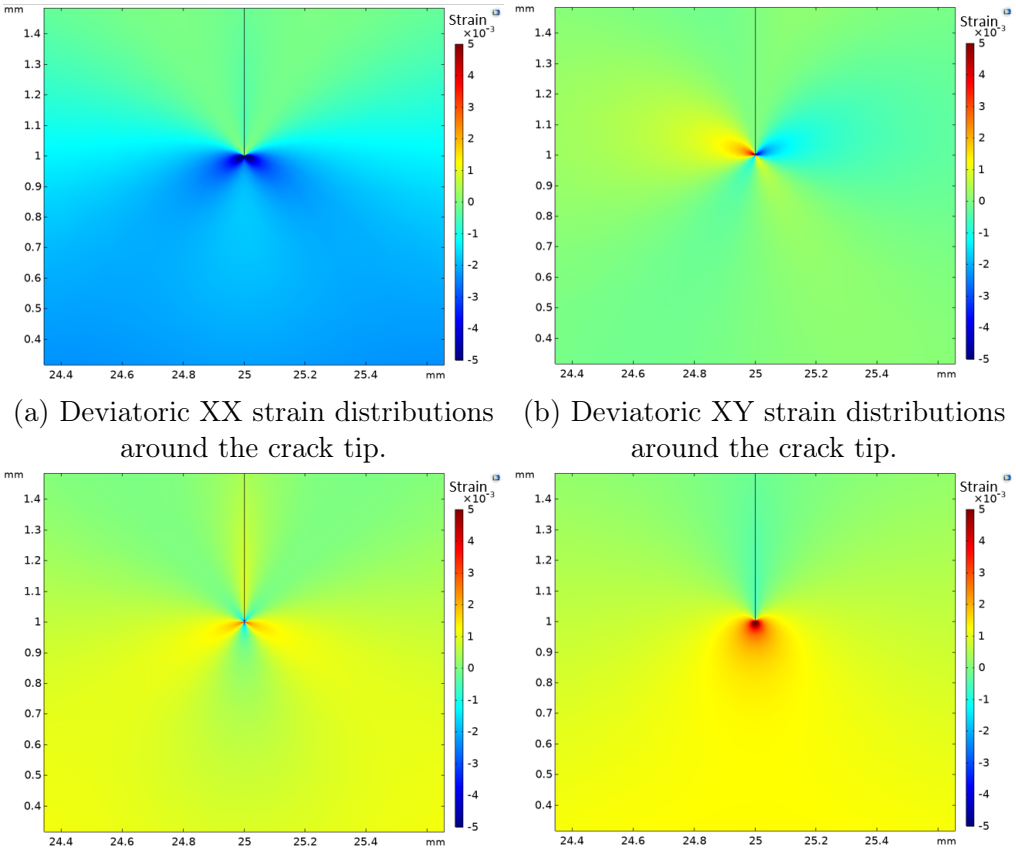


Figure 4.11: The four deviatoric strain distributions calculated for a 2D FEM of a bimetallic strip with a 1 mm long surface crack following cooling from manufacture.



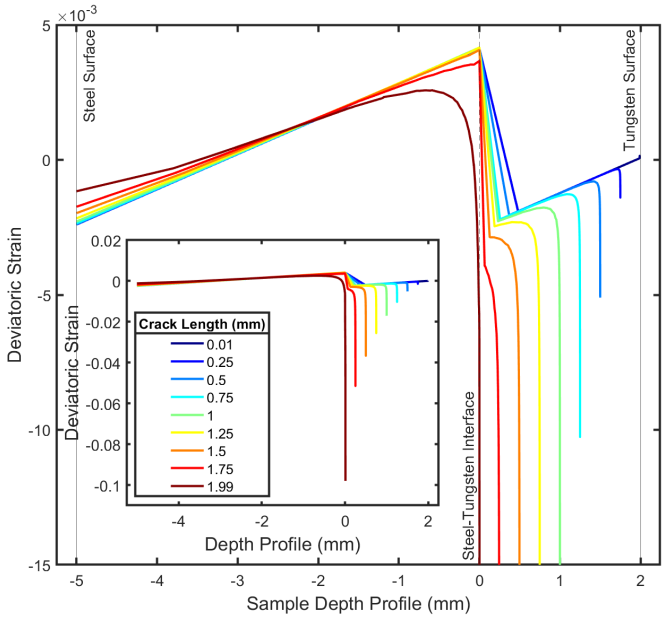
(a) Deviatoric XX strain distributions around the crack tip.

(b) Deviatoric XY strain distributions around the crack tip.

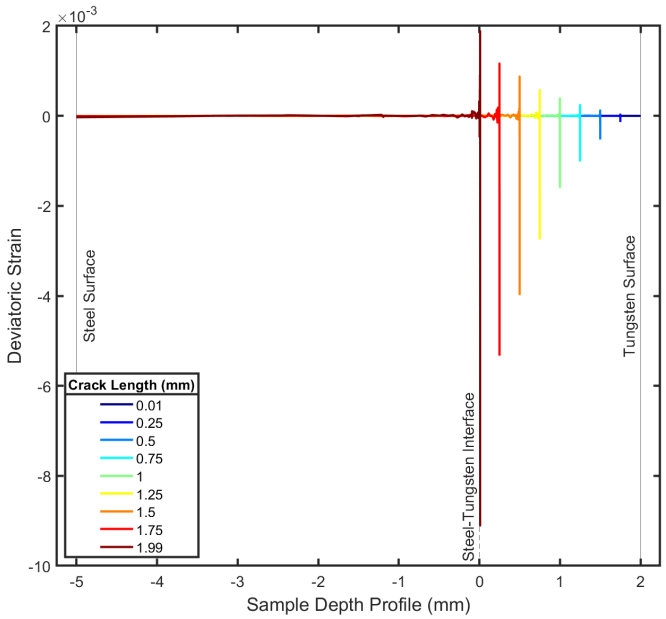
(c) Deviatoric YY strain distributions around the crack tip.

(d) Deviatoric ZZ strain distributions around the crack tip.

Figure 4.12: Deviatoric strain distributions around the crack tip calculated for a 2D FEM of a bimetallic strip cooled by 1000 °C.

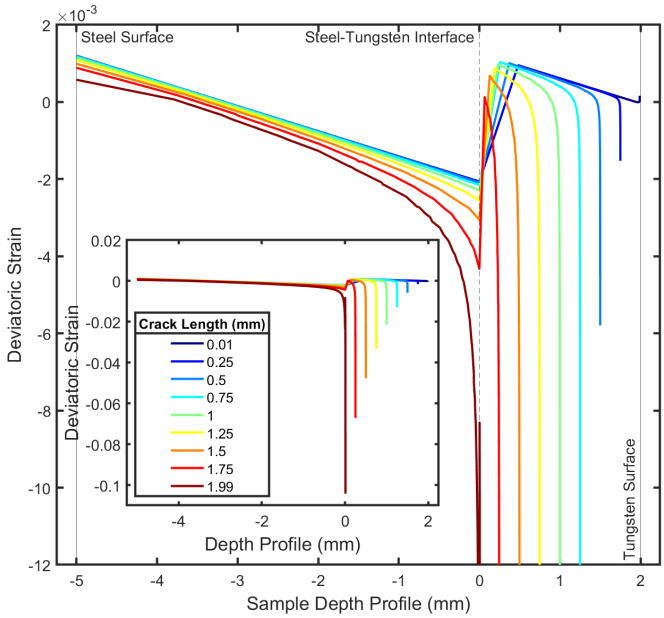


(a) Through-thickness deviatoric XX strain distributions in the centre of the bimetallic strip.

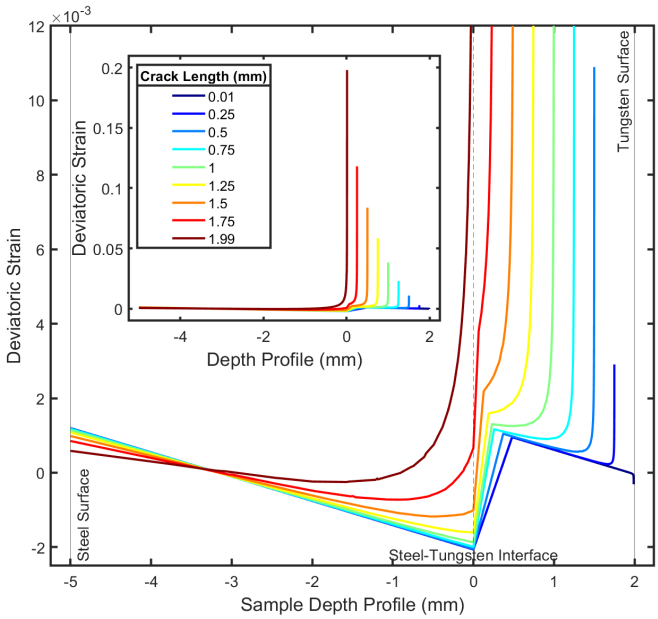


(b) Through-thickness deviatoric XY strain distributions in the centre of the bimetallic strip.

Figure 4.13: Through-thickness deviatoric strain distributions calculated along line 'D' in Figure 4.11 up to the crack tip for various surface crack lengths.



(c) Through-thickness deviatoric YY strain distributions in the centre of the bimetallic strip.



(d) Through-thickness deviatoric ZZ strain distributions in the centre of the bimetallic strip.

Figure 4.13: Through-thickness deviatoric strain distributions calculated along line 'D' in Figure 4.11 up to the crack tip for various surface crack lengths.

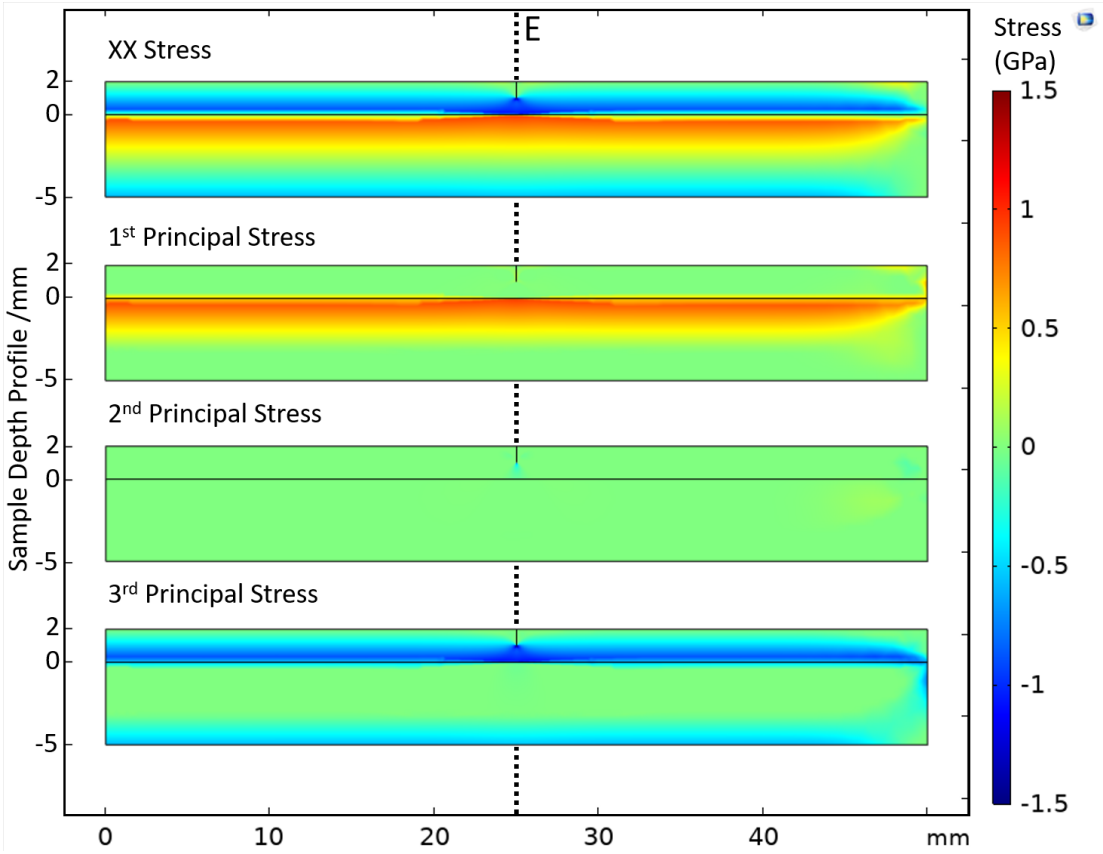
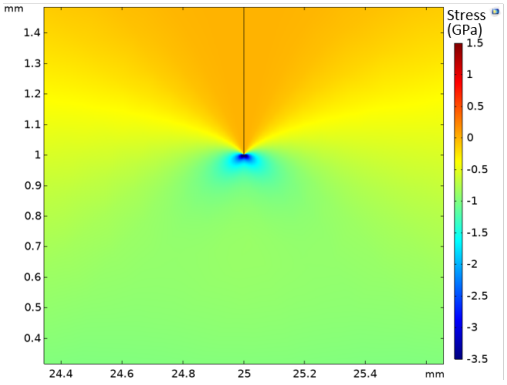
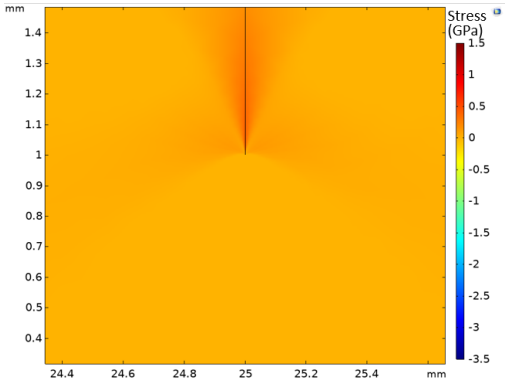


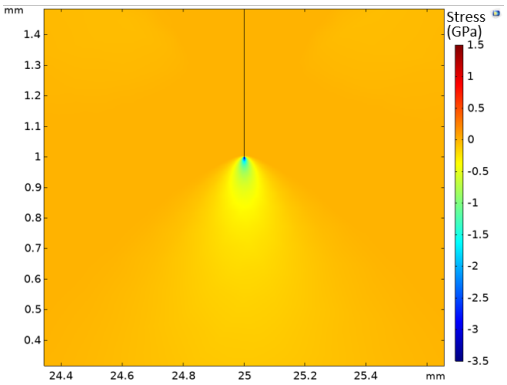
Figure 4.14: XX and the three principal stress distributions calculated for a 2D FEM of a bimetallic strip with a 1 mm long surface crack following cooling from manufacture.



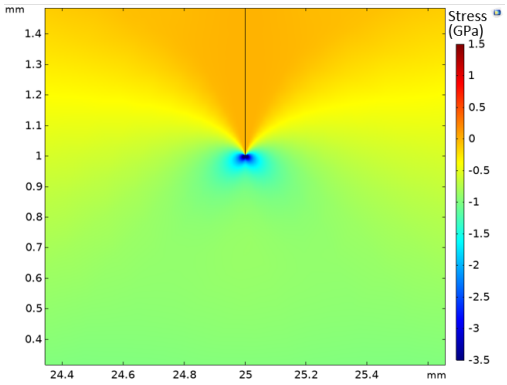
(a) XX stress distributions around the crack tip.



(b) First principal stress distributions around the crack tip.

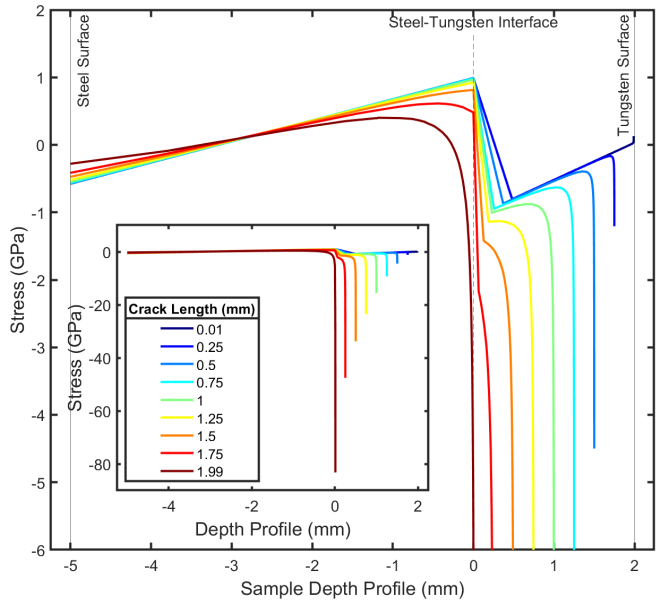


(c) Second principal stress distributions around the crack tip.

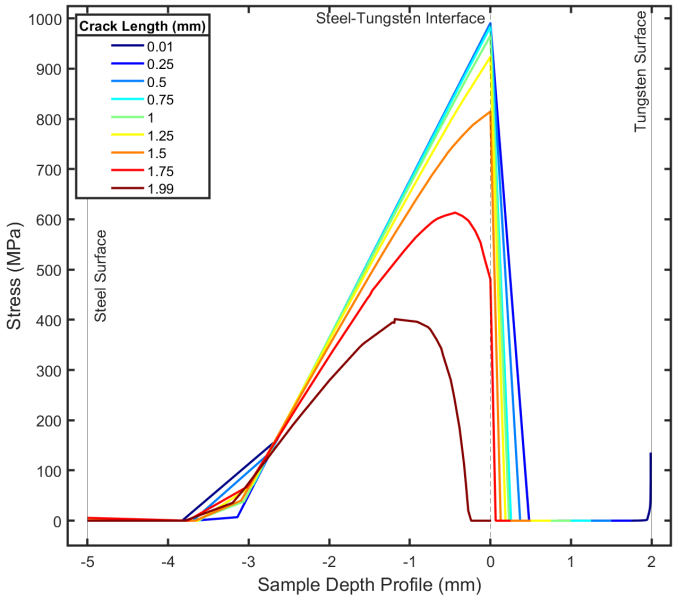


(d) Third principal stress distributions around the crack tip.

Figure 4.15: XX and principal stress distributions around the crack tip calculated for a 2D FEM of a bimetallic strip cooled by 1000 °C.

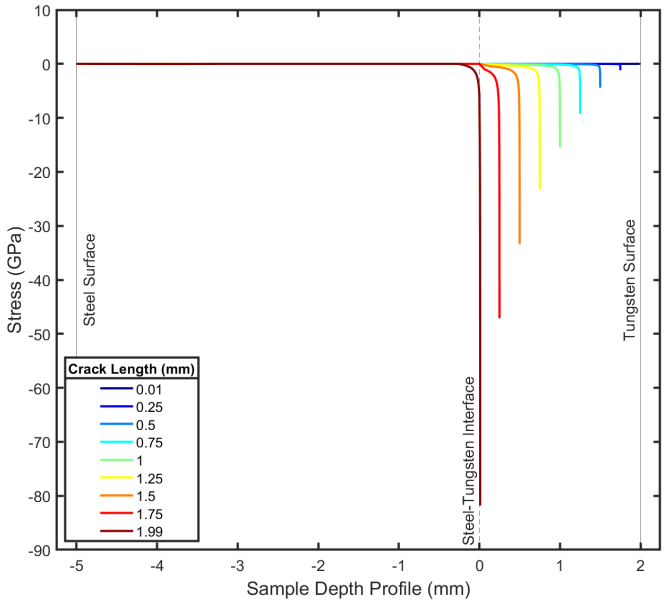


(a) Through-thickness XX stress distributions in the centre of the bimetallic strip.

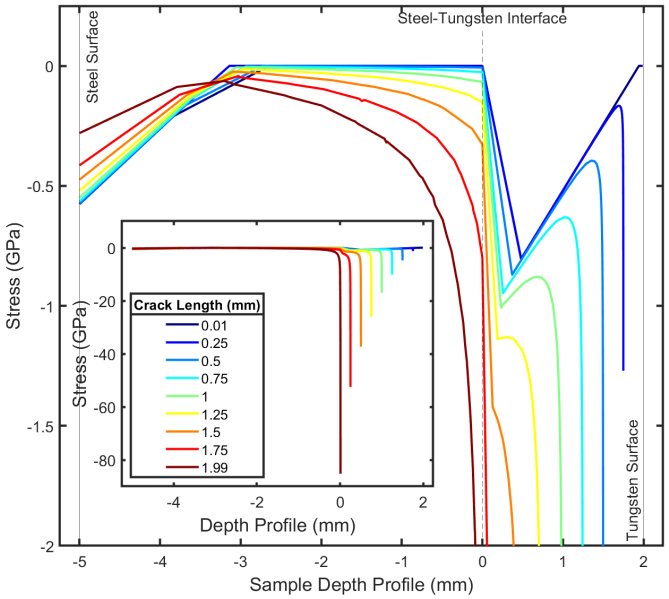


(b) Through-thickness first principal stress distributions in the centre of the bimetallic strip.

Figure 4.16: Through-thickness stress distributions calculated along the dashed line 'E' in Figure 4.14 up to the crack tip for various surface crack lengths.

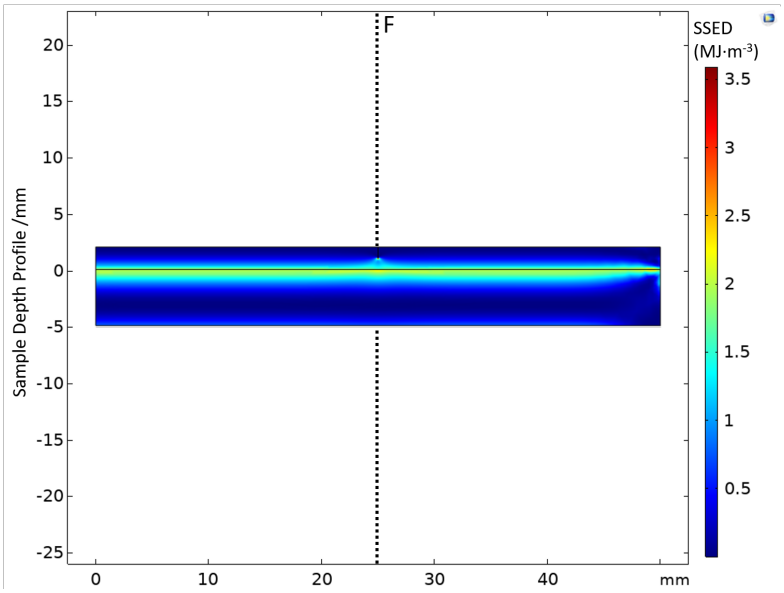


(c) Through-thickness second principal stress distributions in the centre of the bimetallic strip.

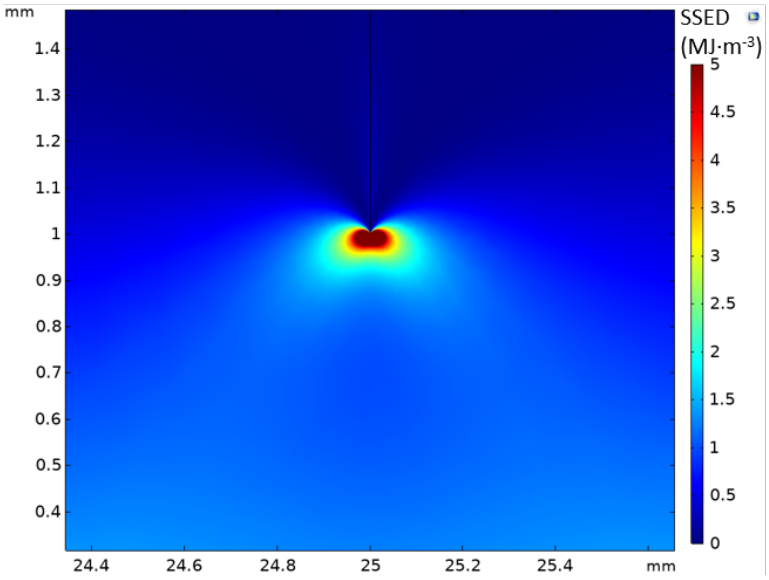


(d) Through-thickness third principal stress distributions in the centre of the bimetallic strip.

Figure 4.16: Through-thickness stress distributions calculated along the dashed line 'E' in Figure 4.14 up to the crack tip for various surface crack lengths.

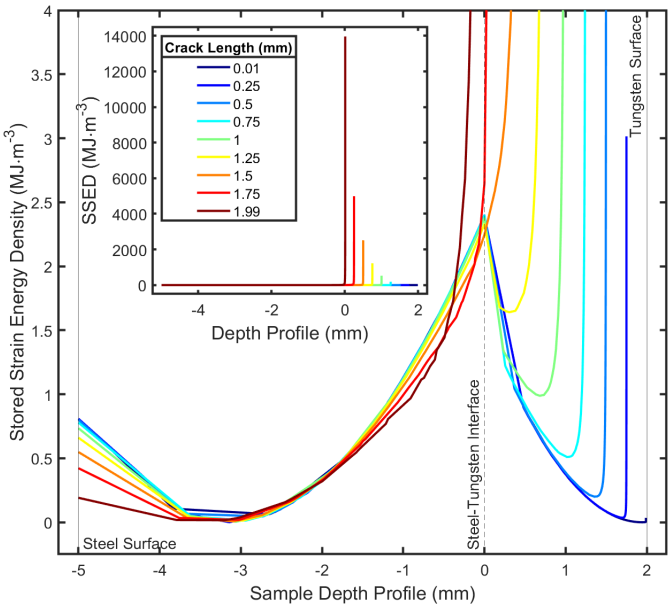


(a) SSED distribution calculated for a 2D FEM of a bimetallic strip with a 1 mm long surface crack following cooling from manufacture.

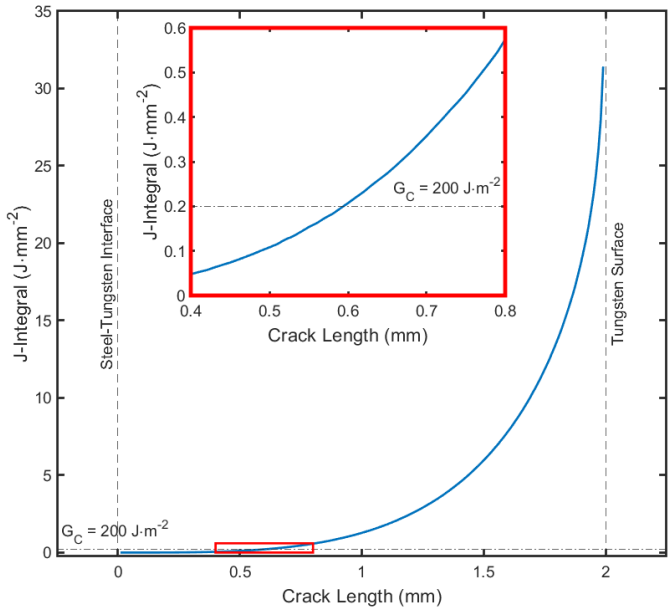


(b) SSED distribution calculated around crack tip.

Figure 4.17: SSED distributions calculated for a 2D FEM of a bimetallic strip cooled by 1000 °C.



(a) Through-thickness SSED distribution calculated along dashed line 'F' in Figure 4.17 (a) up to the crack tip for various surface crack lengths.



(b) J-integral as a function of crack length. Critical energy release rate (G_C) for W is marked by the dot-dashed line.

Figure 4.18: SSED distribution for various surface crack lengths and J-integral calculated for each crack length increment.

Interface cracking

A bimetallic strip with a crack initiated, this time at the W-steel interface halfway along the beam, was then modelled.

Figures 4.19–4.21 show the deviatoric strain distributions for a 1 mm long crack and how the deviatoric strains vary through the thickness of the bimetallic strip for user-selected crack lengths. Data within the crack (rather than in the extant material either side) was ignored. In a similar manner to the surface crack, as the length of the crack increased, the strain in the W coating increased and the strain at the steel surface decreased. The crack made the W coating more compliant which reduced the misfit strain. However, strain in the steel increased towards the interface due to the presence of the second crack tip there. Overall, the strain distributions followed the same trends as the previous two models (no crack and surface crack), but peak strains were larger than in the surface crack model. Figure 4.20 demonstrates that higher deviatoric strains were present throughout the sample. The differences between this interfacial crack model and the previous surface crack model can be observed by comparison with Figure 4.12, with a strain field ahead of the crack tip in the W coating for the interfacial crack case. However, the strain fields were less clear and elongated towards the interface in the surface crack model. This was because of the overall strain distribution in the bimetallic strip, seen in the non-cracked model (Figure 4.8), where strain in the the W coating increased in magnitude towards the interface.

Stress distributions are shown in Figures 4.22–4.23 and exhibited similar trends to the strain distributions, with maximum compressive stresses in the interfacial model (Figure 4.24) considerably larger than in Figure 4.16 (d) for the surface crack model. Overall stress in the steel substrate was reduced and stress in the W coating increased as the interfacial crack length increased. The inset images in Figure 4.24 show that the maximum stresses (found at the crack tip) tended to increase sharply up to a crack length of ∼0.75 mm, after which the stress approached a plateau until ∼1.5 mm. At crack lengths greater than 1.5 mm, the maximum stresses increased dramatically. This trend was also seen in the strain distributions around the crack tip (Figure 4.23), which were more pronounced than those seen in the surface crack model (Figure 4.15). This was attributed to the overall stress distributions in the bimetallic strip and the direction of the crack, as with the strain distributions. Tensile stress in Figure 4.24 (b) increased towards the free surface of the W coating, in a similar manner to the non-cracked model, shown in Figure 4.9 (b). The longer the crack was, the closer to the surface this stress gradient occurred — gradients increased, approximately stabilised and increased again in a similar range as the maximum stresses noted above.

Figure 4.25 shows the stored elastic strain energy density distribution. Figure 4.26 (a) shows that the through-thickness SSED distribution followed a similar overall shape to that observed in both the no crack model and surface crack model. There was a steep peak in the steel as the non-propagating crack tip was at the interface and induced increasingly large strain gradients as the crack length increased. The trend observed in peak stress and strain distributions was repeated for the peaks associated with the crack tip propagating towards the W surface. This shape was

repeated in Figure 4.26 (b) which shows the calculated J-integral as a function of crack length. The slight stabilisation in the 0.7–1.7 mm crack length region was thought to occur because the crack was propagating into less-strained material, as seen in the SSED distribution plot (and was the same shape as discussed above for strains and stresses). Additionally, as long as the surface of the coating remained uncracked, the 'bridge' of residual material held the W coating together as an integral continuum of material even as the crack continued to propagate, which resulted in less strain energy being released than otherwise would have been the case. The J-integral exceeded this G_C at a crack length of 0.04 mm, beyond which the crack would propagate. This occurred much sooner than in the surface crack (0.6 mm), and indicated that large cracks were more likely to originate from the interface, rather than the surface.

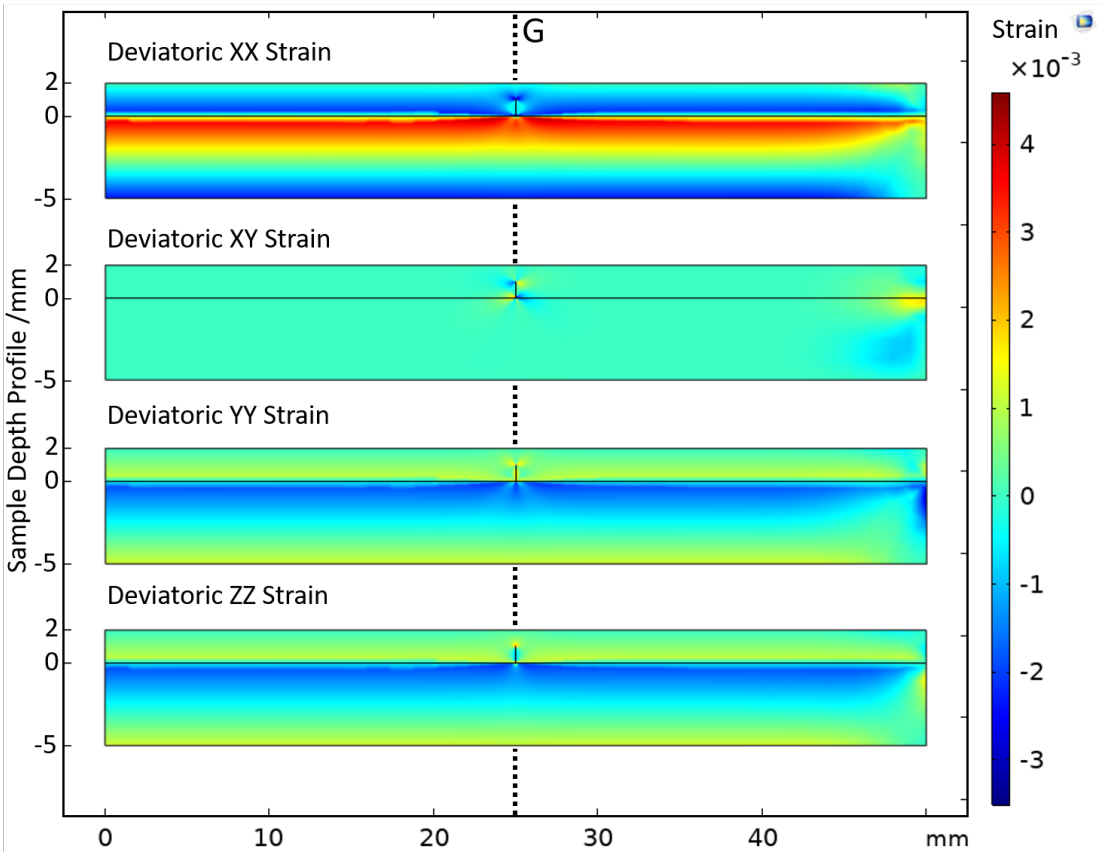
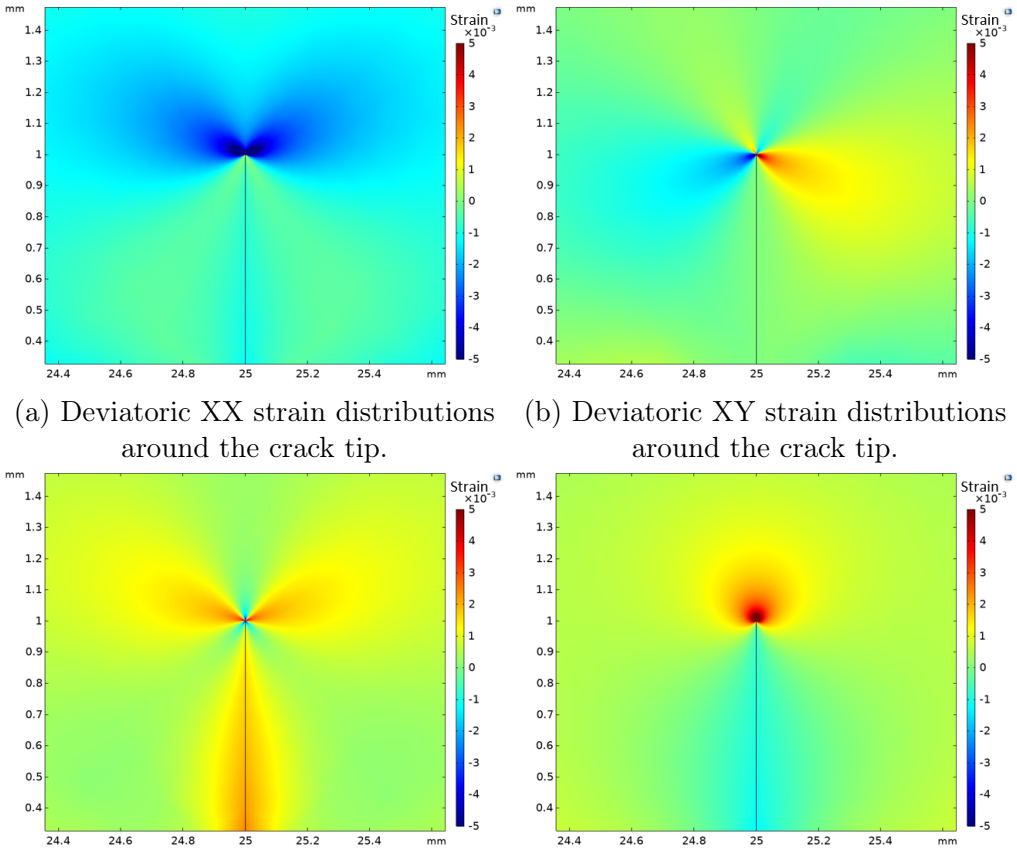


Figure 4.19: The four deviatoric strain distributions calculated for a 2D FEM of a bimetallic strip with a 1 mm long interface crack following cooling from manufacture.



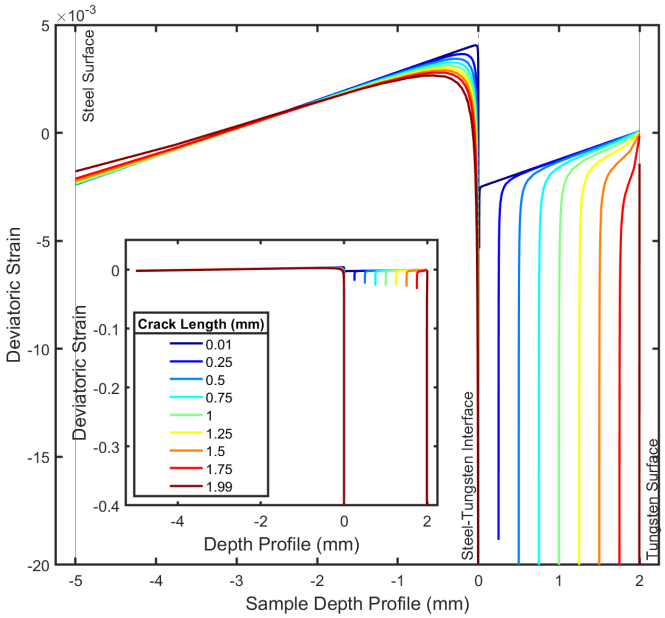
(a) Deviatoric XX strain distributions around the crack tip.

(b) Deviatoric XY strain distributions around the crack tip.

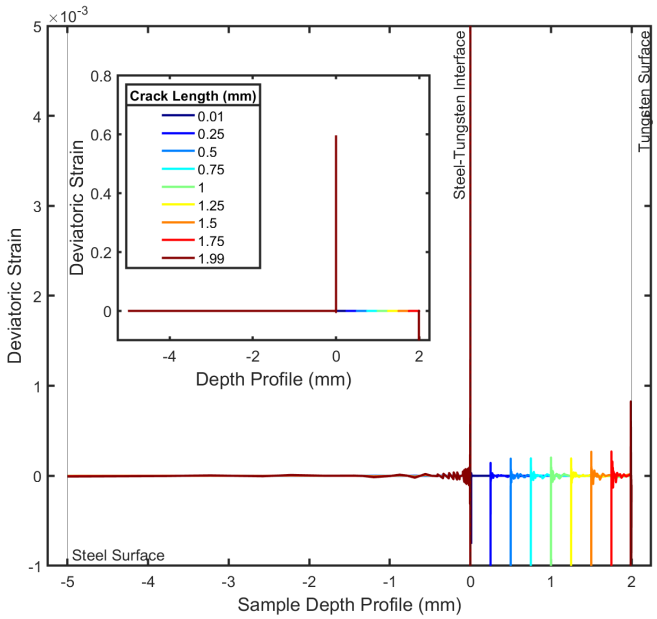
(c) Deviatoric YY strain distributions around the crack tip.

(d) Deviatoric ZZ strain distributions around the crack tip.

Figure 4.20: Deviatoric strain distributions around the crack tip propagating towards the surface of the W coating calculated for a 2D FEM of a bimetallic strip cooled by 1000 °C.

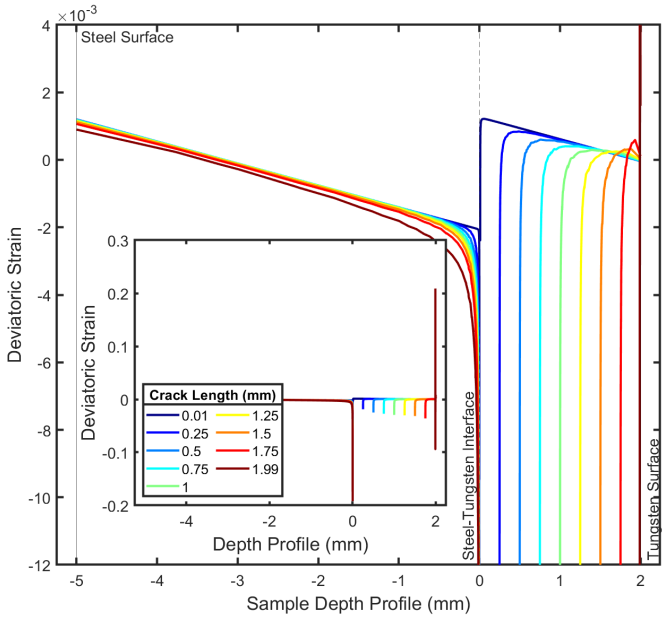


(a) Through-thickness deviatoric XX strain distributions in the centre of the bimetallic strip.

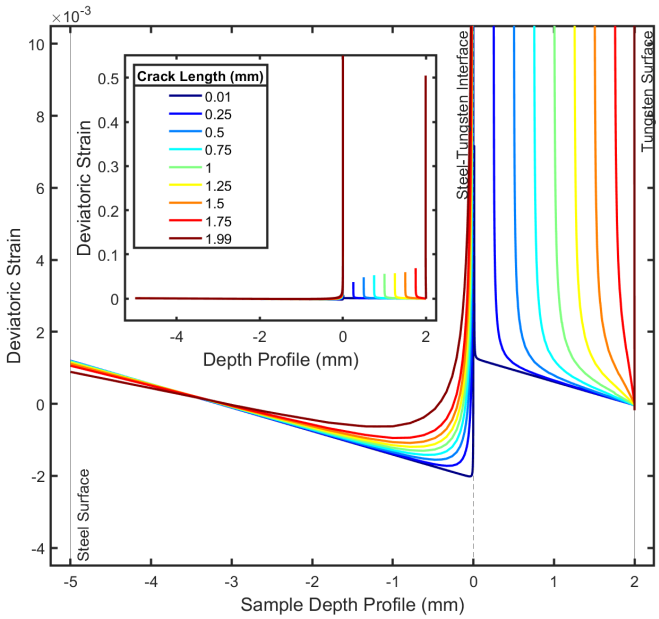


(b) Through-thickness deviatoric XY strain distributions in the centre of the bimetallic strip.

Figure 4.21: Through-thickness deviatoric strain distributions for various interfacial crack lengths. Analysis was performed along line 'G' in Figure 4.19.



(c) Through-thickness deviatoric YY strain distributions in the centre of the bimetallic strip.



(d) Through-thickness deviatoric ZZ strain distributions in the centre of the bimetallic strip.

Figure 4.21: Through-thickness deviatoric strain distributions for various interfacial crack lengths. Analysis was performed along line 'G' in Figure 4.19.

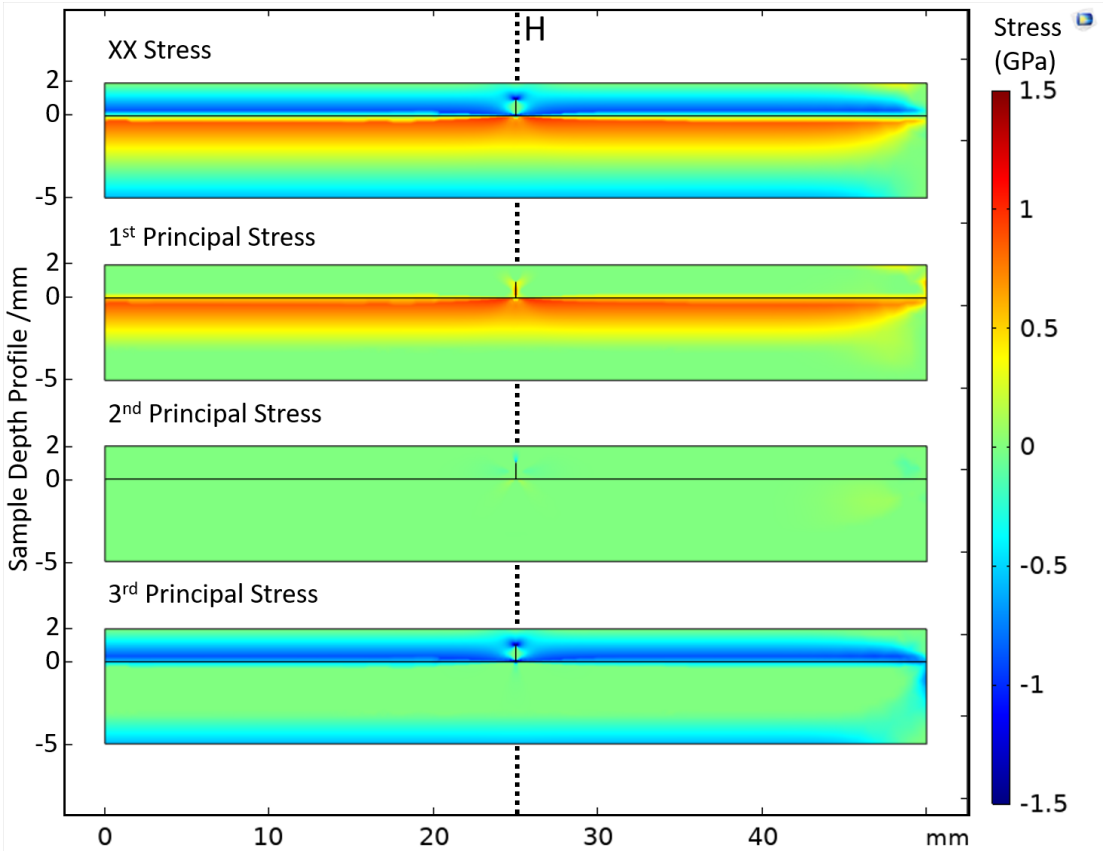
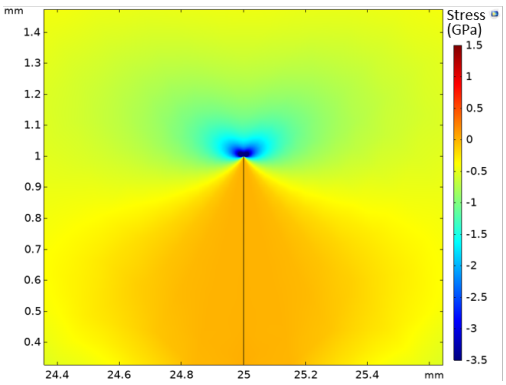
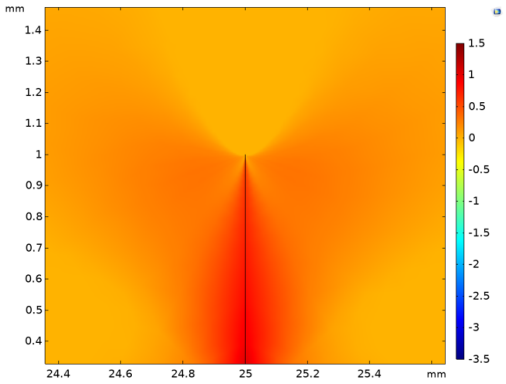


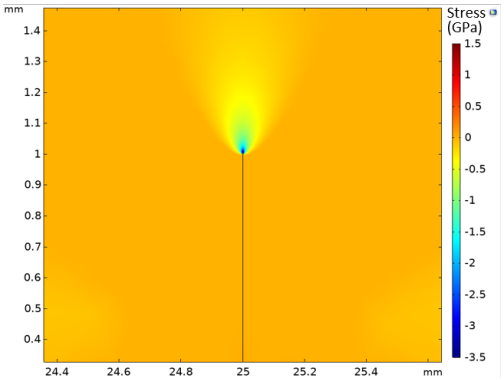
Figure 4.22: XX and the three principal stress distributions calculated for a 2D FEM of a bimetallic strip with a 1 mm long interface crack following cooling from manufacture.



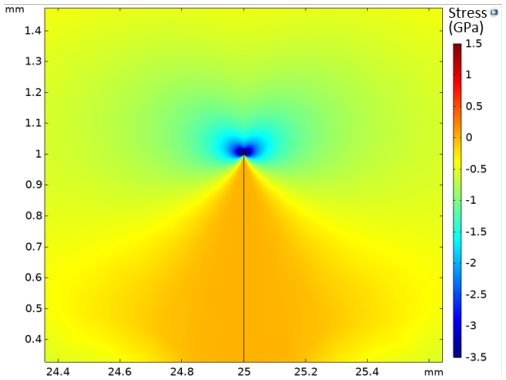
(a) XX stress distributions around the crack tip.



(b) First principal stress distributions around the crack tip.

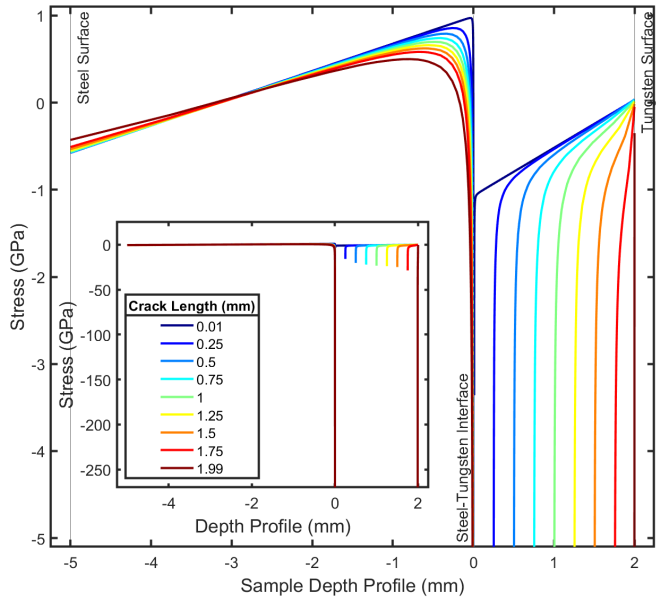


(c) Second principal stress distributions around the crack tip.

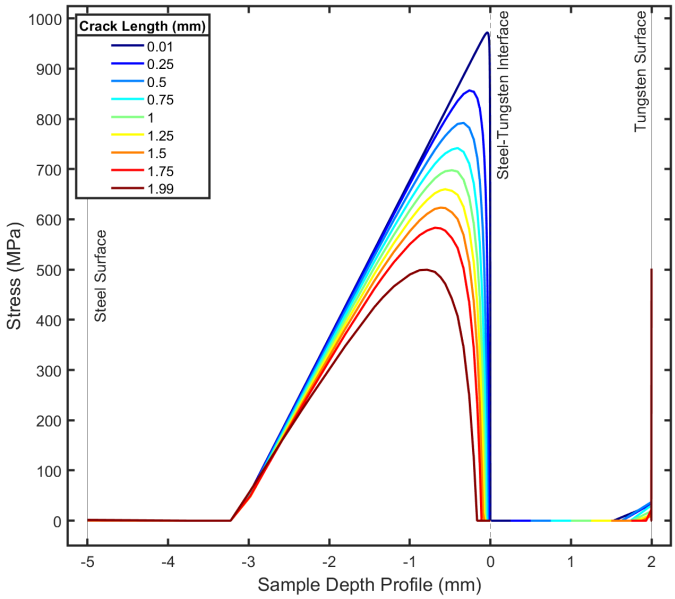


(d) Third principal stress distributions around the crack tip.

Figure 4.23: XX and principal stress distributions around the crack tip propagating towards the surface of the W coating calculated for a 2D FEM of a bimetallic strip cooled by 1000 °C.

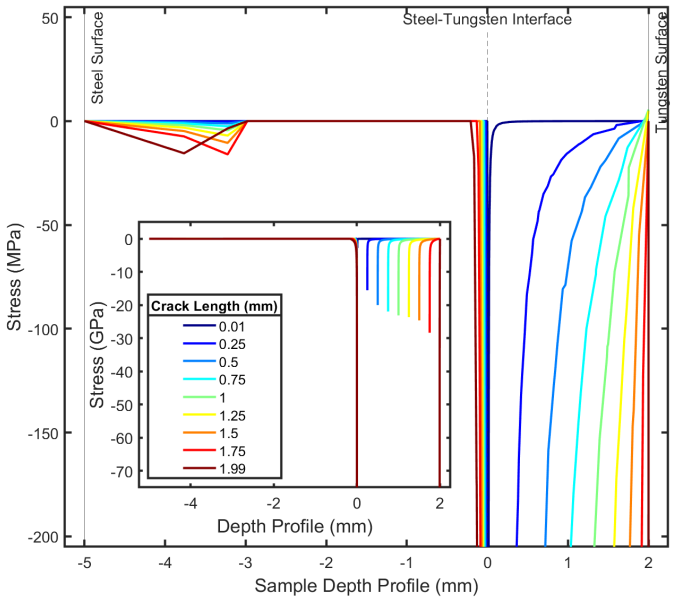


(a) Through-thickness XX stress distributions in the centre of the bimetallic strip.

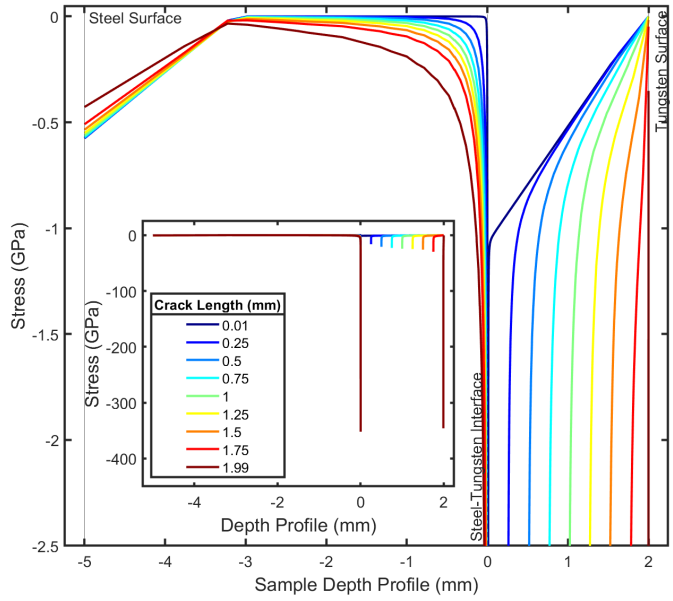


(b) Through-thickness first principal stress distributions in the centre of the bimetallic strip.

Figure 4.24: Through-thickness stress distributions for various interfacial crack lengths. Analysis was performed along the dashed line 'H' in Figure 4.22.

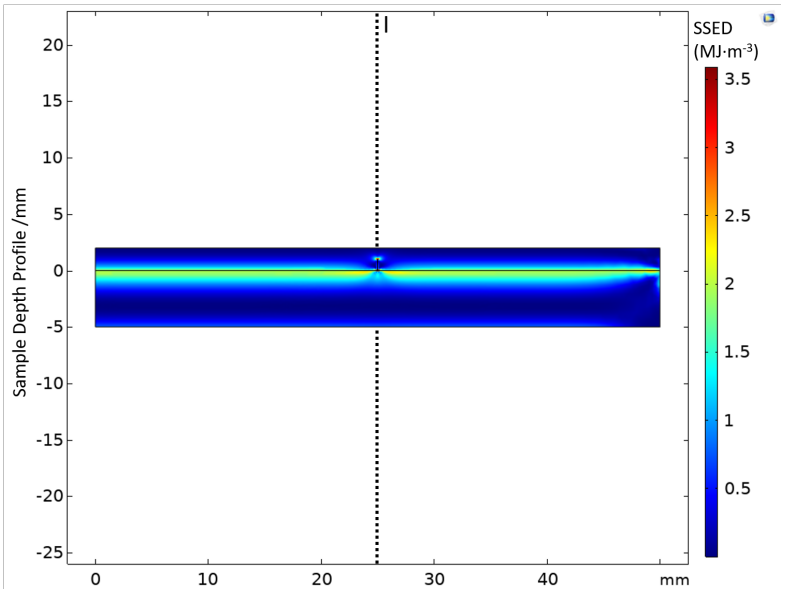


(c) Through-thickness second principal stress distributions in the centre of the bimetallic strip.

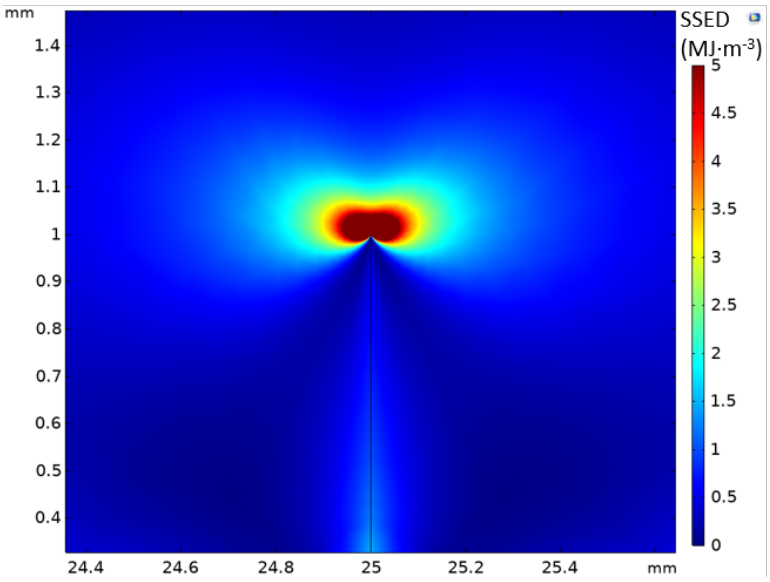


(d) Through-thickness third principal stress distributions in the centre of the bimetallic strip.

Figure 4.24: Through-thickness stress distributions for various interfacial crack lengths. Analysis was performed along the dashed line 'H' in Figure 4.22.

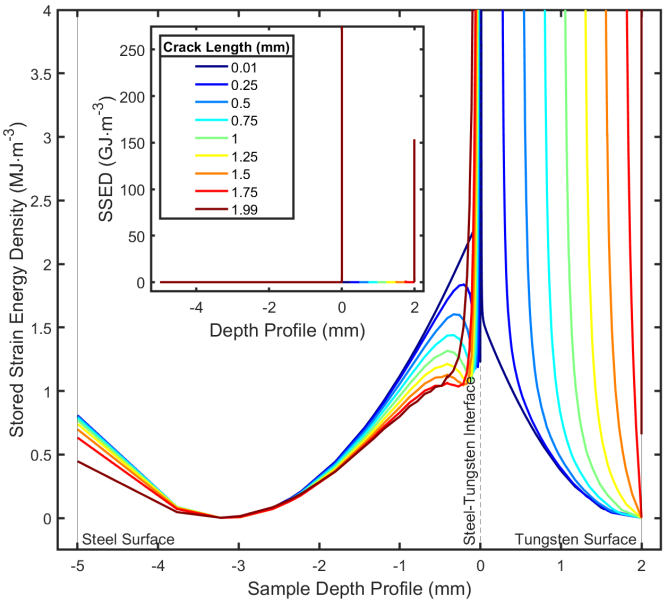


(a) SSED distribution calculated for a 2D FEM of a bimetallic strip with a 1 mm long interface crack following cooling from manufacture.

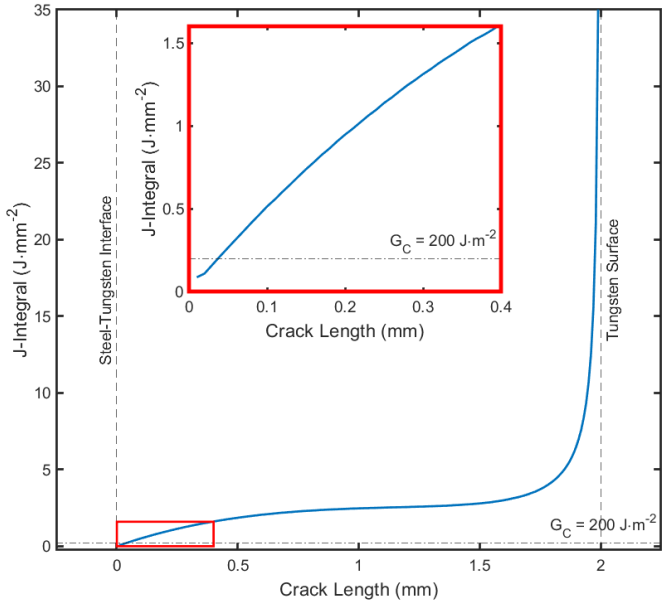


(b) SSED distribution calculated around crack tip propagating towards the surface of the W coating.

Figure 4.25: SSED distributions calculated for a 2D FEM of a bimetallic strip cooled by 1000 °C.



(a) Through-thickness SSED distribution for various crack lengths along dashed line 'I' in Figure 4.25 (a).



(b) J-integral as a function of crack length. Critical energy release rate (G_C) for W is marked by the dot-dashed line.

Figure 4.26: SSED distribution for various interfacial crack lengths and J-integral calculated for each crack length increment.

Hatched substrates with vertical cracks

Following the analyses of flat substrates above, models for hatched substrates were produced using the same conditions to investigate whether the addition of substrate texturing (to introduce stress concentrators) affected crack growth behaviour. Figures 4.27–4.28 show comparative plots of the J-integral for three different models/crack locations (flat, hatched with crack 'in the groove', and hatched with 'out of the groove') for cracks originating from the surface (Fig. 4.27), and cracks originating from the interface (Fig. 4.28). Inset images of the XX stress distribution around the crack tip are colour-coded for each data set in the graph. The G_C for cracking has also been included again as a dot-dashed line. The maximum XX strains, stresses and the SSED calculated along the crack lines in an equivalent non-cracked, hatched model are shown in Table 4.3 (flat model values previously stated have been included for comparison). All maximum values were at the interface between the W coating and steel substrate. It is unlikely that these values of stress would be observed in practice, as the model does not take into account the mechanical system of the FAST (applied pressure, surrounding graphite dies) or the dynamic cooling. Moreover, the critical flaw length of 40 μm for interface cracks, seen in the J-integral plots shown in Figures 4.18 (b) & 4.26 (b), would mean that sufficiently large cracks would propagate vertically through the coating and therefore quickly reduce the system stresses. This critical flaw size is similar to the size of the powder agglomerations meaning it is plausible that such flaws would exist.

Model	XX Strain		XX Stress (GPa)		SSED ($MJ \cdot m^{-3}$)	
	W	Steel	W	Steel	W	Steel
Flat	-0.014	0.032	-0.68	0.74	1.41	
Hatched ('in the groove')	-0.028	0.037	-1.27	0.97	2.15	
Hatched ('out of the groove')	-0.016	0.049	-0.83	1.12	0.91	4.44

Table 4.3: The maximum values of strain, stress and SSED for the W coating and steel for flat and hatched (two user-selected locations) substrate models.

Figure 4.27 shows that for both hatched models with various surface crack lengths the J-integral increased more gradually than the flat substrate model. G_C was only exceeded at 0.68 mm and 0.69 mm for the 'out of the groove' and 'in the groove' crack locations respectively. This was because there was fractionally more W in the coating as the hatch pattern 'cut' into the steel, removing part of the substrate. This resulted in a higher tensile stress at the surface of the W and a larger compressive stress in the W at the interface. At a crack length of $\sim$1.5 mm, the 'out of the groove' crack followed similar J-integral behaviour to the flat interface model because the interfacial strain and stress fields interacted with the the crack tip strain and stress distributions. At a crack length of 2 mm, the J-integral for the 'in the groove' crack was significantly lower than for the 'out of the groove' crack — the gap between the two cracks at an equivalent J-integral value was $\sim$0.16 mm. This was a similar order of magnitude to the depth of the hatching as seen in Figure 3.3 (a).

Figure 4.28 shows the J-integral for the 'out of the groove' hatched model followed the trend of the flat substrate model very closely when the crack propagated from the interface. Compared with the other two models, the crack 'in the groove' again showed a displacement in crack length for the same value of J-integral attributed to the crack starting in the hatch. This was highlighted at the point of intersection with the critical energy release rate; G_C was exceeded at 0.04 mm for the 'out of the groove' hatched model and at 0.14 mm for the 'in the groove' hatched model.

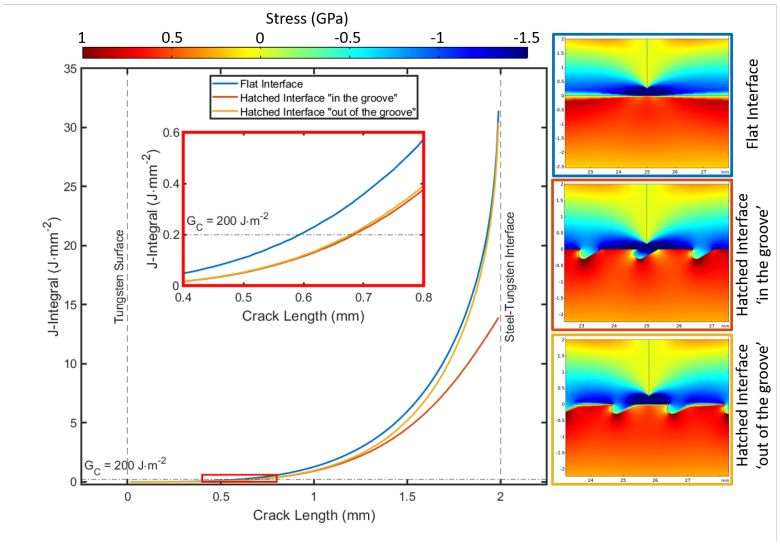


Figure 4.27: J-integral as a function of surface crack length. The critical energy release rate (G_C) for W is marked by the dot-dashed line. Inset images show XX stress distributions (colour scale shown above) and inset boxes are colour-coded for each data set.

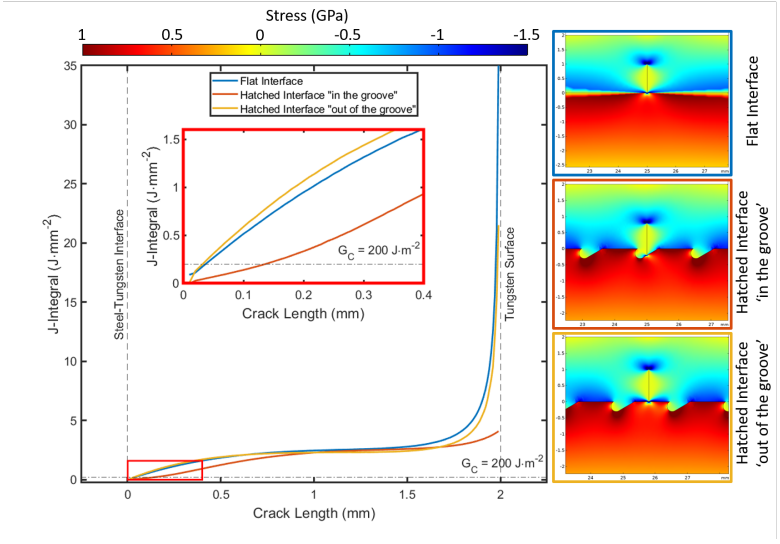
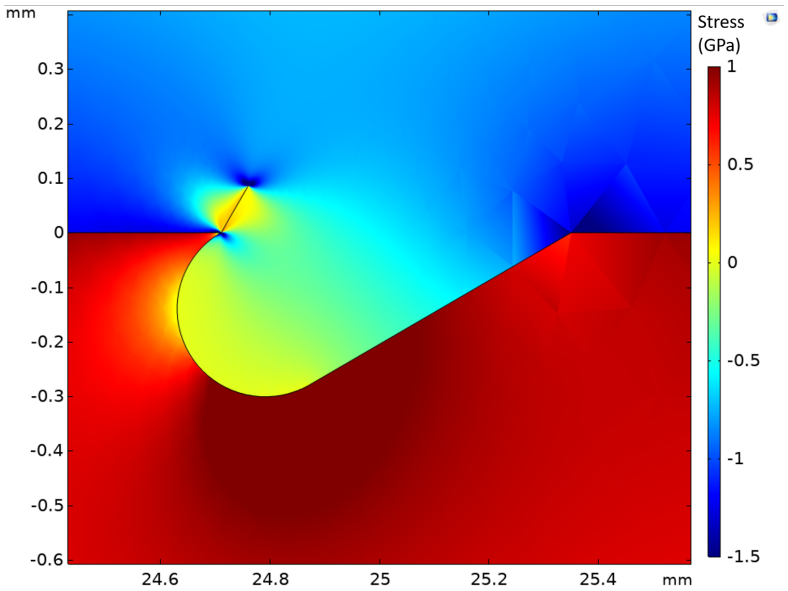


Figure 4.28: J-integral as a function of interfacial crack length. The critical energy release rate (G_C) for W is marked by the dot-dashed line. Inset images show XX stress distributions (colour scale shown above) and inset boxes are colour-coded for each data set.

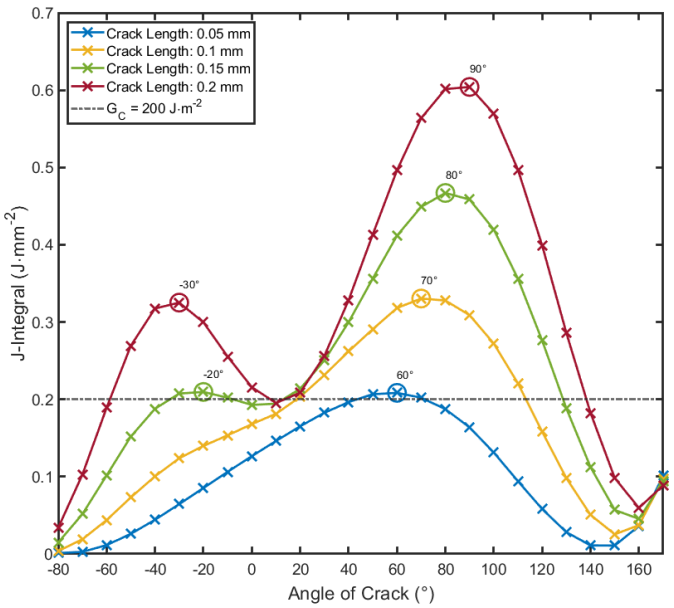
Hatched substrates with cracks initiated at stress concentrators

Figure 4.29 shows the XX stress distribution for an interface crack modelled at the overhanging part of the substrate hatching (a) and J-integrals at different crack lengths as a function of the angle of the crack (b). The critical energy release rate, G_C, is indicated by the dot-dashed line. For a crack 0.05 mm long, the only angles at which the J-integral exceeded this limit (meaning the crack would continue to propagate) were 50–70 °. As the crack length increased, more angles became viable for crack propagation to occur. It was observed that two J-integral peaks formed as the crack length increased. These occurred at optimum angles of -30 and 90 ° because these represented the most direct path to the boundary of the W coating (to the other side of the crack for -30 °, or towards the free surface of the W coating for 90 °). The most direct path means that the maximum stored strain energy was released for the smallest increase in crack area.

Figure 4.30 shows the XX stress distribution for an interface crack located at the sloped part of the substrate hatching (a) and J-integrals at different crack lengths as a function of the angle of the crack (b). Again, the critical energy release rate, G_C, is indicated by the dot-dashed line. For a crack 0.05 mm long, the J-integrals for a much wider range of angles (30–130 °) exceeded this limit. This wider range means that far more angles would be viable for crack propagation to occur from this location, in comparison to the overhang location. There was only one optimum angle at this location, as a crack would be unable to form a direct path to a flat boundary on the other half of the hatching.

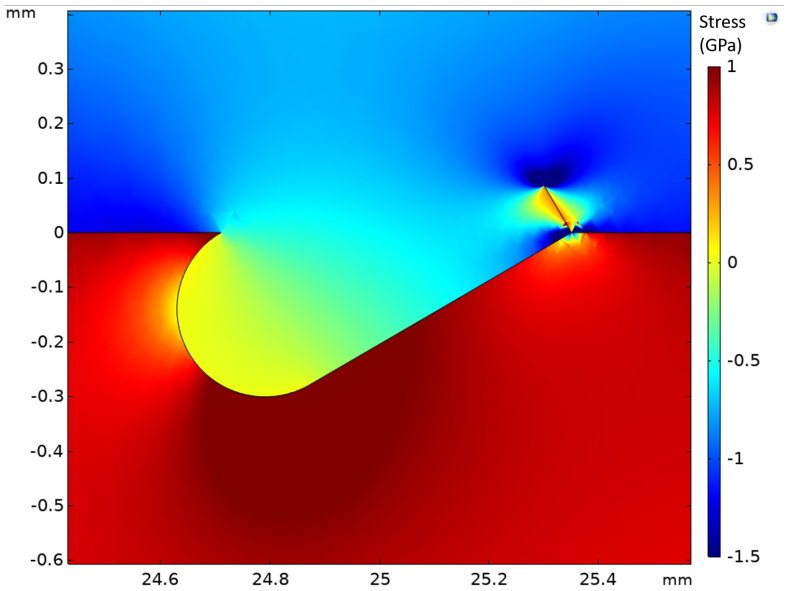


(a) XX stress distribution for a 0.1 mm crack originating at the overhanging portion of the interfacial substrate hatching.

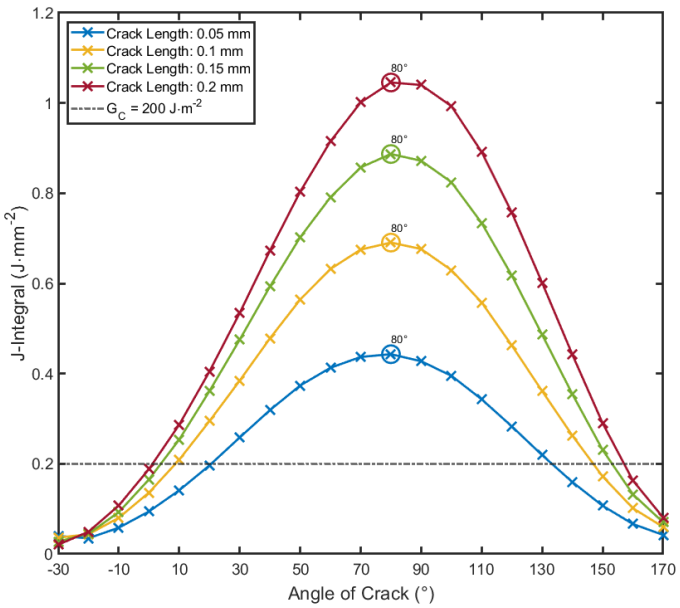


(b) J-integral as a function of crack angle for various crack lengths. Critical energy release rate (G_C) for W is marked by the dot-dashed line.

Figure 4.29: XX stress distribution and J-integral calculations for different crack lengths for each crack angle increment.



(a) XX stress distribution for a 0.1 mm crack originating at the sloped portion of the interfacial substrate hatching.



(b) J-integral as a function of crack angle for various crack lengths. Critical energy release rate (G_C) for W is marked by the dot-dashed line.

Figure 4.30: XX stress distribution and J-integral calculations for different crack lengths for each crack angle increment.

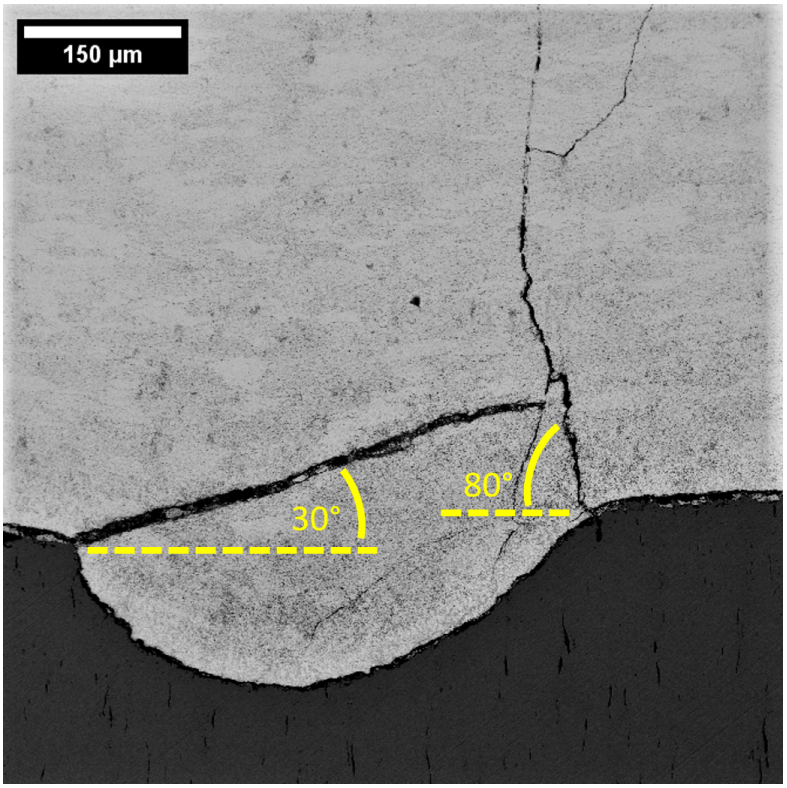
4.3.3 Comparison of experiments with modelled predictions

Experiments were performed on FAST samples of W coatings on hatched steel substrates and were compared to the model insights and predictions. Representative micrographs of the interface between the W coating and the steel substrate are shown in Figure 4.31, demonstrating cracking that had occurred at the interface.

Figure 4.31 (a) denotes two cracks originating from both the overhang and sloped sections of the hatched groove; the overhang crack angle was approximately 30 ° and the slope angle was approximately 80 °. The sample was fabricated in previous work [74] but not cycled, and was subjected to thermal ageing at 800 °C for one week before analysis.

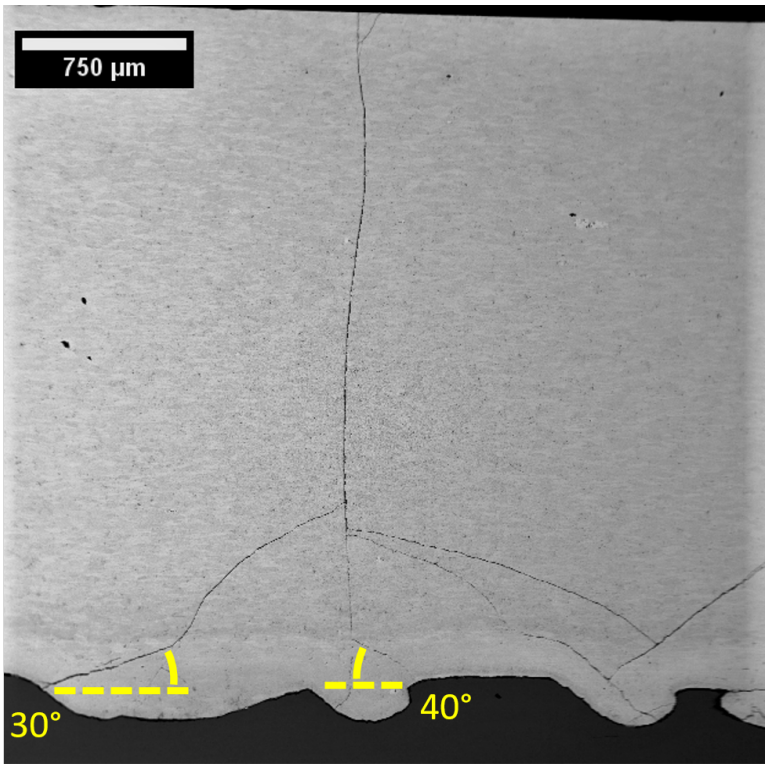
Figure 4.31 (b) is a micrograph from a hatched steel substrate with a 2 mm W coating (H2mm) that was thermally cycled in the HIVE facility (outlined in Chapter 5). The overhang crack angle (in the centre of the image) was approximately 40 ° and the slope crack angle (to the left of the image) was approximately 30 °.

In both samples, the substrate surface was not as uniform as assumed in the model, due in part to the cross-sectional cut angle and the other perpendicular array of hatching. Whilst the J-integral values corresponding to overhang crack angles did not exceed G_C for the smallest assumed crack length, they were within 20 ° and did exceed the threshold for a crack length of 0.1 mm. Due to the porosity observed in the FAST samples (Table 3.10), cracks of this length could have existed following manufacture. The corresponding J-integral values for the sloped crack angles were greater than G_C and there was a wide range of measured crack angles (as predicted in the model). These results provide confidence to the credibility of the model.



(a) Micrograph of aged (1 week at 800 °C) W coating on steel [74] showing cracking occurring at the hatched substrate interface.

Figure 4.31: SEM images of experimental W coatings on hatched steel substrates showing cracking behaviour similar to that predicted by the FE model.



(b) Micrograph of H2mm sample from Chapter 5 showing cracks at various angles at the sample interface joining into a vertical crack that reaches the surface of the W coating.

Figure 4.31: SEM images of experimental W coatings on hatched steel substrates showing cracking behaviour similar to that predicted by the FE model.

4.4 Summary

FE models were developed using COMSOL Multiphysics® software and validated with analytical solutions to predict strains, stresses and stored elastic strain energy in W-steel bimetallic strips and discs in 2D, 3D and axisymmetric modelling set-ups. A two-stage mesh refinement process was applied to ensure that steep function gradients, such as stress and strain, were accurately captured at the sharp geometries found at the tip of cracks and at the textured coating-substrate interface (as used in experiments to improve adhesion).

These models were then used to investigate the tendencies of crack propagation from the W coating surface and the W-steel interface for both flat and textured substrates at user-selected crack locations. Deviatoric strains, principal stresses, stored strain energy densities and J-integrals were calculated for each increase in crack length; analysis indicated that cracking was most likely to propagate vertically from the coating-substrate interface, as the critical energy release rate (G_C) was exceeded at crack lengths around 50 µm (in comparison with ∼650 µm for surface cracks).

Further modelling of short cracks originating at sharp geometries of the 'hatched' substrates revealed that cracking was more likely to begin at an angle before propagating vertically, due to localised stresses caused by the substrate texturing. Cracking behaviour analysed in representative micrographs of W coatings on textured substrate geometries showed that predicted crack angles aligned within 20 ° for the smallest crack length modelled for simulation of crack initiation. This is a reasonable level of error as perfect behaviour of the samples is not expected given the level of porosity measured in FAST samples shown in Table 3.10.

It is considered that extending the FEM to incorporate dynamic cooling with temperature-dependent materials properties and phase field fracture mechanics (where the model updates and selects the crack path using specified parameters) would further the understanding of crack behaviour and how this is affected by substrate texturing. This might facilitate development of substrate-texturing techniques, such as tailored vertical segmentation displacements or cheaper/faster texturing for equivalent adhesion, to achieve improved bonding of dissimilar materials with a large CTE mismatch.

5 Effects of Thermal Ageing and Cycling

5.1 Introduction

Using the W coatings manufactured using VPS and FAST in Chapter 3, the coatings were assessed for use in a fusion-like environment, by thermal ageing and thermal cycling. More complex transient thermal cycling is investigated in Chapter 6.

Thermal ageing is used to determine the resilience, longevity and quality of coatings. At fusion-relevant temperatures inter-diffusion between coating and substrate materials will occur [93, 94], and is assessed by quantitative microscopy, usually based on image 'thresholding' that employs image segmentation to generate high-contrast images of different phases for analysis. For example, in another field, Lim et al. developed a simple method where a cell-covered area was partitioned into three sub-areas using objectively-set threshold pixel intensities [148].

A similar approach can be taken for samples where micrographs show contrast between phases. Ireti et al. compared two types of structural steel and utilised image segmentation to calculate various characteristics, such as grain size and area percentage of each phase [149]. Figure 5.1 shows each step of the image segmentation process.

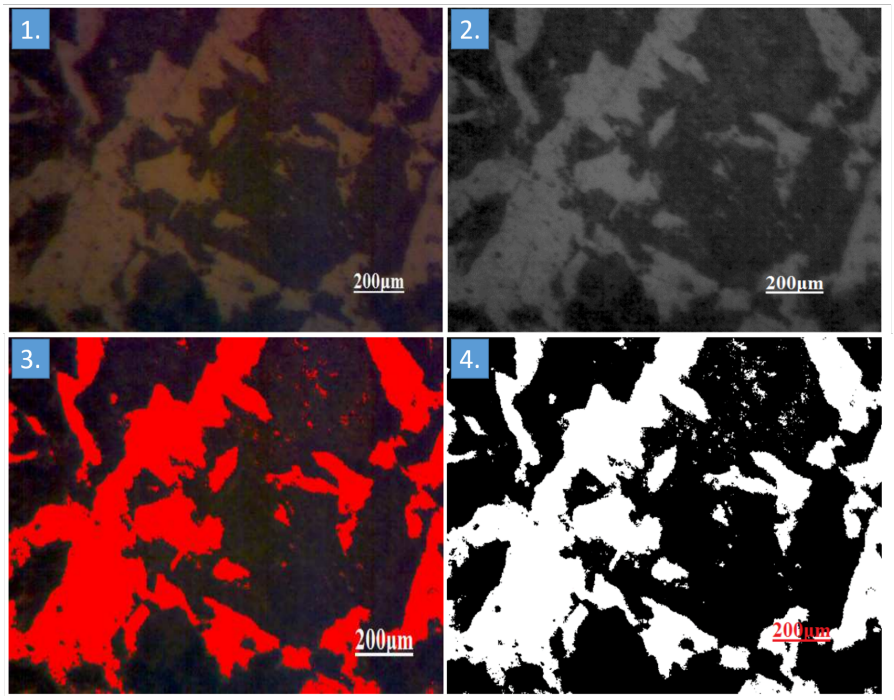


Figure 5.1: Summary of segmentation process used by Ireti et al. to analyse steel micrographs [149]. Four stages were used: 1. original micrograph, 2. conversion to greyscale, 3. selection of pixel intensity threshold, and 4. final partitioned image.

[1]Reprinted from The American Journal of Engineering and Applied Sciences, Vol 11 Issue 1, Alo Francis Ireti et al., Comparision [sic] of Imagej Analysis of Structure of Two Constructional Steel, © copyright (2018), under CC by 3.0.

This process can be applied to observe and calculate phase transformation data. In Fe-W alloys back-scattered electron (BSE) images provide better contrast than secondary electron (SE) images [94]; this is due to the large difference in atomic number, meaning that W appears brighter.

The Fe-W phase diagram [150] shows limited Fe solubility in W, meaning that any interdiffusion is likely to result in formation of the three intermetallic phases: FeW, Fe_7W_6 and Fe_2W. Both Heuer et al. [94] and Qu et al. [151] observed formation of Fe_7W_6 between Fe and W particles in functionally-graded coatings. Qu et al. noted that intermetallic thickness increased with decreasing Fe particle size. Heuer et al. measured the volume increase of Fe_7W_6 under different ageing conditions but did not calculate a growth rate. Reisner et al. [93] observed Fe_2W intermetallic formation at the interface of a W-coated Fe substrate under a variety of annealing conditions and measured corresponding intermetallic thicknesses. Using these data, growth rate coefficients were determined for these intermetallic phases when aged at 1050 K (1×10^{-18} $m^2{\cdot}s^{-1}$) and 1100 K (2.8×10^{-18} $m^2{\cdot}s^{-1}$).

Only Basuki et al. [152] have investigated the thermal stability of the more fusion-relevant steel-W system. Surface chemistry analysis via Auger electron spectroscopy (AES) revealed an intermetallic composition of 37.6 at% Fe, 37.3 at% W, 19.2 at% C and 5.8 at% Cr, which was assumed to be an FeW phase with a large amount of metallic carbides. This assumption is invalid without proper phase analysis, such as X-ray diffraction (XRD) as performed in [93, 94, 151]. This is because any of the Fe-W intermetallics may have formed with a variety of metallic carbides, or even a more complex crystal structure that incorporated all four elements.

There has been little investigation into the effect that common manufacturing impurities, such as C or O, have on phase formation in the steel-W system. Further research is therefore necessary to further the understanding of the inter-diffusion between these two leading candidates for structural/shielding use in a fusion device and of any resulting intermediate phase growth.

Intermediate phase growth follows the parabolic relationship:

$$w = \sqrt{Kt} \tag{5.1}$$

where w is the width of the intermetallic phase, K is the growth rate coefficient and t is the time. This mechanism assumes that growth is controlled by bulk diffusion of the constituent parts to the reaction interface which is increasingly slowed by the intermetallic phase as it forms. Multiple intermetallic phases have been observed to form at the boundary between materials [153].

The growth rate coefficient can be described by an Arrhenius relationship:

$$K = K_0 \cdot e^{\frac{-E_A}{RT}} \tag{5.2}$$

where K_0 is the maximum growth rate coefficient, E_A is the activation energy for phase growth, R is the gas constant, and T is temperature.

The Heating by Induction to Verify Extremes (HIVE) facility (previously mentioned in Chapter 2) is a test facility used to simulate the steady-state thermal cycling loads experienced in a fusion reactor. It comprises a cooled induction coil to heat inductive samples inside a vacuum vessel which can provide water cooling to samples — a schematic of HIVE produced by Pearl et al. is shown in Figure 5.2 [96]. A variety of diagnostics can be utilised, the most prevalently used being the infra-red (IR) camera system to observe any localised heating effects on the surface. The exact heating power is not precisely defined due to the uncertainty of the inductive coupling efficiency between the coil and the sample [96].

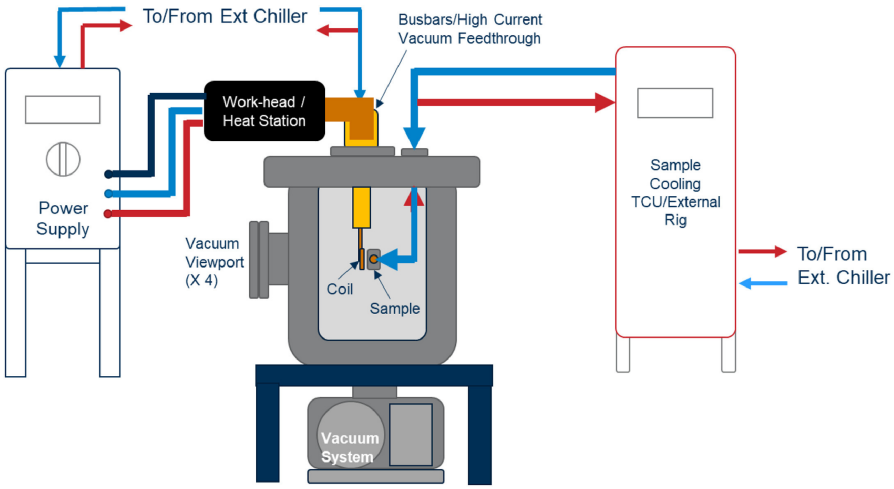


Figure 5.2: Schematic of HIVE produced by Pearl et al. [96][2].

The Upgraded Pilot-PSI (UPP) facility is a linear plasma device housed at the Dutch Institute For Fundamental Energy Research (DIFFER) and is used to investigate transient and steady-state operation on prototype fusion first wall (FW) materials. The plasma is generated by a DC cascaded arc and is magnetised by three sets of Cu coils up to 1.6 T. A variety of plasma elements available: Ar, H_2,

[2]Reprinted from Fusion Engineering and Design, Vol 194, Jonathan Pearl et al., Cyclic medium heat flux testing of a WTa lattice structure on the HIVE facility, 113699, © copyright (2023), under CC by 4.0.

D_2 and He, and heat fluxes of up to 4 $MW \cdot m^{-2}$ can be maintained for extended periods. Electron temperatures and densities in the plasma are in the range of 0.1–2 eV and 10^{19}– 10^{20} m^3 respectively [154]. Whilst these are less than the predicted values for ITER and DEMO divertor strike zones (1–5 eV and 10^{23}– 10^{25} m^3) [105], they are sufficient for initial investigation of plasma-material interactions and component survival.

5.2 Methodology

Three main studies were undertaken in this chapter to investigate the behaviour of samples under intense thermal loading:

1. Thermal ageing at different temperatures and exposure times to observe any diffusional effects that might occur during the lifetime of PFCs.

2. Thermal cycling using the Heating by Induction to Verify Extremes (HIVE) facility at the Culham Centre for Fusion Energy (CCFE), to test survival of FAST W coatings of varying thicknesses on a variety of substrates at fusion-relevant temperatures. Cui et al. conducted thermal cycling tests in the HIVE facility, providing a benchmark for this thesis, as W coatings were manufactured according to the FAST 'recipe' developed by Cui et al. [74].

3. Thermal cycling using the Upgraded Pilot-PSI (UPP) facility at the Dutch Institute for Fundamental Energy Research (DIFFER) to investigate the effect of plasma exposure on FAST W coating survival. Additionally, thermal cycling through plasma irradiation offers greater relevance to fusion conditions compared to testing in HIVE, making it a valuable further research step.

5.2.1 Sample Preparation

Samples studied in this chapter were made using the same VPS and FAST recipes described in Sections 3.2 & 4.2.3 respectively.

A VPS W coating removed from the substrate and a W pellet manufactured by FAST were sent to AMG Analytical Services for elemental analysis using LECO radio-frequency (RF) combustion and inert gas fusion systems to determine the quantity of O and C impurities present.

Cross-sections of samples were made using a Struers Accutom-100 cut-off machine and mounted in Phenolic Carbon Conductive Resin (Kemet).

All W coatings (prior to testing) and sample cross-sections (following testing) were mechanically polished with SiC grinding papers down to 1200 grit before further polishing with 6 and 3 µm diamond suspension on NLH (Kemet) and Floc (Struers) polishing pads. Samples were then cleaned with ethanol and isopropanol. Samples were prepared for testing in UPP with an additional polish with a 1 µm diamond suspension on a Nap (Struers) polishing pad before cleaning.

Micrographs were taken using a ZEISS Merlin SEM with energy dispersive X-ray (EDX) capabilities (Oxford Instruments XMax 150 mm^2 detector) and a ZEISS EVO with EDX capabilities (Oxford Instruments X-act) in both secondary electron (SE) and backscattered electron (BSE) modes.

5.2.2 Thermal Ageing

Heat treatments were carried out in a sealed quartz tube, evacuated to a pressure of $\sim 1 \times 10^{-6}$ mbar. FAST samples were aged at a variety of temperatures for different times, as shown in Table 5.1. Due to the small number of VPS samples available, only two ageings were performed (at 800 °C for 24 hrs and for 1 week) to provide a comparison between the two manufacturing techniques.

	1 Hour	24 Hours	1 Week
600 °C	-	FAST	-
800 °C	FAST	FAST + VPS	FAST + VPS
1000 °C	-	FAST	-

Table 5.1: Combinations of different temperatures and times used for thermal ageing of FAST and VPS samples.

Following ageing, samples were removed from the quartz tube and sectioned. Cross-sectional BSE micrographs were taken across the interface of the samples. The contrast of the grayscale BSE micrograph images was increased in image processing software Fiji [155] until the steel substrate was no longer visible (i.e. completely black pixels), shown in Figures 5.6 (b) & (e). Linescans of pixel intensity were taken across the image (every 5 pixels) from the substrate into the coating. Linescan data was trimmed so that all data began at the first non-black pixel (i.e. at the interface). In an attempt to reduce the noise in the grayscale linescans the pixel intensity was binned (averaged) every 0.5 µm along each linescan. All linescans for each sample were then averaged and then normalised by the point of highest average intensity, to produce a scale of area fraction of W, using the assumption that the brightest pixel will be W, and that completely black pixels are steel (due to the altered contrast).

A key limitation of this method is that black pixels may not necessarily indicate the presence of steel; sample cracks and porosity, oxides and phenolic mounting resin could all contribute to the contrast. This meant that the data sets were noisy and required smoothing in order to fit to Equation 5.1. Smoothing was achieved using a Gaussian-weighted moving average with a carefully selected smoothing

'window'. High smoothing windows are desired to remove as much noise from data as possible, but it is important that 'over-smoothing' does not occur to such an extent that it is no longer representative of the data. Therefore various smoothing windows were trialled and compared with how well they fitted with the original data. Window width started at 15 (i.e. each resulting smoothed point was the average of the surrounding 15 original data points) and decreased in steps of 5 until the R^2 value of the smoothed fit exceeded 0.9 for the first two thirds of the data (as the data tended to get a lot noisier due to cracking in the last third).

The width of the new intermetallic phase was initially determined by examination and measurement of the micrographs. These initial values were then compared to the average area fraction plots, which gave a threshold of approximately 0.89. In an attempt to remove confirmation bias between samples, the final intermetallic width was determined by the location of the first point that exceed 0.89 area fraction of W. The confidence measurement (for data smoothing) boundary and area fraction threshold are both marked along with the first data point marking the width of the intermetallic layer in Figures 5.8–5.9.

Squared intermetallic layer widths were then plotted against ageing time for the different manufacturing processes and ageing temperatures. The gradients of these plots (the growth rate coefficient, K, from Equation 5.1) were calculated and used to produce a plot of the natural logarithm of K against reciprocal heat treatment temperature. From this plot, activation energy for phase growth and a maximum growth rate coefficient were calculated for FAST samples using Equation 5.2.

EDX linescans and maps were then taken in the ZEISS EVO to highlight how W, Fe, Cr, O and C were distributed. A Rigaku MiniFlex Benchtop X-Ray Diffraction Instrument was used to take XRD measurements between 2θ = 30–50 ° on as-manufactured and heat-treated (1 week at 800 °C) FAST and VPS samples. Comparison of peaks in the XRD data with literature values was used to identify apparent phases including oxides and carbides presumed to have formed during manufacture and ageing.

5.2.3 Thermal Cycling: HIVE

Four types of FAST samples were tested at the HIVE facility:

- 2 mm thick W coating on a flat steel substrate (F2mm)
- 2 mm thick W coating on a hatched steel substrate (H2mm)
- 4 mm thick W coating on a hatched steel substrate (H4mm)
- 2 mm thick W coating on a flat W substrate (W2mm)

Flat W substrates, supplied by Goodfellow (99.95% purity), and steel (F91 as used in Section 3.2.1) were cut to size (20 mm diameter and 5 mm thick) using a waterjet before being grit-blasted with 80/120 Guyson Saftigrain blast media with a working distance in the range of 100–200 mm. Hatched steel (also F91) substrates were produced using electro-discharge machining (EDM) according to the engineering drawing shown in Figure 3.3 (b).

HIVE uses a vacuum vessel in which samples are mounted and aligned with a pipe that induced heating at the sample's surface. The induction system is controlled by the HIVE operator who monitors temperature read-outs for the various installed diagnostic instruments.

The thermal measurement systems used were: three (one for W substrate samples) K-type thermocouples, arc-percussion-welded in a 3 mm deep hole in the rear of each substrate; a METIS M322-10319 (350–1500 °C) pyrometer by SensorTherm GmbH, aimed at an angle to the coating surface; and a FLIR SC7500 fixed thermal camera, positioned directly opposite the coating surface for infrared imaging. An Olympus digital camera was also mounted at an angle to the coating surface and recorded each heating pulse. The pyrometer and digital camera were at an angle to the surface due to the location of the view-ports. In-situ diagnostic locations are shown in Figure 5.3.

Samples were individually mounted in a machined MACOR® glass-ceramic mount (no active cooling) with the W coating facing a cooled coiled copper pipe that provided induction heating, as shown in Figure 5.3. After mounting, samples were left in the evacuated HIVE chamber overnight to allow for any sample degassing. Samples subjected to incremental, thermal heating pulses up to 800 °C and allowed to cool down to 300 °C before being thermally cycled between these temperatures 50 times. Optical photographs of the sample surfaces were taken before and after testing.

Following testing, SEM images of each sample surface were taken and three samples (H2mm, H4mm and W2mm) were cross-sectioned, prepared and imaged in the SEM.

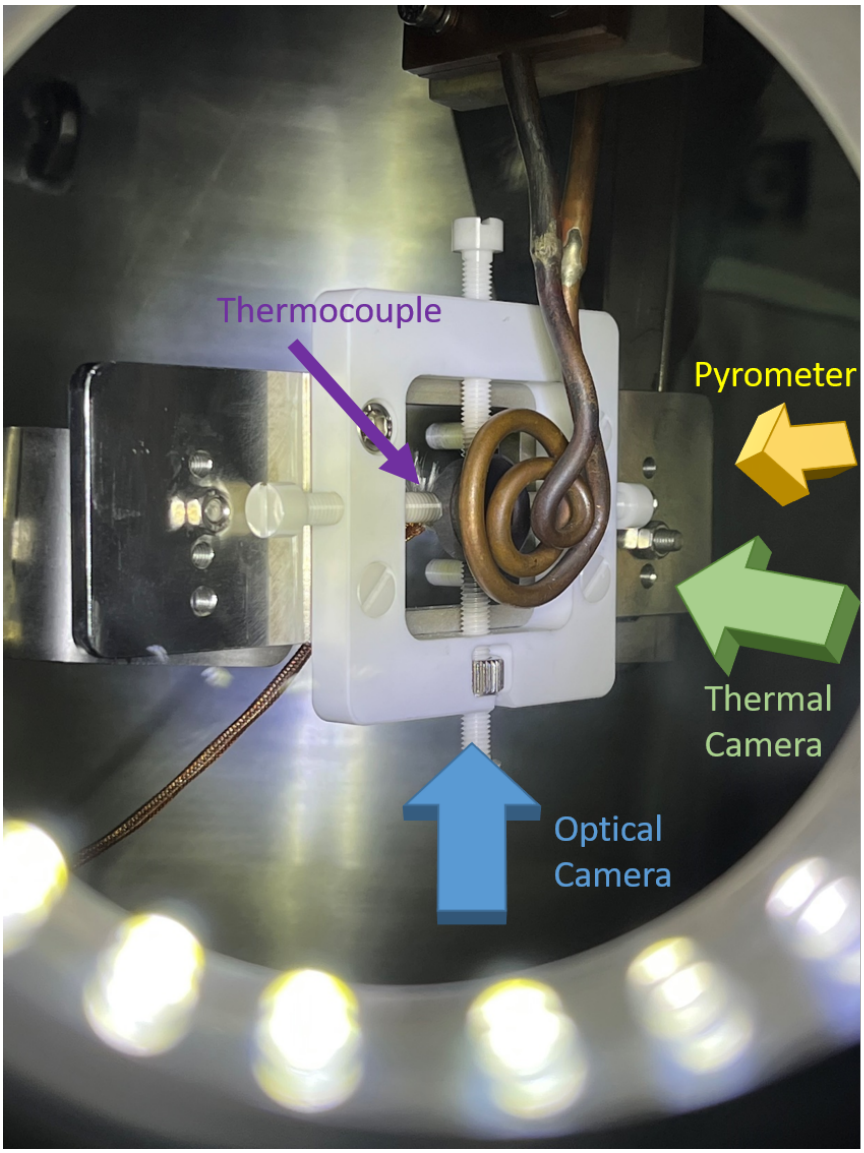


Figure 5.3: Photograph taken through a view-port of the HIVE vacuum vessel of a mounted sample after testing. The coloured arrows and matching text show where various in-situ diagnostic instruments were located behind similar view-ports.

5.2.4 Thermal Cycling: UPP

One of each FAST sample type (F2mm, H2mm, H4mm and W2mm) was also tested in UPP. Each sample had a 1 mm diameter hole drilled through the side of the coating using EDM in order to locate a thermocouple near the centre of the top surface of the coating (Figure 5.4).

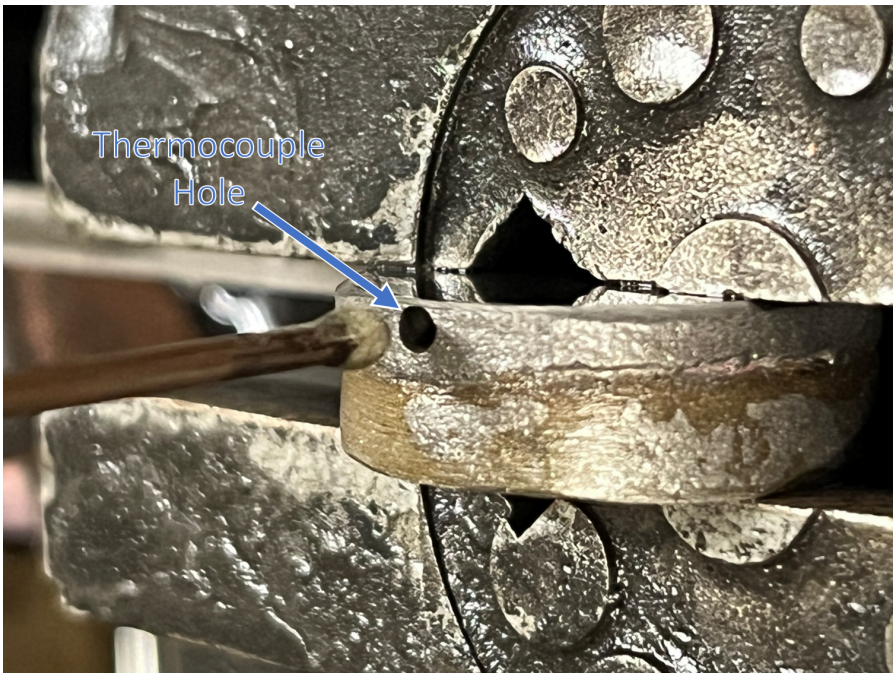


Figure 5.4: Photograph taken during drilling of the thermocouple hole in the side of a coating near the surface.

Figure 5.5 (a) shows a schematic of the UPP set up. Samples were clamped between a water-cooled Cu sample holder and a Titanium-Zirconium-Molybdenum (TZM) alloy clamping ring (which acted a thermal shield to the outside edge of the sample) with GRAFOIL® thermal contact layers between each. Samples were heated when exposed to a magnetised plasma. Figure 5.5 (b) and (c) are photographs

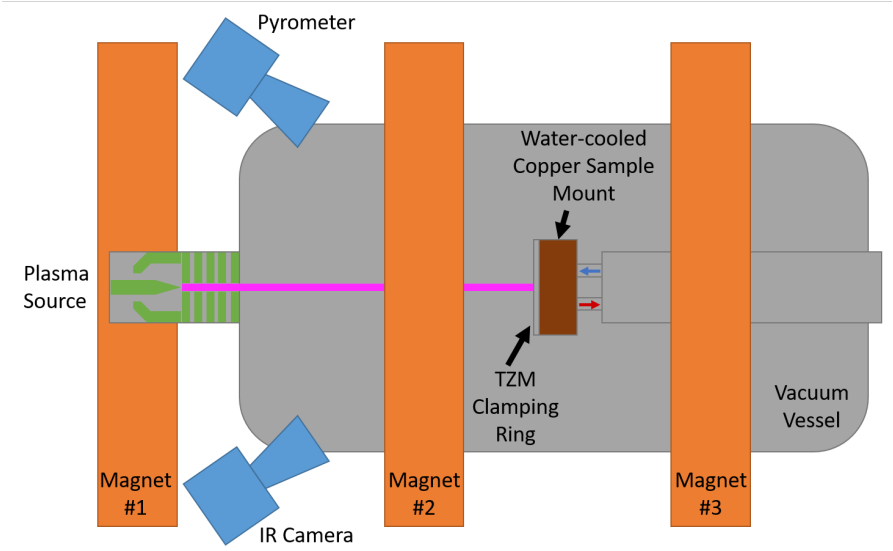
taken during installation of a sample for testing. Fixed in-situ optical and thermal (FLIR SC7500MB) cameras and a FarAssociates FMP1 SpectroPyrometer [156] were installed and used during testing. A K-type thermocouple was placed in the hole drilled in the coating.

UPP was unable to match the temperature range used in HIVE, as 500 °C was the minimum measurement temperature of the pyrometer and 600 °C was the maximum temperature the thermocouple could withstand before melting. Therefore, samples were thermally cycled between approximately 150–550 °C by switching between a magnetised (heating phase) and unmagnetised (cooling phase) H^+ plasma and the data acquired by the pyrometer data was not used. The time taken to switch between the plasma modes led to an error of ∼15 °C (∼50 °C for fast-heating samples). The plasma exposure parameters are listed in Table 5.2.

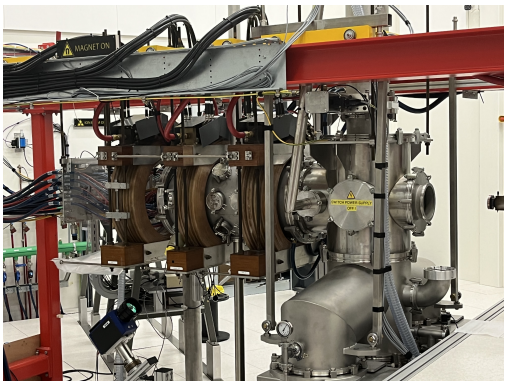
	Sample			
Plasma Parameter	F2mm	H2mm	H4mm	W2mm
H^+ Flow Rate (SLM)	2.5			
Plasma Current (A)	112–126	145	160	180
Magnetic Field (T)	0.14–0.16			
Bias Voltage (V)	0	0	40	45
Bias Current (A)	0	0	24	30
Electron Temperature (eV)	1.79–2.28			
Electron Number Density (10^{20} m^{-3})	0.5–0.68			
Electron Number Density FWHM (mm)	10.7–12.0			

Table 5.2: Plasma parameters for thermally cycled experiments in UPP.

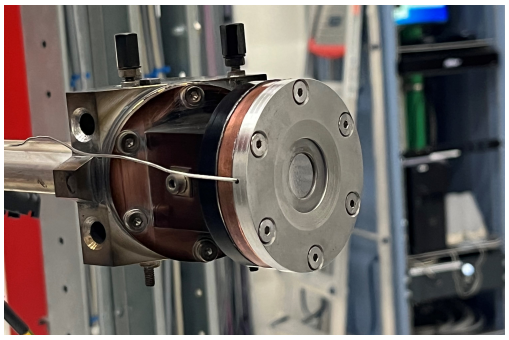
Following testing, SEM images of each sample surface were taken. The H2mm, H4mm and W2mm samples were then cross-sectioned, prepared and imaged in the SEM.



(a) Schematic of UPP set up.



(b) Photograph of UPP during sample changeover. The sample holder can be seen on the right edge of the photograph, just before insertion into the main chamber.



(c) Photograph of a sample mounted in the UPP holder during sample changeover. The thermocouple wire reached the centre of the sample through the side of the holder.

Figure 5.5: Schematic and photographs of the UPP set up.

5.3 Results and Discussion

Table 5.3 shows FAST W contained significant O and C impurities. C was likely to have diffused from the graphite die during manufacture and the surface of the W powder particles may have oxidised prior to sintering (either through glovebox contamination or during transfer from the glovebox to the FAST).

Process	Carbon Content	Oxygen Content
FAST	0.76 wt% / 8.8 at%	2.00 wt% /17.4 at%
VPS	144 ppm / 0.22 at%	0.155 wt% / 1.75 at%

Table 5.3: Carbon and oxygen analysis performed by AMG Analytical Services.

5.3.1 Thermal Ageing

SEM diffusional analysis

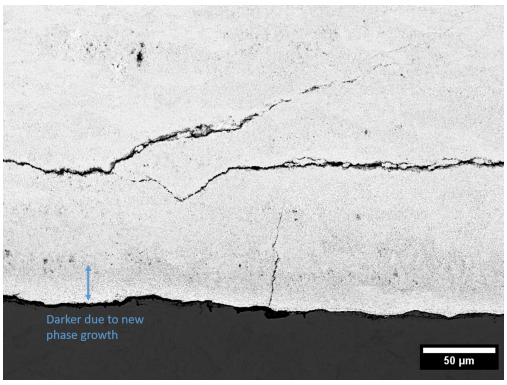
After sectioning, coatings became more fragile, attributed to: the clamping force applied during sectioning, the applied stress/damage incurred during cutting and mechanical polishing of the samples, and potential surface reconfigurations and energy release upon formation of the new surface. During removal from the sealed quartz tube used for heat treatment some FAST samples broke.

Figure 5.6 shows the evolution of a new phase in FAST coatings that grew with increased heat treatment times at 800 °C (a–d), and for 600 °C and 1000 °C for 1 day (e–f). Figures 5.6 (c, d & f) clearly show that the new phase formed via vapour transport along pre-existing cracks from manufacture. It is likely that similar transport also occurred in the voids between powder particles where any residual porosity remained. Figure 5.6 (f) shows a region of depleted grain bound-

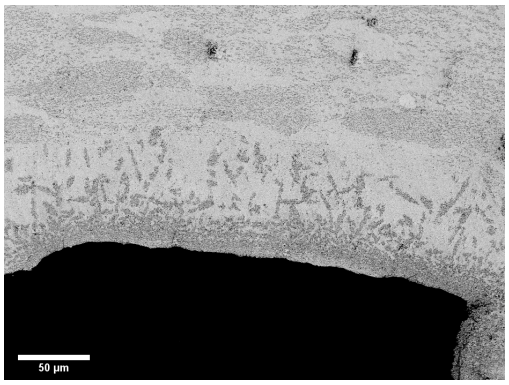
aries in the steel of a comparative width to the intermetallic layer that formed in the W coating. Larger elements present in the steel, such as Fe and Cr, may have diffused substitutionally as well as smaller, more common interstitially-diffusive elements, such as C and O, preferentially from grain boundaries.

Figure 5.7 shows how increasing heat treatment time for VPS coatings affected the growth of a new phase. A comparison of Figures 5.6 (a) and 5.7 (a) shows that no obvious new (grey) phase formed in the sprayed sample during manufacture. This was likely due to the significant temperature difference between the molten droplets and the substrate, inducing very fast cooling rates $>10^3$ K·s^{-1}.

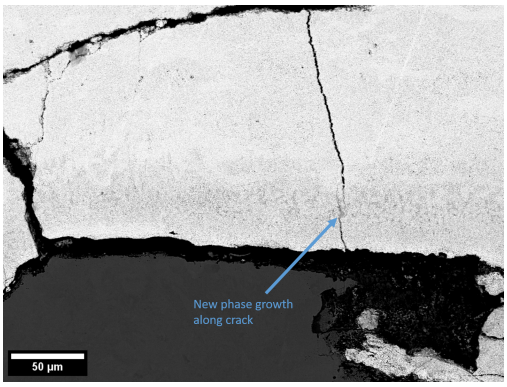
During FAST processing, the high, pulsed-DC current and transient high temperatures >1000 °C may have provided a driving force for diffusion of elements from the steel into the W coating. This would explain why regions such as grain boundaries (less well bonded, and higher in vacancy concentration) were preferentially depleted as seen in Figure 5.6 (f). Figures 5.7 (b & c) show that an intermetallic phase formed between the splats of W powder particles, as vapour transport may have encouraged formation of secondary phases in the gaps.



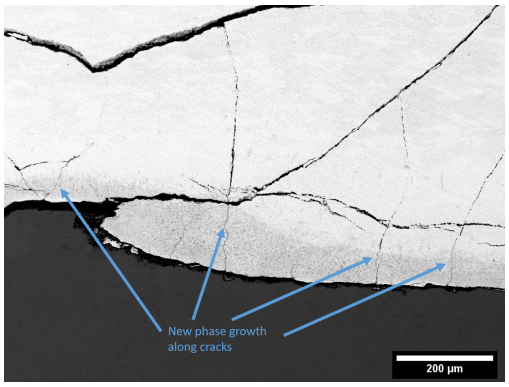
(a) Sample as-manufactured.



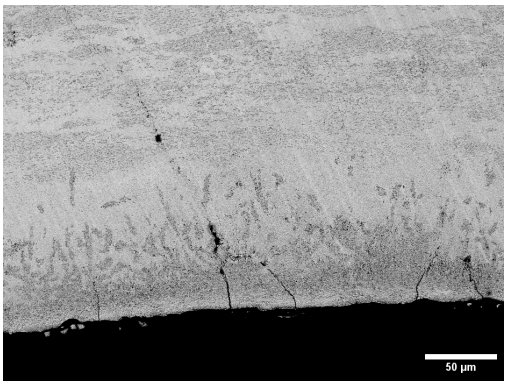
(b) Sample heat treated for 1 hour at 800 °C.



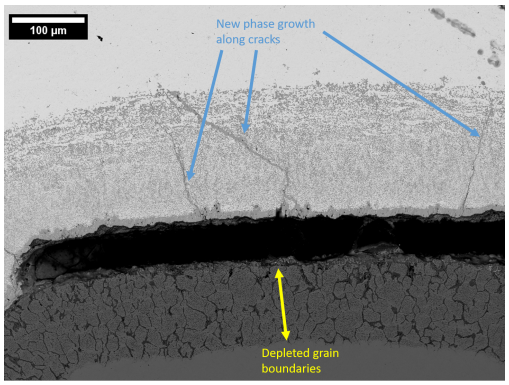
(c) Sample heat treated for 1 day at 800 °C.



(d) Sample heat treated for 1 week at 800 °C.

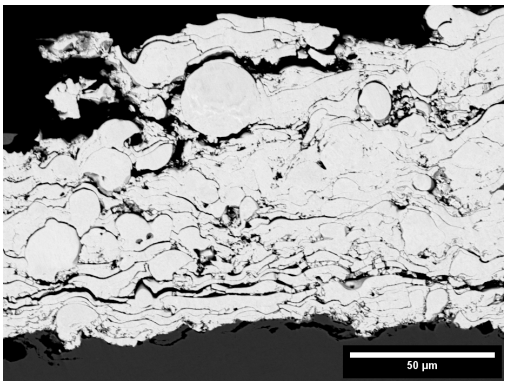


(e) Sample heat treated for 1 day at 600 °C.

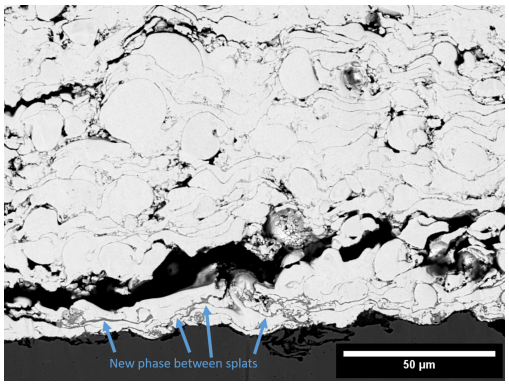


(f) Sample heat treated for 1 day at 1000 °C.

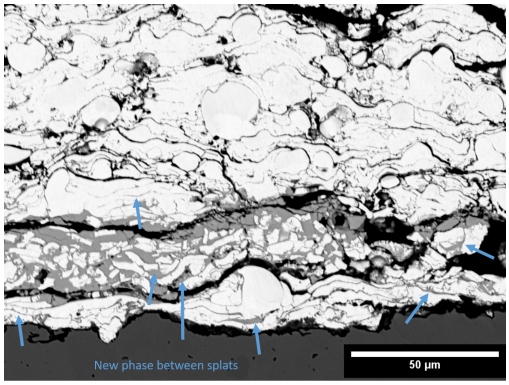
Figure 5.6: BSE SEM images of FAST samples aged for different times and temperatures. W coatings were at the top of each image, and steel substrates were at the bottom.



(a) As-manufactured VPS sample.



(b) VPS sample heat treated for 1 day at 800 °C.

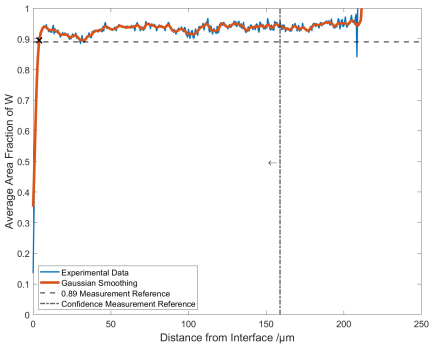


(c) VPS sample heat treated for 1 week at 800 °C.

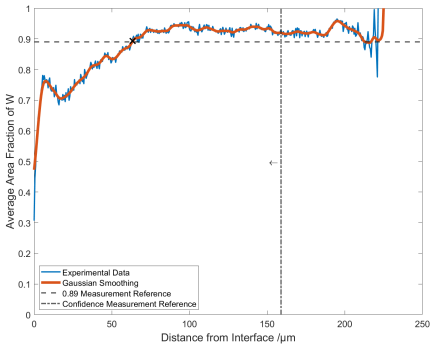
Figure 5.7: BSE SEM images of VPS W samples aged for different times and temperatures. W coatings were at the top of each image, and steel substrates were at the bottom.

Figures 5.8–5.9 show the results of the image processing and phase growth analysis for FAST and VPS samples, respectively. It was apparent that the width of the new phase increased with time and temperature as expected from Equation 5.1. The phase boundary was particularly clear in Figures 5.8 (d & f). Lower magnification was required to observe the full intermetallic layer after ageing for 1 week, shown in Figure 5.8 (e), meaning that the resolution was lower than other samples. Additionally, cracking was more widespread in this sample which led to noisier data. A similar effect due to cracking (where the area fraction of W reduced sharply) was observed in the sprayed data in Figures 5.9 (a & c) at a distance of around 15 µm and 30 µm respectively.

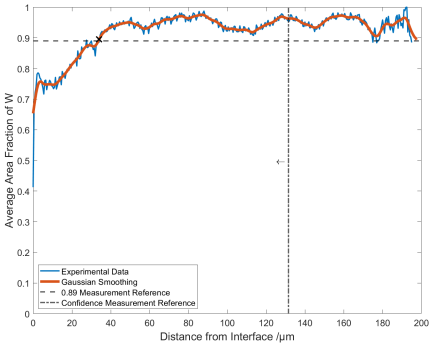
Figure 5.10 shows the results of the phase width analysis graphically. Due to the quadratic relationship in Equation 5.1, the squared value of new phase width is plotted in order to achieve a linear trendline for each data set, where the gradient is equal to the new phase growth rate coefficient, K. As only one ageing time was undertaken for the alternative ageing temperatures it means that there is an exact fit for 600 °C and 1000 °C, in comparison to the more loosely fitted
800 °C FAST data. The measured intermetallic phase width for the 1 week aged sample was lower than expected; potentially due to the lower resolution micrograph and noisier data. Without that data point, the gradient would have been higher than the 600 °C trendline and would have shown that K increased with temperature as expected. The VPS gradient is much lower, which implies that there is a reduced driving force for phase growth. This could potentially be because growth of the new phase via vapour transport in the wider cracks within VPS samples was slower than new phase growth in FAST samples through dif-



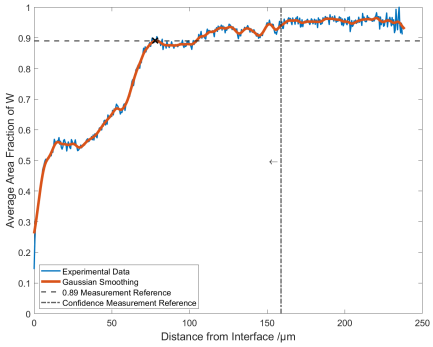
(a) Intermetallic phase growth profile of as-manufactured FAST sample.



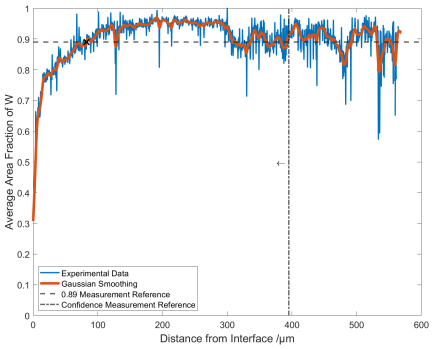
(b) Intermetallic phase growth profile of FAST sample heat treated for 1 day at 600 °C.



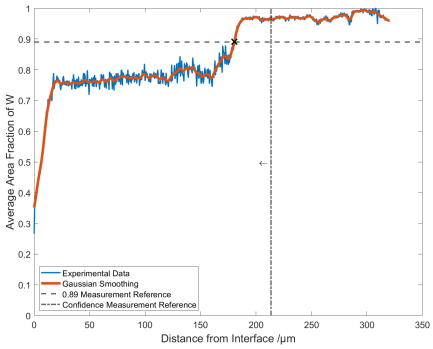
(c) Intermetallic phase growth profile of FAST sample heat treated for 1 hour at 800 °C.



(d) Intermetallic phase growth profile of FAST sample heat treated for 1 day at 800 °C.

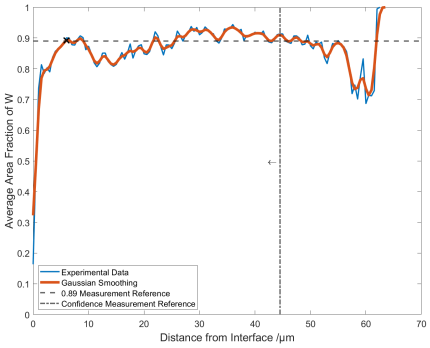


(e) Intermetallic phase growth profile of FAST sample heat treated for 1 week at 800 °C.

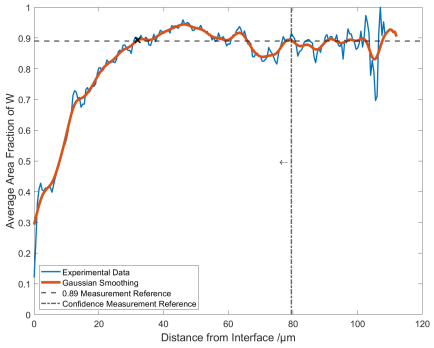


(f) Intermetallic phase growth profile of FAST sample heat treated for 1 day at 1000 °C.

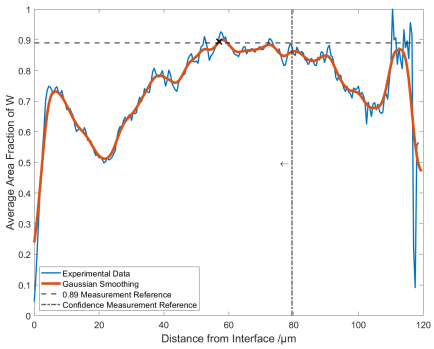
Figure 5.8: Intermetallic phase growth profiles for FAST W coatings using average pixel intensity normalised using the maximum value of average intensity.



(a) Intermetallic phase growth profile of as-manufactured VPS sample.



(b) Intermetallic phase growth profile of VPS sample heat treated for 1 day at 800 °C.



(c) Intermetallic phase growth profile of VPS sample heat treated for 1 week at 800 °C.

Figure 5.9: Intermetallic phase growth profiles for VPS W coatings based on average pixel intensity normalised using the maximum value of average intensity.

fusion along grain boundaries. Alternatively, the FAST data may be artificially high due to the higher content of impurities following manufacture shown in Table 5.3, meaning that impurity elements had shorter distances to diffuse to form new phases in these samples.

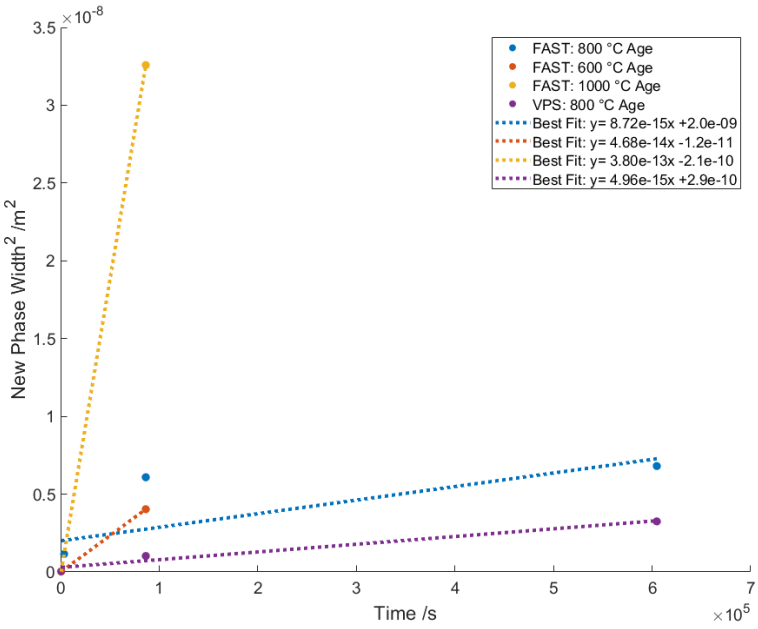


Figure 5.10: Plot showing affect of ageing time and temperature on the width of intermetallic phases that form. New phase width is squared in order to produce a linear relationship, according to Equation 5.1.

Arrhenius kinetics

Figure 5.11 shows an Arrhenius plot constructed using the growth rate coefficient values and corresponding heat treatment temperatures in Figure 5.10. Taking the natural logarithm of the Arrhenius relationship (Equation 5.2) shows the gradient of the line (-4819 mol^{-1}) was equal to $\frac{-E_A}{R}$ and the y-intercept (-26.0) was equal to $ln(K_0)$. Therefore, the calculated activation energy was 40 $kJ{\cdot}mol^{-1}$ and the maximum growth rate coefficient was $5.3{\times}10^{-12}$ $m^2{\cdot}s^{-1}$. Reisner et al. [93] investigated Fe-W interfaces at temperatures similar to those used in this work and their collected growth rate data have been plotted in Figure 5.11 for reference. The associated activation energy and maximum growth rate coefficient are 198 $kJ{\cdot}mol^{-1}$ and $6.9{\times}10^{-9}$ $m^2{\cdot}s^{-1}$ respectively. When compared, the growth rate coefficients found in the present work were significantly higher than those found by Reisner, due to the significantly lower activation energy, likely due to the addition of smaller species such as C and O which diffuse much faster.

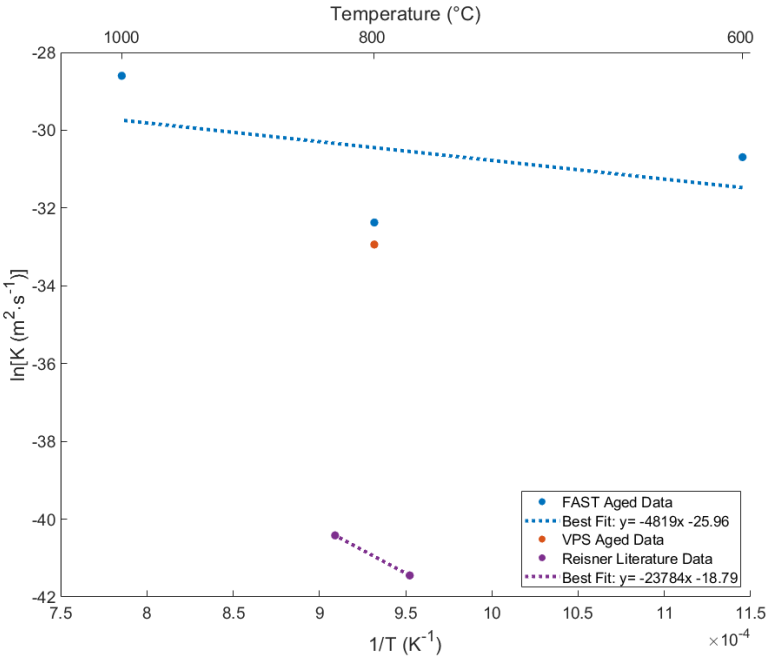


Figure 5.11: Arrhenius plot for new phase growth between steel and W in FAST and VPS samples. The line of best fit was calculated for FAST samples. Fe_2W phase growth data from Reisner et al. [93] (Fe and W only) have been included for reference.

Elemental and phase analysis

Figures 5.12–5.13 show EDX data for each of the aged samples. Each top left image is a BSE SEM image, with the corresponding EDX phase map shown in the top right image. Each bottom image shows the average atomic percentage of each element found in EDX linescans taken across in the area denoted by the purple box (the dashed arrow shows the direction of the scan) in the corresponding SEM image. EDX spectra and phases were automatically identified within the

EDX software, with boundary and grouping tolerance settings set to the minimum possible values for phase selection. EDX linescan data was processed in bins of with a binning factor of 4 (i.e. every four data points were grouped) to reduce data noise.

Four main phase groups were found during EDX analysis: W, Fe (steel), the new phase (FeWCrOC), and WC. Tables 5.4–5.7 show the elemental breakdown of each phase identified.

In the as-manufactured samples, the FeWCrOC interface was significantly thicker in the FAST sample than in the VPS, Figures 5.12 (a) & 5.13 (a) respectively. The FeWCrOC phase was also found along horizontal cracks in the FAST coating. The VPS sample had significant amounts of WC that aligned with cracks and pores in the coating. It was postulated that the carbon was trapped in the coating during the spraying process — after spraying it was necessary to clean soot produced during manufacture off VPS chamber walls.

The FeWCrOC phase at the interface increased in thickness with increasing time, as previously seen in the SEM images and diffusion analysis. Following a day of heat treatment at 800 °C, both the FAST and VPS samples had thicker FeWCrOC interfaces and some FeWCrOC dispersed throughout the coating, shown in Figures 5.12 (c) & 5.13 (b) respectively. The EDX detector struggled to resolve the dispersed FeWCrOC for the FAST sample. This was because X-rays were generated at a depth of 1–2 µm [157] and the powder particles used for FAST samples were smaller than this. The BSE detection depth was 0.5–1.5 nm [158], and thus the BSE image contrast highlights the proliferation of diffusive species far better than EDX. Significant amounts of substitutional diffusion between Fe and W species

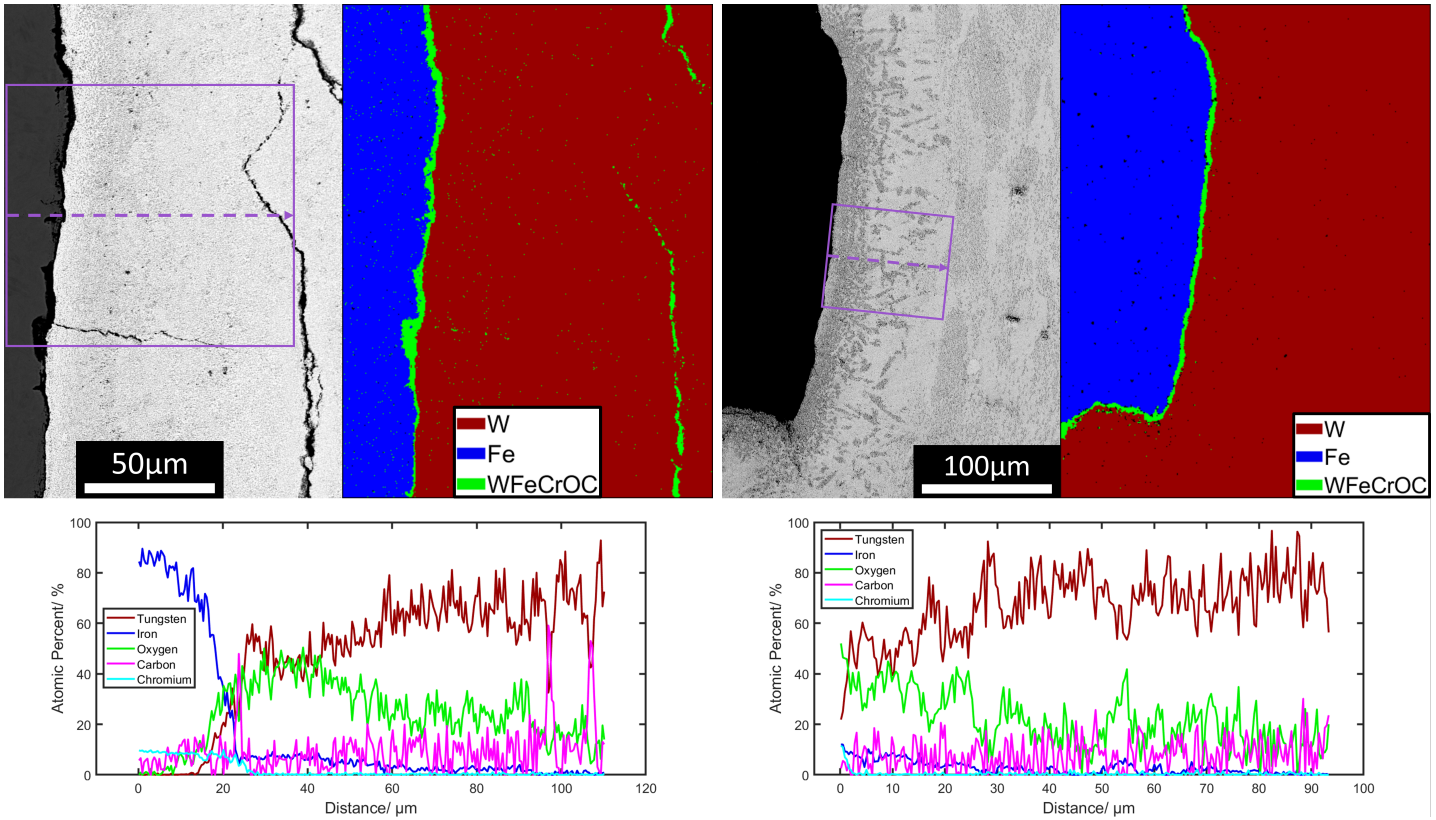
occurred when heated for one week at 1000 °C, whereas nearly no substitutional diffusion occurred at 600 °C in the same time frame, shown in Figures 5.12 (f) & (e) respectively. The VPS samples contained larger, dense powder particles (with larger separations between them) than the FAST samples. The EDX analysis in Figure 5.13 (b) showed the growth of the diffusion phase between the splats more clearly than for the equivalent FAST sample, Figure 5.12 (c). It also showed that larger substitutional elements had not diffused very far into the W coating. Cracking in the day-aged VPS sample appeared to correspond with WC rich areas, which indicates that cracks propagated through the brittle WC regions between the splats.

After a week at 800 °C, substitutional diffusion had time to occur in the VPS sample. This shown in Figure 5.13 (c) by the EDX linescan data, where Fe was detected up to ∼50 µm deep into the coating, and also by the significant increase in the amount of FeWCrOC phase in comparison to the day-aged sample shown in Figure 5.13 (b). O and C were more prevalent than W for significant portions of the linescan. C and O had opposing fluctuations which implied that the phases that formed were either carbides or oxides, rather than a mix of the two. The ratio of FeWCrOC phase to WC also inverted with increased ageing time, as the FeWCrOC incorporated the WC phase in the week-aged sample. This was further evidence that substitutional (Fe and Cr) and oxygen diffusion reached further into the VPS W coating.

In comparison, after a week at 800 °C the FAST W coating had a high oxygen content from the interface for approximately 150 µm. As with the day-aged samples, the EDX struggled to resolve the fine phases around the W powder particles. A finer EDX scan was required as shown in the inset map in Figure 5.12 (d). The inset shows that Fe diffused along a vertical crack, rather than through the finer network between powder particles like C and O. It remains uncertain whether the cracking observed in the FAST samples, spanning all ages, predated the migration of diffusive species or occurred subsequently during cooling or sectioning, due to the increased cracking susceptibility of the new, brittle diffusion phase.

EDX data and phase growth data are both plotted for comparison in Figure 5.14. Sharp gradient changes occur in both data sets around 20 µm and 180 µm — this corroboration between methods provides confidence in intermetallic width measurements highlighted in Figures 5.8–5.9.

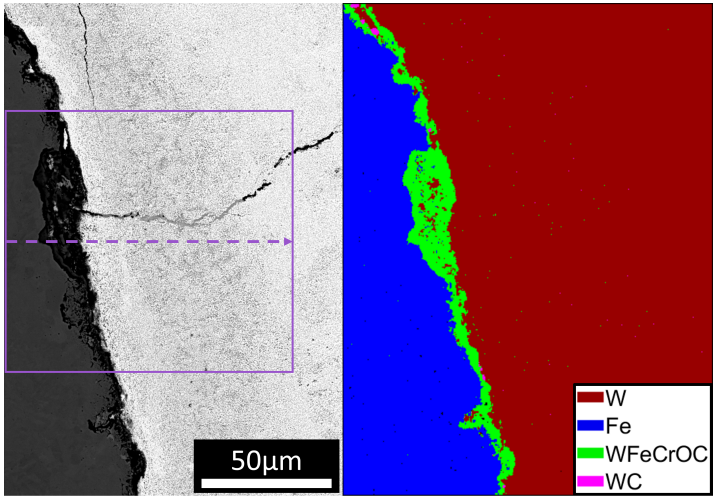
EDX results allowed for more targeted XRD analysis and limited any confirmation bias during interpretation of the XRD data.



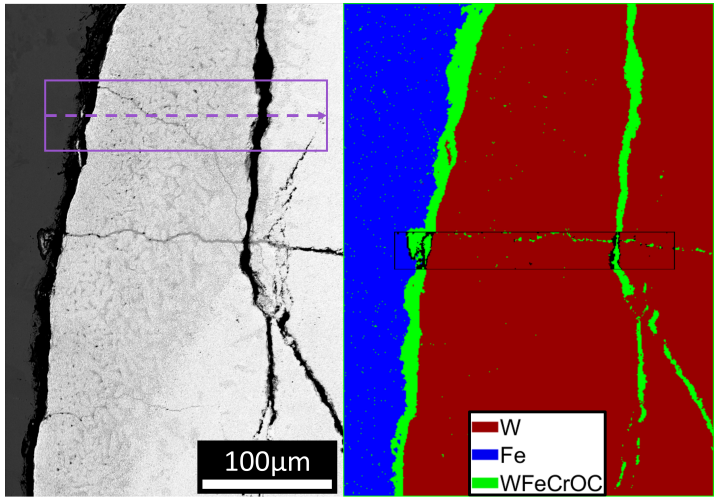
(a) As-manufactured FAST sample. Ten linescans were averaged.

(b) FAST sample, 1 hour at 800 °C. Five linescans were averaged.

Figure 5.12: EDX analysis for aged FAST samples. Each top left image is a BSE SEM image, with the corresponding EDX phase map shown in the top right image. Each bottom image shows the average atomic percentage of each element found in EDX linescans taken across in the area denoted by the purple box (the dashed arrow shows the direction of the scan) in the corresponding SEM image.

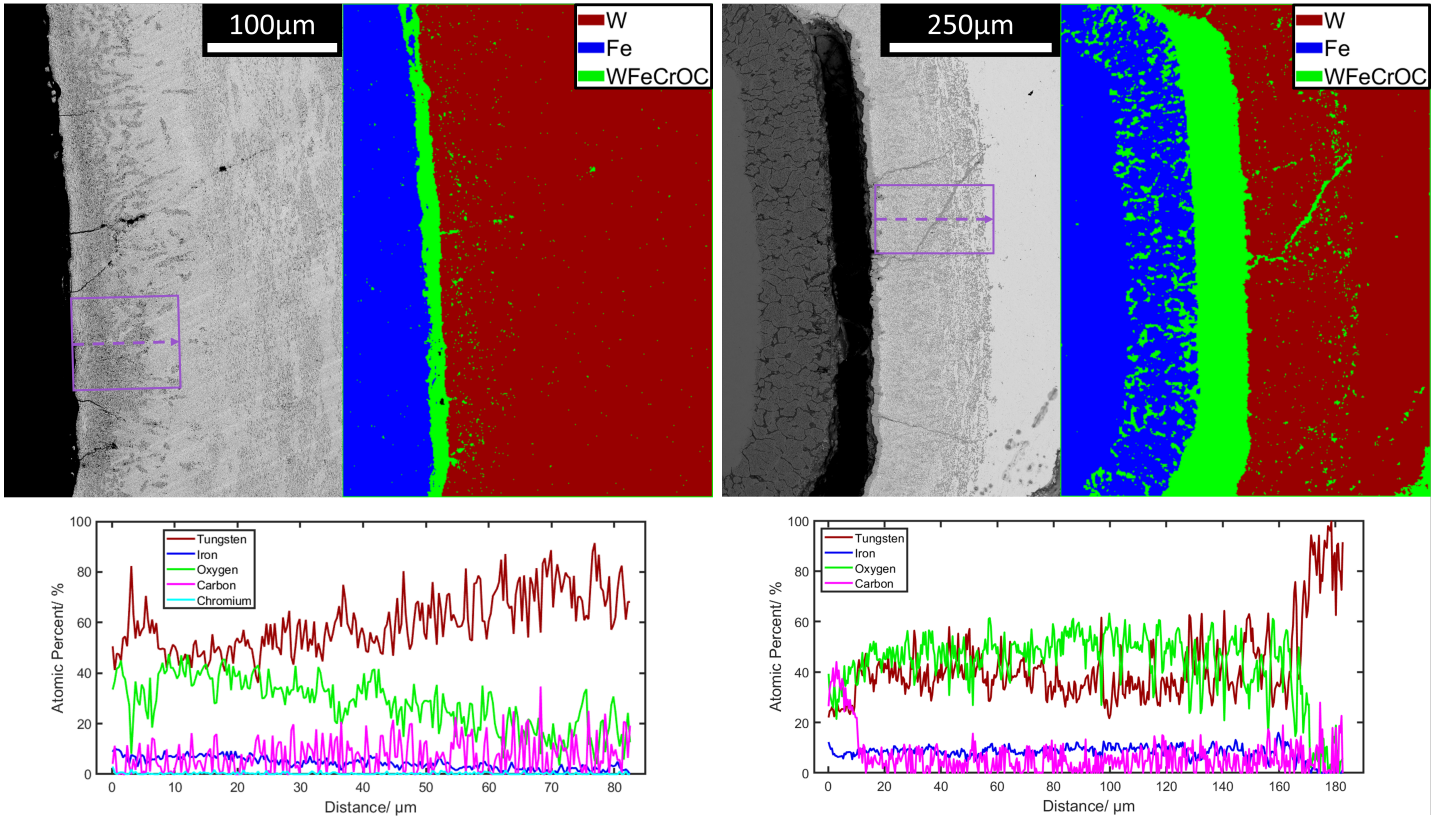


(c) FAST sample, 1 day at 800 °C. Ten linescans were averaged.



(d) FAST sample, 1 week at 800 °C. Three linescans were averaged. The inset EDX phase map shows a higher resolution scan.

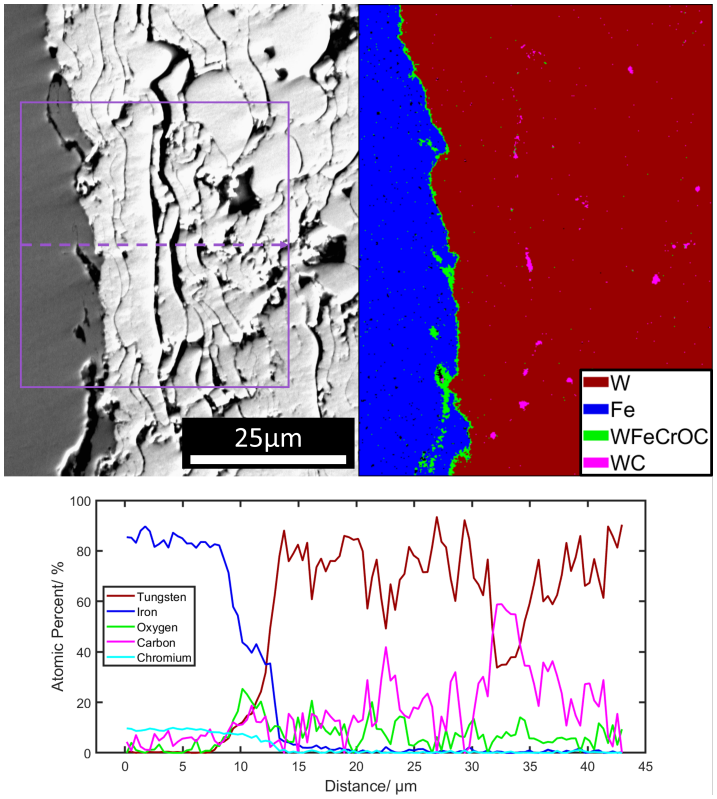
Figure 5.12: EDX analysis for aged FAST samples. Each top left image is a BSE SEM image, with the corresponding EDX phase map shown in the top right image. Each bottom image shows the average atomic percentage of each element found in EDX linescans taken across in the area denoted by the purple box (the dashed arrow shows the direction of the scan) in the corresponding SEM image.



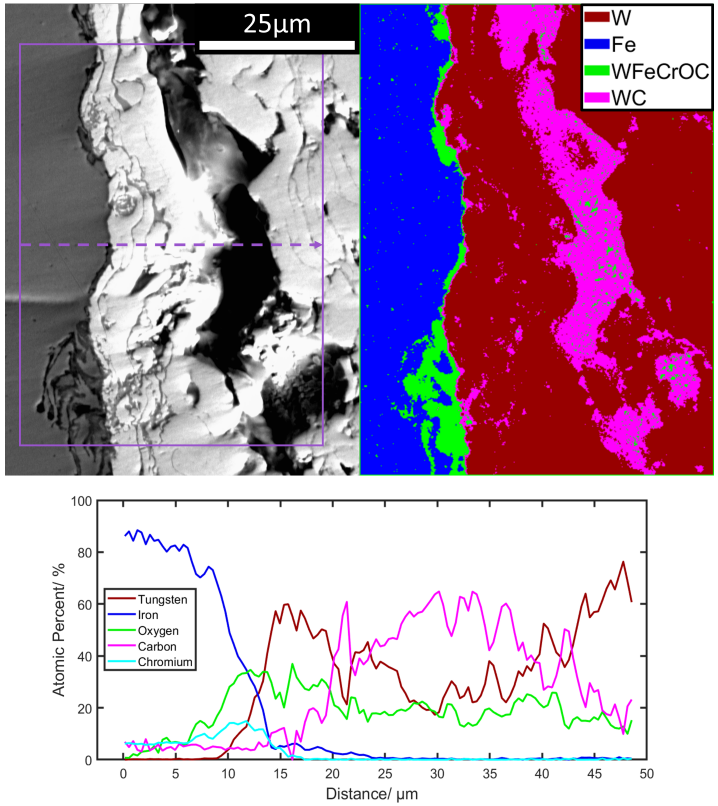
(e) FAST sample, 1 day at 600 °C. Five linescans were averaged.

(f) FAST sample, 1 day at 1000 °C. Six linescans were averaged.

Figure 5.12: EDX analysis for aged FAST samples. Each top left image is a BSE SEM image, with the corresponding EDX phase map shown in the top right image. Each bottom image shows the average atomic percentage of each element found in EDX linescans taken across in the area denoted by the purple box (the dashed arrow shows the direction of the scan) in the corresponding SEM image.

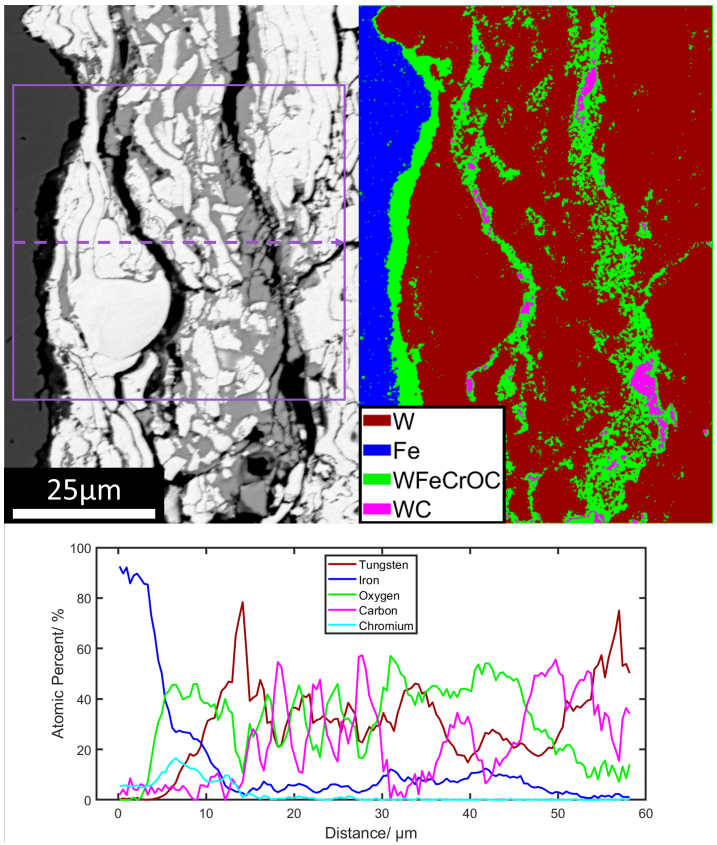


(a) As-manufactured VPS sample. Ten linescans were averaged.



(b) VPS sample, 1 day at 800 °C. 20 linescans were averaged.

Figure 5.13: EDX analysis for aged VPS samples. Each top left image is a BSE SEM image, with the corresponding EDX phase map shown in the top right image. Each bottom image shows the average atomic percentage of each element found in EDX linescans taken across in the area denoted by the purple box (the dashed arrow shows the direction of the scan) in the corresponding SEM image.



(c) VPS sample, 1 week at 800 °C. 15 linescans were averaged.

Figure 5.13: EDX analysis for aged VPS samples. Each top left image is a BSE SEM image, with the corresponding EDX phase map shown in the top right image. Each bottom image shows the average atomic percentage of each element found in EDX linescans taken across in the area denoted by the purple box (the dashed arrow shows the direction of the scan) in the corresponding SEM image.

Element (at%)	FAST AM	FAST 1 Hour 800 °C	FAST 1 Day 800 °C	FAST 1 Week 800 °C	FAST 1 Day 600 °C	FAST 1 Day 1000 °C	VPS AM	VPS 1 Day 800 °C	VPS 1 Week 800 °C
W	65.77	72.02	54.31	50.69	71.81	56.29	98.52	73.53	55.63
O	30.45	25.67	39.2	42.79	25.8	38.07	0	23.61	37.85
Fe	3.39	1.93	5.97	6.52	2.1	5.64	1.48	1.87	5.89
Cr	0	0	0.52	0	0	0	0	0.36	0.62

Table 5.4: Elemental breakdown of W phase identified by EDX software

Element (at%)	FAST AM	FAST 1 Hour 800 °C	FAST 1 Day 800 °C	FAST 1 Week 800 °C	FAST 1 Day 600 °C	FAST 1 Day 1000 °C	VPS AM	VPS 1 Day 800 °C	VPS 1 Week 800 °C
Fe	88.48	88.56	88.97	89.14	88.99	79.64	87.5	90.75	91.85
Cr	9.02	9.5	8.13	8.81	9.38	7.96	9.42	6.61	5.73
Si	1.1	0.87	1.06	1.04	0.81	0.79	0.94	1.2	0.81
Mo	0.62	0.53	0.57	0.75	0.51	0.51	0.6	0.55	0
V	0.21	0.29	0.27	0.26	0.21	0.2	0.23	0.22	0.18
Al	0	0.19	0	0	0	0.16	0.94	0.42	0.43
W	0	0.06	0.03	0	0.1	0.12	0.36	0.26	0.35
O	0	0	0	0	0	10.61	0	0	0

Table 5.5: Elemental breakdown of Fe phase identified by EDX software

Element (at%)	FAST AM	FAST 1 Hour 800 °C	FAST 1 Day 800 °C	FAST 1 Week 800 °C	FAST 1 Day 600 °C	FAST 1 Day 1000 °C	VPS AM	VPS 1 Day 800 °C	VPS 1 Week 800 °C
O	42.53	54.31	53.37	52.08	51.74	54.51	36.1	39.38	44.59
Fe	9.11	19.61	13.46	7.71	26.19	23.37	24.38	22.98	10.86
Cr	8.57	15.28	22.06	13.58	8.23	7.45	6.16	14.69	4.77
W	8.57	6.5	2.46	4.89	9.48	7.04	8.49	6.15	10.42
C	27.34	0	0	20.12	0	0	17.96	9.34	27.15

Table 5.6: Elemental breakdown of FeWCrOC phase identified by EDX software

Element (at%)	FAST 1 Day 800 °C	VPS AM	VPS 1 Day 800 °C	VPS 1 Week 800 °C
C	93.46	83.76	62.74	83.1
O	0	4.08	23.63	10.72
W	4.8	11.14	10.63	4.98
Fe	1.75	0.48	1.12	1.21
Cr	0	0.54	0.85	0

Table 5.7: Elemental breakdown of WC phase identified by EDX software

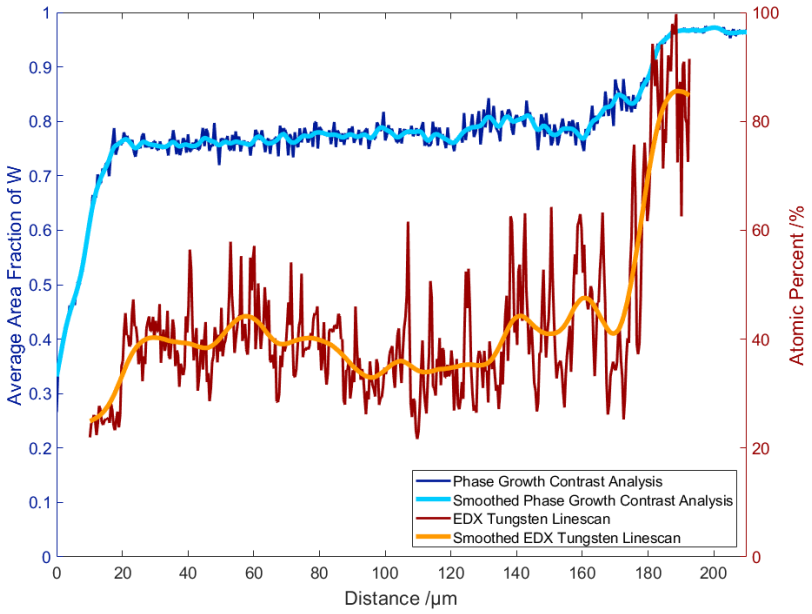


Figure 5.14: Comparison of phase contrast analysis with EDX analysis for FAST sample aged for 1 day at 1000 °C. The value of area fraction of W is relative to the overall contrast level in the micrograph, however still matches the plot overall shape and width of new intermediate phase formed.

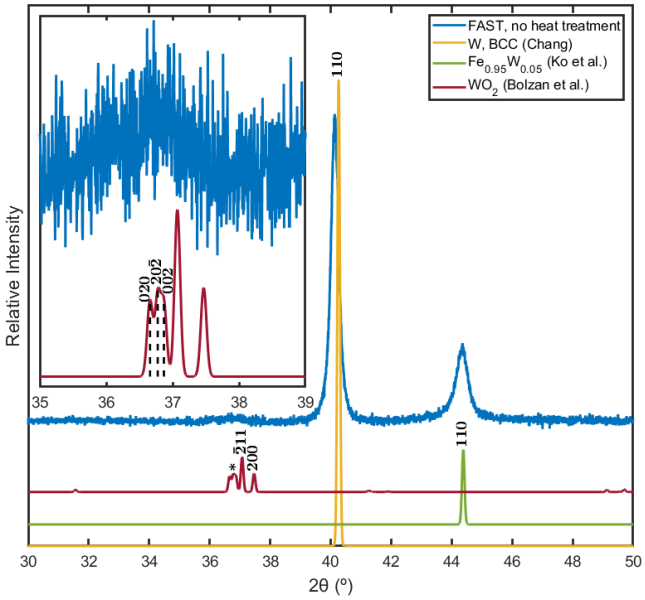
Figure 5.15 shows the results of XRD scans of four samples. Figure 5.15 (a) was scanned transverse to the interface, which was why the $Fe_{0.95}W_{0.05}$ peak was visible. The $Fe_{0.95}W_{0.05}$ peak was closer to the W peak than a pure Fe peak as the lattice was stretched by the larger substitutional W. A small amount of WO_2 was also seen in the as-manufactured FAST sample.

Figures 5.15 (b-d) were scanned across the W side of the fractured interface (which was why no Fe peak was seen). The heat-treated FAST sample shown in Figure 5.15 (b) comprised of small shards, which was why the peaks attributed to the plasticine mount were visible. The plasticine peaks have been manually shifted to the left to highlight the overlap with the measured XRD pattern for the heat-treated sample. The offset occurred because the plasticine was lower than the target height for the XRD (as the sample was protruding from the plasticine at the correct height for the XRD). No WO_2 peaks were seen in the heat-treated FAST sample. A mix of other oxides were apparent: $FeCr_2O_4$, Fe_3O_4 and $FeWO_4$. $FeCr_2O_4$ and Fe_3O_4 are same crystal structure, where two substituted Cr atoms result in a tighter crystal lattice, shown by an increase in peak angle. In comparison to the as-manufactured FAST sample, the increase in Fe and Cr that had diffused into the W coating and then reacted with the original W oxides corroborated with the EDX data.

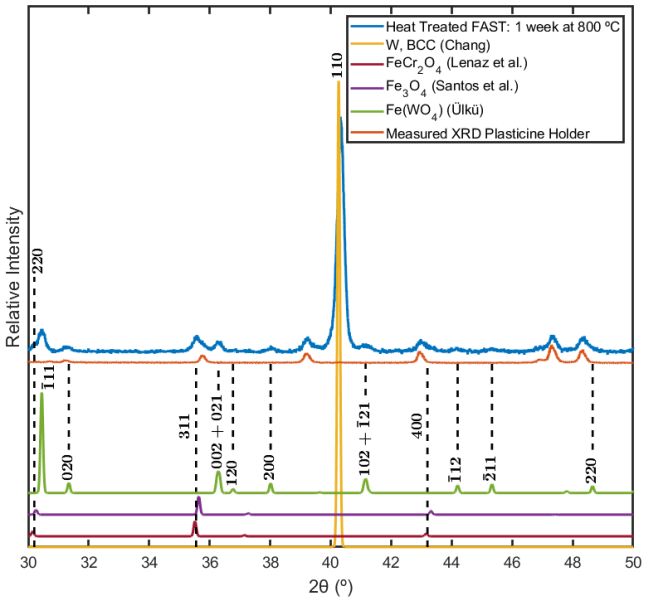
Conversely, very few differences were seen between the two VPS samples. Relatively small amounts of W_2C, WCr_2O_6 and Cr_3C_2 were seen in both sprayed samples, which confirmed that carbon from the VPS process was trapped in the coating. The presence of Cr, but no Fe, was suspected to have occurred due to the

surface passivation of the stainless steel substrates prior to spraying which then reacted at the interface. The heat-treated sample had a thinner W peak, which indicated that there was less strain in the sample. Strain was probably relieved slightly during thermal ageing.

Figure 5.15 (e) shows a profile comparison of the four samples. The two VPS samples and the as-manufactured FAST sample all had W peaks that corresponded with a larger-than-normal lattice parameter for W, due to residual strain following manufacturing. The vertical segmentation in the FAST sample relieved some of this strain, as did the thermal ageing in the heat-treated VPS sample. The as-manufactured VPS had no strain relief mechanisms and was therefore the most stretched, resulting in the largest peak shift. The heat-treated FAST sample had a smaller-than-normal lattice parameter because Fe had diffused into the lattice substitutionally and, being a smaller element than W, contracted the lattice. Linear regression analysis of the lattice parameters for Fe-W BCC crystals predicted that the heat-treated FAST sample contained approximately 1.7 at% Fe at the interface. This matches the solubility limit of Fe in W (0.5 wt%) shown in the Fe-W phase diagram [150].

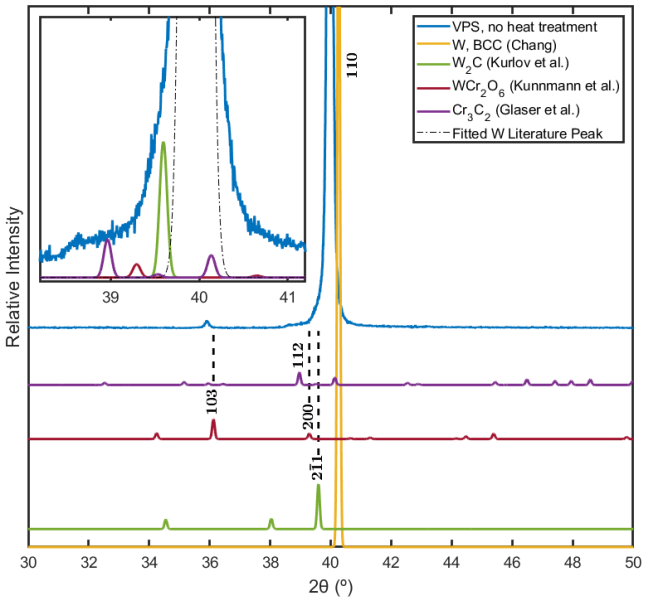


(a) XRD profile of as-manufactured FAST sample. The * denotes the location of the three indexed peaks in the inset.

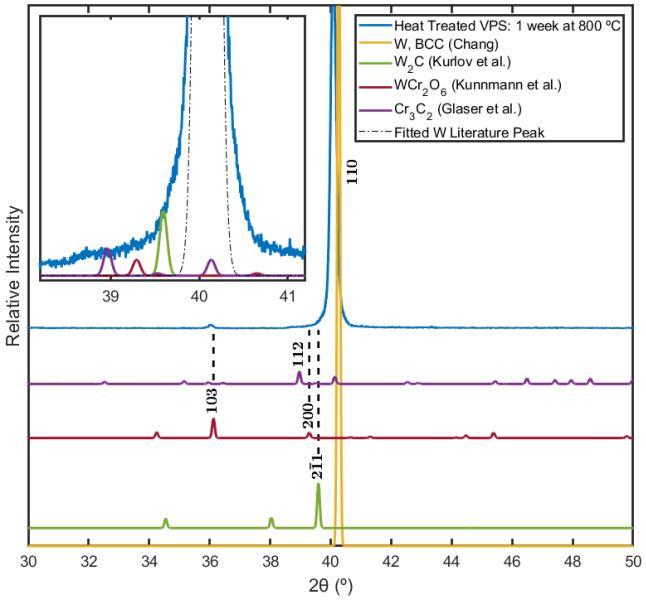


(b) XRD profile of heat treated (1 week at 800 °C) FAST sample.

Figure 5.15: XRD profiles for as-manufactured and heat treated FAST and VPS samples.

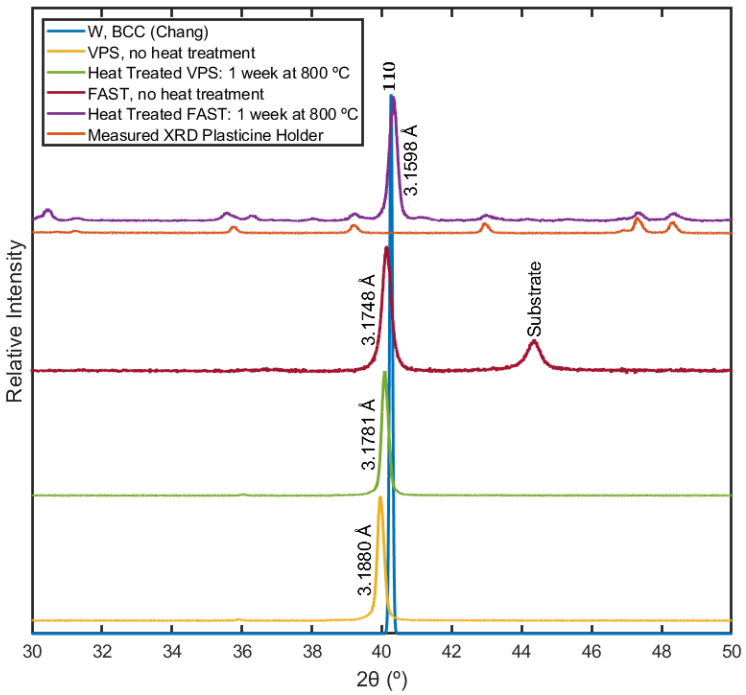


(c) XRD profile of as-manufactured VPS sample. The dot-dashed, aligned literature line highlights the one-sided peak broadening due to other phases.



(d) XRD profile of heat treated (1 week at 800 °C) VPS sample. The dot-dashed, aligned literature line highlights the one-sided peak broadening due to other phases.

Figure 5.15: XRD profiles for as-manufactured and heat treated FAST and VPS samples.



(e) A normalised comparison of the four XRD profiles shown above. W lattice parameters corresponding to the peak offset are shown next the respective experimental peak.

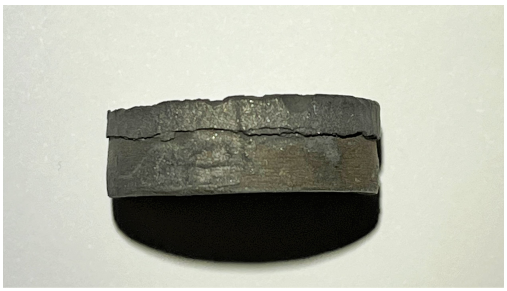
Figure 5.15: Measured XRD profiles for as-manufactured and heat treated FAST and VPS samples with corresponding phase profiles from literature [159–167].

5.3.2 Thermal Cycling: HIVE

Figure 5.16 shows photographs of the four sample types (F2mm, H2mm, H4mm and W2mm) and the surface finish obtained prior to testing. Some surface scratching was visible, as seen in Figure 5.16 (e), but no surface cracking from manufacture was seen in any sample tested.

In-situ analysis during thermal cycling

Figure 5.17 (a) shows the thermocouple and pyrometer data measured for the F2mm sample during testing in HIVE. The yellow arrows indicate the cycle number. The pyrometer data was representative for all samples, cycling between 350–800 °C (350 °C was the lower limit of the pyrometer). The initial temperature ramping region indicates the preliminary treatment to out-gas the samples, as seen by the corresponding spike in vacuum in Figures 5.17 (b–e). The 2 mm coatings on hatched steel and flat W effectively transferred heat through to the steel, as the thermocouple temperature closely matched the coating surface temperature. In comparison, the flat steel substrate sample only reached ∼400 °C. Upon release of the vacuum, the coating fell off the substrate. This indicated that the sample failed early in the process (most likely around the temperature spike seen just before cycling began) and stayed loosely connected, meaning that very little energy was transferred across the interface. The 4 mm coating on hatched steel also had a lower measured maximum thermocouple temperature. As the mass of W coating doubled, the total thermal energy capacity of the coating effectively increased by the same factor. The decrease in maximum substrate temperature occurred be-



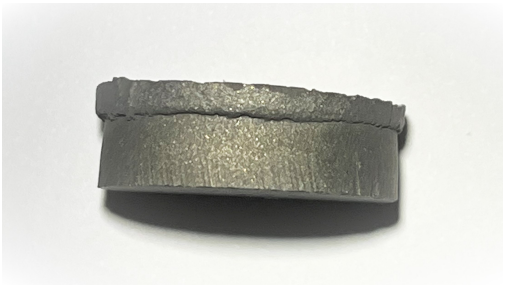
(a) 2 mm thick W coating on a flat steel substrate (F2mm).



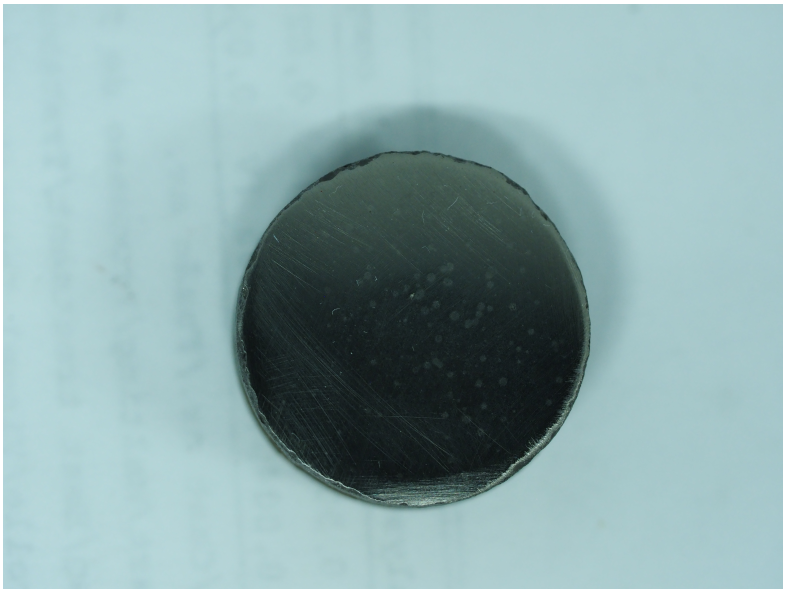
(b) 2 mm thick W coating on a hatched steel substrate (H2mm).



(c) 4 mm thick W coating on a flat steel substrate (H4mm).



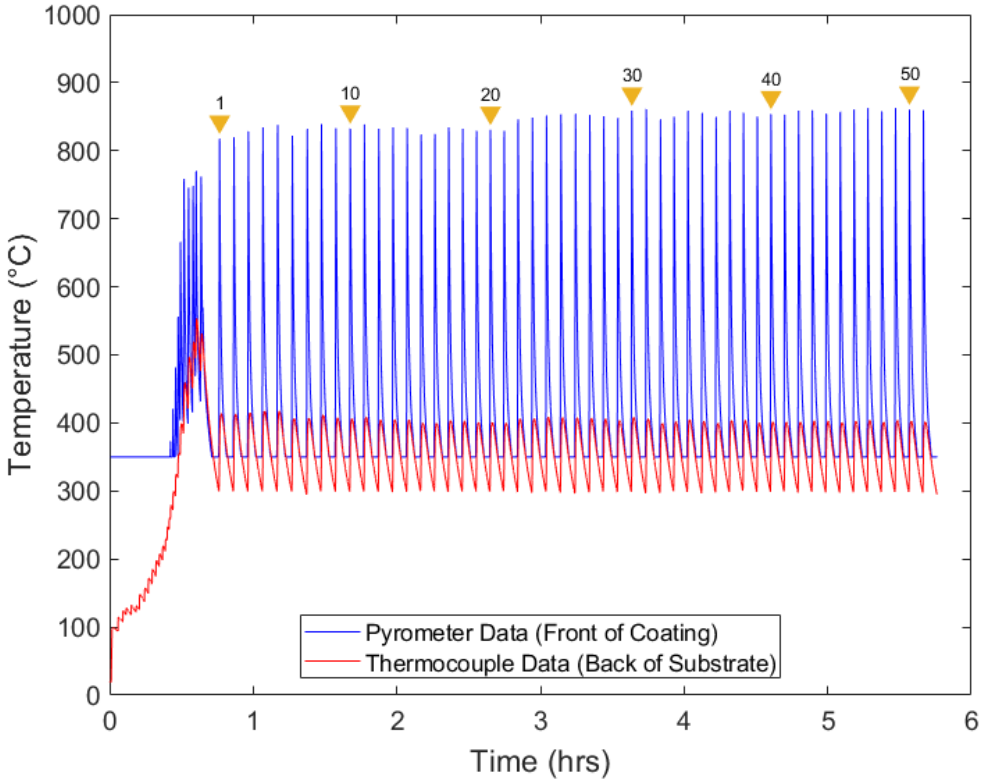
(d) 2 mm thick W coating on a flat W substrate (W2mm).



(e) Example of coating surface finish before testing at HIVE.

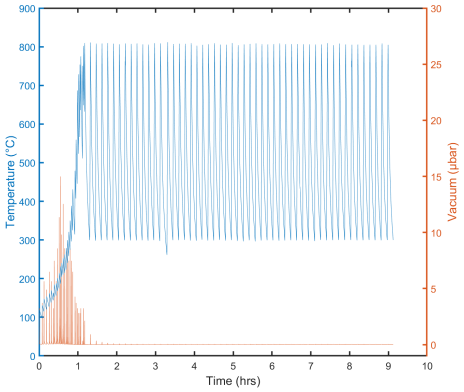
Figure 5.16: Photographs of samples prior to HIVE testing.

cause the coating successfully acted as a thermal shield (as desired for operation in a nuclear reactor), rather than due to interfacial failure. Table 5.8 shows the average maximum thermocouple temperature and difference from target surface temperature for each sample.

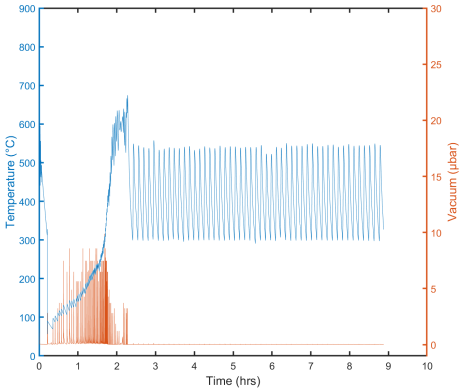


(a) Example of thermocouple and pyrometer data collected with each HIVE experiment. The abrupt cut-off at the end of each pyrometer cycle was because the temperature has dropped below the lower operation limit of 350 °C.

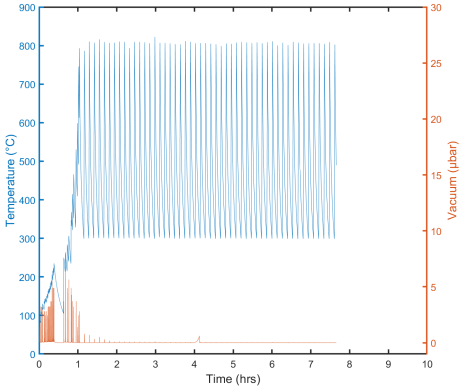
Figure 5.17: Comparisons between: (a) pyrometer and thermocouple data and (b–e) thermocouple and vacuum data for different sample types.



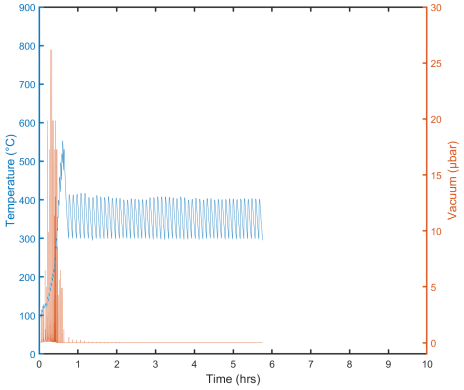
(b) Thermocouple temperature and vacuum profile for H2mm sample.



(c) Thermocouple temperature and vacuum profile for H4mm sample.



(d) Thermocouple temperature and vacuum profile for W2mm sample.



(e) Thermocouple temperature and vacuum profile for F4mm sample.

Figure 5.17: Comparisons between: (a) pyrometer and thermocouple data and (b–e) thermocouple and vacuum data for different sample types.

Sample	Average Cyclic Peak Thermocouple Temperature (°C)	Average Difference from Target Surface Temperature (°C)
F2mm	405	395
H2mm	806 807	6.4
H4mm	542 532 678	216
W2mm	807 805 807	6.0

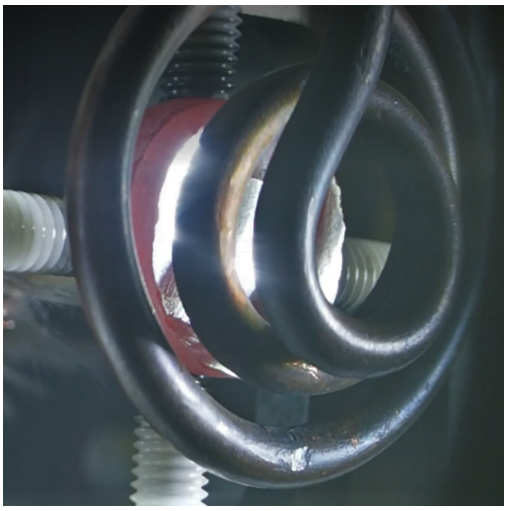
Table 5.8: Average cyclic peak thermocouple temperatures measured for each type of sample in HIVE and the average difference between this and the coating face target temperature (800 °C).

Figure 5.18 shows frames taken from optical videos recording during thermal cycling. The hatched steel with a 2 mm coating was clearly very hot as it turned red at peak temperature (which corresponds to 760–815 °C [168]). The 4 mm coating sample turned a dull red (∼540 °C) and the flat steel substrate did not appear to change colour.

Infrared in-situ imaging was used to confirm at what point in the cycling process a sample initially cracked, as this technique highlighted larger cracks particularly clearly. When cracking occurred, the change in topography increased the emissivity locally, which meant that the cracks were highlighted because they appeared hotter than they actually were. The resolution of the camera was not high enough to see small cracks, but was sufficient to compare the samples. Figure 5.19 shows the frame at peak pulse for the final cycle for each of the four sample types. Neither the W2mm nor F2mm samples formed any vertical cracks due to a lack of mismatch



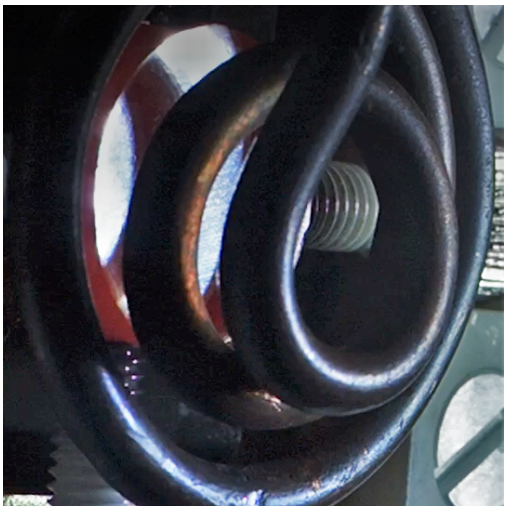
(a) 2 mm thick W coating on a flat steel substrate.



(b) 2 mm thick W coating on a hatched steel substrate.



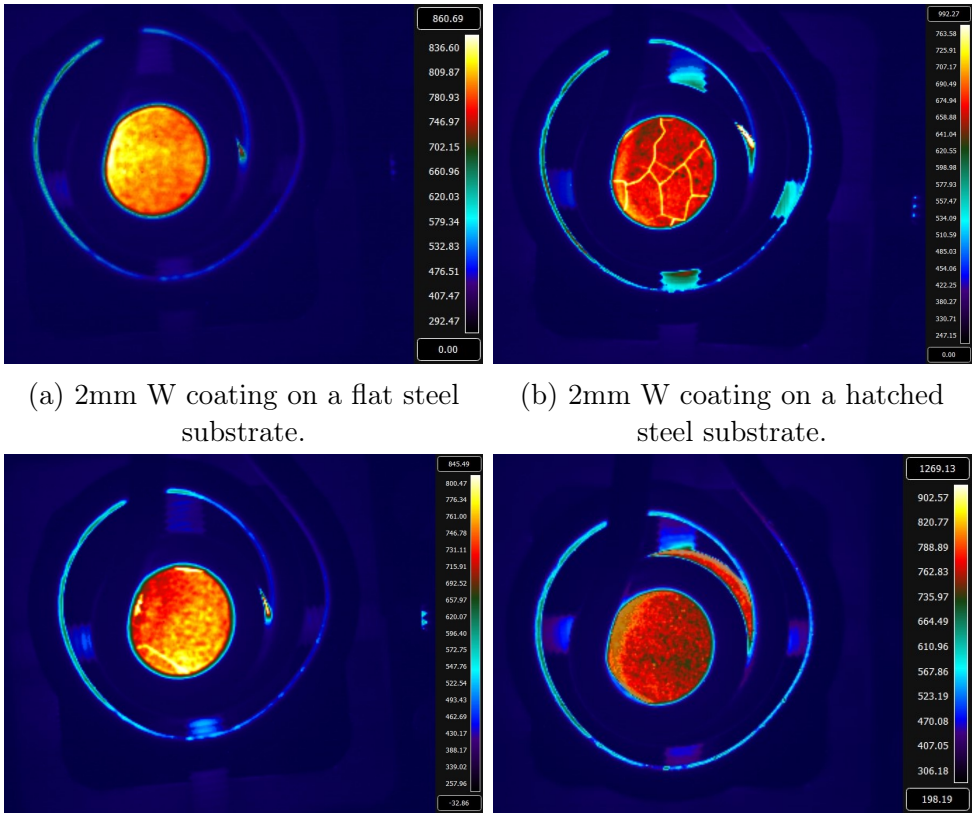
(c) 4 mm thick W coating on a hatched steel substrate.



(d) 2 mm thick W coating on a flat W substrate.

Figure 5.18: Photographs of the side of samples during HIVE testing.

strains and stresses. This was because there was no thermal expansion coefficient mismatch for the W2mm sample and because the W coating had delaminated during the initial out-gassing for the F2mm sample. Both the H2mm and H4mm samples exhibited cracking, this was more apparent in the 2 mm coating than in the 4 mm coating. Cracks in the 4 mm coating appeared to be wider and closer to the edge of the sample. FE modelling predicted that thicker coatings would have higher stresses at the surface, and showed that the edge of the sample was a concentration point for stresses, so it was expected that cracks in the H4mm sample would be larger. Wider cracks increased the compliance of the coating more, meaning that fewer cracks were required to relieve any stored mismatch strain/stress. Cracking occurred in the initial out-gassing cycling process for both hatched samples. Cracking in the H2mm sample appeared to be similar to that observed in the 2 mm W coating produced by Cui et al. [74], the thickest coating that they produced.



(a) 2mm W coating on a flat steel substrate.

(b) 2mm W coating on a hatched steel substrate.

(c) 4mm W coating on a hatched steel substrate.

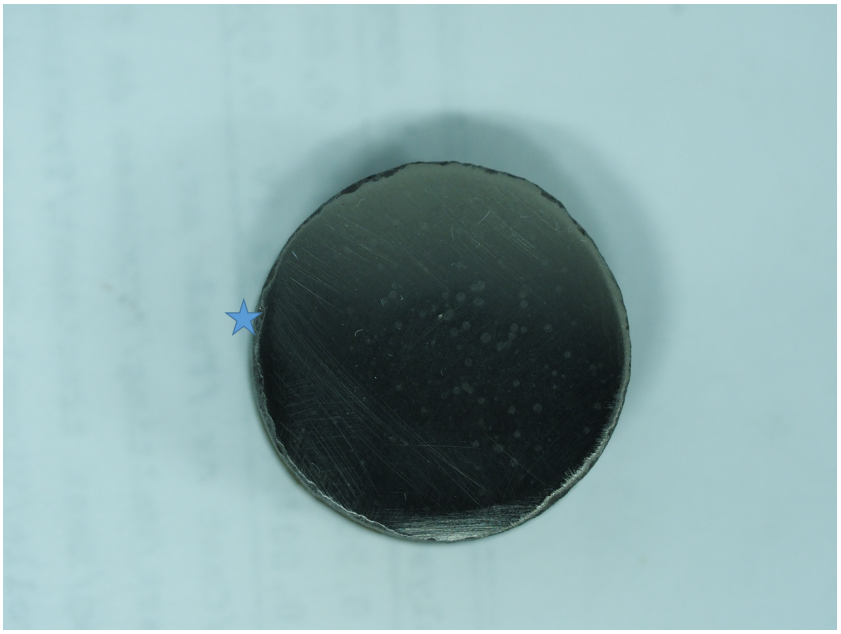
(d) 2mm W coating on a flat W substrate.

Figure 5.19: Frames of different samples taken at the moment of maximum temperature at the peak of a cyclic heat pulse in HIVE testing.

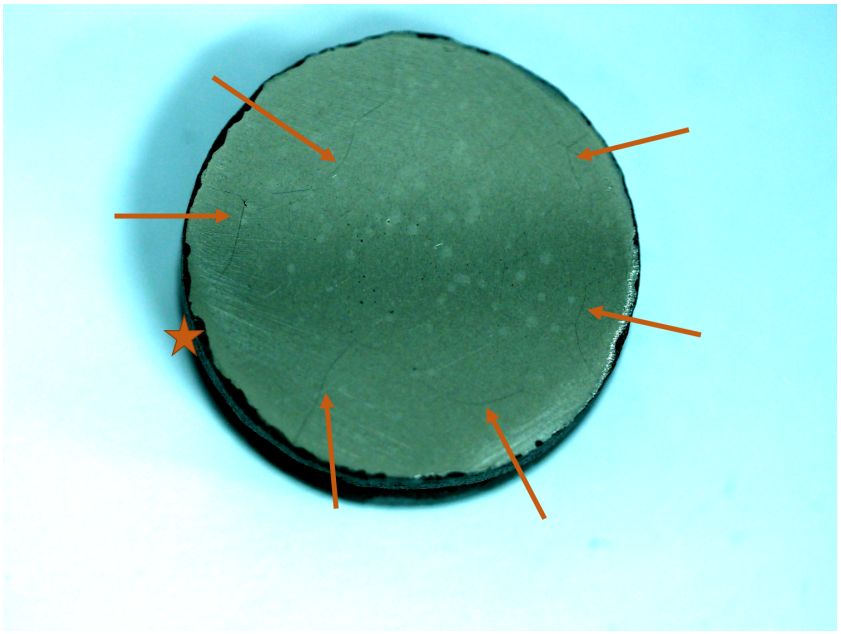
Surface crack analysis and debonding

Figure 5.20 (a–b) compares the H2mm steel sample before and after testing. Surface cracks were visible across the entire surface of the coating following testing in HIVE. The cracks appeared to be interconnected; this was far clearer when observed in the SEM. Cracking in the thicker H4mm samples was also observed,

shown in Figure 5.20 (c), whereas the W substrate samples showed no signs of cracking occurring during or after testing. In comparison, roughly half of the thickest coating (2 mm) produced by Cui et al. delaminated during handling following testing [74].

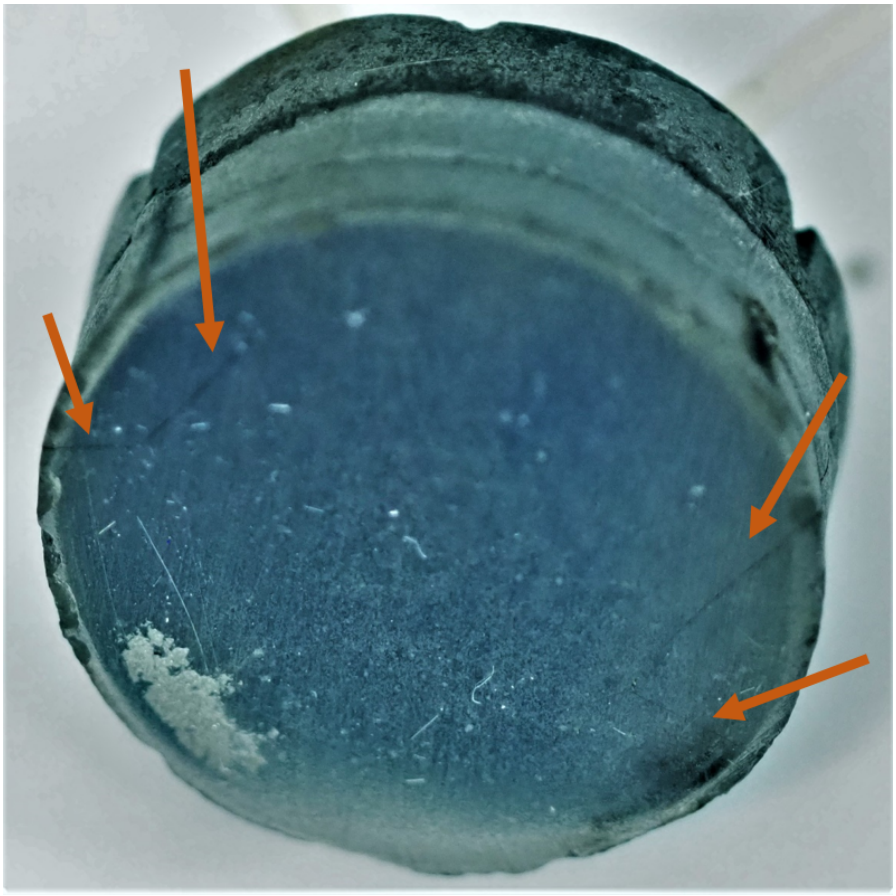


(a) Annotated version of Figure 5.16 (e) (prior to testing) for comparison with Figure 5.20 (b).



(b) Surface of the H2mm sample shown in Figure 5.16 (e) following testing. Arrows highlight crack locations.

Figure 5.20: Photographs of an H2mm sample before (a) and after(b) testing in HIVE and an H4mm sample after testing (c). The star in (a–b) is a reference point at the same location on the sample for each image.

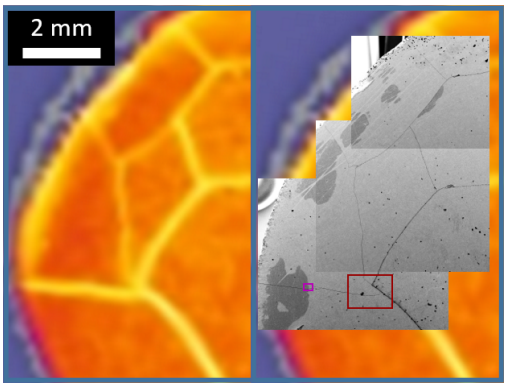


(c) Surface of a H4mm sample following testing. Arrows highlight crack locations.

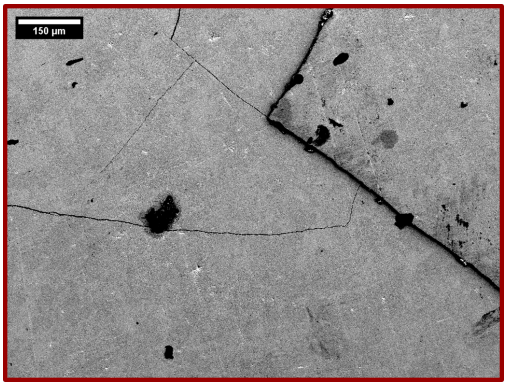
Figure 5.20: Photographs of an H2mm sample before and after testing in HIVE and an H4mm sample after testing. The star in (a–b) is a reference point at the same location on the sample for each image.

Figure 5.21 (a) shows a comparison of surface cracking in an H2mm sample. The red and pink boxes denote the enlarged portions detailed in Figures 5.21 (b–c). Figure 5.21 (b) shows a section of the surface that lifted during thermal cycling in HIVE as the coating expanded and became wedged in place as the sample contracted. The smaller cracks to the left were unresolvable in the IR. Figure 5.21 (c) provides another comparison between a large crack, resolvable by IR imaging, and a finer crack that was only visible in the SEM at higher magnifications. The yellow box in the top left of the image denotes the location of the end of the small crack, shown in Figure 5.21 (d). The crack appears to have propagated intergranularly, due to the porosity and brittle oxides discussed in Section 5.3.1. An underlying network of smaller cracks was observed throughout the rest of the sample.

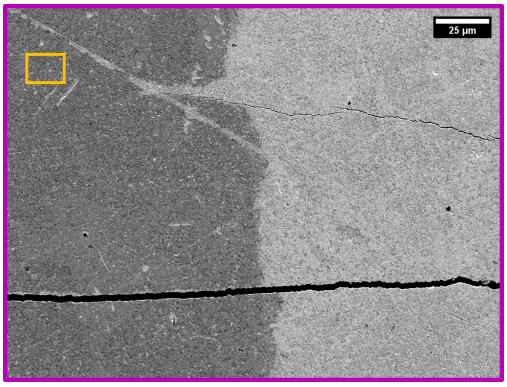
Figure 5.22 shows cracking in the H4mm sample shown in Figures 5.19 (c) & 5.20 (c) with increasing magnification. As noted in Figure 5.20 (c), cracking was predominantly observed towards the edges of the sample. Figure 5.22 (b) shows the area in the middle of Figure 5.22 (a) where the surface has cracked and a fragment has fallen out. This was significantly worse than the slight protrusion observed in Figure 5.21 (b). The large crack in Figure 5.22 (c) was approximately 6.25 µm wide, in comparison the large crack in Figure 5.21 (c) was approximately 3.3 µm, almost half the width. Fewer cracks were seen in the H4mm sample because the thicker coating had a higher stress at the surface, meaning that when cracks initiated and propagated they opened significantly more. Wider cracks would have made the coating more compliant than thinner cracks, which was why fewer cracks were required to relieve the stress.



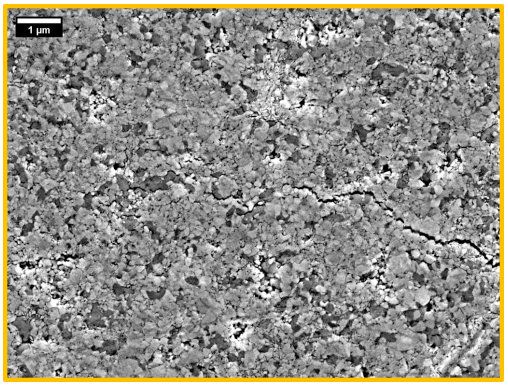
(a) Comparison between IR image and stitched SEM images of H2mm sample. Locations of (b) and (c) are shown by the red and pink boxes, respectively.



(b) Protruding cracked segment, where coating expanded during heating and cooled in a different configuration. Smaller cracks can be seen to the left.

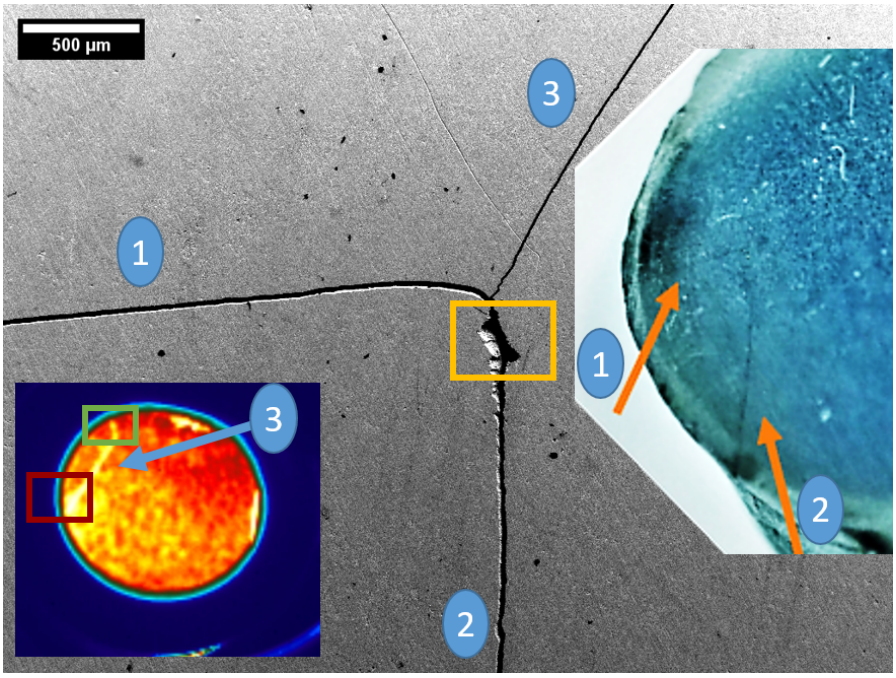


(c) SEM image highlighting the size difference between cracks visible using IR imaging (bottom) and smaller cracks that were unresolvable (top).

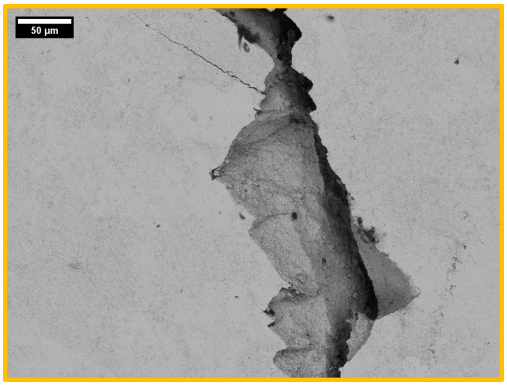


(d) High magnification image of the top crack in Figure 5.21 (c), shown by the yellow box. The crack propagated between between W grains.

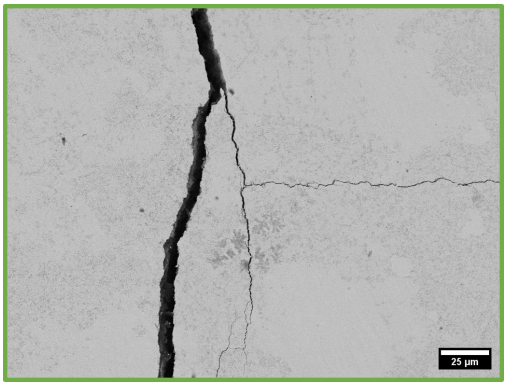
Figure 5.21: Comparison between IR and SEM images of H2mm sample surface.



(a) Cracks seen in IR and optical photograph, inset and annotated for clarity. Locations of (b) and (c) are shown by the yellow and green boxes, respectively.



(b) Large fragment of surface that had fallen out of crack shown in Figure 5.22 (a).



(c) Large crack located near the edge of the sample, shown in the inset in Figure 5.22 (a).

Figure 5.22: SEM images of the surface of the H4mm sample, shown in Figures 5.19 (c) & 5.20 (c).

In W2mm samples no cracks were seen anywhere on the surface in the SEM.

The F2mm sample was not put in the SEM, as the coating delaminated upon removal of the vacuum. Figure 5.23 shows an image of it. No cracks can be seen in the sample because it cracked (and failed) horizontally rather than vertically. Cui et al. experienced similar problems and were unable to produce W coatings on flat substrates without immediate delamination following manufacture [74].

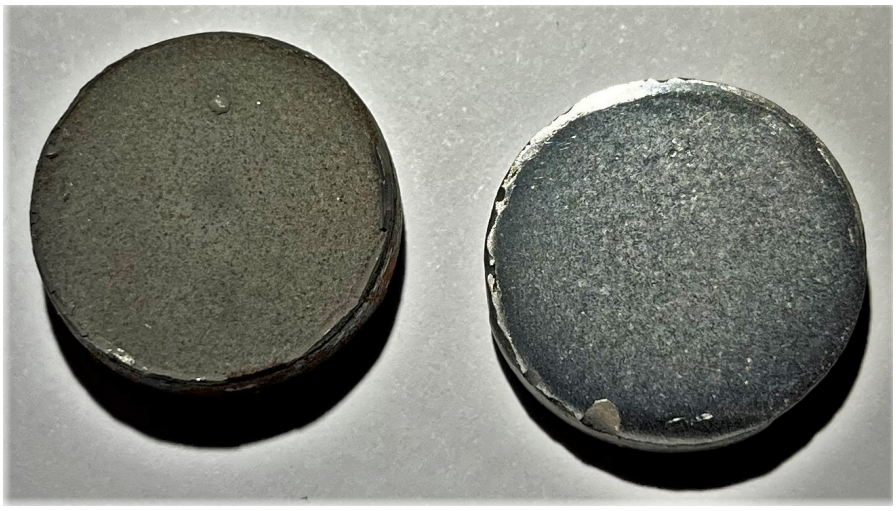


Figure 5.23: Photograph of the two halves of the F2mm sample following testing in HIVE. On the left side is the steel substrate, on the right side is the delaminated W coating. No cracks can be seen on the surface of the W.

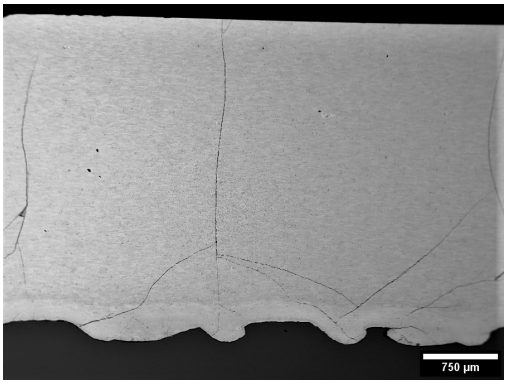
Cross-sectional examination of cracking

Figure 5.24 shows SEM images of cross-sections of the three types of sample that did not catastrophically fail in HIVE: H2mm (a), W2mm (b) and H4mm (c–d).

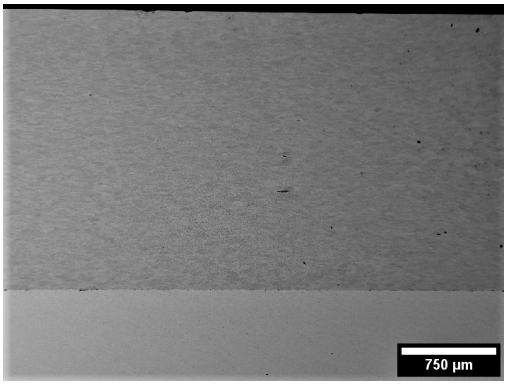
Regular vertical cracks formed throughout the H2mm sample shown in Figure 5.24 (a). Cracking originated from the textured substrate, as predicted in Chapter 3. Several cracks were seen and all were relatively thin. This was similar to the cracking observed by Cui et al. prior to testing [74], however no cross-sectional microscopy was performed following testing.

Figure 5.24 (b) shows that the W2mm sample did not crack. This was as expected as there was no difference in thermal expansion coefficient between substrate and coating, so there were no residual stresses or mismatch strains.

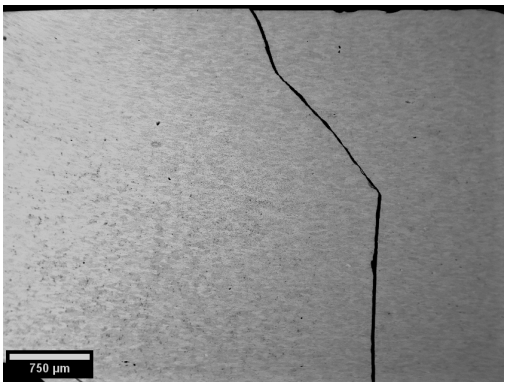
Figures 5.24 (c–d) show a thick vertical crack that has propagated from the textured substrate to the surface of the W coating. Cracking at the edge of the sample, which were seen on the left side of Figure 5.24 (d), followed the stress and strain profiles modelled at the end of the bimetallic beam (shown in Figures 4.8–4.9). The vertical crack was thicker than the cracks seen in the H2mm sample in Figure 5.24 (a). This again implies that the thicker W coating had higher residual stresses which meant that wider cracks formed, resulting in fewer cracks occurring to relieve the thermal strain mismatch between the steel substrate and W coating. This corroborates the results of the comparisons made between the observed surface cracking in Figures 5.21–5.22.



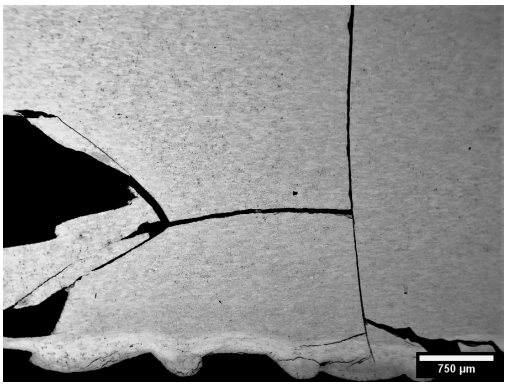
(a) H2mm sample with regular cracks.



(b) W2mm sample with no cracks.



(c) Top of H4mm coating with one large crack.



(d) Bottom of H4mm coating with cracking at interface and edge.

Figure 5.24: SEM BSE images of (a) 2 mm coating on hatched steel, (b) 2 mm coating on flat W and (c–d) 4 mm coating on hatched steel.

5.3.3 Thermal Cycling: UPP

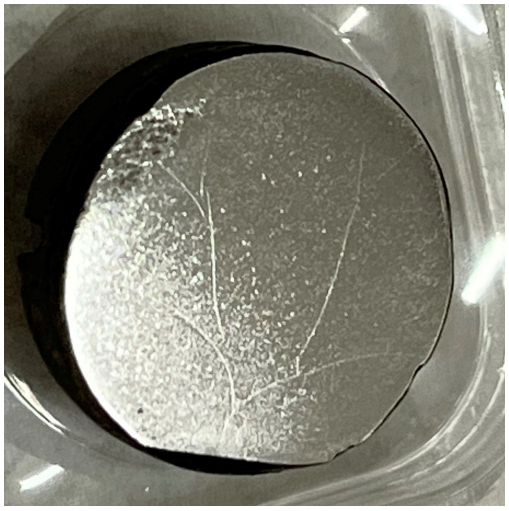
Figure 5.25 shows photographs of surfaces of the four samples prior to testing. Figure 5.25 (b) shows that the H2mm sample already had some surface cracking following manufacture. In Figure 5.25 (a) a small amount surface scratching was visible along with a failed section of the coating, where the EDM drill for the thermocouple hole was placed too close to the surface.

In-situ analysis during thermal cycling

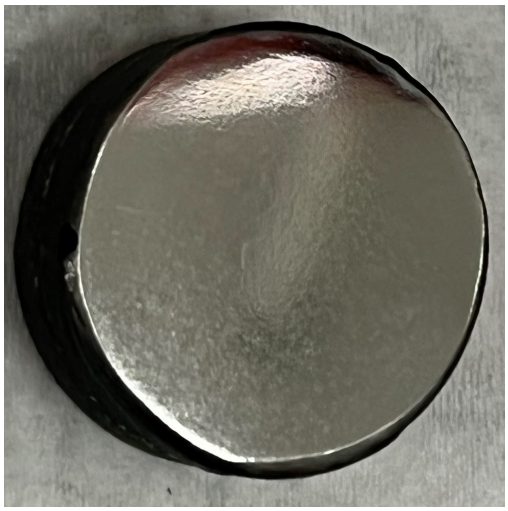
Figures 5.26 (a–d) show the temperature profiles from the surface thermocouple for each sample during testing. Figure 5.27 (a) shows a frame from the infrared data for the H2mm sample (at the highest point in a thermal cycle pulse) with a green ellipse denoting the region of interest (sample surface that was visible to the IR camera). Figure 5.27 (b) shows the corresponding average and maximum temperatures for the region of interest shown by the green circle in Figure 5.27 (a) for the duration of the IR recording. Due to the large quantity of data stored in an IR file, several IR files were required to capture and store all of each test. All IR data was set to a material emissivity of 0.15 for each sample. The maximum temperature for the H2mm sample was particularly high in comparison to the other samples, which consequently raised the average temperature as well. A small surface region corresponding to the maximum temperature was damaged by the plasma because the thermocouple hole was directly underneath it. The remaining



(a) 2 mm thick W coating on a flat steel substrate.



(b) 2 mm thick W coating on a hatched steel substrate.



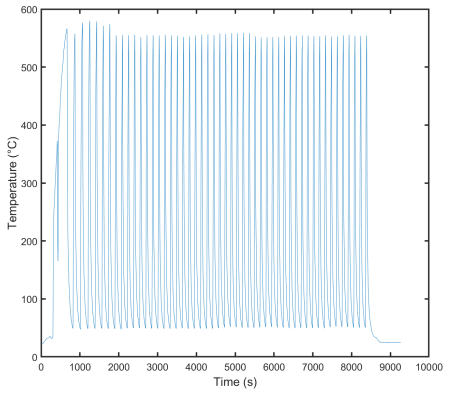
(c) 4 mm thick W coating on a flat steel substrate.



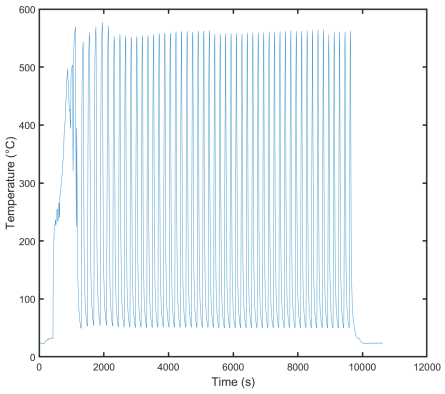
(d) 2 mm thick W coating on a flat W substrate.

Figure 5.25: Photographs of samples prior to UPP testing.

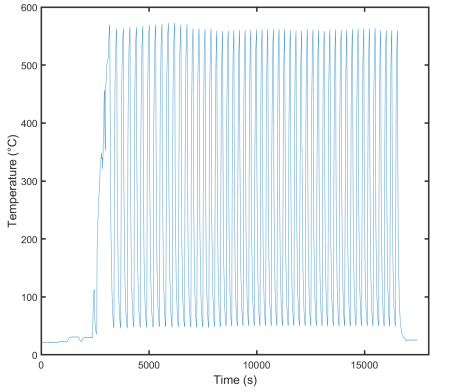
W at the surface in that spot was too thin to be able effectively to transfer heat to the rest of the sample, which was why the hot spot occurred. It was likely that the damage at this point also caused a change in the emissivity of material in that area.



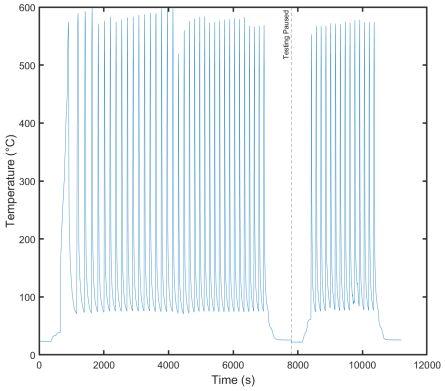
(a) Thermocouple temperature profile for H2mm sample.



(b) Thermocouple temperature profile for H4mm sample.

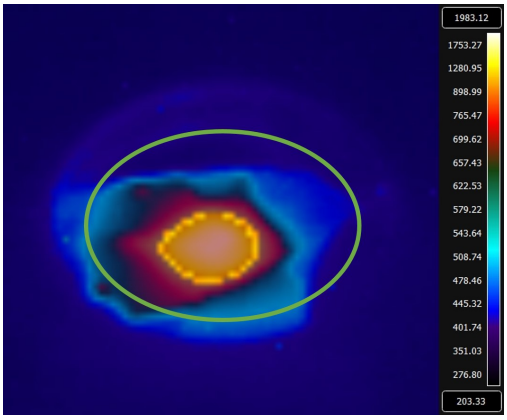


(c) Thermocouple temperature profile for W2mm sample.

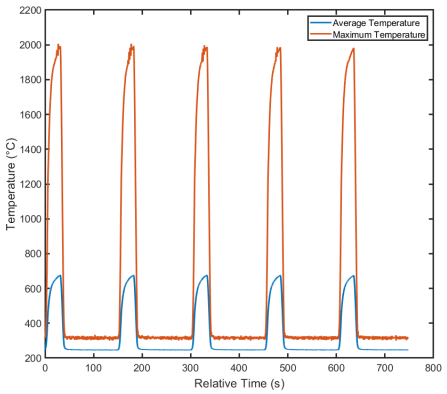


(d) Thermocouple temperature profile for F2mm sample.

Figure 5.26: Thermocouple data for each sample.



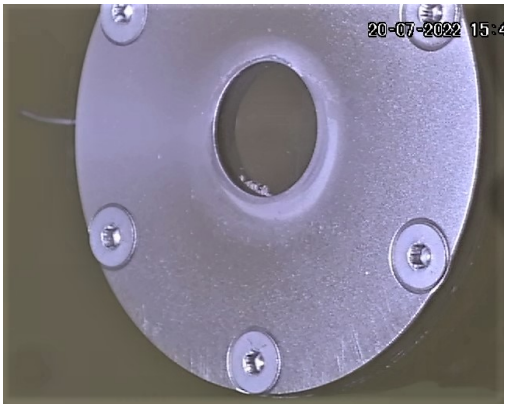
(a) Infrared image of 2 mm thick W coating on a hatched steel substrate.



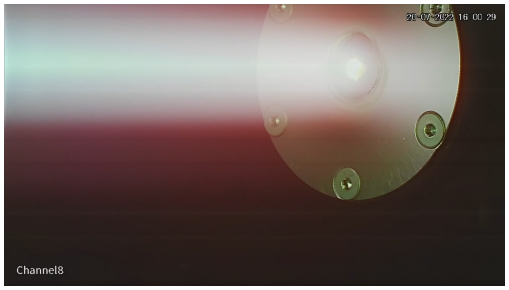
(b) IR camera temperature data taken from region of interest shown by green circle in Figure 5.27 (a).

Figure 5.27: IR data for the H2mm sample.

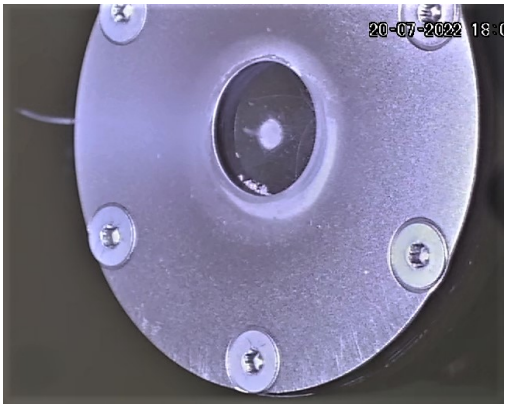
Figure 5.28 shows three photographs taken in-situ in UPP: before, during and after thermal cycling of the H2mm sample. Video footage taken of the H2mm sample during cycling shows the damage spot seen in Figure 5.28 (c) appearing to be 'burnt out' (with a large blue glare) initially in the first two cycles before settling to a bright yellow spot as seen in Figure 5.28 (b). This spot was the same surface region observed in seen in Figure 5.27 (a). Figure 5.28 (d) is a QR code linked to a video hosted on YouTube which shows a single pulse from the F2mm testing, with synchronised optical in-situ videos and IR data.



(a) H2mm sample prior to testing in UPP.



(b) H2mm sample during testing in UPP.

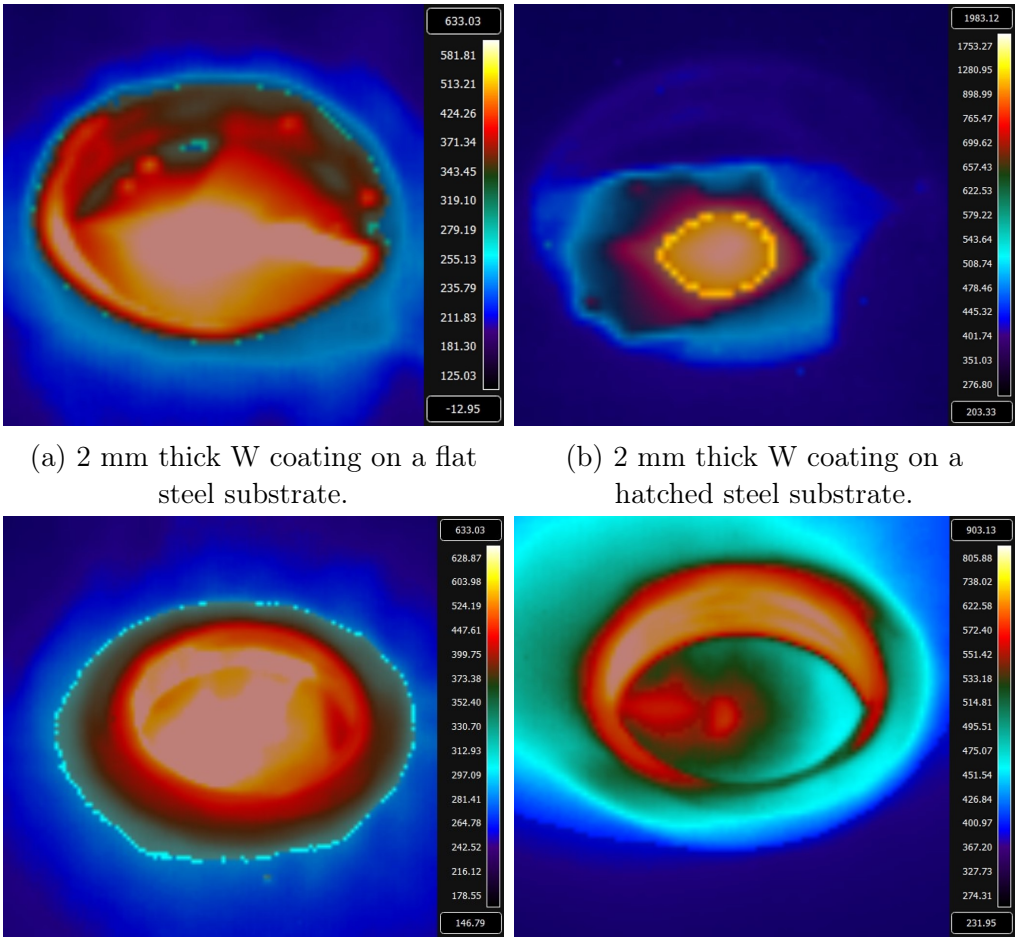


(c) H2mm sample following testing in UPP.

(d) QR code linking to a video hosted on YouTube of the F2mm sample during testing in UPP. (*https://youtu.be/2LcWIfSKDbU*)

Figure 5.28: Photos of the H2mm sample taken in-situ at various points during UPP steady-state thermal cycling testing and a QR code linking to a video that shows one pulse from the thermal cycling of the F2mm sample.

Figure 5.29 shows frames from the IR data that corresponded with the highest temperature measured during a thermal cycle pulse for each sample. Hot spots can be seen in the F2mm (a), H2mm (b) and W2mm (d) samples in line with the thermocouple hole (and failed thermocouple hole for the F2mm sample). These hot spots occurred because there was less W between the thermocouple hole and the surface of the coating to locally distribute the incident heat flux from the plasma. Because the H4mm sample had a thicker coating, it was easier to drill the thermocouple hole without getting so close to the coating surface. Similar localised heating effects were observed by Ganesh et al. during high heat flux testing, just before complete failure of the functionally-graded (via SPS) joint to the W tile.



(a) 2 mm thick W coating on a flat steel substrate.

(b) 2 mm thick W coating on a hatched steel substrate.

(c) 4 mm thick W coating on a flat steel substrate.

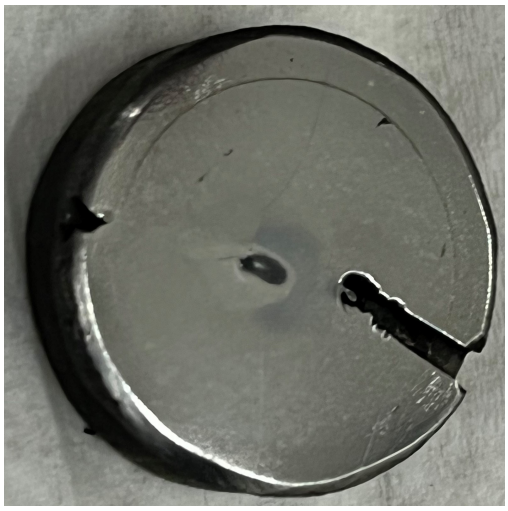
(d) 2 mm thick W coating on a flat W substrate.

Figure 5.29: Frames from infrared data of different samples taken at the moment of maximum temperature at the peak of the cyclic heat pulse in UPP testing.

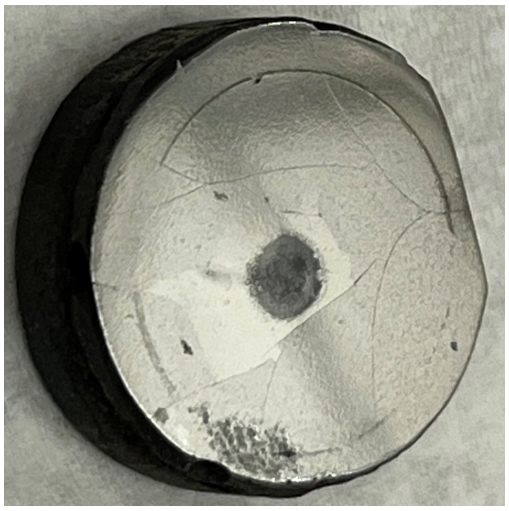
Surface crack and plasma damage analysis

Figure 5.30 shows photographs of the surface of the four samples following testing. Plasma damage spots were seen in the F2mm and H2mm samples shown in Figures 5.30 (a–b) respectively. Surface cracking was also observed in all steel substrate samples, with fewer cracks seen in the H4mm sample. The H2mm sample cracked in the centre of the sample, in addition to the cracks seen prior to testing. On every sample, a ring was seen near the sample edge where it was mounted; however there were no obvious signs of plasma damage on these samples other than at the specific areas previously mentioned.

Figure 5.31 shows SEM images taken of the surfaces of the four samples after testing. The F2mm sample had cracks distributed evenly across the sample surface and through the plasma damage spot seen in Figure 5.31 (a). As observed in Figure 5.31 (b), it appears the coating material became fibrous in this region; it was postulated that this was due to a combination of the pre-existing structure of the powder (following manufacture in the FAST) and the retained O and C that was outgassed when that area of the W coating experienced the high localised temperatures (due to the positioning of the thermocouple hole directly beneath the surface). These high temperatures could have also caused W oxides to sublime. Upon removal from the SEM, the W coating of the F2mm sample delaminated at the interface from the steel.



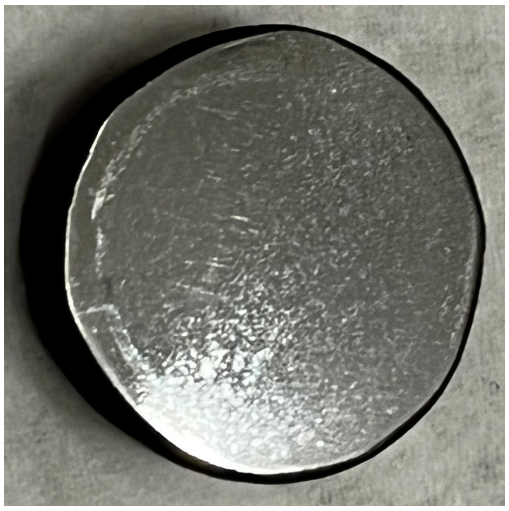
(a) 2 mm thick W coating on a flat steel substrate.



(b) 2 mm thick W coating on a hatched steel substrate.



(c) 4 mm thick W coating on a flat steel substrate.



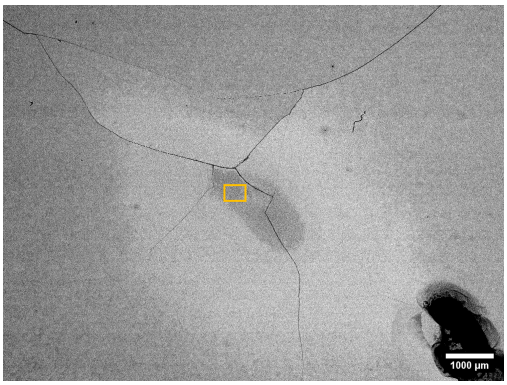
(d) 2 mm thick W coating on a flat W substrate.

Figure 5.30: Photographs of samples following UPP testing.

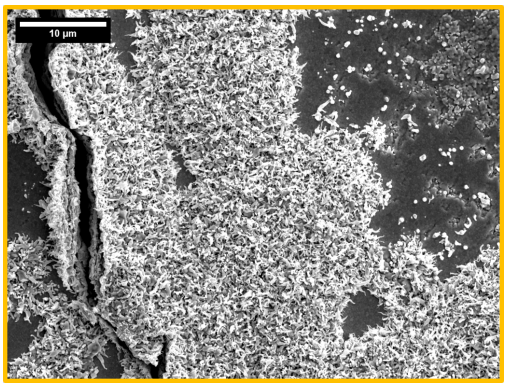
In comparison, the H2mm sample had significantly more cracks, although it was noted that some of these were already apparent following sample manufacture. Figure 5.31 (c) highlights finer cracks that were not visible in the photographs. Figure 5.31 (d) shows the surface modifications that occurred at the plasma-damaged spot. Blisters (some of which were cracked) were covered and surrounded with tendrils similar to the F2mm sample in Figure 5.31 (b).

The H4mm sample had fewer surface cracks than both 2 mm coatings on steel substrates. In a similar manner to the samples tested in HIVE, cracks in the H4mm sample were thicker than the cracks observed in the H2mm sample. Figure 5.31 (f) shows areas at the bottom and top of the image where the coating had failed and chipped away.

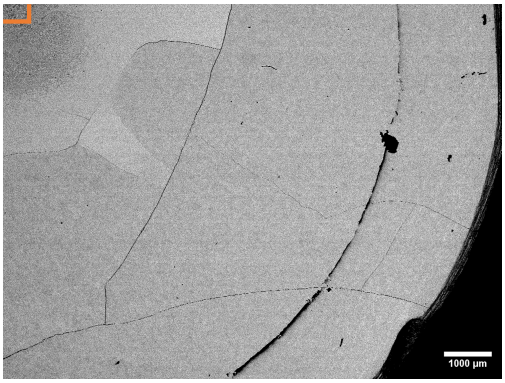
Figures 5.31 (g–h) show that there was no surface cracking in the W2mm sample.



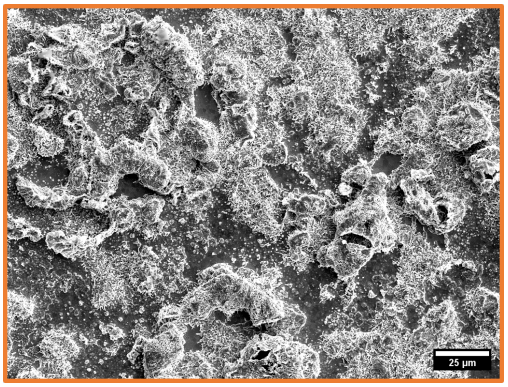
(a) F2mm: BSE image shows surface cracks at centre of coating.



(b) F2mm: SE image shows cracks near plasma damage.

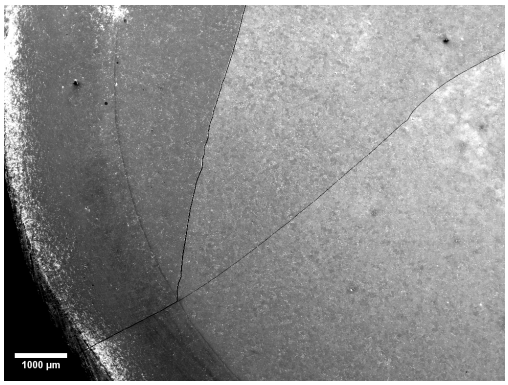


(c) H2mm: BSE image shows surface cracking.

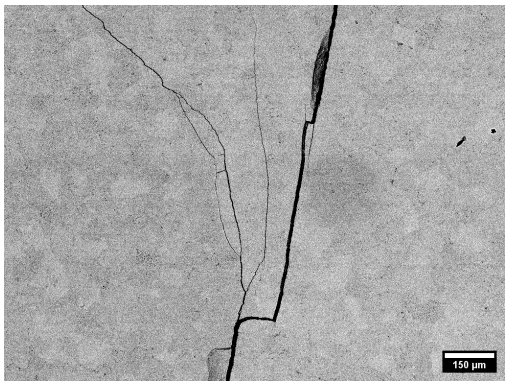


(d) H2mm: SE image shows plasma damage tendrils.

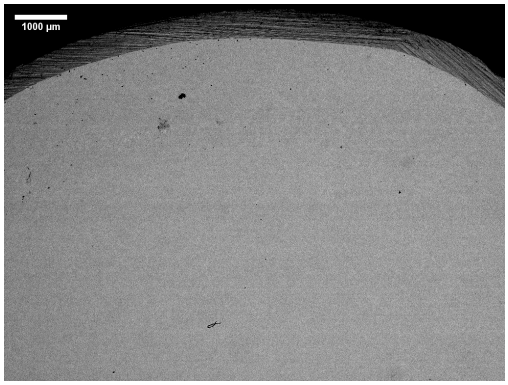
Figure 5.31: SEM images of the surface of each samples: 2 mm coating on flat steel (a–b), 2 mm coating on hatched steel (c–d), 4 mm coating on hatched steel (e–f) and 2 mm coating on flat W (g–h).



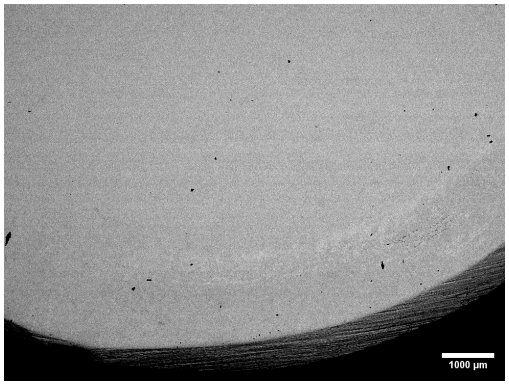
(e) H4mm: SE image shows surface cracks near coating edge.



(f) H4mm: BSE image shows thick cracks with chipped damage.



(g) W2mm: BSE image shows no damage on coating surface.



(h) W2mm: BSE image shows no damage on coating surface.

Figure 5.31: SEM images of the surface of each samples: 2 mm coating on flat steel (a–b), 2 mm coating on hatched steel (c–d), 4 mm coating on hatched steel (e–f) and 2 mm coating on flat W (g–h).

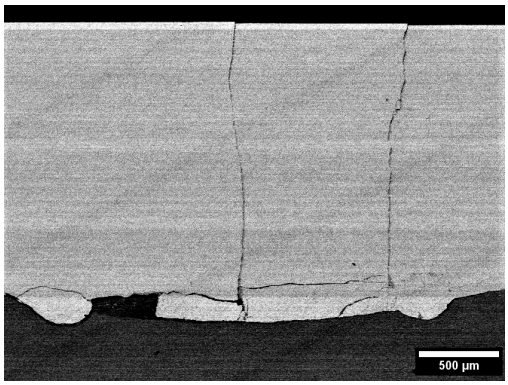
Cross-sectional examination of cracking and plasma damage

Figure 5.32 shows cross-sectional SEM images taken of the H2mm, W2mm and H4mm samples. Vertical cracking was seen in both steel substrate samples, in a similar way to the samples tested in HIVE. Vertical displacements were seen at the surface near cracks, shown in Figures 5.32 (a) & (f), which highlight the nature of the cracks forming to relieve the thermal strain within the coating.

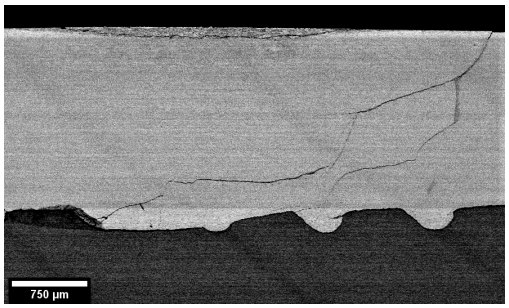
Figures 5.32 (b–d) illustrate the plasma damage at the surface of the coating. The plasma damage spot was visible by eye. Figure 5.32 (c) shows cracking occurred towards the boundary between plasma-damaged and non-plasma-damaged material. This crack potentially formed following the large temperature difference within the W (as the surface W was thermally isolated due to the the thermocouple hole) which led to significant thermal strain. Figure 5.32 (d) shows a cross section of a blister at the surface. The rest of the surface also had a brighter, $\sim$2 µm thick region, which indicated that the surface was composed of densified and purer W. Voids were seen within the blister, along with some powder particles that were shielded from the incident plasma by a denser outer layer. It was noticeable that this layer did not follow the line under the blister, which indicates that they formed at similar times during testing. Powder particles appear to increase in size towards the surface, likely due to an imposed temperature gradient which permitted more particle growth (akin to Ostwald ripening).

The H4mm sample had fewer cracks, but more significant damage than the H2mm sample, which was considered in keeping with trends previously observed. Horizontal cracking was seen on the right side of Figure 5.32 (e) from failure at the edge of the coating, similar to the cracking that was seen in Figure 5.24 (d).

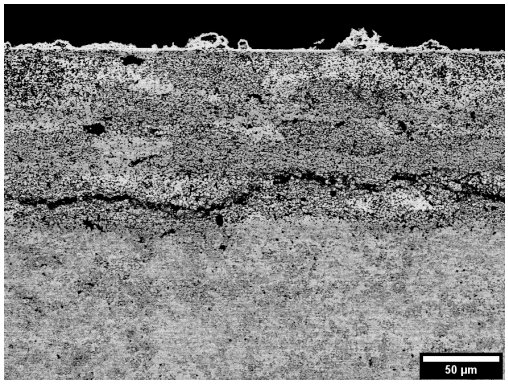
As with the surface SEM images, no cracks were seen in the W2mm sample in Figure 5.32 (h). This was expected as there was no difference in thermal expansion coefficients between the coating and the substrate, as previously observed.



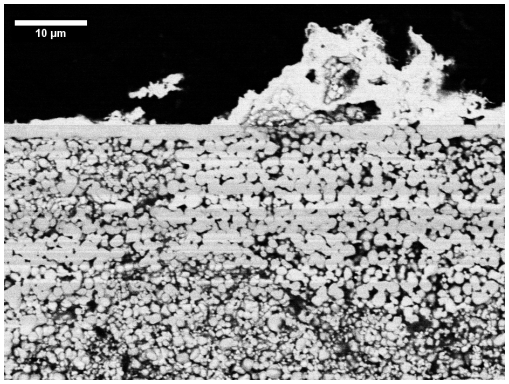
(a) H2mm: BSE image shows regular vertical cracking.



(b) H2mm: BSE image shows plasma damaged spot.

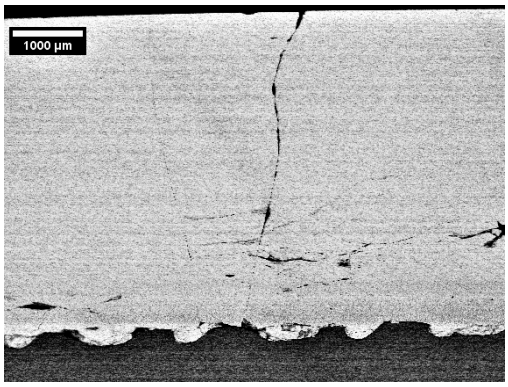


(c) H2mm: BSE image shows plasma damaged surface.

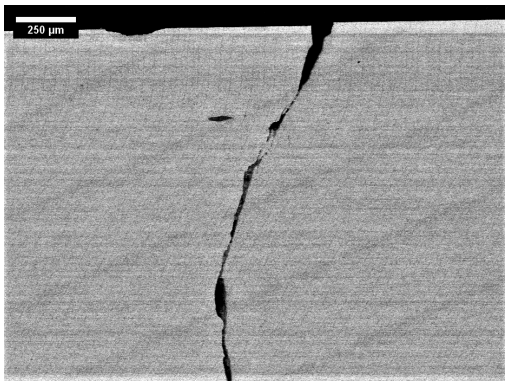


(d) H2mm: BSE image shows blistering at surface of plasma damage.

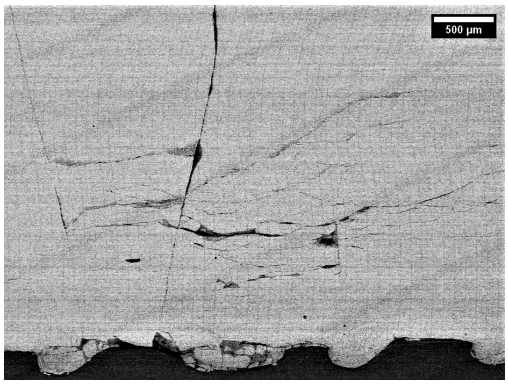
Figure 5.32: SEM images of cross-sections of three different samples: 2 mm coating on hatched steel (a–d), 4 mm coating on hatched steel (e–g) and 2mm coating on flat W (h).



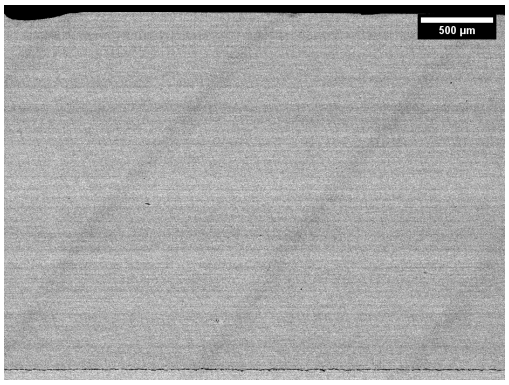
(e) H4mm: BSE image shows vertical cracking.



(f) H4mm: BSE image shows vertical cracking at surface.



(g) H4mm: BSE image shows cracking at interface.



(h) W2mm: BSE image shows no cracking.

Figure 5.32: SEM images of cross-sections of three different samples: 2 mm coating on hatched steel (a–d), 4 mm coating on hatched steel (e–g) and 2mm coating on flat W (h).

5.4 Summary

Understanding the behaviour of W coatings under high thermal loads is an issue of paramount importance for deployment in a fusion environment. In this work, three forms of thermal loading were applied to a variety of coatings: thermal ageing, thermal cycling via induction, and thermal cycling via plasma exposure.

Following manufacture, FAST samples contained high quantities of impurity C (8.8 at%) and O (17.4 at%). This was significantly higher than equivalent VPS values, 0.22 and 1.75 at% respectively. These impurities had a large knock-on effect when samples were thermally aged as cracking and failure occurred in regions with high levels of impurity.

Thermal ageing analysis of samples allowed values for the activation energy for intermetallic phase growth and maximum growth rate coefficient to be determined as 40 $kJ \cdot mol^{-1}$ and 5.3×10^{-12} $m^2 \cdot s^{-1}$ respectively. Both these values were smaller than those calculated from data gathered by Reisner et al. [93]. However, the growth rate coefficients found in the present work were much higher than those observed by Reisner because of the significantly lower activation energy. This is most likely due to the addition of smaller species such as C and O which diffuse much faster than Fe or W. EDX and XRD data confirmed the presence of mixed oxides: $FeCr_2O_4$, Fe_3O_4 and $Fe(WO_4)$ in aged FAST samples and W_2C, Cr_3C_2 and WCr_2O_6 in VPS samples. The location of these impurities also depended on manufacture method, as impurities grew between powder 'splats' in VPS samples but surrounded the fine W powder particles in the FAST.

Several similarities were found between thermal cycling tests. In both processes, flat steel substrate samples (F2mm) failed at the interface. Delamination took longer for the UPP sample, as it was clamped during testing, whereas the mounting system in HIVE allowed for catastrophic failure to occur. In steel samples where the interface did not fail (H2mm and H4mm), vertical cracking was prominent throughout the sample and often matched closely with predicted crack formations from FEM in Chapter 3. Thicker (H4mm) coatings acted as better thermal armour, as a larger difference between coating surface and base temperature was observed. There were also fewer, but larger, cracks in comparison to the H2mm samples. Plasma damage and surface modification was significant in localised areas where the surface temperature increased due to thermal isolation resulting from the positioning of the thermocouple hole. This result was particularly interesting, as the plasma used was not particularly aggressive, and wall materials will ideally need to withstand large amounts of heat in loss of confinement scenarios (such as ELMs). The following chapter investigates this further, using a more aggressive plasma. W coatings on W substrates performed well, with no cracks occurring. This was anticipated as there was no change in coefficient of thermal expansion between the coating and substrate material.

6 Repair of Plasma Facing Components

6.1 Introduction

The results from the Upgraded Pilot-PSI (UPP) steady-state thermal cycling in Chapter 5 raised concerns about the quality of the W coatings and the likelihood of survival under plasma irradiation. However, this was not the case for all tested samples and therefore warranted further investigation. In order to avoid localised, sample-specific plasma damage the use of thermocouples should be avoided.

Chapter 2 showed that transient thermal cycling was an important part of fusion-relevant testing and was particularly useful when combined with a base steady-state heat load. Magnum-PSI is a DC cascaded arc linear plasma device that has the capability to impose transient cycling during plasma exposure in two different ways: a high-powered pulsed Neodymium:Yttrium Aluminium Garnet (Nd:YAG) laser that applies an additional heat flux, or a capacitor bank which increases the heat flux of the plasma by discharging pulses into the plasma generator system. One advantage of the pulsed laser over the capacitor bank system is that only a

targeted section of the sample is exposed to the transient heat loads rather than the entire sample, which facilitates comparison with the rest of the sample that is not exposed to the laser. Table 6.1 details parameters used in three transient cycling tests to highlight the range of achievable temperature regimes. Resultant micrographs for the three tests are shown in Chapter 2.

Figure	Plasma Species	Transient System Type	Base Temperature (°C)	Number of Pulses	Transient Temperature (°C)
Fig 2.20 (g)	H_2	Capacitor Bank	∼1500	5000	50
Fig 2.21	Ar	Nd:YAG laser	∼300	10000	280
Fig 2.22 (a)	H_2	Nd:YAG laser	∼750	65000	690

Table 6.1: Parameters used for transient experiments shown in Chapter 2.

For commercial operation, W coatings are required to be at least 5 mm thick [63]. However, results from Chapter 5 indicated that cracking, due to the difference between the coefficients of thermal expansion (CTE) of W and the structural materials, was more severe for thicker coatings. If a method of in-situ W coating repair can be developed, it may be more economically viable to stop more regularly, but for less time than for tile replacement, to 'top up' the thickness of the coating as it is gradually eroded during operation. Various in-situ robotic solutions are already being investigated for remote inspection and maintenance, particularly for aerospace applications. The REINER[1] and FLARE[2] projects developed by the University of Nottingham utilise snake-arm robots with combined functionality of

[1] **Re**mote **In**spection and **E**ngine **R**epair

[2] **Fl**ame Spray **A**dder for In-situ Patch **R**epair of Aero-**E**ngine Combustors

inspection and repair for removal of foreign debris (boreblending) embedded in compressor blades and application of a ceramic coating to patch cracks within the combustor respectively [169, 170]. Facilities such as RACE[3] are being formed to develop remote maintenance for nuclear fusion environments. RACE leads the EUROfusion DEMO remote maintenance programme using experience garnered from the remote handling of JET [171].

Currently, only two papers have explored whether W coatings can be repaired. Diez et al. investigated the process of removing W from CuCrZr using different methods to produce a clean surface on which a new W coating could be deposited. Unfortunately, no deposition study accompanied this research [172]. Li et al. studied laser repair of various W faults likely to be observed during operation in a fusion reactor. Blisters, fuzz and cracks were all healed via laser remelting which often produced microstructures that resembled fully recrystallised W. Blistering and nanostructured fuzz appeared to be almost entirely healed following two rastered passes of the laser. Fatigue cracks (similar damage is shown in the micrographs listed in Table 6.1) were the most difficult to repair, with significant cracking still observed after three rounds of passes (though still a notable improvement on the original exposure damage) [173]. At present, no literature has postulated a practical repair solution to erosion damage of W PFCs.

This chapter explores the viability of a W repair coating for PFCs and whether any residual damage in the original coating affects the lifetime performance of the component following repair.

[3] **R**emote **A**pplications in **C**hallenging **E**nvironments

6.2 Methodology

Three stages of the plasma-facing component (PFC) life cycle were simulated:

1. Initial damage: samples were tested in UPP with an Ar plasma and a high power laser to simulate steady-state erosion and off-normal events (such as ELMs[4]), respectively.

2. Repair of samples: HIVE[5]- (from Chapter 5) and UPP- (from the Ar plasma and laser) damaged samples were repaired in the FAST[6] by adding a fresh $\sim$1 mm thick layer of W on top of the damaged surface.

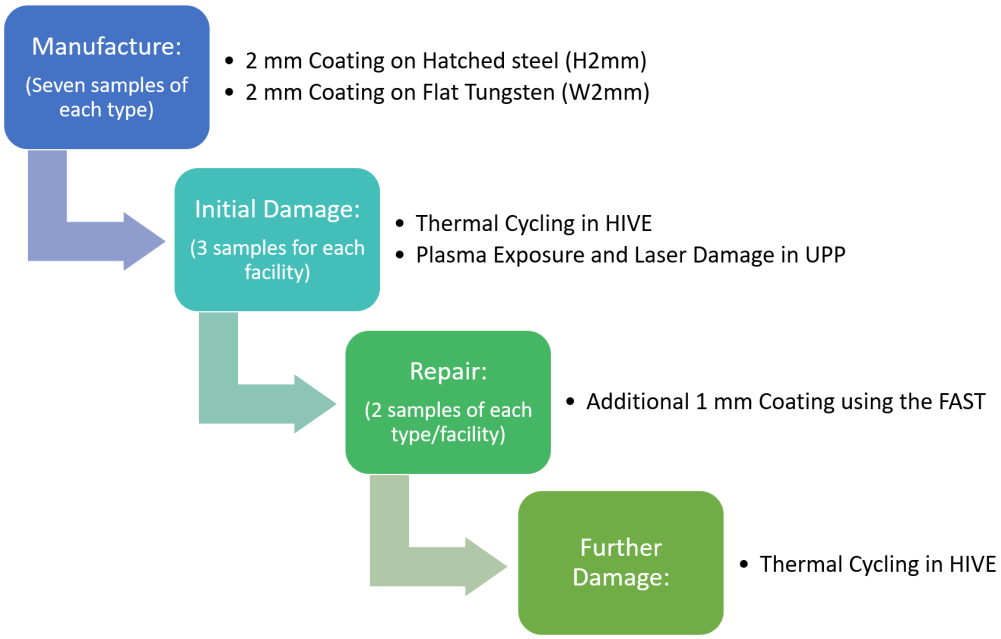
3. Further damage: repaired samples were tested in HIVE again, under the same conditions, to investigate whether pre-existing damage would propagate through to and/or create new defects in the new layer.

All coated samples studied in this chapter were made using the FAST process described in Chapter 3. Samples comprised 2 mm thick coatings on either hatched steel (H2mm) or flat W (W2mm) substrates (20 mm diameter, 5 mm thick). Seven identical samples of each type were produced, so that characterisation could be performed at each stage shown in Figure 6.1. One W substrate, supplied by Goodfellow (99.95% purity), was also used as a 5 mm reference sample for the plasma and laser exposure in UPP. The W substrates were rolled, with the short axis of the grains oriented perpendicularly to the sample surface. Rolling temperature was not provided. Two 2 mm W coatings on hatched steel substrate (H2mm) samples

[4] **E**dge **L**ocalised **M**ode
[5] **H**eating by **I**nduction to **V**erify **E**xtremes
[6] **F**ield-**A**ssisted **Sintering** **T**echnique

were produced and set aside as undamaged reference samples for assessment of the repair process. Both were submitted to the repair process in the FAST; one was characterised without further exposure and the other was subjected to the second round of testing in HIVE.

The experimental methods for as-sintered samples and samples initially damaged in HIVE were reported in Section 5.2.



(a) Flow chart of sample life cycle.

Figure 6.1: Flow chart and table detailing sample life cycles.

Sample/Process	H2mm	W2mm
As-Sintered (AS)	✓	✓
Initial Damage: HIVE (H)	✓	✓
Initial Damage: UPP (U)	✓	✓
Initial Damage: Reference W sample	–	Substrate only
Repair: HIVE-damaged (HR)	✓	✓
Repair: UPP-damaged (UR)	✓	✓
Repair: Reference (RR)	✓	–
Further Damage: HIVE-damaged (HRH)	✓	✓
Further Damage: UPP-damaged (URH)	✓	✓
Further Damage: Reference (RRH)	✓	–

(b) Table showing the process for each sample characterised.

Figure 6.1: Flow chart and table detailing sample life cycles.

6.2.1 Initial Damage: UPP

Samples were mechanically polished with SiC grinding papers up to 2500 grit before further polishing with 6, 3 and 1 µm diamond suspensions on NLH (Kemet), Floc and Nap (Struers) polishing pads respectively. Samples were cleaned with ethanol and isopropanol. Samples were polished to ensure a consistent surface finish across all tested samples.

Plasma exposure was performed in UPP using the same water-cooled mounting system, pyrometer and infrared camera set-up as described in Section 5.2.4. Thermocouples were not used, as the temperature was expected to exceed 600 °C, and localised heating due to the thermocouple hole (as seen in Section 5.3.3) was to be avoided. Samples were exposed to an Ar plasma for 30 mins; Ar was used (rather than H_2, as in the thermal cycling) as Ar ions are heavier and therefore produce higher erosion rates. The plasma exposure parameters are listed in Table 6.2.

Plasma Parameter	Value
Ar Flow Rate (SLM)	1.5
Plasma Current (A)	180
Magnetic Field (T)	0.16
Bias Voltage (V)	-40
Electron Temperature (eV)	1.21 ± 0.10
Electron Number Density (10^{20} m^{-3})	1.87 ± 0.09
Electron Number Density FWHM (mm)	15.3

Table 6.2: Plasma parameters for transient (laser) thermal cycled experiments in UPP.

To simulate the increased heat flux of plasma disruptions, a Nd:YAG laser (model FLS 352-302, made by LASAG AG) was fired at 400 V at a rate of 20 Hz for 25,000 pulses. The number of pulses was comparative to the samples damaged under similar testing conditions 10,000–65,000 pulses, shown in Figures 2.21 & 2.22 (a), by Li & Morgan [124, 125] whilst ensuring identical testing for each sample in the time available at the UPP facility. In order to ensure that all experiements could be completed on schedule, the laser was pulsed at a rate of 20 Hz. The highest

voltage achievable with this frequency was 400 V which produced a power of 1.6 kW. The total transmission of the optical path in Magnum-PSI was previously measured to be 75 ± 1% [174] – it was assumed that optical transmission in UPP was similar.

Before the 'repair' stage, SEM and optical microscope images were taken of the samples' surfaces. SEM images were taken using a ZEISS Merlin SEM with energy dispersive X-ray (EDX) capabilities (Oxford Instruments XMax 150 mm^2 detector) in both secondary electron (SE) and backscattered electron (BSE) modes. Optical microscope images were taken using a ZEISS AxioPhot.

One sample of each substrate and damage type (steel and W; HIVE and UPP, respectively) was not repaired, and was cross-sectioned using a Struers Accutom-100 cut-off machine and mounted in Phenolic Carbon Conductive Resin (Kemet) before being mechanically ground and polished to 1 µm using the grinding papers and diamond suspensions detailed above. Images of the cross-sections were taken in a ZEISS Merlin SEM and a ZEISS EVO with EDX capabilities (Oxford Instruments X-act) in both secondary electron (SE) and backscattered electron (BSE) modes.

6.2.2 Sample Repair

Prior to repair, the backs of UPP-damaged samples were engraved to mark the location of the laser damaged spot. Samples were placed in the graphite die for the FAST and approximately 5.5 g of W powder was placed on top, before using the same FAST procedure as described in Section 4.2.3 to achieve a repair coating thickness of ∼1 mm.

Two pristine sample were also produced to act as references; they were polished to 1 µm using the same method as before, then they were repaired in the same manner as the damaged samples.

Once repaired, samples were carefully grit-blasted clean and then re-engraved on the base of the sample to ensure the previous markings were still clear. Sample surfaces were again polished to 1 µm.

One sample of each substrate and damage type (steel and W; HIVE, UPP, and non-damaged reference, respectively) was not damaged further, but was cross-sectioned, prepared and imaged as described in Section 6.2.1. UPP-damaged samples were aligned for cross-sectioning to ensure they were cut through the laser spot (using the engraved mark).

6.2.3 Further Damage

Sample were subjected to further damage using the same set up and procedure as described in Section 5.2.3; 50 thermal cycles under vacuum between 300–800 °C.

Following testing in HIVE, sample surfaces were imaged before being cross-sectioned, prepared and imaged again as described in Section 6.2.1. As in Section 6.2.2, cross-sections were taken through the laser spot for UPP-damaged samples.

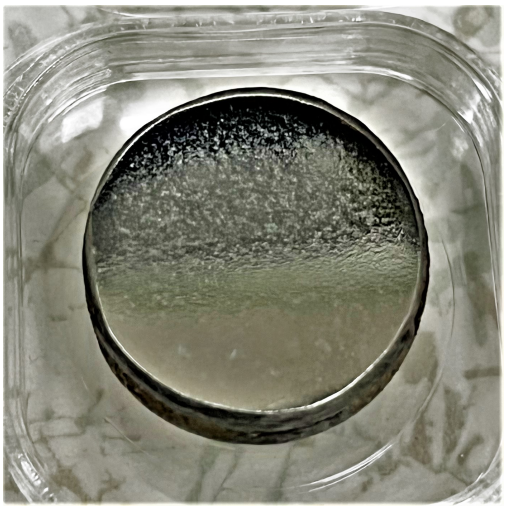
6.3 Results and Discussion

6.3.1 Initial Damage: UPP

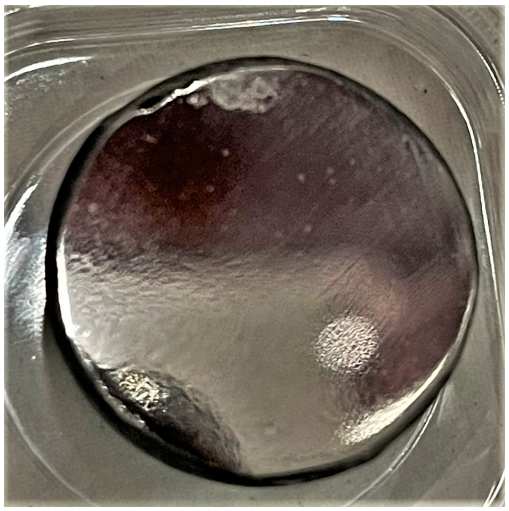
Figure 6.2 shows representative photographs taken of the surface of each type of sample prior to testing in UPP. No cracks were apparent and the characteristic 'speckle' effect from the grains (produced from powder agglomeration observed in Figure 4.4) was visible on each sample. Occasionally there were rough patches as seen in Figures 6.2 (b–c) due to manufacturing defects (commonly found near the sample edge) that were not easily removable during grinding and polishing without significantly altering the thickness of the coating.

In-situ analysis during thermal cycling

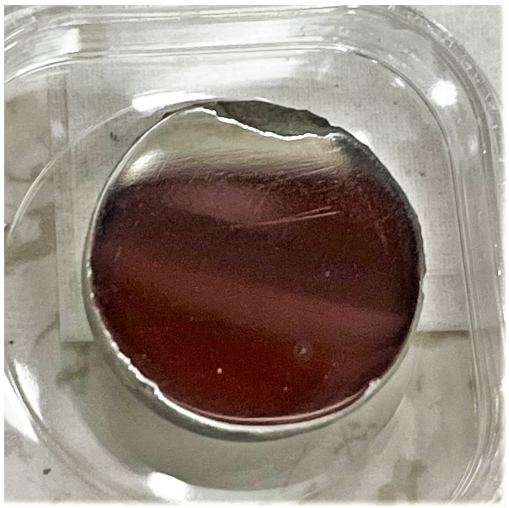
Figure 6.3 shows the recorded pyrometer data for each type of sample (H2mm, W2mm and reference W). Temperature, tolerance and pyrometer signal were all recorded and were plotted together; temperature in blue with tolerance as error bars, and signal in orange. Signal strength was the value of emissivity at a wavelength of 1550 nm (assuming clean optics and correct calibration). The point at which the laser pulsing began and ended was clearly visible, due to the change in pyrometer signal and the corresponding step change in temperature. Due to software limitations the laser pulses had to split it into two sets of 9999 pulses and a set of 5002 pulses (totalling 25,000 pulses).



(a) 2 mm thick W coating on a hatched steel substrate.



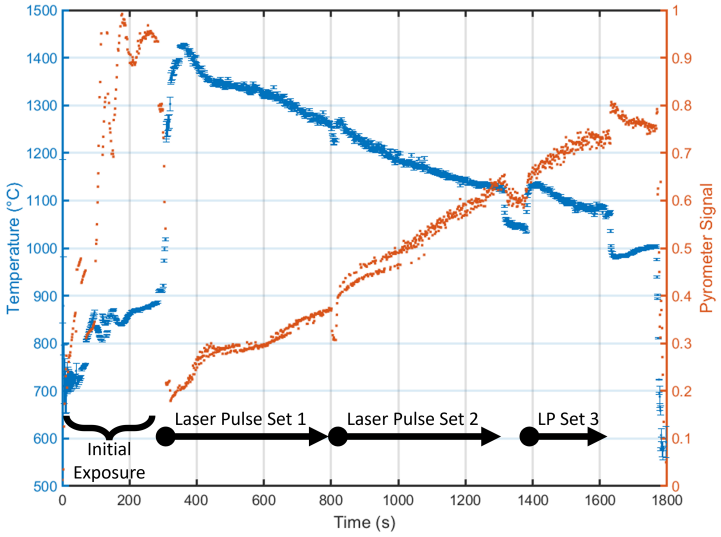
(b) 2 mm thick W coating on a flat W substrate.



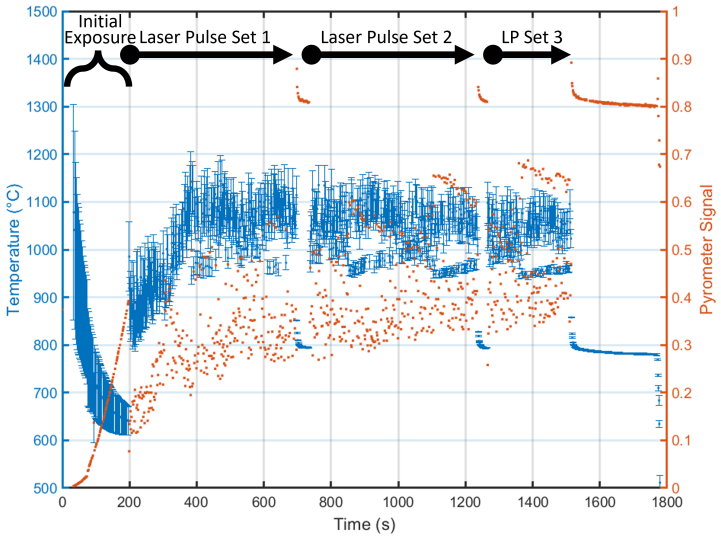
(c) Reference W sample.

Figure 6.2: Representative images of samples prior to testing in UPP.

Errors at the beginning of testing runs were high due to the poor signal strength, as the samples were polished so had low emissivity. The surfaces of the samples were identical prior to experimentation; however, both coated samples blackened significantly (due to impurity expulsion) when exposed to the plasma, causing the emissivity to rise. When the laser began to pulse, the additional light caused the surface to shine, which reduced emissivity, with the exception of the reference W, where surface modifications caused by the laser resulted in a slightly higher emissivity. As testing continued, the surface of the H2mm sample consistently deteriorated, both with surface roughening and cracking similar to that observed in HIVE (in Chapter 5), which resulted in a gradual increase in signal. The surface of the W2mm sample also roughened, which resulted in a slight increase in emissivity during testing, which appeared to reach a plateau. There was significantly more scatter in the W2mm signal (and therefore temperature measurement) due to the flashing of the laser on the sample surface. In comparison the flash of the laser on the sample surface was less for the H2mm sample, which meant that the signal (and resulting temperature) was less noisy. In the final set of laser pulses, the reference sample noticeably deteriorated (increased surface roughness) as the emissivity rose once again. Overall, the signal was particularly low for the reference sample because it was more dense (resulting in reduced surface roughening) and because the sample was thinner, meaning that heat dissipated into the water-cooled mount faster, resulting in a lower temperature closer to the minimum operating limit of the pyrometer.

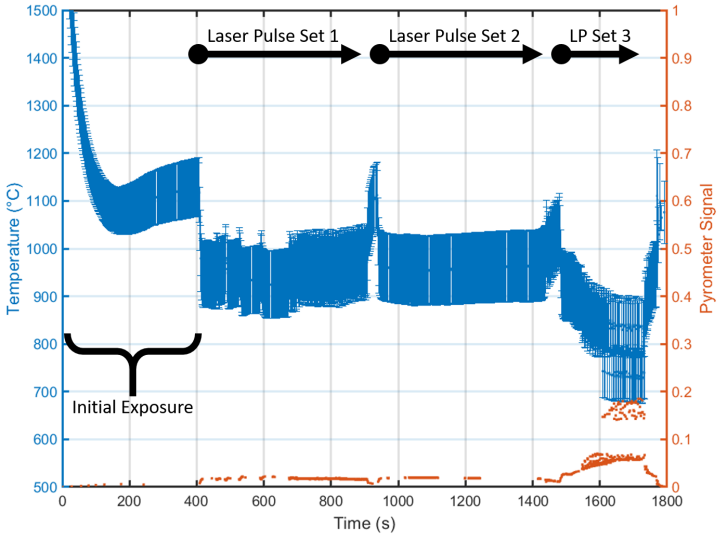


(a) 2 mm thick W coating on a hatched steel substrate.



(b) 2 mm thick W coating on a flat W substrate.

Figure 6.3: Representative pyrometer data of samples during testing in UPP.



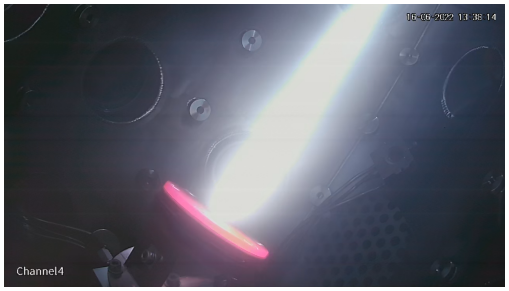
(c) Reference W sample.

Figure 6.3: Representative pyrometer data of samples during testing in UPP.

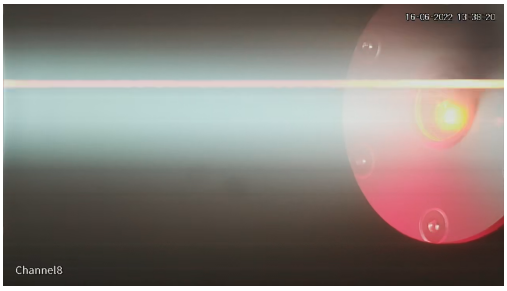
Figure 6.4 shows three images taken during testing. Figures 6.4 (a–b) show the front and side view of the sample and mounting set-up between the second and third sets of pulses. The laser spot was visible in the front view. The intense heat flux of the plasma caused the TZM clamping ring to become red hot, indicative of temperatures around 900 °C [175], as seen in Figure 6.4 (b). This aligned with the pyrometer data in Figure 6.3 (a) (the corresponding test to the images in Figure 6.4) before the laser pulses began (identical to the condition of the TZM clamping ring). Figure 6.4 (c) shows the front view during laser pulsing — it was apparent that the laser provided significant localised heating, which produced a 'hole' in the surface. The QR code links to a YouTube video of the start of the third set of pulses for this sample; this slow-motion video shows the front and side optical camera recordings alongside the IR camera recording and plotted IR data.



(a) Front view of H2mm sample between second and third sets of laser pulses.



(b) Side view of H2mm sample between second and third sets of laser pulses.

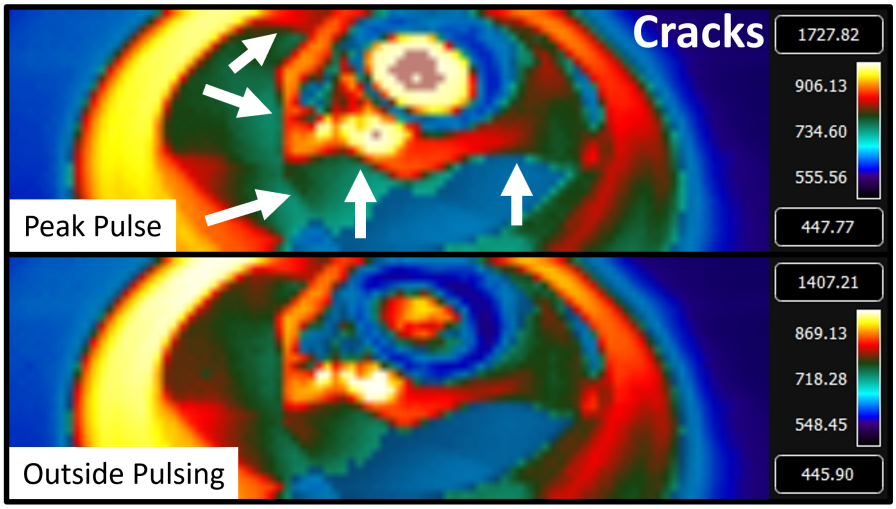


(c) Front view of H2mm sample during a laser pulse.

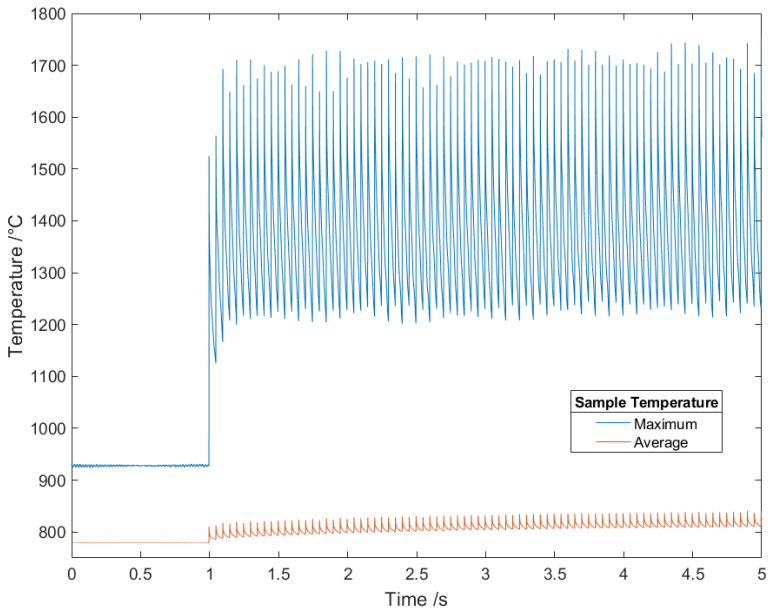
(d) QR code linking to a video hosted on YouTube of the H2mm sample during transient thermal cycling testing in UPP. (*https://youtu.be/3sbjh6bES34*)

Figure 6.4: Representative in-situ optical images of H2mm sample during transient thermal cycling testing in UPP and QR code linked to a video showing a part of the in-situ recording.

Figure 6.5 shows representative IR images and data collected for H2mm (a–b), W2mm (c–d), and reference (e–f) samples. As with the H2mm samples during HIVE and UPP thermal cycling in Chapter 5, surface cracks were observed in the H2mm sample in Figure 6.5 (a), indicated by white arrows. No cracking outside of the laser spot was visible in the W2mm sample in Figure 6.5 (c). Peak pulse temperatures were similar (∼1700 °C) for both types of sample, however the average temperature of the H2mm samples was higher by approximately 75 °C. It was postulated that this was due to the lower thermal conductivity of steel substrate and poorer interfacial bonding between the dissimilar materials, meaning that less heat would have been dissipated from the surface. This fitted with the trend observed in the in-situ photographs taken at HIVE, shown in Figure 5.18, where the coatings on the steel substrate samples were visibly hotter. The reference W sample data further supported this, as the peak temperature reached was ∼1090 °C (which was significantly lower in comparison to the other two samples) in the first set of pulses and little damage was seen in the IR images. As mentioned previously, the reference sample was thinner (5 mm, in comparison to 5 mm substrates with a 2 mm coating for other samples) and it comprised fully dense, homogeneous W. This meant it had superior thermal conductivity and could therefore dissipate the heat more evenly across the surface and faster to the water-cooled Cu mount. Furthermore, surface quality appeared to remain in better condition than the FAST W coatings, so it was likely that the laser was reflected more by the coating surface, which would result in a lower amount of absorbed laser energy.

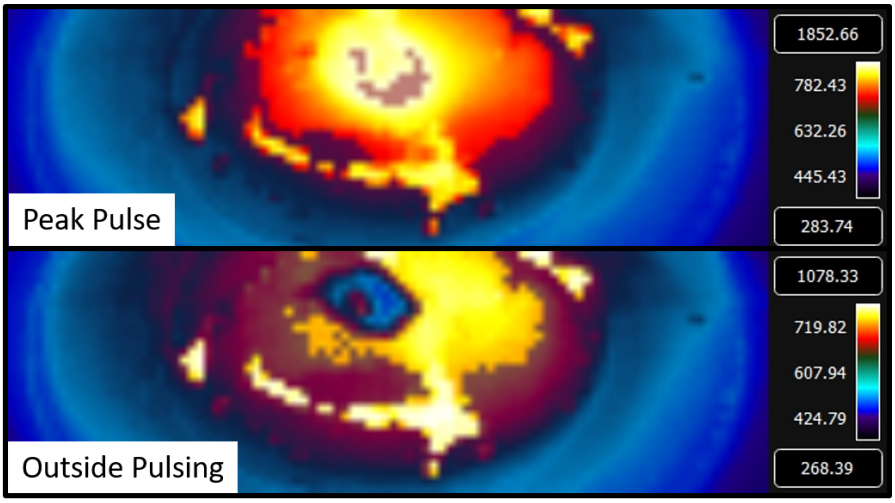


(a) 2 mm thick W coating on a hatched steel substrate.

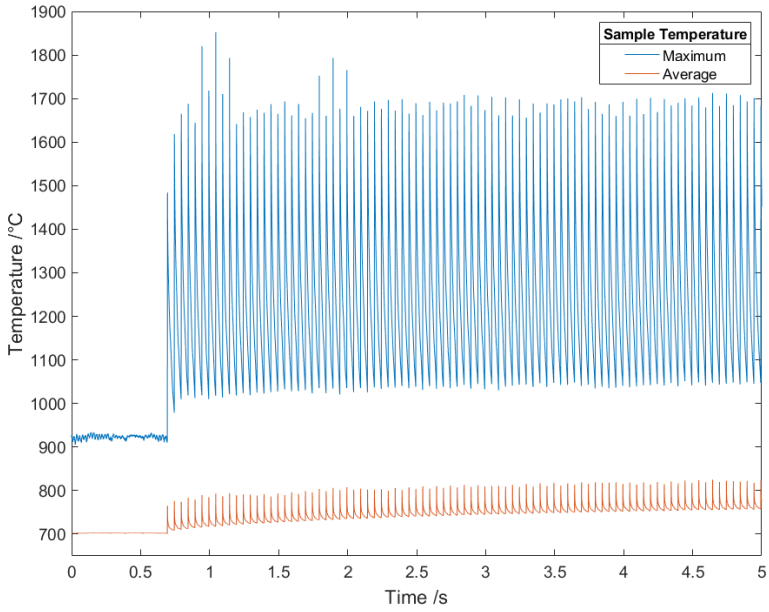


(b) Measured IR temperature profiles of H2mm sample.

Figure 6.5: Representative IR data of samples during testing in UPP.

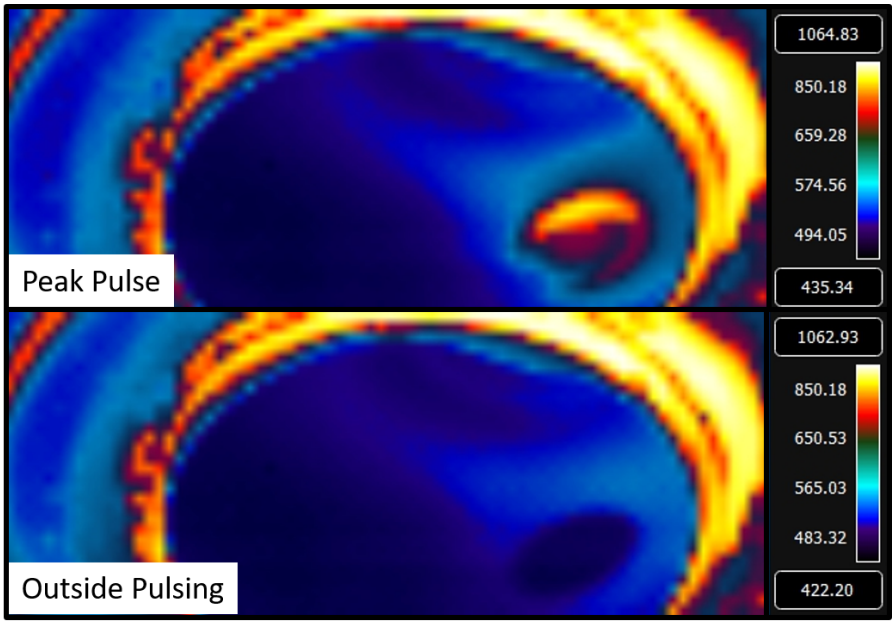


(c) 2 mm thick W coating on a flat W substrate.

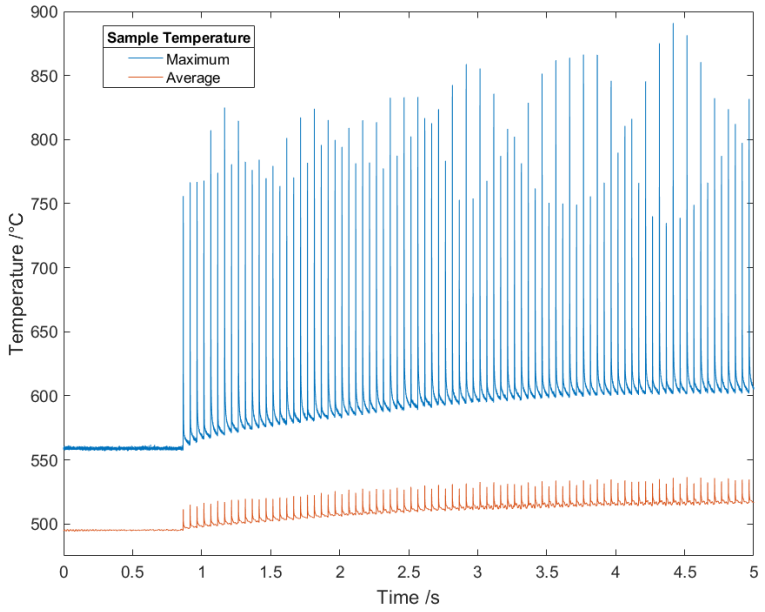


(d) Measured IR temperature profiles of W2mm sample.

Figure 6.5: Representative IR data of samples during testing in UPP.



(e) Reference W sample.

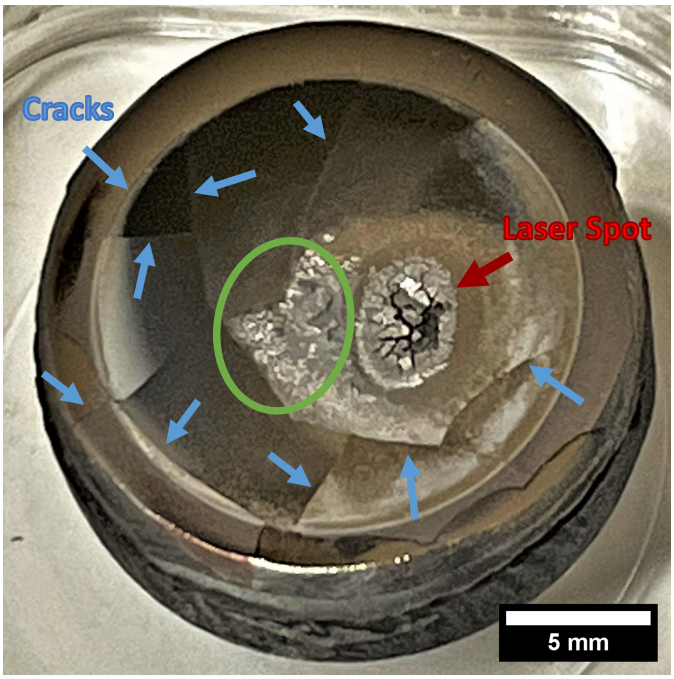


(f) Measured IR temperature profiles of reference W sample.

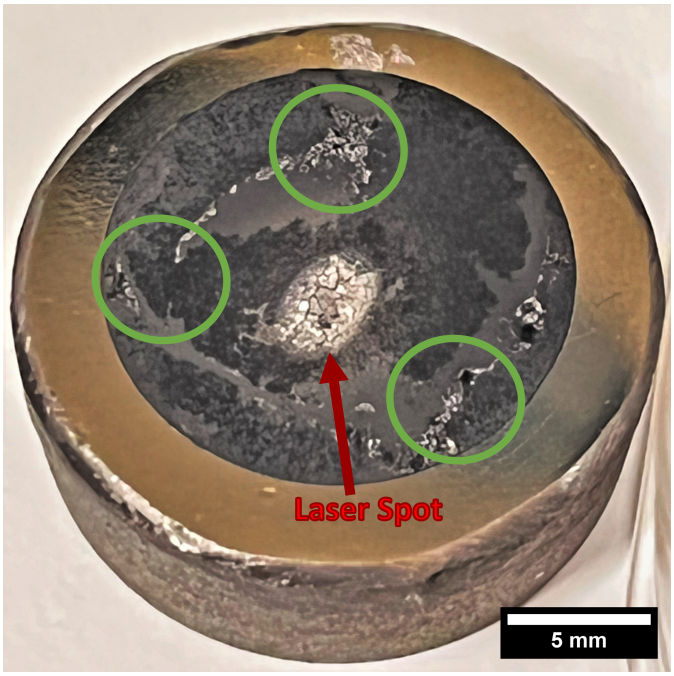
Figure 6.5: Representative IR data of samples during testing in UPP.

Surface crack and plasma damage analysis

Figure 6.6 shows the same samples as Figure 6.2 following damage in UPP. The laser affected areas were of a similar size; the minor axis was ∼2.8 mm and the major axis was ∼4.0 mm (∼8.8 mm^2). These values were used to fit a 2D Gaussian profile to the beam, assuming that the major and minor radii were equal to three standard deviations. The resulting heat flux was approximately 30 $MW{\cdot}m^{-2}$. The areas exposed to the plasma were also discoloured and turned black; surface modifications attributed to erosion damage and cracking of the top layer of the W were observed (highlighted by green circles). Wide-spread cracking was only seen in the H2mm sample (highlighted by blue arrows) and extended to the edge of the sample, beyond the clamping ring shielding. No coating delamination at the interface occurred for any sample tested.

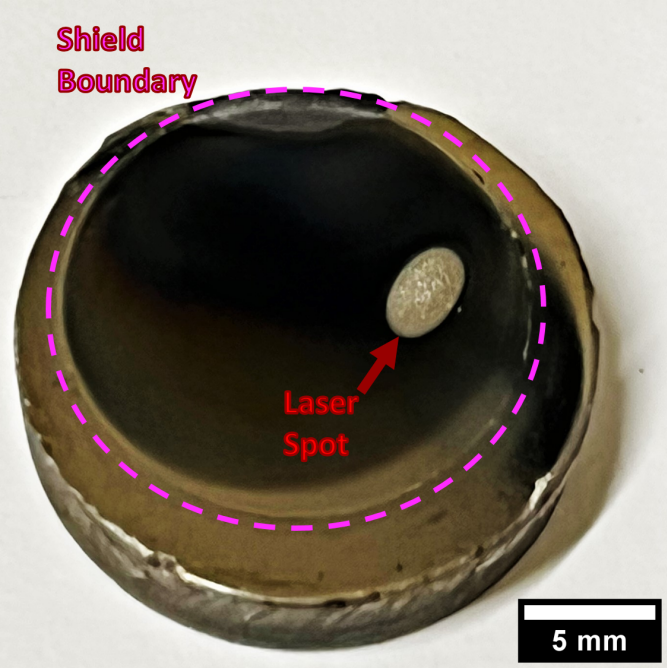


(a) 2 mm thick W coating on a hatched steel substrate.



(b) 2 mm thick W coating on a flat W substrate.

Figure 6.6: Representative images of samples following to testing in UPP.



(c) Reference W sample.

Figure 6.6: Representative images of samples following to testing in UPP.

Figure 6.7 shows SEM images of hatched steel substrate samples. Figure 6.7 (a) shows an enlarged view of the resultant damage at the laser spot in the sample in Figure 6.6 (a) and was representative of other damage spots for H2mm samples. It was apparent that a layered structure had evolved due to the laser and plasma damage; parts of the top layer had blistered and broken off as flakes. Blistering (circled in orange) occurred around the edge of the damage spot and appeared to connect to the crack network through the centre of this area, which suggested that the location of large cracks may be dictated by early blister formation. It

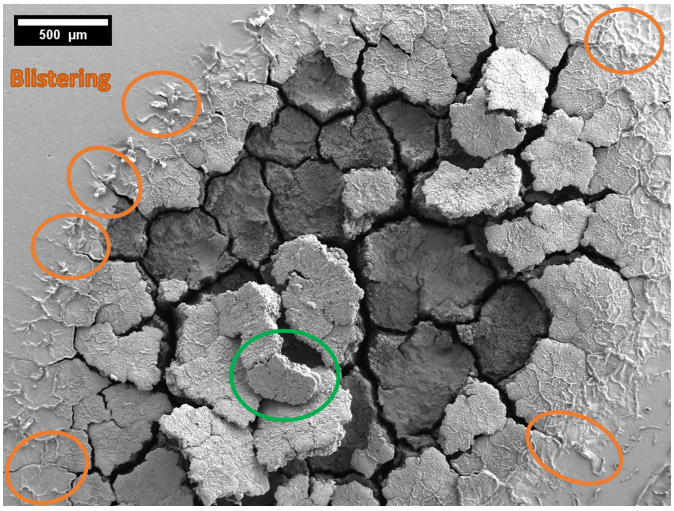
was postulated that as blisters formed and developed, more material was raised to the surface, which left a weaker, more open microstructure underneath which allowed cracks to propagate. Fan et al. observed similar subsurface microstructural behaviour in He ion irradiated blisters [176].

Figure 6.7 (b) shows the centre of a damaged spot at higher magnification. Grains were visible at this level (shown in the pink circle and highlighted between cracks in the yellow circle), indicating that recrystallisation had occurred at the surface due to prolonged exposure to a temperature above the recrystallisation temperature for W (1000-1500 °C [177, 178]), as they appeared to be orders of magnitude larger (10–50 µm) than the initial grain size stated by Cui (227 nm) [74]. Various surface modifications were seen on the large flakes: small blisters (blue circle), cracks (yellow circle) and ridges (red circle) similar to those observed by Parish [115]. The green box denotes the location of Figure 6.7 (c).

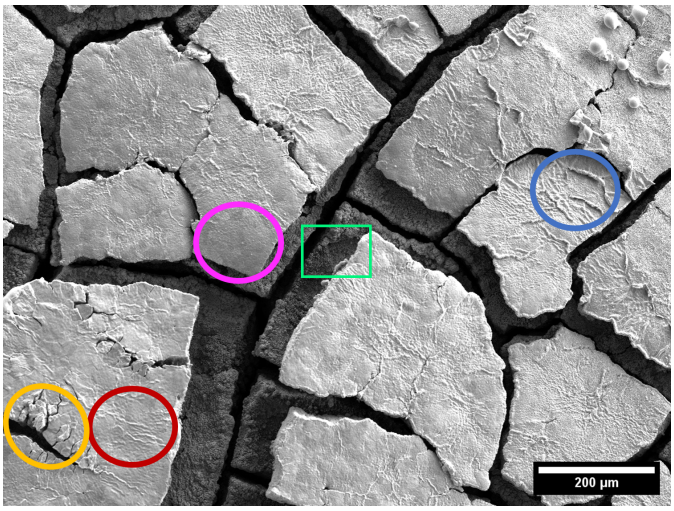
Figure 6.7 (c) highlights four distinct areas of differing microstructure observed in the laser damage spots. The top surface layer (shown in orange) which, as discussed already, contained blisters and ridges as well as a small amount of melting (seen at the left of the orange circle). This layer was directly exposed to the laser and was furthest from the cooled mount. It would therefore have had the largest change in temperature. The other three regions were below the top surface, which partly sheltered them from the incident laser energy, resulting in a temperature gradient across this area. The region highlighted in yellow, at the edge of the deep crack, was the next most exposed area (as it had the least shielding from the surface layer). Particles at the edge were large and faceted, with some areas containing observable ridges as well. Heat loads were less than the top surface,

so no blistering or melting had occurred but samples had been exposed to enough heat for enough time for powder particles to recrystallise and grow into larger, faceted particles. The adjacent region, highlighted in green, received less thermal energy, so particle growth and faceting occurred to a lesser extent. The blue circle denotes the region which was the most sheltered by the upper surface and received the least laser energy; this contained much smaller faceted particles, indicating that recrystallisation had occurred with only limited particle growth.

Figure 6.7 (d) shows blistering at the very outer edge, like those highlighted by orange circles in Figure 6.7 (a), of the laser-damaged region, with the blister covered in particles. These particles were likely eroded and/or ablated from the laser spot into the plasma before being redeposited outside this area. Closer inspection, seen in Figure 6.7 (e), shows that even smaller particles were scattered on top of the larger particles. It was suggested that the larger particles were ablated during pulsing, and that the smaller particles were erosion products from plasma interactions. This redeposition was seen across the sample up to where it was covered by the TZM clamping ring. Figure 6.7 (f) shows the boundary between plasma-exposed material and sheltered material. Particles can be seen covering the darker, exposed side of this boundary. Cracking continued from one region into the other, but also followed the edge of this boundary, potentially due to the localised temperature difference that the shelter from the TZM clamping ring provided. It was also noticeable that cracking shifted the surface sufficiently that the exposure boundary no longer lined up.

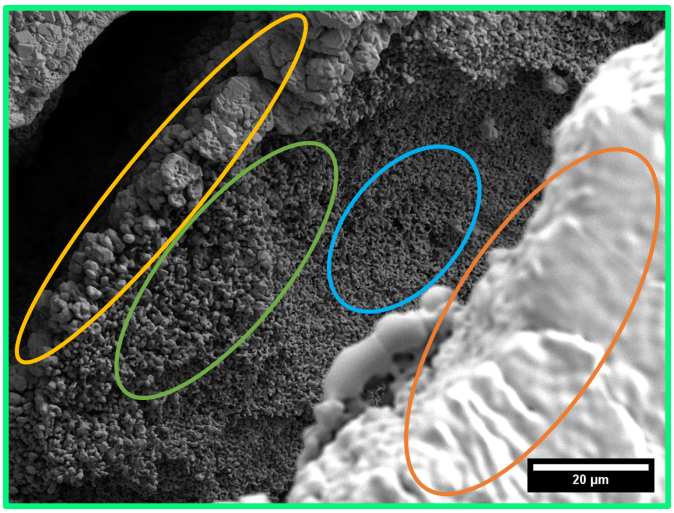


(a) SEM image showing surface of H2mm sample. Orange circles highlight some blistering. The green circle highlights a flake in the process of breaking away.

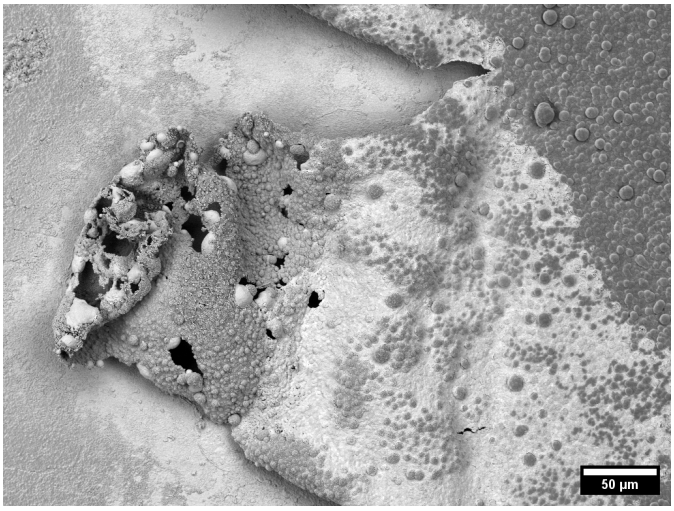


(b) SEM image highlighting various surface modifications: recrystallised grain growth (pink & yellow) small blisters (blue), cracks (yellow) and ridges (red). The green box denoted the location of Figure 6.7 (c)

Figure 6.7: Representative SEM images of H2mm samples.

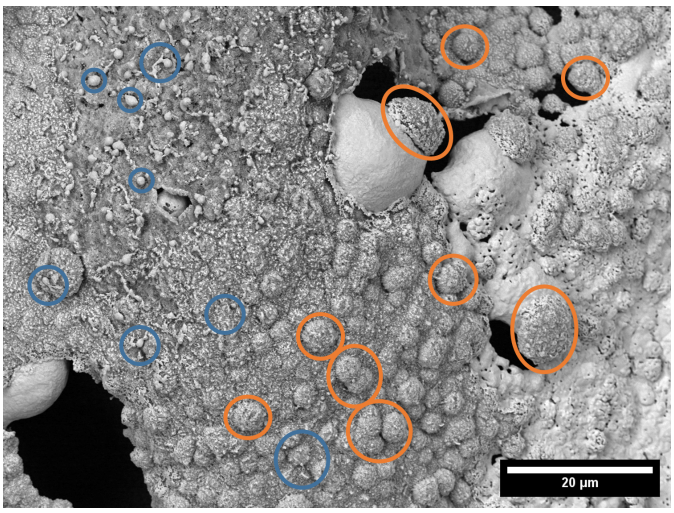


(c) SEM image denoting four microstructures observed: melted (orange), large facets with ridges (yellow), smaller facets (green) and porous network with some faceting (blue).

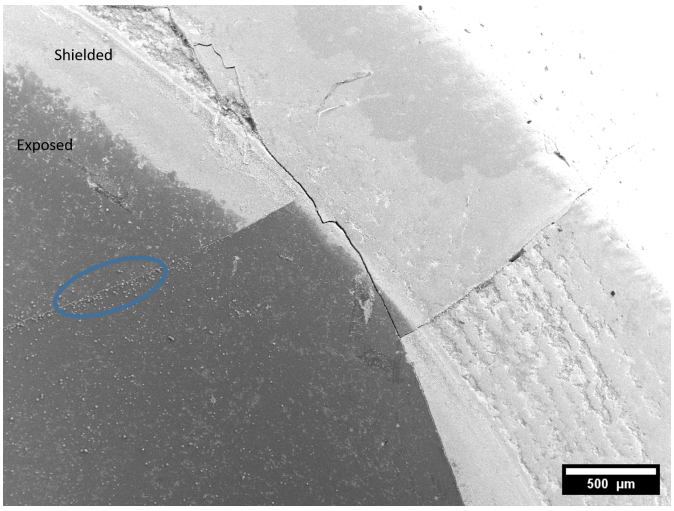


(d) BSE image showing blister at edge of laser-damaged region. Cracks can be seen in the blistered layer and ablated particles have been redeposited on the surface by the plasma.

Figure 6.7: Representative SEM images of H2mm samples.



(e) Higher magnification BSE image of redeposited particles on blistered surface. Suspected large ablated particles are shown in orange, finer eroded W particles are highlighted in blue.



(f) SEM image at the edge of the coating. The exposed (dark) and shielded (light) regions have been labelled. The blue oval shows redeposited W particles.

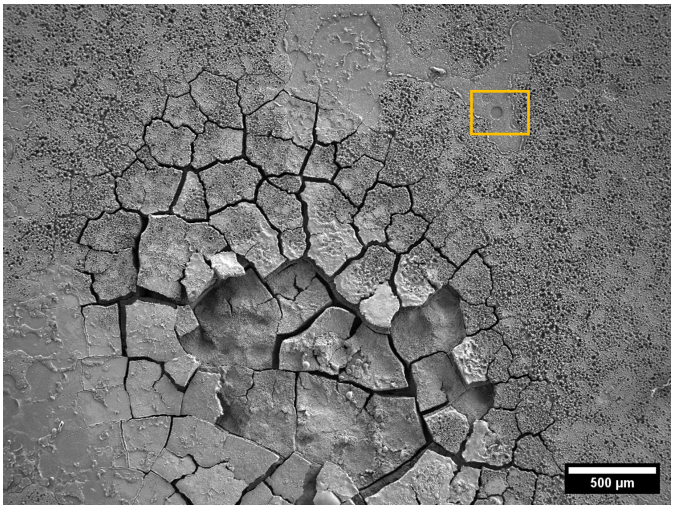
Figure 6.7: Representative SEM images of H2mm samples.

Figure 6.8 shows SEM images of W substrate samples. Figure 6.8 (a) shows the laser damage spot and some of the surrounding area. Similar regions and layers formed as in the H2mm samples because the laser damage was very localised, indicating that the type of substrate had little impact on the damage caused. Figure 6.8 (b) is a higher magnification image of the centre of the laser damage. Most of the top layers had broken away, but some near the edge of the centre were still intact. There was a mix of surface modifications; some areas were ridged with high levels of grain growth and faceting (orange circles), whilst others had significant amounts of deposition and open porosity (purple circle). Some molten particles were deposited in the centre of the spot (green circle).

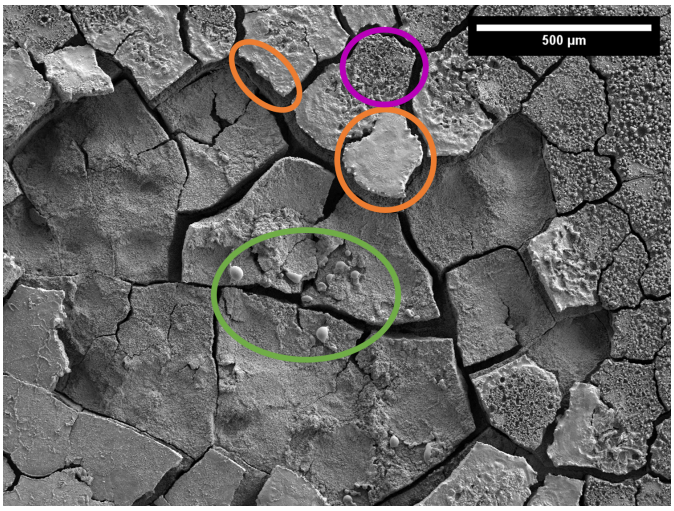
Figure 6.8 (c) shows blistering that occurred away from the laser spot, in yellow-bordered area in Figure 6.8 (a). Two circular blisters were observed, one which collapsed on itself (top left) and one that completely broke away (and was likely redeposited elsewhere). Allen et al. observed similar blistering phenomena under He ion irradiation; cracks occurred at the edges of blisters and led to blister 'pop-out' [179]. The immediate surrounding area had a finer distribution of deposits, although some large particles created large craters and cracked the surface (yellow circles). The finer deposits probably resulted from localised, minor material erosion by the plasma; larger deposits were likely redeposited after being melted into the plasma from the laser spot or from blister fragmentation. Further away from the two blisters, larger deposits were observed more frequently and formed a porous network on top of the surface. At the boundary between the fine and coarse deposition regions, blistering and peeling was observed, with some cracks beginning to propagate into the finer deposit region (blue circles). It was inferred that the

larger deposits may have eroded the surface over time in a repeating cycle. Large deposits created blisters that were then broken, eroded and became new large deposits to continue the cycle and increase the eroded area. Near the boundary on the right side of the image, the original boundary was seen underneath large deposits where it had broken away from the new boundary.

Figure 6.8 (d) shows the boundary between the plasma-exposed material (dark) and the material shielded by the TZM clamping ring (bright). As with the H2mm samples, there was significant contrast, and deposits were prevalent in the plasma-damaged region. However, no cracking was observed along or across the boundary. The location of Figure 6.8 (e) is denoted by the orange box in Figure 6.8 (d), where blistering was seen at the boundaries between areas with high large-deposit density and low large-deposit density. The green box indicates the area of the blister boundary shown in higher magnification in Figure 6.8 (f). Figure 6.8 (f) is a higher magnification image of the blister boundary. The large deposit area on the right was out of focus because of the difference in depth of field caused by the raising of the blister and the suppression of the surface by the large deposits.

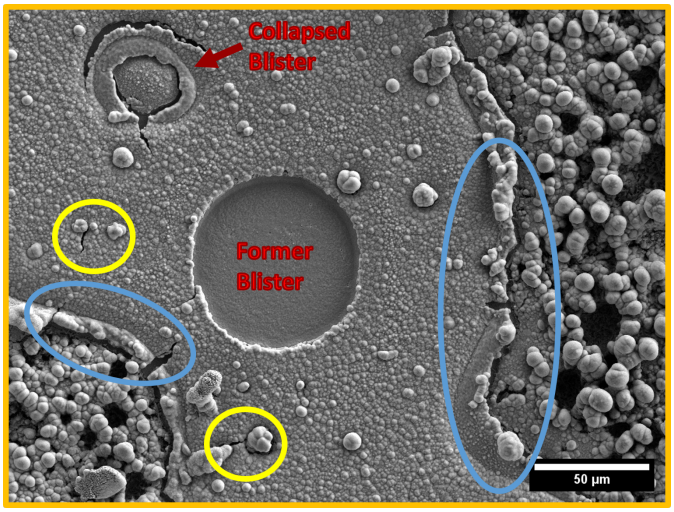


(a) SEM image of the laser-damaged region on a W2mm sample. The yellow box highlights the location of Figure 6.8 (c).

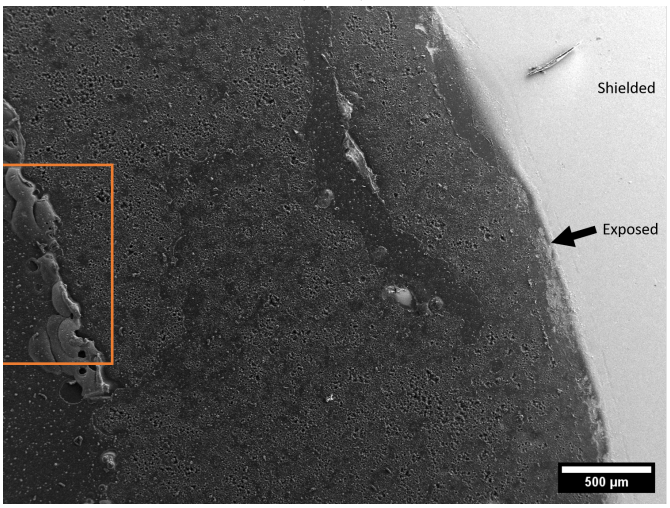


(b) Higher magnification SEM image highlighting surface modifications: grain growth and faceted ridges (orange), porous deposition (purple) and deposited molten droplets (green).

Figure 6.8: Representative SEM images of W2mm samples.

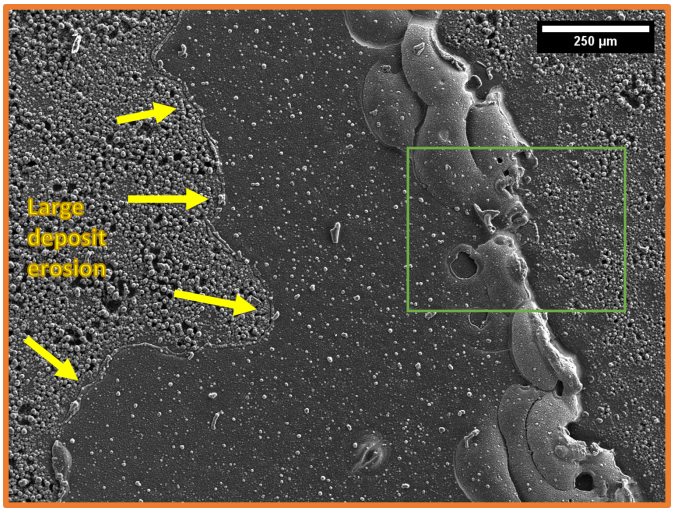


(c) SEM image highlighting two blisters (red), cracking caused by large deposits (yellow) and the blister boundary between fine and coarse deposits (blue).

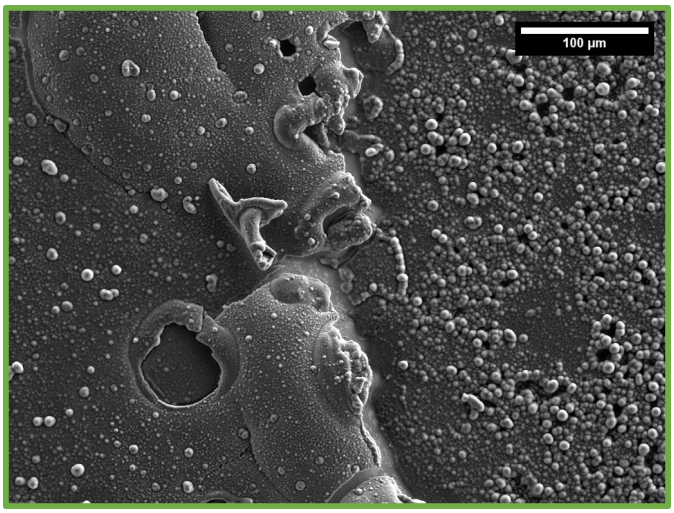


(d) SEM image at the plasma exposure boundary at the edge of the sample. The orange box denotes the location of Figure 6.8 (e).

Figure 6.8: Representative SEM images of W2mm samples.



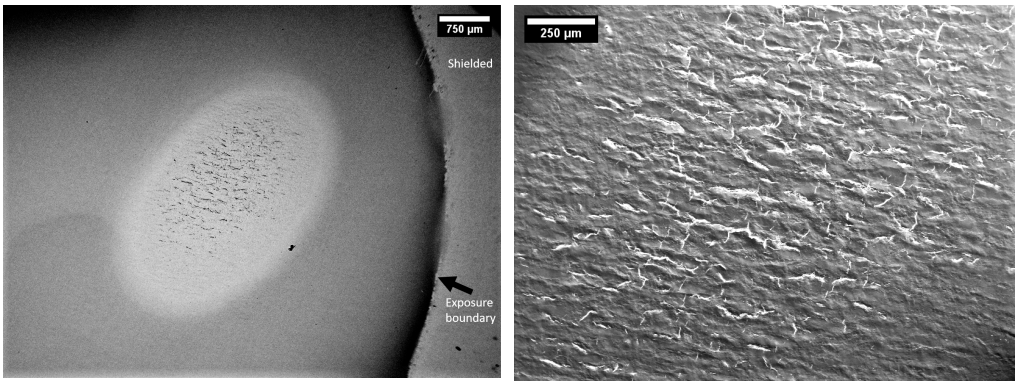
(e) SEM image highlighting large deposit erosion boundary. The green box shows the location of Figure 6.8 (f).



(f) Higher magnification image highlighting the difference (by depth of field) in surface height between the blistered boundary and the large-deposit areas.

Figure 6.8: Representative SEM images of W2mm samples.

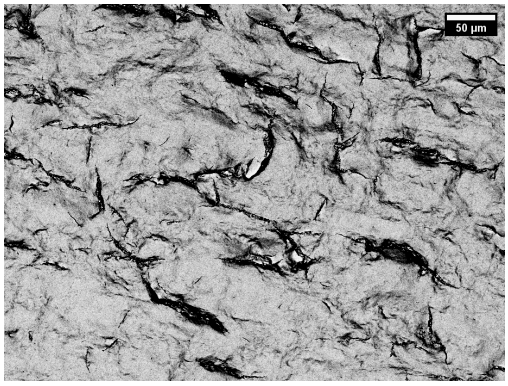
Figures 6.9 (a–c) show the laser spot damage of the reference W sample at different magnifications. The damage was significantly less than any of the FAST samples tested under the same conditions, as seen in the IR recording and data in Figures 6.5 (e–f). Relatively small amounts of blistering were observed across the laser-damaged region, however the blisters did not form a network and were shallower in comparison to the other tested samples. Figure 6.9 (d) shows the plasma-exposure boundary of the sample. The exposed section of the sample was darker, as with the FAST samples, however there were no visible deposits or failure of any kind. This reiterates the trend seen in the other two samples: as fracture and erosion of the surface by the laser increases, more W was released into the plasma which leads to increased particle deposition and further erosion away from the laser-damaged area.



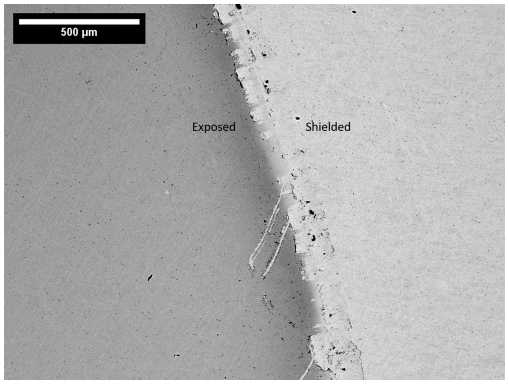
(a) BSE SEM image of surface of reference W sample showing laser-damaged spot and plasma exposure boundary.

(b) Higher magnification image showing blistering caused by laser on surface

Figure 6.9: SEM images of reference W sample.



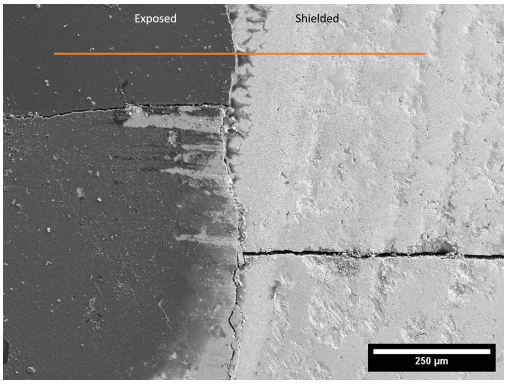
(c) Higher magnification BSE image highlighting blistering caused by the laser.



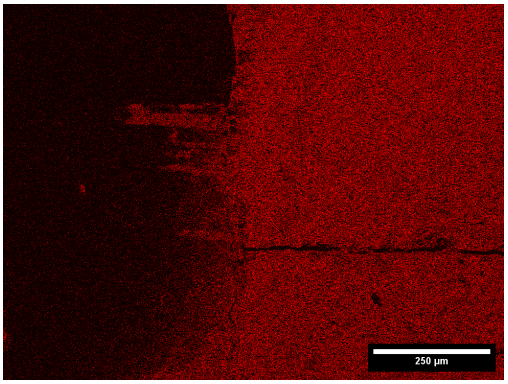
(d) BSE image of plasma-exposure boundary. No W deposits were seen on the coating surface.

Figure 6.9: SEM images of reference W sample.

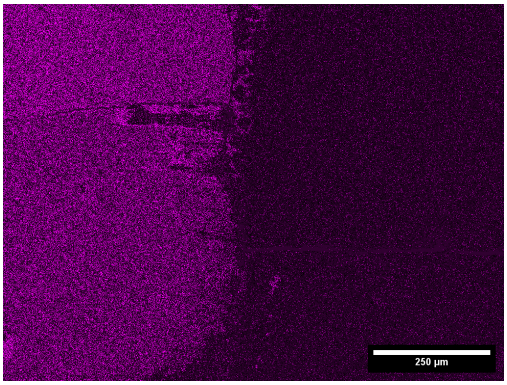
Figure 6.10 shows a SEM image taken at the edge of the plasma-exposed area on a H2mm sample and the corresponding EDX maps of W, C and O. The dark region corresponds to C which was deposited from the vacuum chamber by the plasma (in a similar way to the VPS). The chamber was not cleaned between testing, so C and other impurities will have built up from general use of the facility. This layer of C was easily removable, as seen by the scratching in Figure 6.10 (a) and Figure 6.9 (d). Figure 6.10 (e) shows the linescan data collected from the orange line shown in Figure 6.10 (a). Because of the difference in atomic size between C and W, impurities such as Mo (from the plasma source) and Fe and Cr from the steel vacuum vessel appear to be in lower quantities in the exposed section of the linescan in comparison to the unexposed. However, Figure 6.10 (f) shows a comparison between two EDX spectra acquired at either end of the linescan. In the exposed spectrum, impurity elements registered higher counts than the unexposed spectrum; this was as expected because the unexposed area was shielded from these impurities.



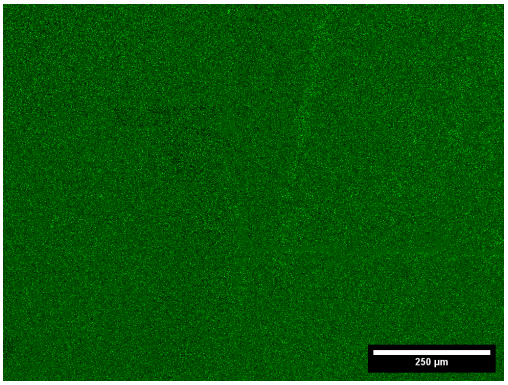
(a) BSE image of plasma-exposure boundary. The orange line denotes the location of the linescan data shown in Figure 6.10 (e).



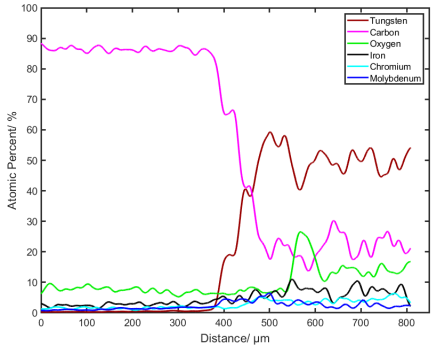
(b) Corresponding EDX map for W.



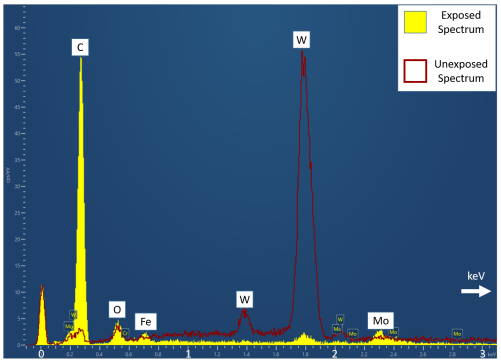
(c) Corresponding EDX map for C.



(d) Corresponding EDX map for O.



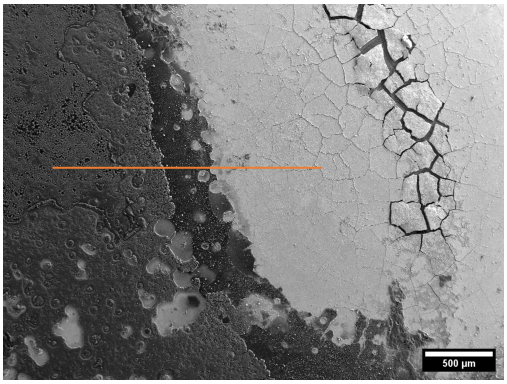
(e) EDX linescan taken across plasma-exposure boundary shown by the orange line in Figure 6.10 (a).



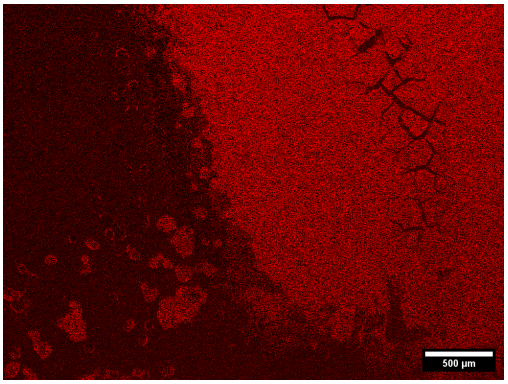
(f) EDX spectra taken at either end of the linescan indicated in Figure 6.10 (a) in the exposed and unexposed regions.

Figure 6.10: EDX maps, linescan and spectra of a plasma-exposure boundary.

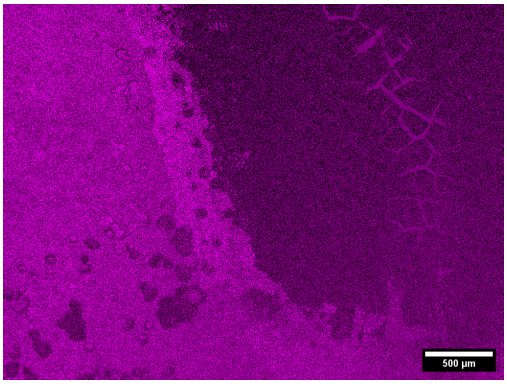
Figure 6.11 shows (a) a SEM image taken at the edge of the laser-damaged area of a W2mm sample and the corresponding EDX maps of (b) W, (c) C and (d) O. Three distinct regions were observed: the light, central area of the laser spot as seen in the SEM image, which corresponded to W; the darker region towards the edge of the image and furthest away from the laser spot, which corresponded to C and O; and the darkest region which immediately surrounded the laser spot which had the highest C content. It was postulated that C and O were expelled by the intense temperatures produced by the laser, leaving a purer W region in the centre of this area. Figure 6.11 (e) is a linescan taken from the orange line and shows that the darkest region was almost entirely C. Other impurity elements may have reacted away due to the high temperatures in close proximity to the laser spot, but the exact mechanism was unclear. This linescan suggests that O content remained constant and that levels of Mo increased in the laser-damaged area, but this was misleading because of the conversion to atomic percentage (due to the large difference in atomic mass between C and W). Figure 6.11 (f) shows the spectra associated with the laser-damaged spot and with the dark region at the opposite end of the linescan, indicating that there were higher relative quantities of O and Mo away from the laser-damaged region.



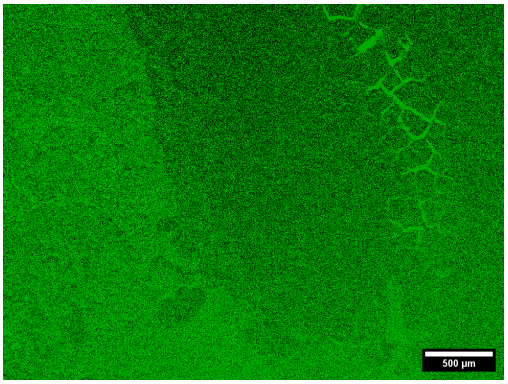
(a) SEM image of laser-damaged area. The orange line denotes the location of the linescan shown in Figure 6.11 (e).



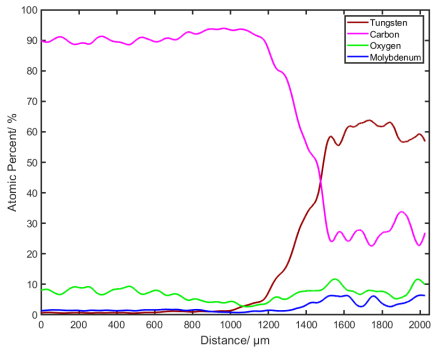
(b) Corresponding EDX map for W.



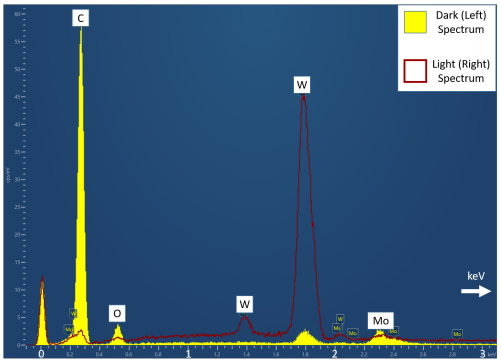
(c) Corresponding EDX map for C.



(d) Corresponding EDX map for O.



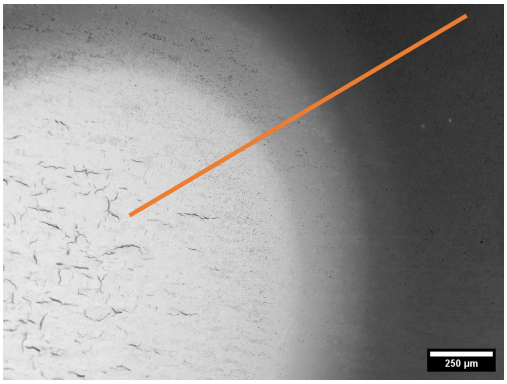
(e) EDX linescan taken across laser spot-blister boundary shown by the orange line in Figure 6.11 (a).



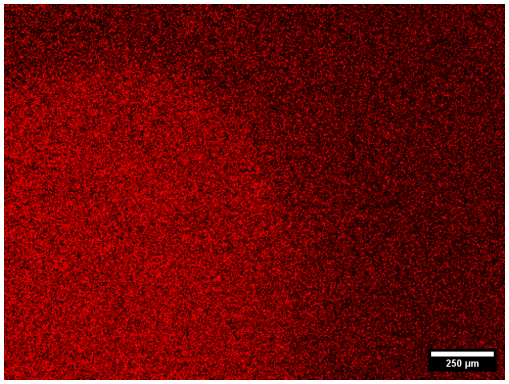
(f) EDX spectra taken at either end of the linescan indicated in Figure 6.11 (a) in the dark (left side) and bright (right side) regions.

Figure 6.11: EDX maps, linescan and spectra of a laser spot and surrounding area.

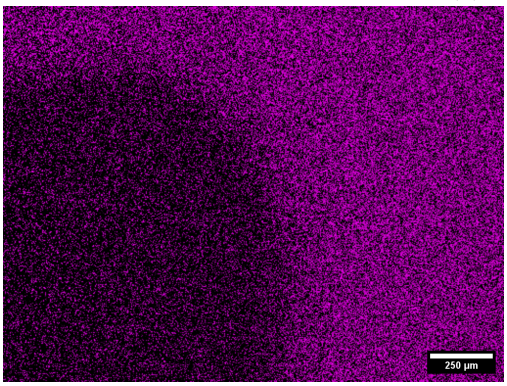
The SEM image taken at the edge of the laser-damage area of the reference W sample is shown in Figure 6.12 (a) together with the corresponding EDX maps of (b) W, (c) C and (d) O. Figure 6.12 (e) is a linescan taken from the orange line and shows that, as seen for other samples, the laser-damage spot had a high W concentration. Further away from the laser-damage, C content increased but did not reach the high concentrations seen in Figures 6.10–6.11. This indicated that some of the C in the FAST samples was expelled, increasing the concentration on the surface elsewhere. Figure 6.11 (f) denotes the spectra associated with the laser-damaged spot and with the dark region at the opposite end of the linescan. These spectra confirm that less concentrated elements such as O and Fe registered more counts away from the laser spot, which aligns with the O linescan signal.



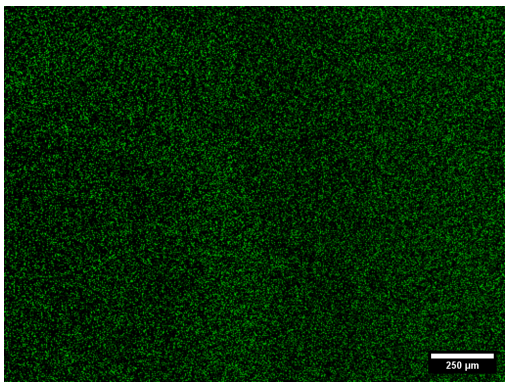
(a) SEM image of laser-damaged area. The orange line denotes the location of the linescan shown in Figure 6.12 (e).



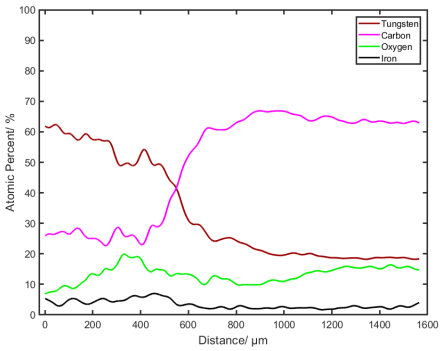
(b) Corresponding EDX map for W.



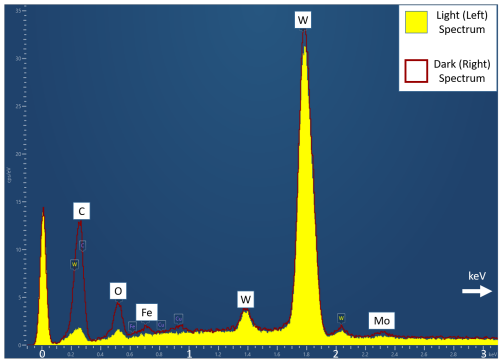
(c) Corresponding EDX map for C.



(d) Corresponding EDX map for O.



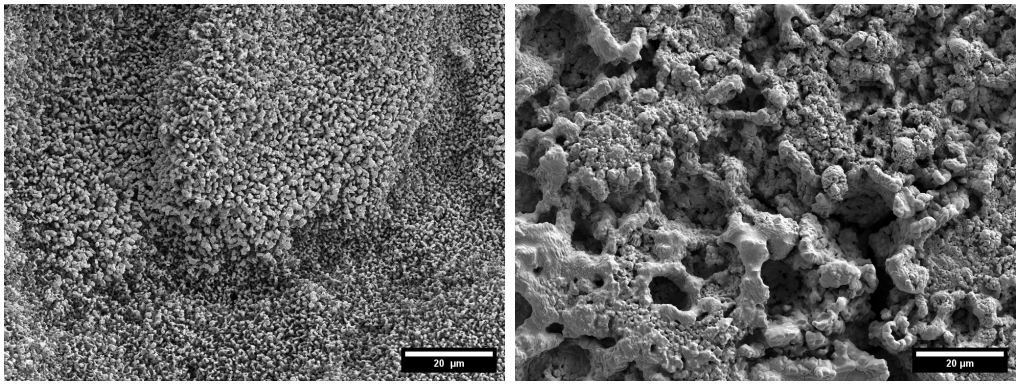
(e) EDX linescan taken across the laser spot-blister boundary shown by the orange line in Figure 6.12 (a).



(f) EDX spectra taken at either end of the linescan indicated in Figure 6.12 (a) in the bright (left side) and dark (right side) regions.

Figure 6.12: EDX maps, linescan and spectra of a laser spot and surrounding area.

SEM images illustrating the porosity seen in both the H2mm and W2mm samples were recorded. Figure 6.13 (a) shows an area that was more sheltered from the laser by higher layers of material. The combination of residual porosity from sintering and prolonged heat exposure produced an open, faceted structure. This occurred because thermal energy was not high enough for widespread recrystallisation and grain growth which would have densified the coating. Areas like the one shown in Figure 6.13 (b) were more exposed to the laser and consequently temperatures exceeded the sublimation point for W oxide (∼800 °C). Although particle growth occurred, there were fewer, but larger, pores because residual W oxides and trapped C were hot enough to sublime, evaporate or react away.



(a) SEM image of slightly faceted growth in a porous region of the coating that was mostly sheltered from the laser by higher material.

(b) SEM image of residual porous microstructure following plasma and laser exposure where it was believed that sublimation of W oxides occurred.

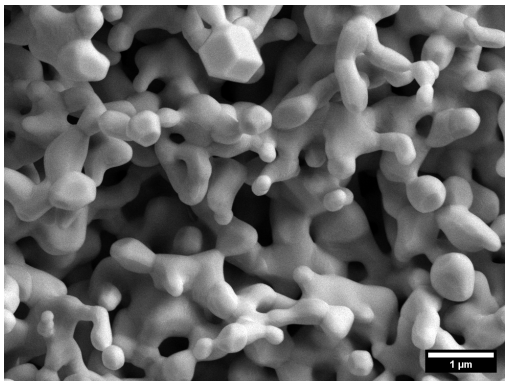
Figure 6.13: Secondary electron images of H2mm and W2mm samples showing evolution of retained porosity.

Residual porosity meant that the overall thermal conductivity of the FAST coatings would have been significantly lower than that of pure W, and particles would have experienced higher temperatures than a fully dense coating. These elevated temperatures (as seen in Figure 6.5) would have exceeded the recrystallisation temperature for W and would have caused grain growth to occur.

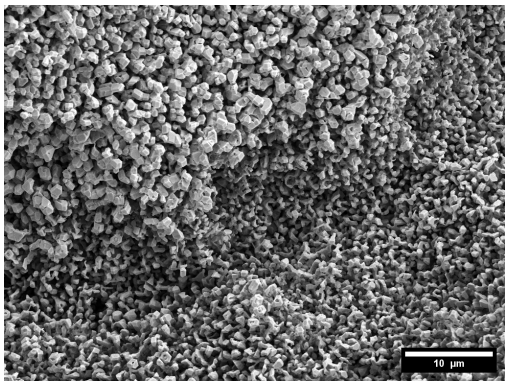
Figure 6.14 shows SEM images where significant amounts of recrystallisation led to faceted growth and terracing. Figure 6.14 (a) was taken in the fairly well-sheltered region highlighted by the blue oval shown in Figure 6.7 (c). Large particles appeared cube-like and formed on one end of a thin strand; others that were connected to thicker strands exhibited a rounder structure because the heat was dissipated away faster. Due to the shelter provided most particles did not become fully faceted because they had not been subjected to sufficient thermal energy. In contrast, Figure 6.14 (b) shows a less sheltered region in which most particles were fully faceted, but had not grown significantly in size.

At the surface of the sample, all particles were faceted with sharp edges and had increased in size by an order of magnitude, as seen Figure 6.14 (c). The SEM image in Figure 6.14 (d) was taken at the edge of a surface flake where significant amounts of faceted growth had occurred and particles were sintered together. A large particle appeared to have been deposited and was in the process of faceting, presumably having started as a round droplet. Figure 6.14 (e) is a higher magnification micrograph of the particle and shows that as well as faceting, terraces and pyramids had formed. Figure 6.14 (f) shows a smaller deposited particle that had just started to facet. The faceted growth in Figures 6.14 (e) and (f) align with the {100} and {110} planes respectively in the Wulff construction

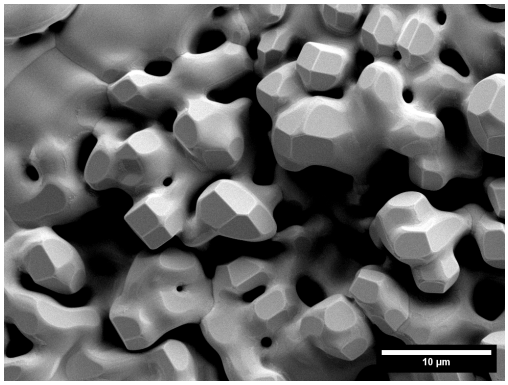
presented by Forslund et al. [180]. Figures 6.14 (g–h) show terracing that occurred at the surface of flakes by the centre of the laser spot. The observed ridges resemble the 'wave' and 'pyramid' formations found by Parish et al. [115] in W following He-ion irradiation. Waves appeared to flow across grain boundaries, indicating that the crystal structure was very closely aligned. The number of particles consolidated into full grains and grain growth was significant, reaching ∼15–40 µm in diameter.



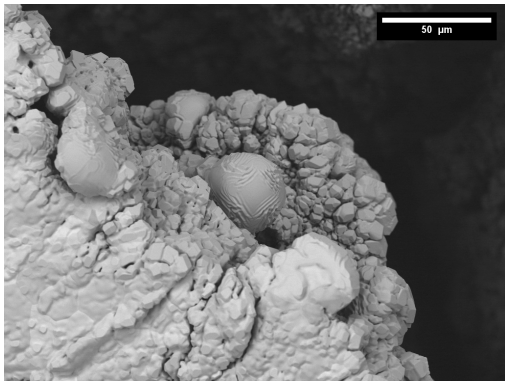
(a) SEM image of sheltered region of microstructure denoted by the blue oval in 6.7 (c).



(b) SEM image of less sheltered region where more faceted growth has occurred.

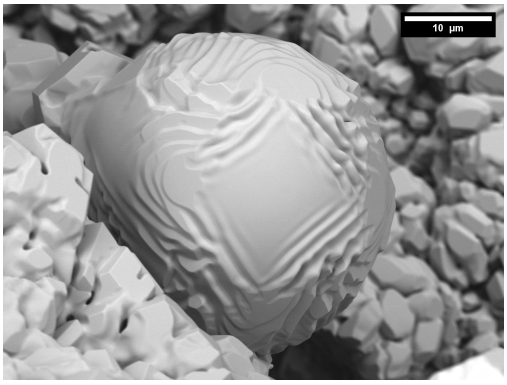


(c) SEM image of coating surface, where powder particles densified, grew and were fully faceted.

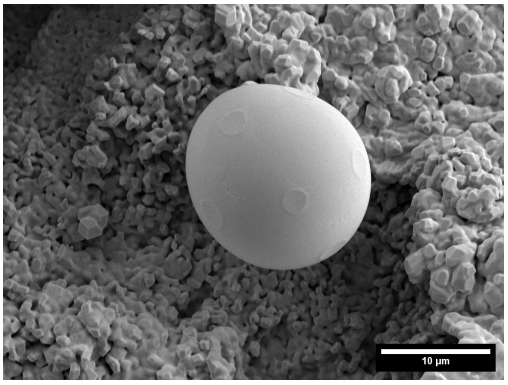


(d) BSE image of a large deposited particle surrounded by highly faceted growth at the edge of a surface flake.

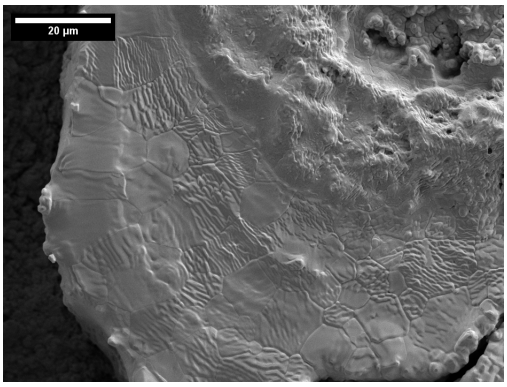
Figure 6.14: SEM images of H2mm and W2mm samples showing terracing and faceted particle growth.



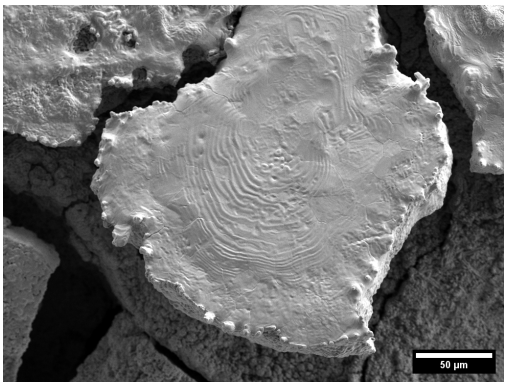
(e) Higher magnification image of the particle shown in Figure 6.14. Terraces and pyramids were observed to have formed on the surface of the particle.



(f) SEM image of a deposited particle that had begun to facet.



(g) SEM image of flake surface where significant grain growth and surface modifications similar to those observed by Parish [115] occurred.

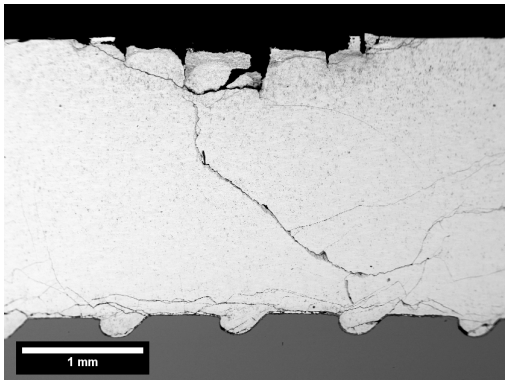


(h) SEM image of wavy terraces on flake surface that extended across grain boundaries, which indicated that grain orientations were similar.

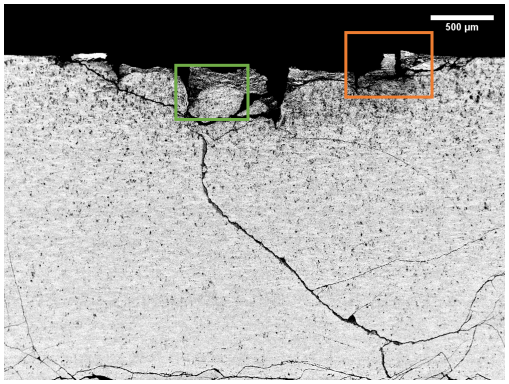
Figure 6.14: SEM images of H2mm and W2mm samples showing terracing and faceted particle growth.

Cross-sectional examination of cracking and plasma damage

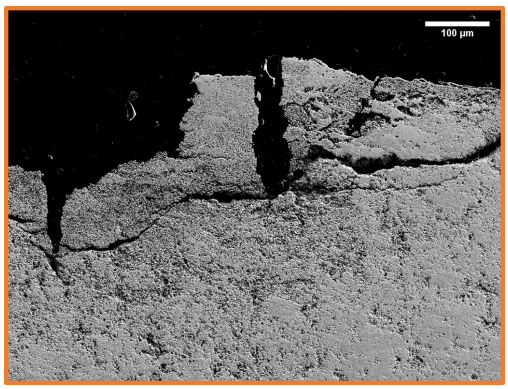
Figure 6.15 shows cross-sectional SEM images of the H2mm sample following damage in UPP. Figure 6.15 (a) illustrates that significant cracking had occurred between the laser spot and substrate interface. Further cracking around the laser spot was observed in Figure 6.15 (b), where a vertical crack formed under the centre and propagated towards the edges of the laser-damaged area. It was possible that some of the damage was sustained during sectioning due to the fragile nature of the surface resulting from prior processing and/or flaws. The location of Figure 6.15 (c) is shown by the orange box in Figure 6.15 (b). A deep crack was seen between two flakes, and a very porous structure was visible underneath a more dense surface. Figures 6.15 (d–e) show the densified surface layer ($\sim$5 µm, blue circles) and some blistering (green circles) that were apparent on the flake to the right of Figure 6.15 (d). Figure 6.15 (f) highlights the difference between oxide regions (dark grey, purple circles) further into the coating and open porosity regions (black, yellow circles) where oxide has reacted and/or burnt away.



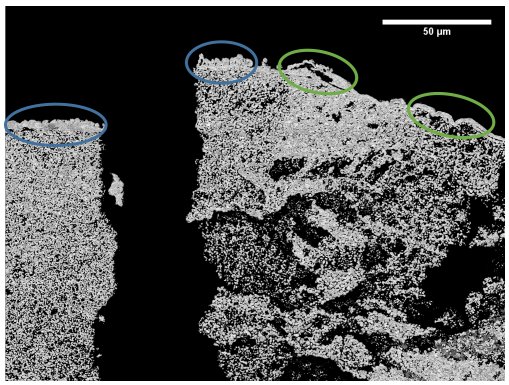
(a) BSE cross-section showing significant cracking around laser-damage spot.



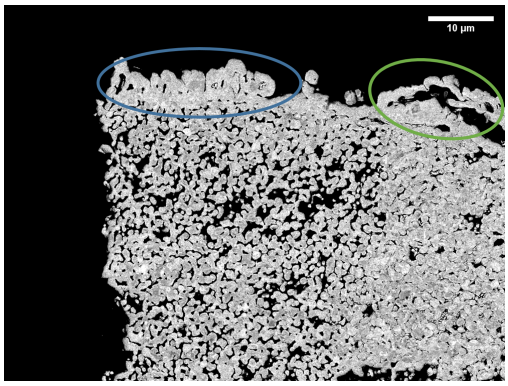
(b) Higher magnification BSE image that highlights the porosity depth near the laser-damage region.



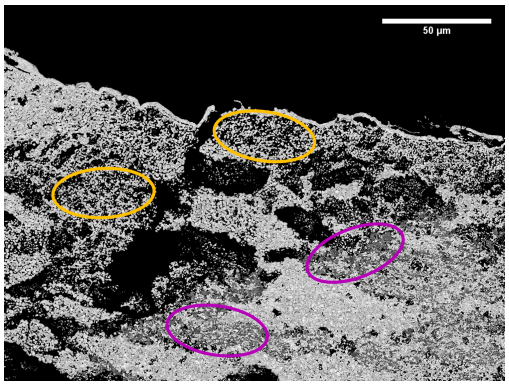
(c) BSE image that shows crack that follows laser-damage depth from the edge (image right) to the centre (image left).



(d) BSE image that highlights blistering (green) and the densified surface (blue) and porous microstructure beneath.



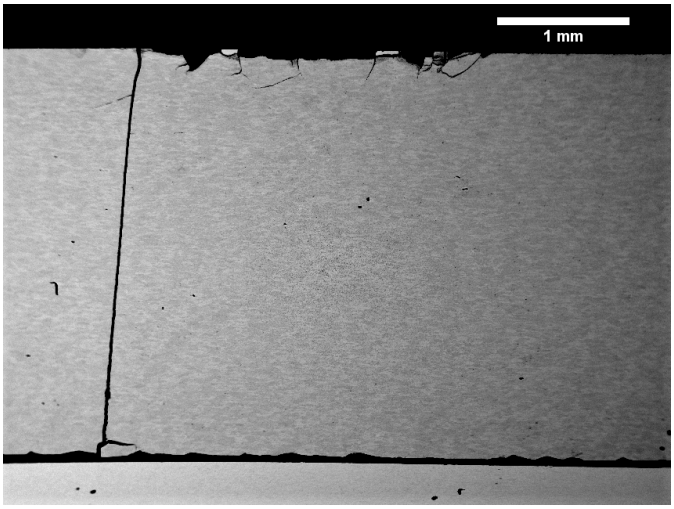
(e) Higher magnification BSE image that shows surface densification layer and a blister that formed.



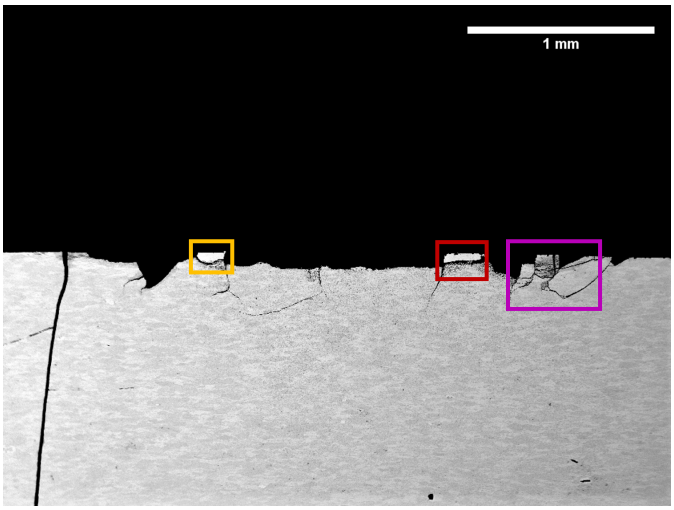
(f) Comparison between oxide (dark grey, purple circles) and open porosity (black, yellow circles).

Figure 6.15: Cross-sectional SEM images of H2mm sample.

Figure 6.16 (a) shows cracking from the surface laser damage that travelled vertically to the interface. Some delamination occurred, but this was thought to have happened following sectioning and mounting in resin. A distinct difference in W purity between the coating and substrate was also observed, as the substrate appeared lighter in the BSE image. Two flakes are highlighted (with yellow and red boxes) in Figure 6.16 (b) that were also lighter than the rest of the coating; these are shown in Figures 6.16 (c–d). The flakes were noticeably less porous than the surrounding material, as they were fully sintered by the laser. In both images, large, faceted grain growth was seen between the rest of the coating and the bottom of the flake, particularly towards the edge where there was little shelter from the incident heat flux from the laser. Figure 6.16 (e) is a higher magnification image of the flake surface shown in green in Figure 6.16 (d). Large vertical grains ($\sim$15 µm) had formed, with small dispersed pores where the grains had recrystallised and grown around the porous structure. Figure 6.16 (f) is an image taken from the right side of the laser-damaged area. Cracks followed the semi-circular arc (denoted by the dashed red line) of the laser damage. Again there was a noticeable difference between the oxide (dark grey) and now-porous, former-oxide (black) regions. The inset in Figure 6.16 (f) is a magnified image of the surface, in the region where significant levels of blistering were observed above the densified surface.

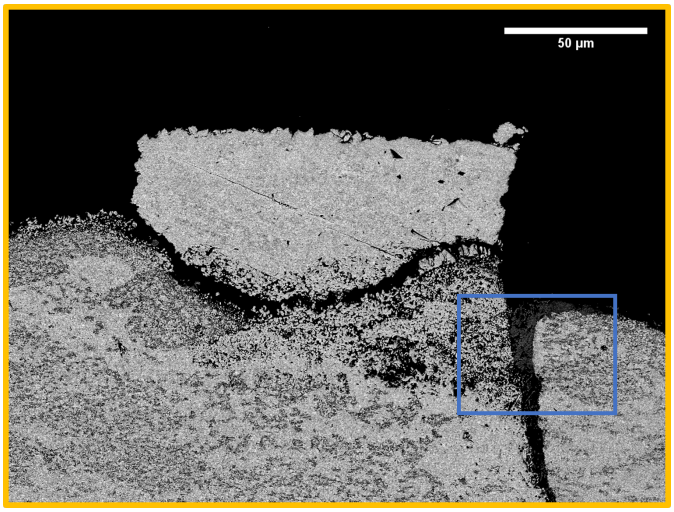


(a) Cross-sectional BSE image showing laser-damage spot on top surface and a vertical crack that formed during sample sectioning that led to slight delamination.

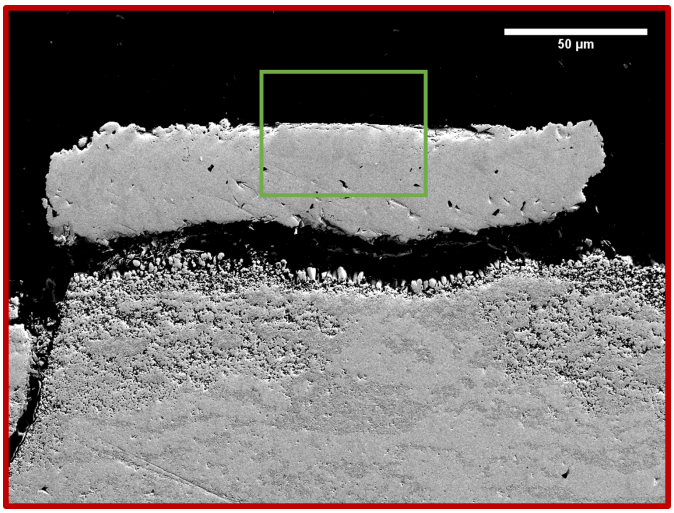


(b) Higher magnification BSE image of the laser-damage region. The yellow, red and purple boxes highlight three surface flakes that survived exposure and denote the locations of Figures 6.16 (c, d & f) respectively.

Figure 6.16: X-Sectional SEM images of W2mm samples.

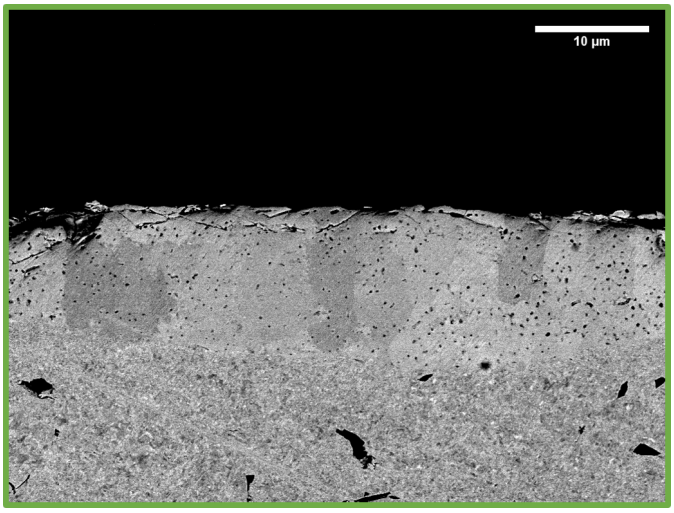


(c) Higher magnification BSE image showing faceted growth at the interface between the flake and the rest of the coating.

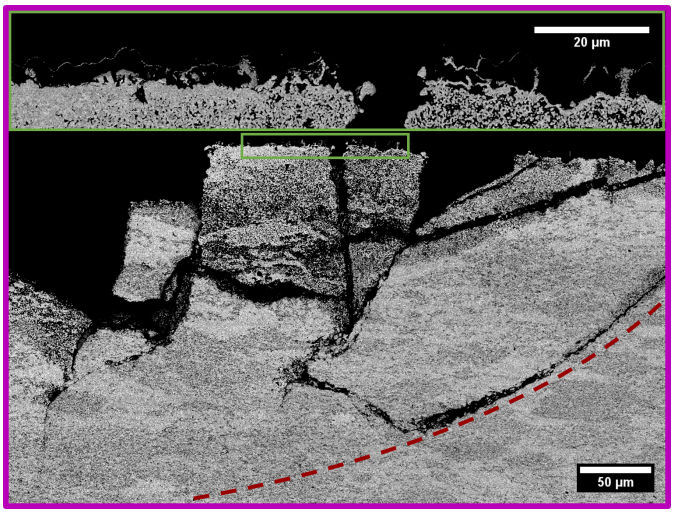


(d) Higher magnification BSE image showing grain growth underneath the flake. The green box denotes the position of Figure 6.16 (e).

Figure 6.16: X-Sectional SEM images of W2mm samples.



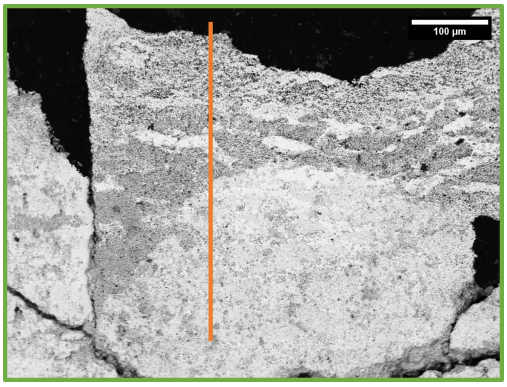
(e) BSE image of flake surface highlighting the columnar grain growth produced by the incident heat flux from the laser.



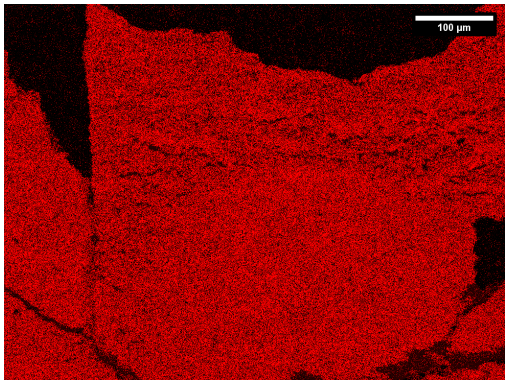
(f) BSE image that shows the layered porosity induced by the laser. The inset image highlights the blistering observed above the densified W surface.

Figure 6.16: X-Sectional SEM images of W2mm samples.

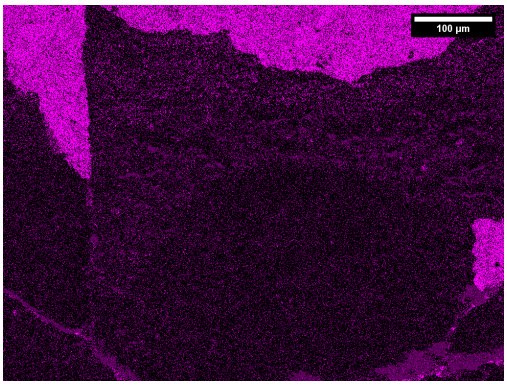
The green box in Figure 6.15 (b) shows the location of Figure 6.17 (a). Figures 6.17 (b–d) are the corresponding EDX maps of W, C and O. The top surface of this section of the laser-damaged spot broke away during testing and the EDX maps highlight the porosity and impurity content beneath where this layer would have been. Figure 6.17 (e) shows the linescan data acquired along the orange line in Figure 6.17 (a). O content increased with sample depth up to approximately 20 at% (the same amount as measured by LECO analysis), which verified the proposed explanation that W oxides near the surface were sublimed during exposure. The remaining porous top layer contained a significant amount of C which decreased with sample depth. It was uncertain whether this was because residual C was more likely to be present near the laser spot after other species had sublimed or evaporated into the plasma, or whether the sublimation of other species produced space for the C-dense phenolic resin to infiltrate.



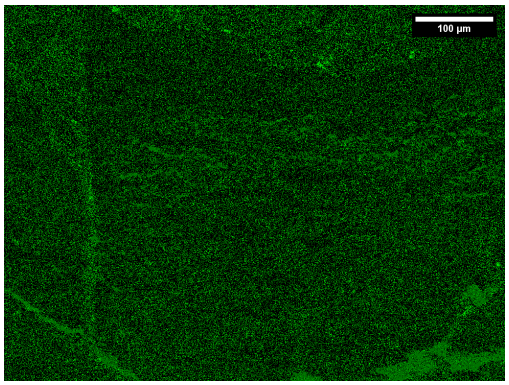
(a) BSE image of laser-damaged area. The orange line denotes the location of the linescan shown in Figure 6.17 (e).



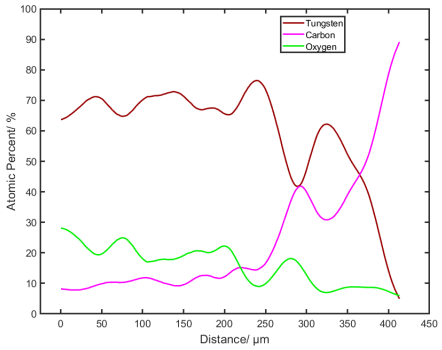
(b) Corresponding EDX map for W.



(c) Corresponding EDX map for C.



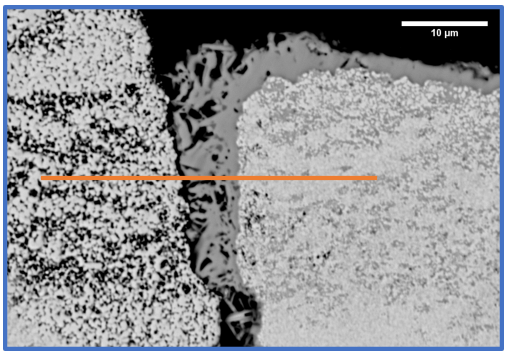
(d) Corresponding EDX map for O.



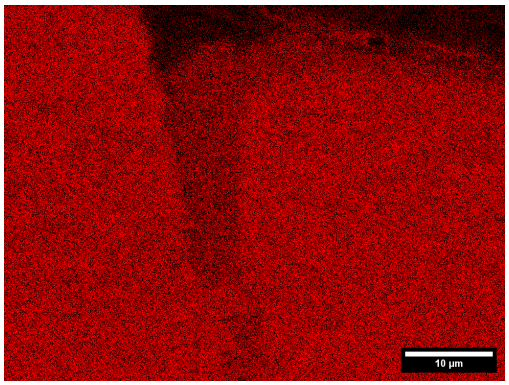
(e) Vertical EDX linescan taken up through laser-damaged area shown by the orange line in Figure 6.17 (a).

Figure 6.17: Cross-sectional SEM and EDX images of H2mm sample.

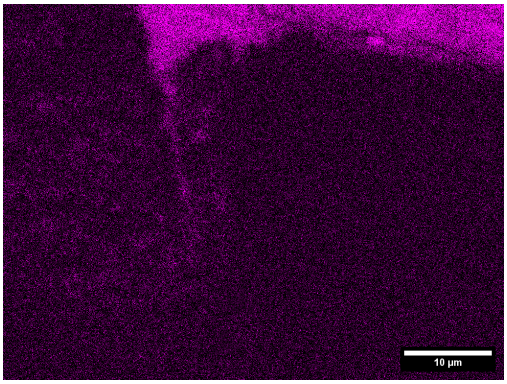
The blue box in Figure 6.16 (c) shows the location of the SEM cross-section in Figure 6.18 (a). Figures 6.18 (b–d) are the corresponding EDX maps of W, C and O. The EDX maps provided a good comparison between the porous regions and oxide regions, as they were highlighted by the C and O maps respectively. The slight speckling in the O map on the right hand side of the image corresponded to slightly darker regions in the W map. Likewise, the left-hand side of the C map corresponded with darker areas on the W map (indicating very little W). These trends were confirmed by the linescan in Figure 6.18 (e), measured along the orange line in Figure 6.18 (a). Pores were likely to be less than 2 µm deep and therefore did not occupy the entire EDX interaction volume. However, W concentration was significantly (∼25%) lower on the left side of the crack than on the right. The steep change in O and C content observed in the linescan corresponds to the change between the mounting resin (C and O) and the W oxide in the crack. On the right hand side of the crack, O concentration approximates to the value determined by LECO (20 at%), but varies corresponding to the brightness (purity) of W seen in the BSE image, Figure 6.18 (a).



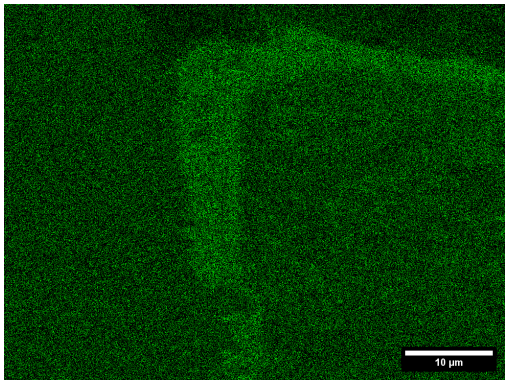
(a) BSE image of laser-damaged area. The orange line denotes the location of the linescan shown in Figure 6.18 (e).



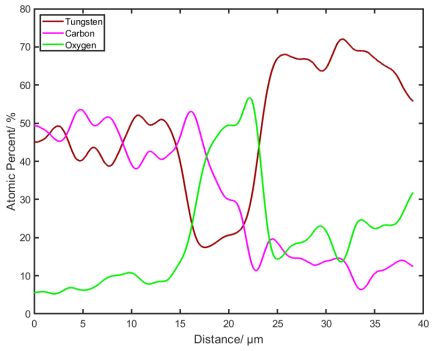
(b) Corresponding EDX map for W.



(c) Corresponding EDX map for C.



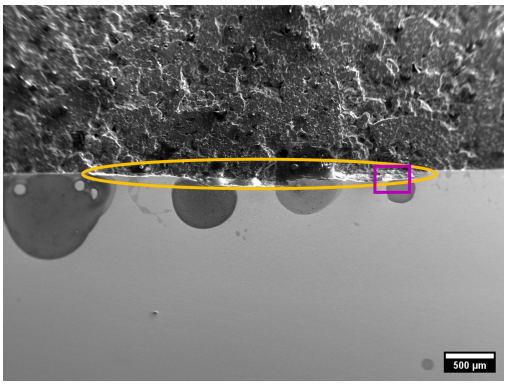
(d) Corresponding EDX map for O.



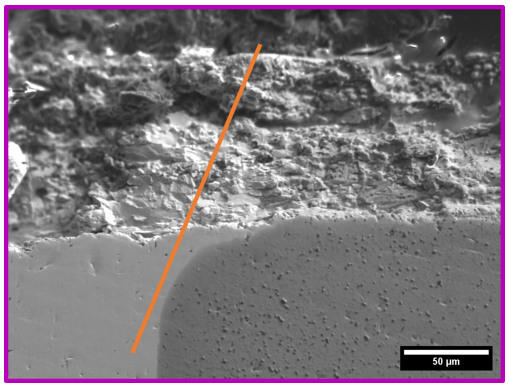
(e) Horizontal EDX linescan taken across crack in laser-damaged area shown by the orange line in Figure 6.18 (a).

Figure 6.18: Cross-sectional SEM and EDX images of W2mm sample.

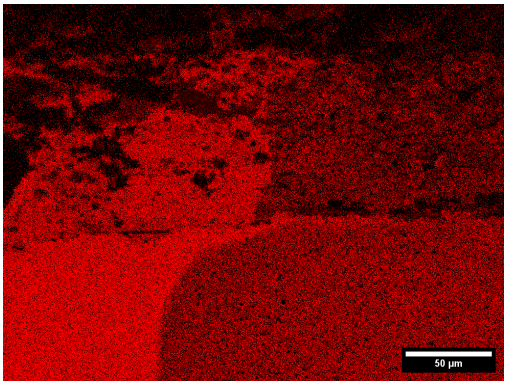
Upon sectioning the reference W sample, the blistered region caused by the laser during testing broke away. Figure 6.19 (a) shows the laser-damaged region, highlighted with a yellow oval. The purple box denotes the location of Figure 6.19 (b). A lamellar microstructure (common for rolled materials) approximately 100 µm thick was observed in the fractured area. It was postulated that the blistered material lifted along the lamellar boundaries and then experienced brittle failure when sectioned and mounted. Figures 6.19 (c–e) show the corresponding W, C and O EDX maps, and Figure 6.19 (f) the linescan data acquired along the orange line in Figure 6.19 (b). Contamination from the phenolic mounting resin around the fractured surface presented a challenge in acquiring reliable data, however it was observed that the O and C concentrations decreased further into the W. The W reference sample had a stated purity of 99.95%, which was why an opposing trend to FAST coatings was seen for O content. C and O both decreased together, which indicated that the signals came from reducing quantities of the phenolic resin, rather than residual oxides or carbides as seen in the FAST samples.



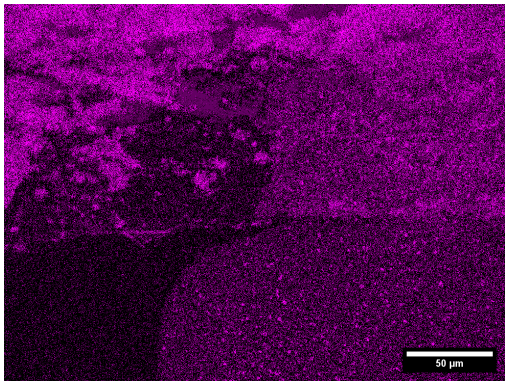
(a) SEM image showing the cross-section of the laser-damage spot at the surface of the reference W sample. The purple box denotes the location of 6.19 (b).



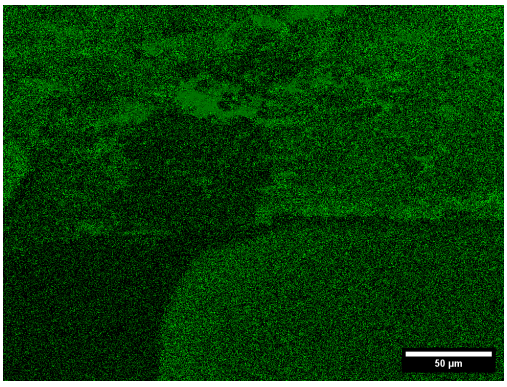
(b) High magnification SEM image of laser-damaged area. The orange line denotes the location of the linescan shown in Figure 6.19 (f).



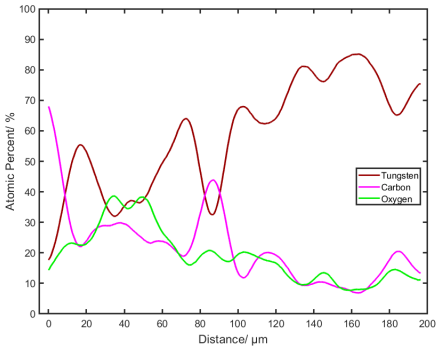
(c) Corresponding EDX map for W.



(d) Corresponding EDX map for C.



(e) Corresponding EDX map for O.

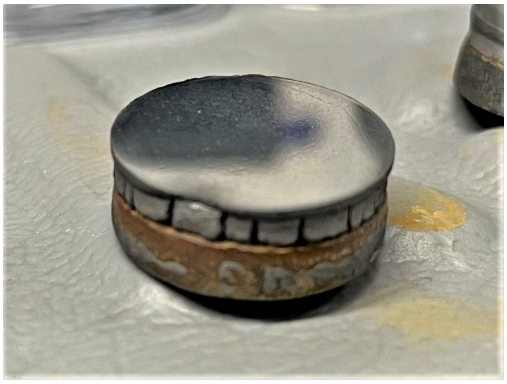


(f) EDX linescan taken across crack in laser-damaged area shown by the orange line in Figure 6.19 (b).

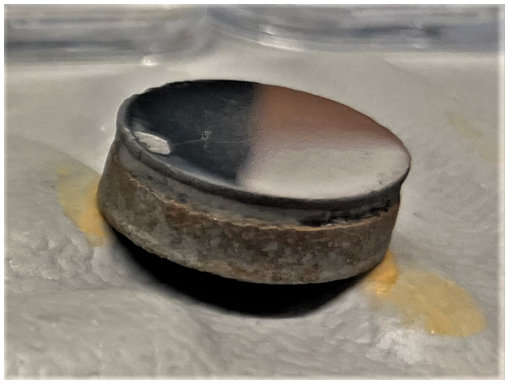
Figure 6.19: Cross-sectional SEM and EDX images of reference W sample.

6.3.2 Sample Repair

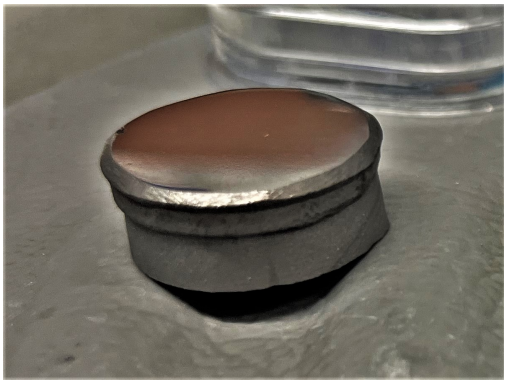
Figure 6.20 shows photographs of samples after they had been repaired in the FAST. Some small surface cracking was observed in both H2mm samples and can be seen in Figures 6.20 (a–b). No surface cracking was observed on either W2mm samples or the repaired reference samples. Cracking was seen in the original W coating at the edge of the sample in both H2mm samples and the repaired reference samples — this occurred during manufacture, most likely when the pressure was initially increased to 50 MPa, causing pre-existing cracks in the already-sintered material to propagate to the edge.



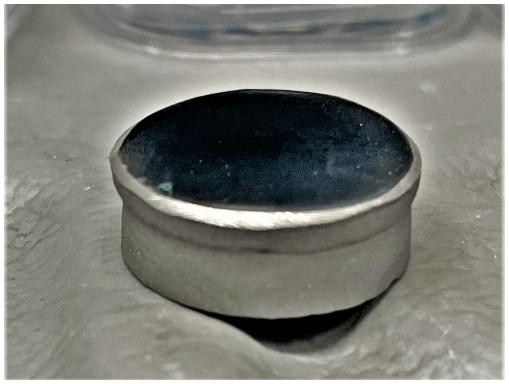
(a) Repaired HIVE-damaged H2mm.



(b) Repaired UPP-damaged H2mm.



(c) Repaired HIVE-damaged W2mm.



(d) Repaired UPP-damaged W2mm.

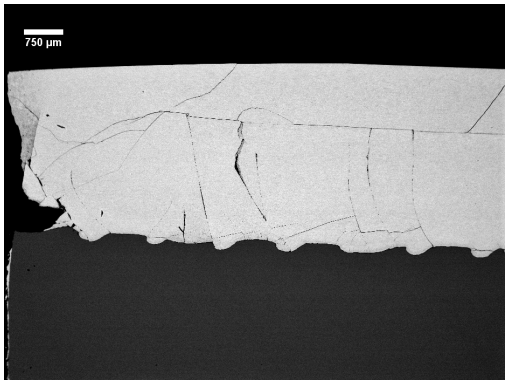


(e) 'Repaired' reference H2mm.

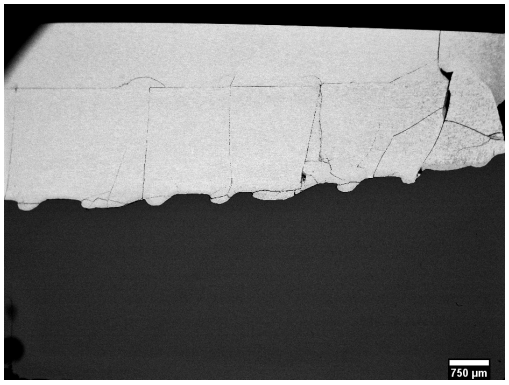
Figure 6.20: Photographs of repaired samples.

Cross-sectional examination of repair

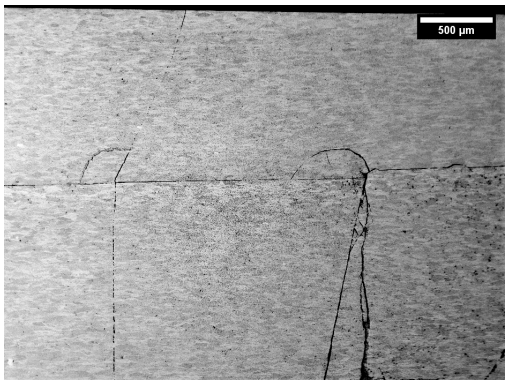
Figure 6.21 shows cross-sectional SEM images of the repaired reference sample. Cracking was prevalent in the original coating and was focussed towards the sample edges, as observed previously in other samples (Figures 5.24 & 5.32). Cracking was vertical in the centre of the sample. When cold, the W nanopowder would have entered the surface cracks (as they were open and the powder would be compacted into the cracks to form a green body). When heated, the W would not have been able to expand to its original shape as the new powder would prevent the cracks from closing, and would therefore expand in the only other direction — towards the steel as demonstrated in Figures 6.21 (a–b); this would have become more pronounced once the steel began to contract in the same direction once sintering was complete. To compensate for the bowing steel, the original W coating repositioned itself in 'columns' along pre-existing cracks in order to maintain contact with both the steel and the new coating (which could reconfigure somewhat during sintering, as the powder would not have yet been fully dense). The resulting steps at the interface between the two W coatings was observed in Figures 6.21 (c–d). Figure 6.22 shows schematic illustrations of the crack development process during the lifetime of the samples.



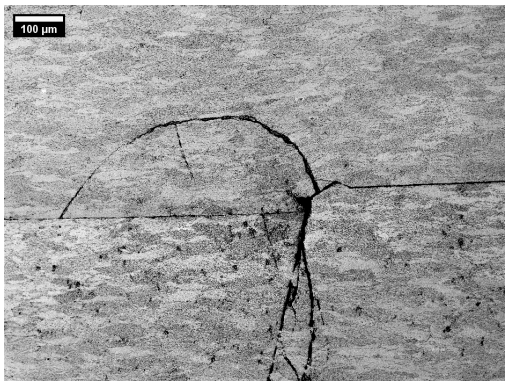
(a) BSE image showing the left side of the sample, with the steel bowing in the centre.



(b) BSE image showing the right edge of the sample, with the steel bowing in the centre.

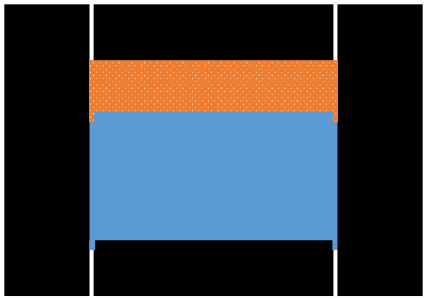


(c) BSE image of vertical cracks in original coating causing further cracking in new interface.

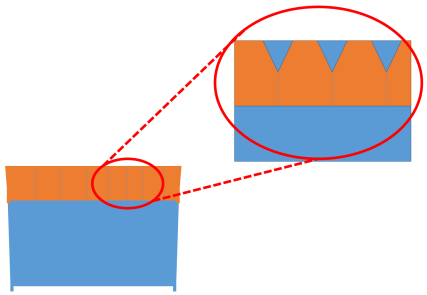


(d) BSE image of vertical crack facilitating interface 'step' between the two coatings in order to maintain contact.

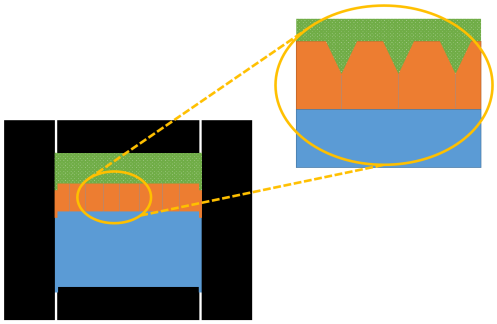
Figure 6.21: Cross-sectional SEM images of 'repaired' reference H2mm sample.



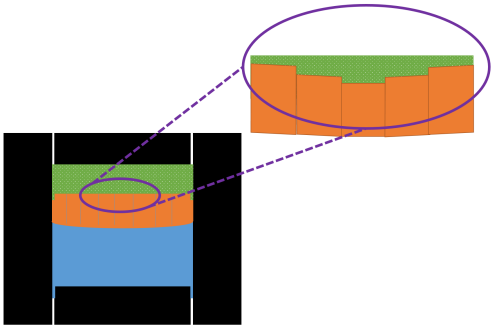
(a) 'Tails' are produced at bottom of coating and substrate due to applied pressure and higher CTE of steel (in comparison to graphite), respectively.



(b) Cracks in the W form upon cooling to relieve thermal stresses, which allow the W and steel to bend more than they otherwise would (W coating is much more compliant).



(c) New W powder is pushed around edges of original W coating and fill in surface cracks.



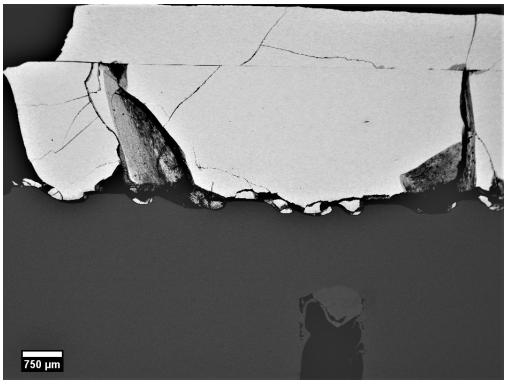
(d) Steel 'tails' are even more prominent. Combination of applied pressure and filled cracks force steel to bow downwards. Vertical segmentation in the W allows steps to form in order to maintain contact.

Figure 6.22: Schematic illustrations showing crack development across sample lifetime.

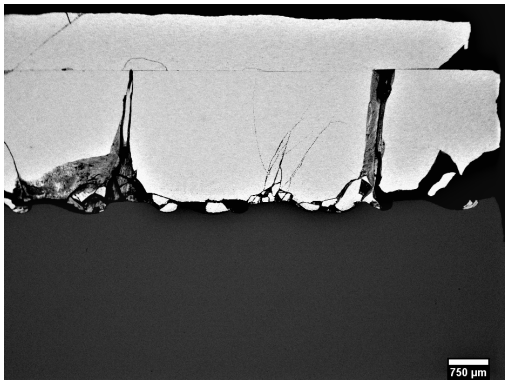
In Figure 6.23 cross-sectional SEM images of the repaired H2mm sample tested in HIVE are presented. Cracking was more prominent than observed in the non-repair sample in Figure 5.24 (a); the large missing chunks at the interface broke away during sectioning. The damage arose from pre-existing cracks that were interconnected, allowing the segment to fall out when sectioned. The formation of the cracks in the original W layer matched those seen in the non-repaired, HIVE-damaged H2mm sample, shown in Figures 5.24 (a). There were fewer cracks in the new W coating, as was the case for the repaired reference sample, but new cracks appeared to have originated from cracks in the original coating which acted as stress concentrators. This was illustrated particularly clearly in Figure 6.23 (d).

Figures 6.24 (a–b) show cross-sectional SEM images of the repaired H2mm sample that was laser-damaged in UPP. Cracking was prominent, as in the equivalent HIVE-damaged sample, and occurred during sectioning and mounting in resin. This sample exhibited significantly more damaged than the cracking seen in the non-repaired, UPP-damaged H2mm sample in Figure 6.15, indicating that further cracking may have occurred during repair sintering due to the high pressures employed in this process.

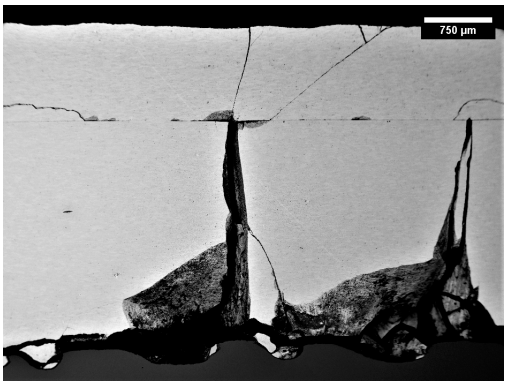
The laser-damaged spot was investigated in Figure 6.24 (c). Further cracking had occurred nearby and the repair W was well incorporated into the damaged area. Figure 6.24 (d) shows the boundary between the two W coatings at higher magnification. It was believed that the raised area in the bottom right of the image was the surface of the original W coating after testing in UPP (not necessarily the original surface of the coating). The pressure during sintering may have pushed repair W into the damaged spot, dislodging the original surface, as seen by the



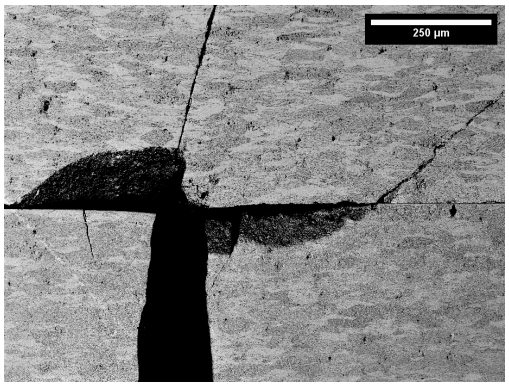
(a) BSE image of cross-section of left side of HIVE-damaged sample. Large chunks broke away from the interface during sectioning.



(b) BSE image of cross-section of left side of HIVE-damaged sample. Crack formations similar to those predicted in Chapter 3 were observed.



(c) BSE image of the centre of the HIVE-damaged sample. Vertical cracks initiated new cracks in the new coating.



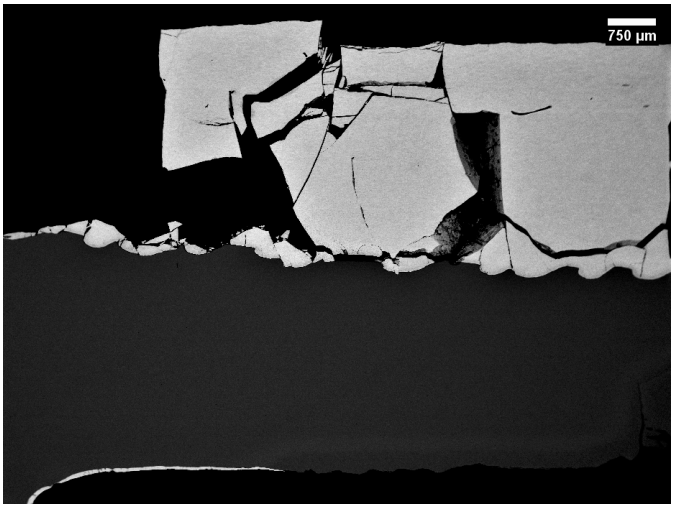
(d) Higher magnification BSE image of new coating interface highlighting crack propagation in new coating that arose from pre-existing cracks.

Figure 6.23: Cross-sectional SEM images of a repaired, HIVE-damaged H2mm sample.

semi-circular crack in Figure 6.24 (c). The newer W above it appeared to be more porous due to poor local packing density of the W powder, due to the local change in geometry when the old surface moved. Figure 6.24 (e) shows the original W coating at a higher magnification for comparison new, undamaged W as shown in Figure 6.24 (f). Faceted particle growth was apparent in the damaged W, whereas open porosity was seen in the newer W.

Figure 6.25 shows cross-sectional SEM images of the repaired, HIVE-damaged W2mm sample. Each layer of W was individually distinguishable. The W substrate was much brighter than the FAST W coatings in the BSE images shown in Figure 6.25 (a–b), indicating that it was purer. From examination in Figures 6.25 (c–d) of the interface between the two W coatings (denoted by the blue arrows) at higher magnifications, very little difference was seen between the two coatings other than the slightly darker appearance of the repair coating, which indicated a marginally lower W concentration.

Figures 6.25 (e–f) show the location (green line) and results of an EDX linescan taken across the three W regions to quantify the variation in composition and therefore the quality of both the coating and the repair. There was a noticeable decrease in W concentration between the substrate and original coating, which corresponded with an increase in O content; which corroborated well with the values obtained from the LECO testing, found in Table 5.3. A large peak was observed at the substrate interface as suspected surface oxidation had occurred prior to sintering. The O signal corresponding to the substrate W in the linescan was artifically elevated due to noise; this was confirmed by an EDX spectrum taken in the respective area which produced a value in the region of 2.1–2.7 at% O. This

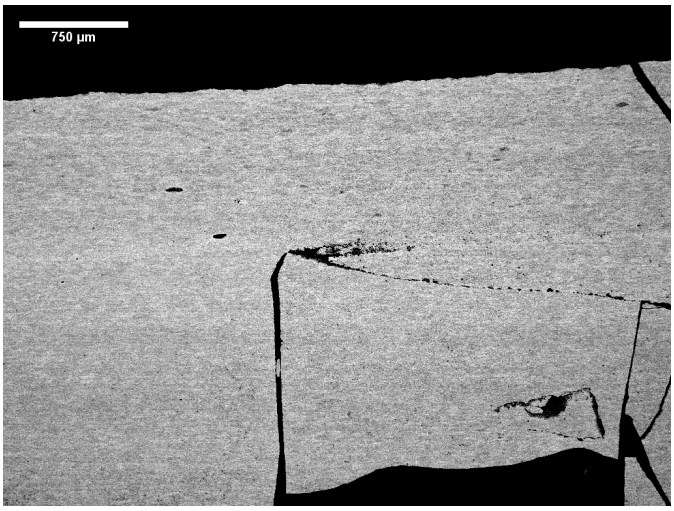


(a) BSE image of H2mm sample. Significant amounts of delamination occurred at both interfaces.

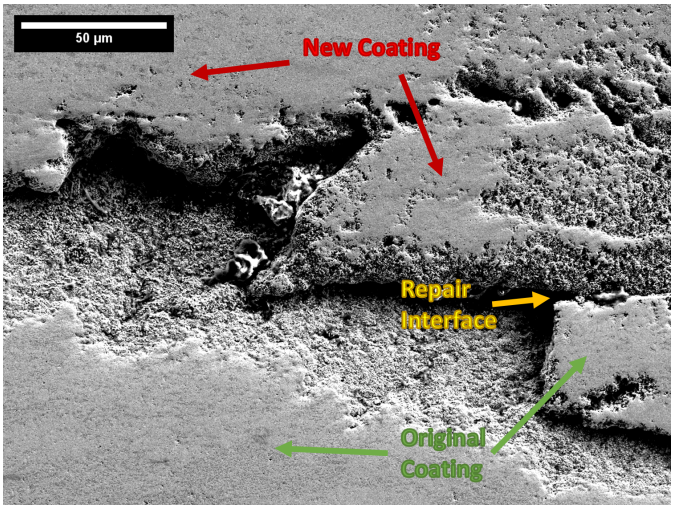


(b) BSE image of H2mm sample. Several vertical and horizontal cracks were observed and lead to large sections of coating breaking away.

Figure 6.24: Cross-sectional SEM images of a repaired, UPP-Damaged H2mm sample.

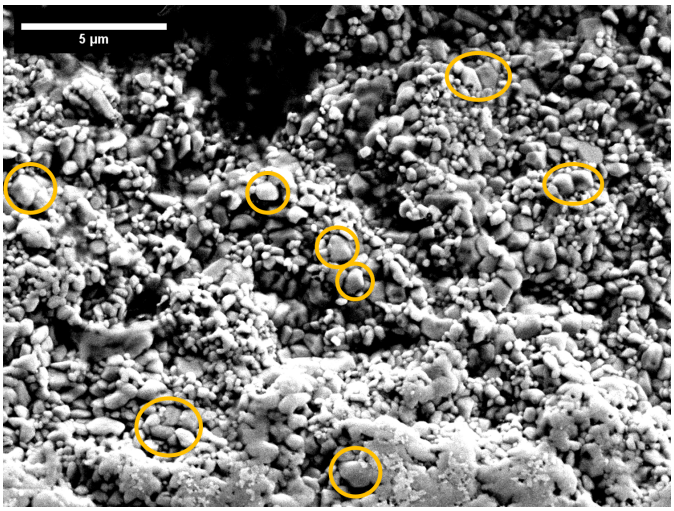


(c) BSE image of the edge of the laser-damaged spot. A vertical crack reached the edge of the spot and a semi-circular crack propagated as the original coating was shifted during repair sintering.

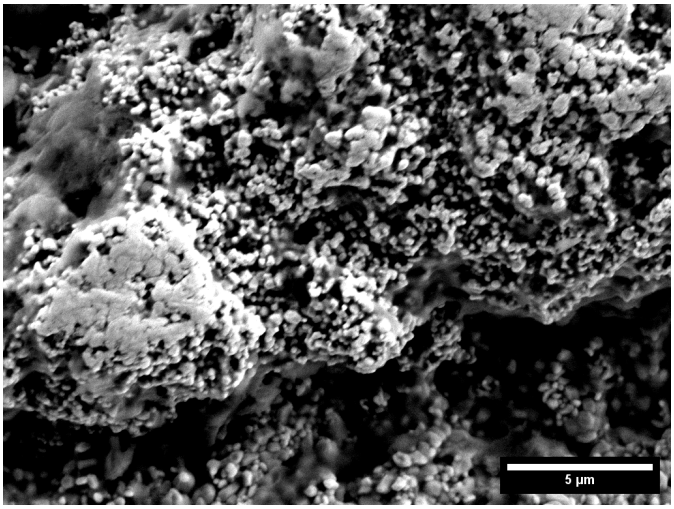


(d) Higher magnification BSE image of edge of laser damage spot. Porosity was observed in the new W coating in contact with damaged layer because the damage layer shifted and reduced the new powder packing density.

Figure 6.24: Cross-sectional SEM images of a repaired, UPP-Damaged H2mm sample.



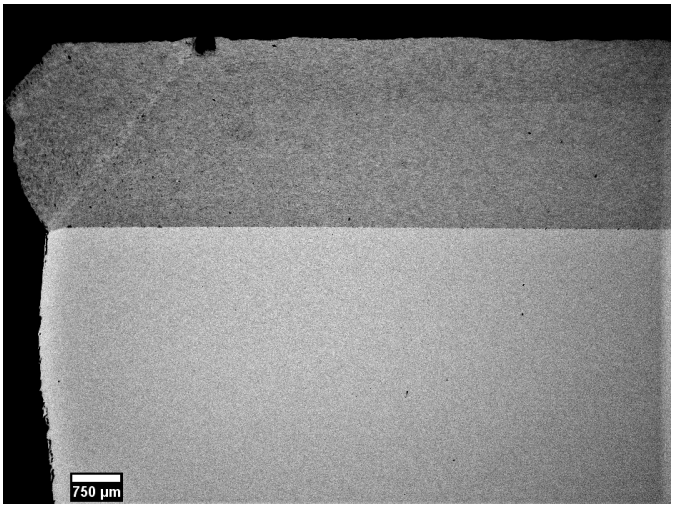
(e) High magnification BSE image of laser-damaged material. Significant faceted particle growth was observed (highlighted in yellow).



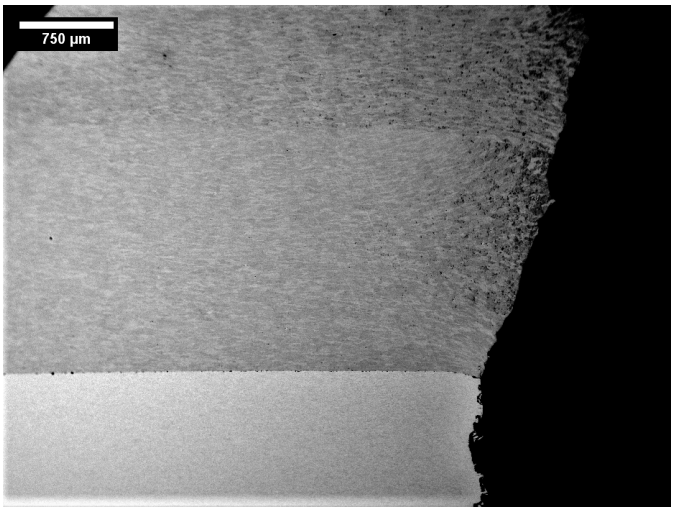
(f) High magnification BSE image of new repair material. Particles were much smaller and more porosity was observed.

Figure 6.24: Cross-sectional SEM images of a repaired, UPP-Damaged H2mm sample.

was at the limits of detection, as the O peak was not recognised by the AutoID function in the Aztec EDX software, so O content was likely to be lower. The O content in the FAST W was consistent across both coatings, however a peak was again identified at the interface between the two coatings.

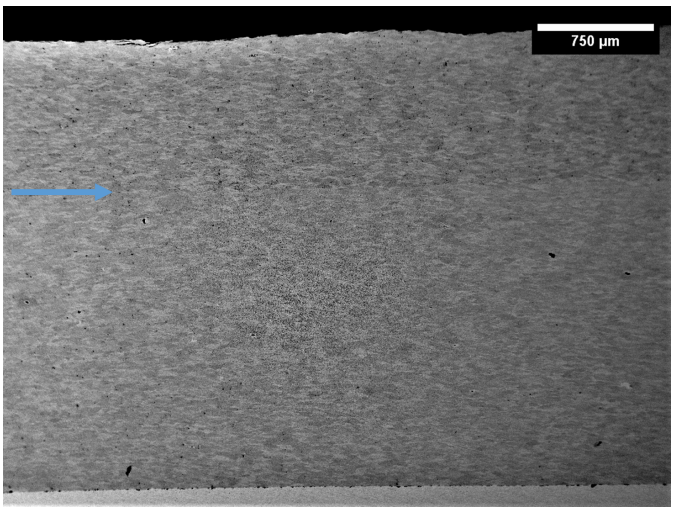


(a) BSE image of repaired HIVE-damaged W2mm sample. No cracking or delamination was observed.

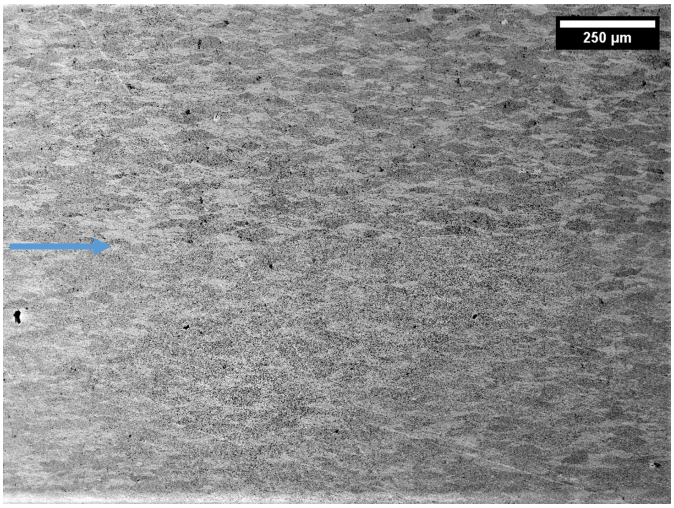


(b) BSE image of repaired HIVE-damaged W2mm sample. Some porosity was observed at the edge of the W coatings.

Figure 6.25: Cross-sectional SEM images and EDX linescan of a repaired, HIVE-damaged W2mm sample.

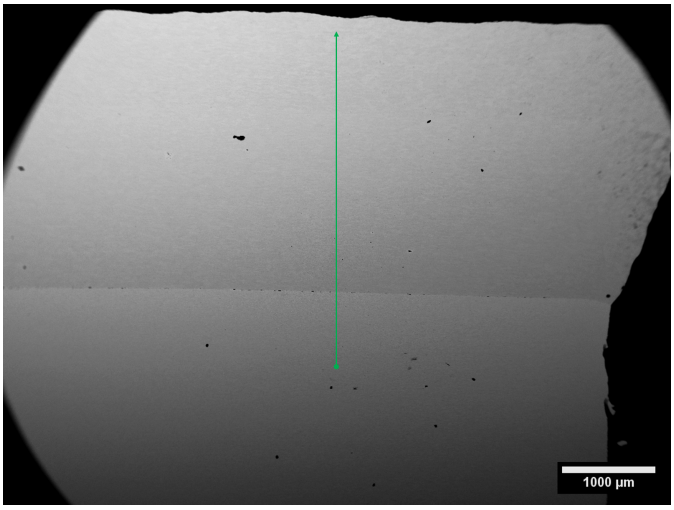


(c) BSE image of repair coating interface indicated by blue arrow.

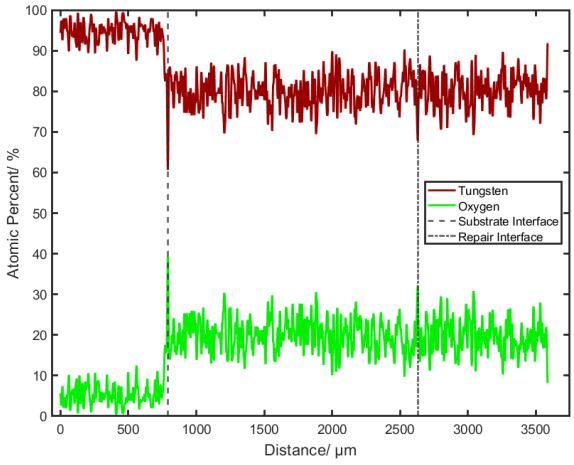


(d) Higher magnification BSE image of repair interface highlighted by blue arrow.

Figure 6.25: Cross-sectional SEM images and EDX linescan of a repaired, HIVE-damaged W2mm sample.



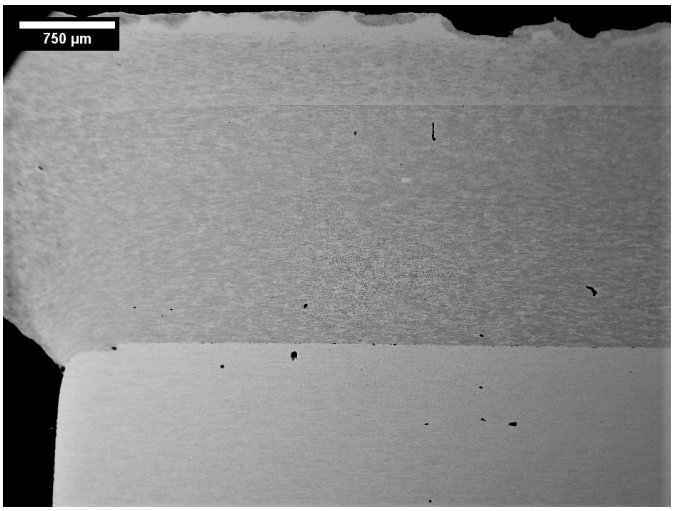
(e) BSE image showing location of line scan across all three W layers with green line.



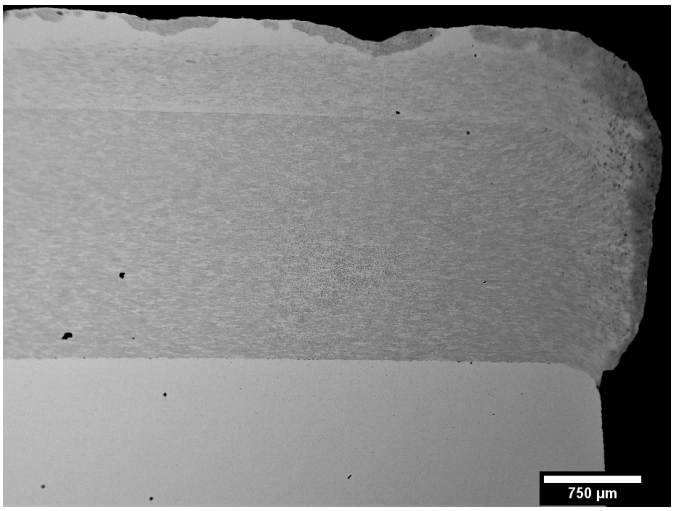
(f) Linescan data acquired from green line in Figure 6.25 (e).

Figure 6.25: Cross-sectional SEM images and EDX linescan of a repaired, HIVE-damaged W2mm sample.

For the repaired, W2mm sample that was laser-damaged in UPP, the cross-sectional SEM images in Figures 6.26 (a–b) indicated that, as with the HIVE-damaged equivalent sample, there was a distinct difference in appearance of the three layers of W. Locating the laser spot to take micrographs was particularly difficult, as residual damage was minimal after repair. Figure 6.26 (c) shows the whole laser target area with coloured boxes that correspond to higher magnification images taken across this region shown in Figures 6.26 (d–f). The characteristic, denser (brighter in BSE) original top layer formed as a result of the laser damage was clearly visible, and very little porosity was seen at the boundary. Cracks from the laser-damaged spot into the original W coating were visible for ∼50 µm, and were then too difficult to track as the purity of the W decreased meaning there was less contrast between the crack and the W. Cracks were sealed and slightly filled by the repair coating. Notably, no cracks propagated into the repair layer of W.

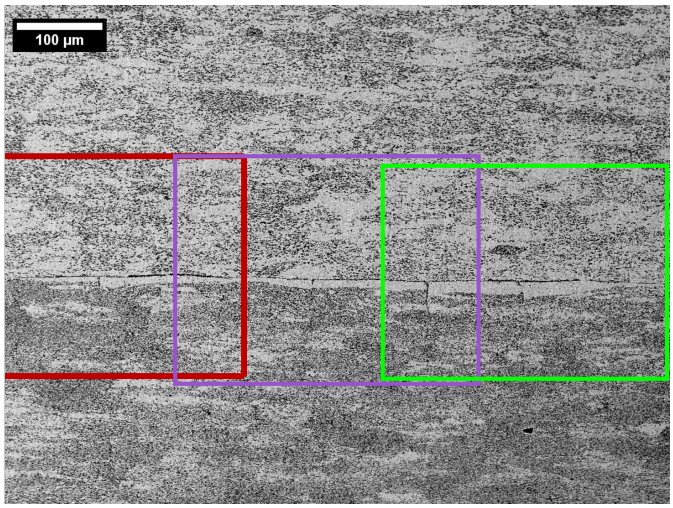


(a) BSE image of repaired, UPP-damaged W2mm sample. No delamination was observed.

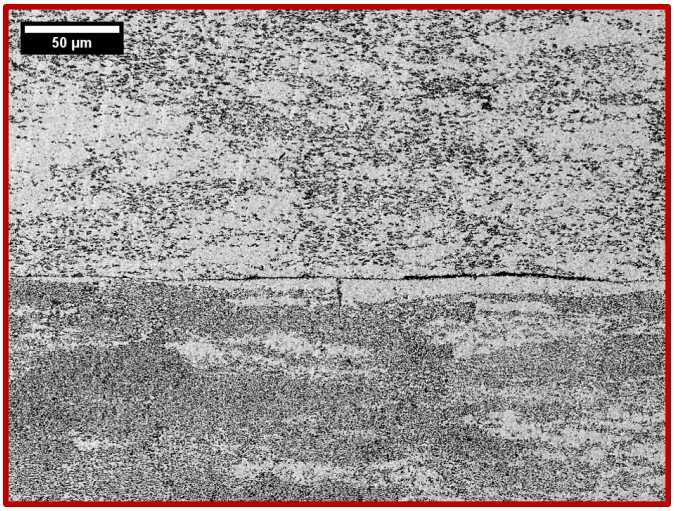


(b) BSE image of repaired, UPP-damaged W2mm sample. Dark regions at surface were suspected porosity infiltrated by phenolic resin or cleaning product (e.g. ethanol).

Figure 6.26: Cross-sectional SEM images of a repaired, UPP-Damaged W2mm sample.

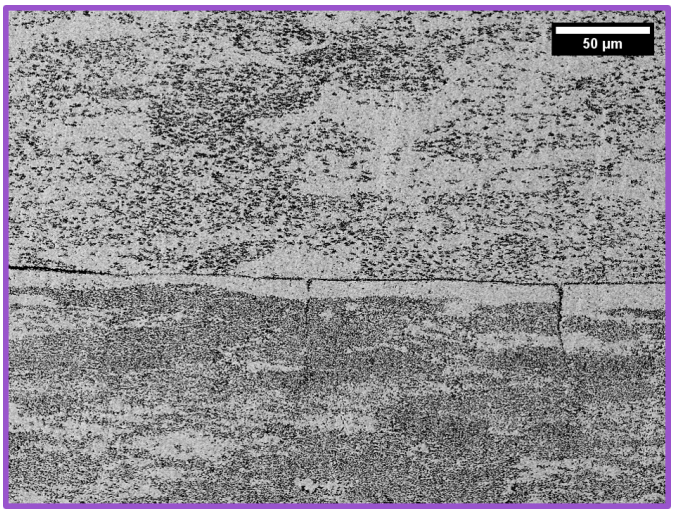


(c) BSE image showing whole laser-damaged spot in repaired, UPP-damaged W2mm sample. The coloured boxes denote the locations of Figures 6.26 (d–f).

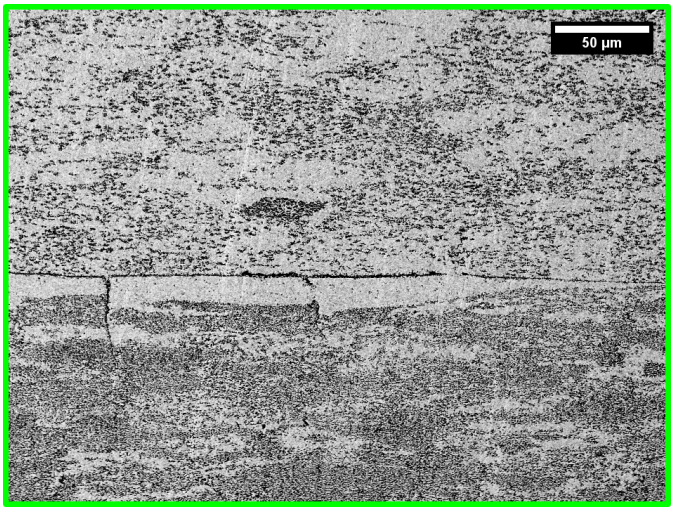


(d) BSE image showing left side of laser-damaged spot. A slight gap between the damaged layer and the new W coating was observed.

Figure 6.26: Cross-sectional SEM images of a repaired, UPP-Damaged W2mm sample.



(e) BSE image showing centre of laser spot. Small amounts of cracking into the original W coating were observed to have sealed.



(f) BSE imaging showing right side of damaged area. A brighter W surface layer was seen as with previous UPP-damaged coatings.

Figure 6.26: Cross-sectional SEM images of a repaired, UPP-Damaged W2mm sample.

6.3.3 Further Damage

Prior to re-testing in HIVE, coating surfaces were polished. Small cracks were observed on the surface of the previously-damaged H2mm samples, but no cracks were seen on the W2mm and the repaired, undamaged reference H2mm sample, as seen in Figure 6.20.

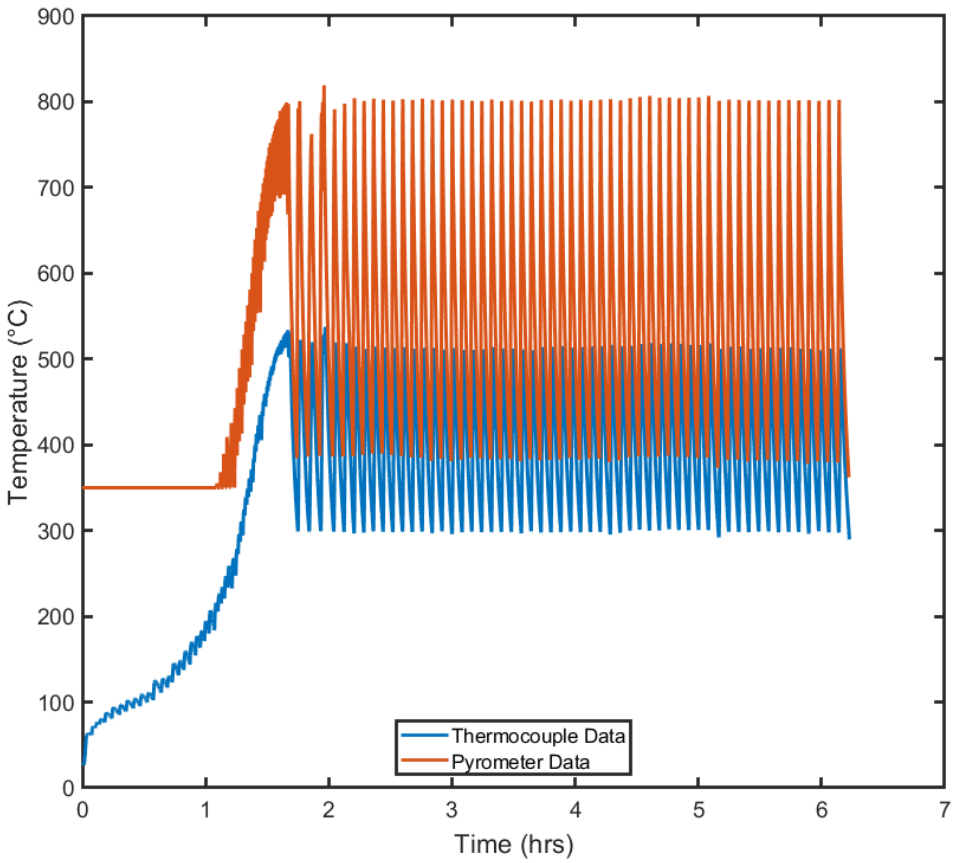
In-situ analysis during thermal cycling

Figure 6.27 (a) shows the thermocouple and pyrometer data measured for the repaired, UPP-damaged H2mm sample during testing in HIVE. The pyrometer data was representative for all samples, and (as seen previously in Figure 5.17) cycled between 350–800 °C, as 350 °C was the lower operating limit of the pyrometer. The initial temperature ramping region indicates the preliminary treatment to out-gas the samples, as seen by the corresponding increase in vacuum in Figures 5.17 (b–f). The temperature at the back of the substrate was between 300–500 °C for the repaired reference H2mm sample and the repaired, UPP-damaged H2mm sample as measured by the thermocouple. This was a similar maximum temperature to the H4mm samples seen in the preliminary HIVE testing; this indicated that the increased W coating thickness (from the repair) once again acted as thermal armour (as desired). The MACOR® mount broke at the end of commissioning for the repaired reference sample, as marked in the left side plot in Figure 6.27 (b); however this 'pre-exposure' did not appear to impact the sample negatively during the full test, as the second commissioning pulses were near-identical and the measured temperature range of the thermocouple was consistent throughout.

In comparison, the substrate temperature for the repaired, HIVE-damaged H2mm sample cycled between 300–400 °C. Two thermocouple joints survived for this sample and their readings closely agreed, providing confidence that the true temperature was measured. This temperature range aligned more closely with the F2mm sample from the initial HIVE testing where the coating had delaminated. The vacuum spike towards the end of the commissioning pulses also matched the F2mm sample data. It was suspected that the sample might also delaminate during testing, but it survived and did not delaminate upon removal from the vacuum.

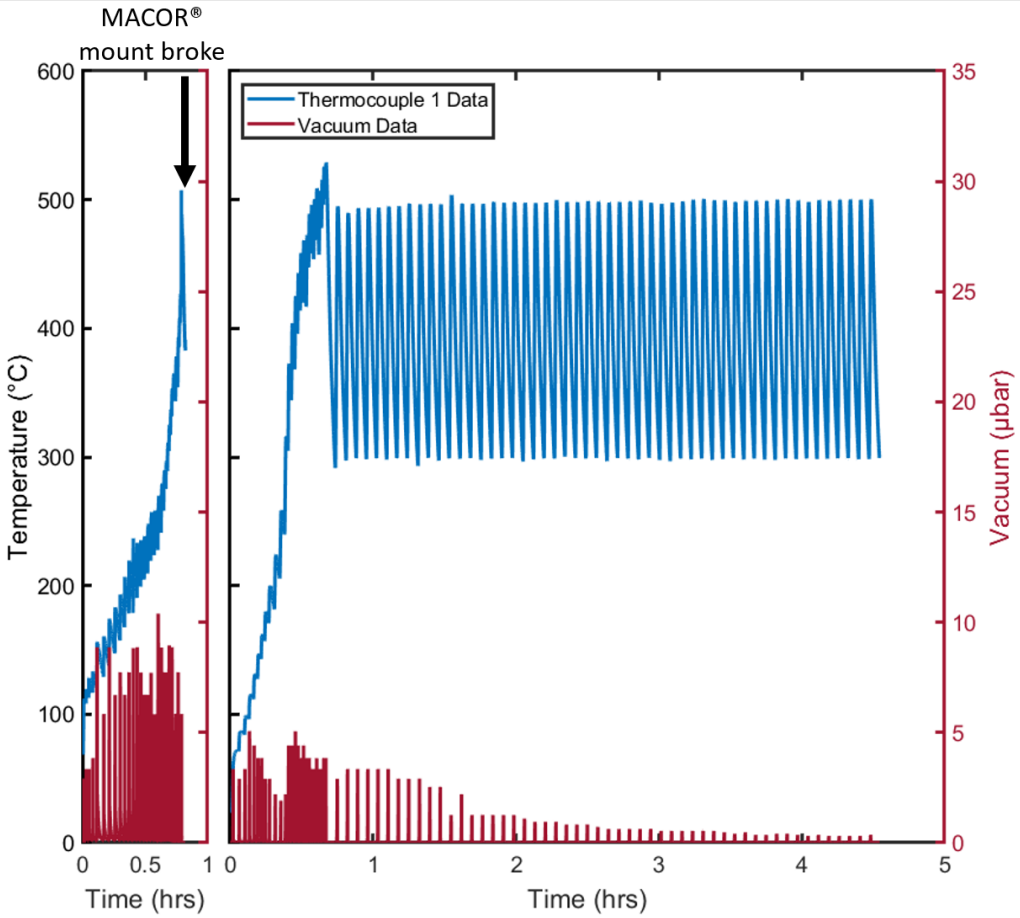
The W substrate samples effectively transferred heat through to the steel, as the thermocouple temperature closely matched the coating surface temperature. This was very similar to the H2mm and W2mm samples investigated previously in Section 5.3.2 that effectively transferred the heat to the substrate. Vacuum levels were also consistently lower for these samples than the steel substrate samples.

Figure 6.28 shows frames captured (from optical video recordings) at peak temperature during thermal cycling for comparison with Figure 5.18. The repaired reference H2mm sample substrate turned a dull red (similar to the H4mm sample shown in Figure 5.18 (c) previously) but the repaired HIVE-damaged H2mm sample substrate did not appear to change colour (similar to the F2mm sample shown in Figure 5.18 (a) previously). The W substrate samples were the same colour throughout and mirrored the H2mm in Figure 5.18 (b).



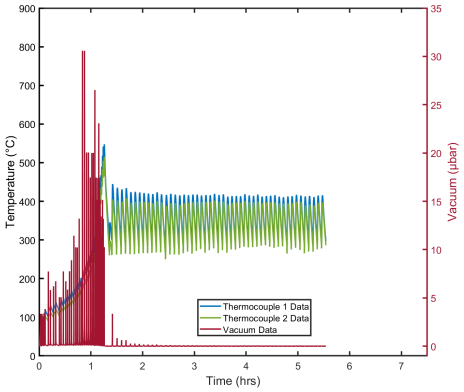
(a) Thermocouple and pyrometer data collected from the repaired, UPP-damaged H2mm sample, for which the pyrometer data was representative for each HIVE experiment. The abrupt cut-off at the end of each pyrometer cycle was because the temperature has dropped below the lower operation limit of 350 °C.

Figure 6.27: Comparisons between: (a) pyrometer and thermocouple data and (b–e) thermocouple and vacuum data for different sample types.

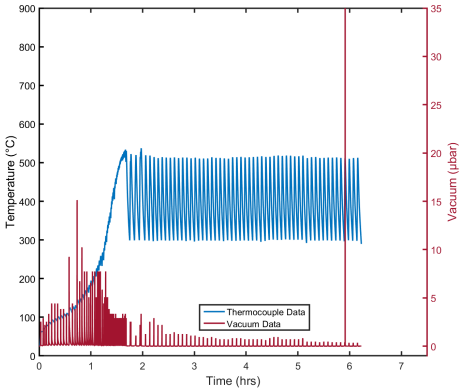


(b) Thermocouple temperature and vacuum profile for repaired reference H2mm sample. The MACOR® mount broke during commissioning (left plot) but did not seem to affect the sample as the second commissioning ramp aligns well with the first and remained consistent throughout the rest of testing.

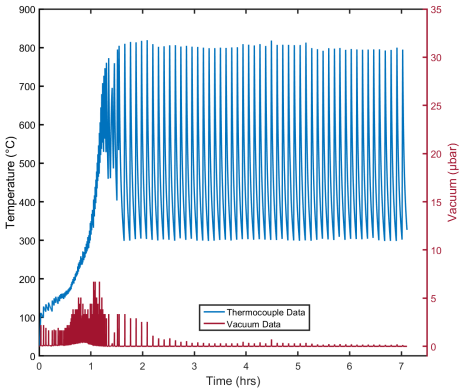
Figure 6.27: Comparisons between: (a) pyrometer and thermocouple data and (b–f) thermocouple and vacuum data for different sample types.



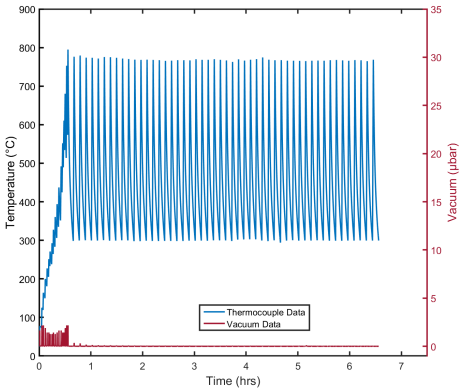
(c) Thermocouple temperature and vacuum profile for repaired, HIVE-damaged H2mm sample.



(d) Thermocouple temperature and vacuum profile for repaired, UPP-damaged H2mm sample.

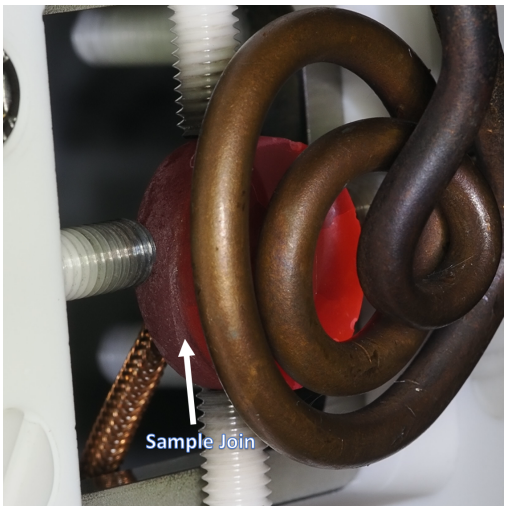


(e) Thermocouple temperature and vacuum profile for repaired, HIVE-damaged W2mm sample.

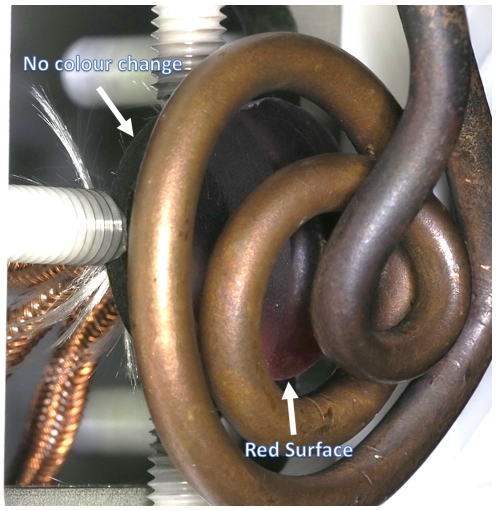


(f) Thermocouple temperature and vacuum profile for repaired, UPP-damaged W2mm sample.

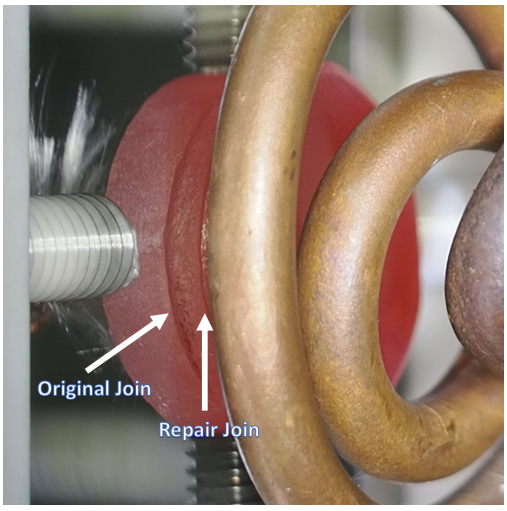
Figure 6.27: Comparisons between: (a) pyrometer and thermocouple data and (b–f) thermocouple and vacuum data for different sample types.



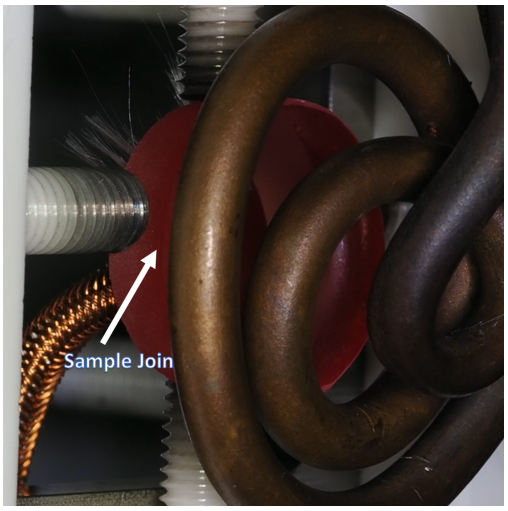
(a) Repaired reference H2mm sample.



(b) Repaired, HIVE-damaged H2mm sample.



(c) Repaired, HIVE-damaged W2mm sample.



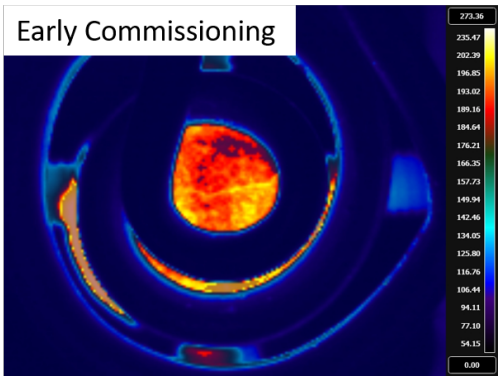
(d) Repaired, UPP-damaged W2mm sample.

Figure 6.28: Photographs of the side of samples during HIVE testing.

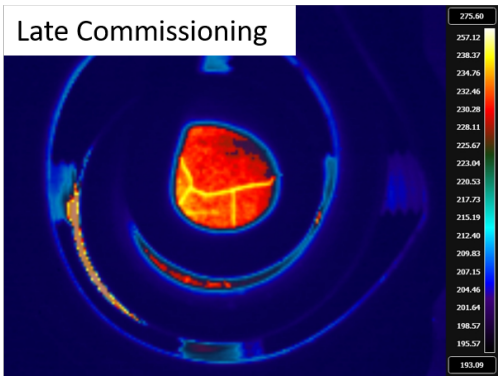
Infrared in-situ imaging was again used to confirm at what point in the cycling process a sample initially cracked. This technique highlighted larger cracks particularly clearly due to the change in emissivity related to a change in topography, explained in Section 5.3.2. Figure 6.29 (a–c) shows that cracking initially occurred and developed during commissioning but did not develop further during the main thermal cycling.

Figure 6.29 (d) highlights a crack that existed prior to testing in the repaired, HIVE-damaged H2mm sample. The frame was from the final pulse and no further cracking was observed during testing. This again supported the theory that the coating may have delaminated, as no cracking was observed in the F2mm sample previously in Section 5.3.2.

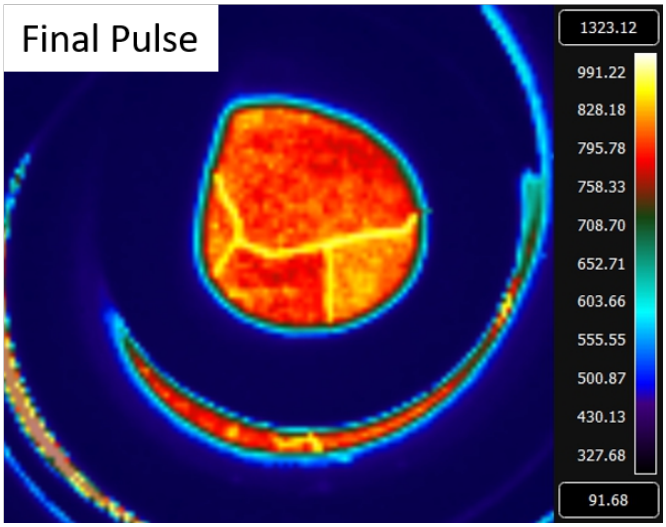
Figure 6.29 (e) shows cracking that occurred during commissioning for the repaired, UPP-damaged H2mm sample. Neither W substrate sample formed any vertical cracks, due to a lack of mismatch strains and stresses as seen previously for the W2mm samples.



(a) IR capture towards the start of commissioning pulses for the repaired reference H2mm sample.

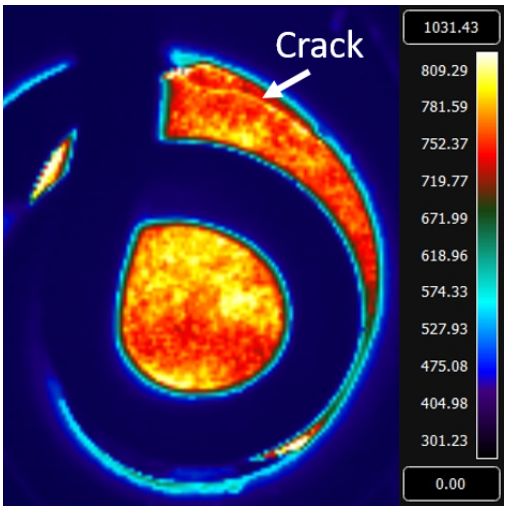


(b) IR capture towards the end of commissioning pulses for the repaired reference H2mm sample.

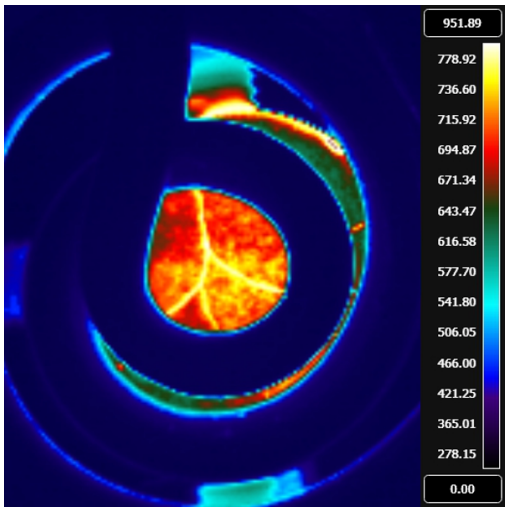


(c) IR capture of final pulse for the repaired reference H2mm sample.

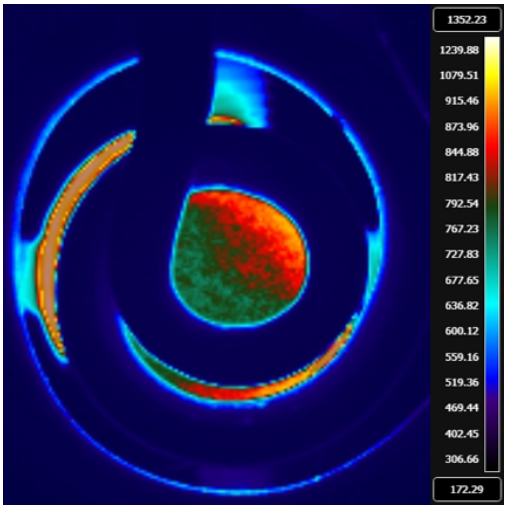
Figure 6.29: IR frames of different samples taken at the moment of maximum temperature at the peak of a cyclic heat pulse in HIVE testing.



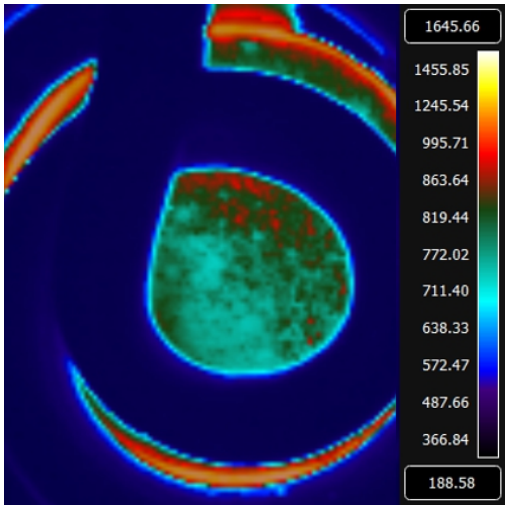
(d) Repaired, HIVE-damaged H2mm sample.



(e) Repaired, UPP-damaged H2mm sample.



(f) Repaired, HIVE-damaged W2mm sample.



(g) Repaired, UPP-damaged W2mm sample.

Figure 6.29: Frames of different samples taken at the moment of maximum temperature at the peak of a cyclic heat pulse in HIVE testing.

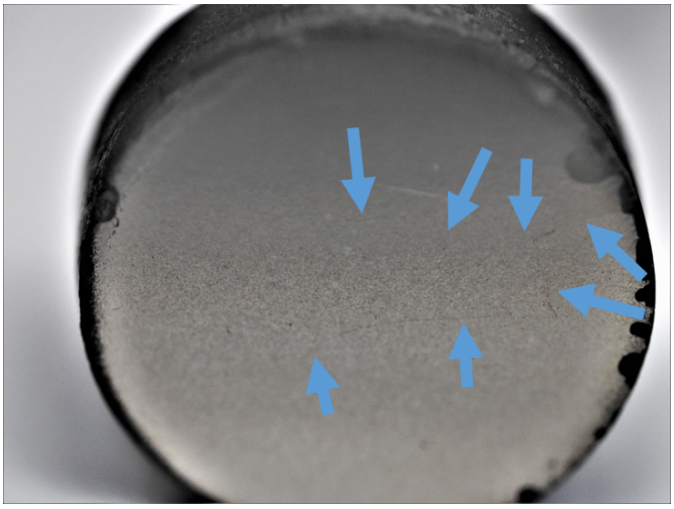
Surface crack analysis

Figure 6.30 shows photographs taken of the repaired H2mm samples after testing. Cracking was very fine and difficult to observe in the repaired reference sample shown in Figure 6.30 (a). Figure 6.30 (b) illustrates the pre-existing crack for the repaired, HIVE-damaged H2mm sample that did not change during testing. Figure 6.30 (c) shows a network of cracks on the surface of the repaired, UPP-damaged H2mm sample that were again more difficult to observe than the equivalent HIVE-damaged sample because they were finer. W substrate samples showed no signs of cracking occurring during or after testing.

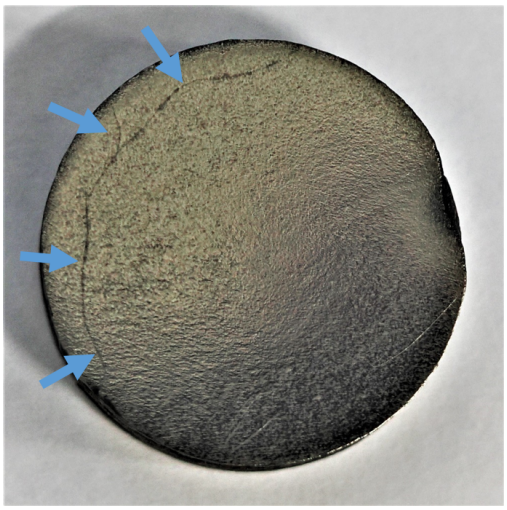
Figure 6.31 comprises SEM images of the surfaces of the repaired samples following further testing in HIVE. Figure 6.31 (a) shows the repaired reference H2mm sample; cracking was fine and difficult to observe even at the higher magnification of the inset.

Figures 6.31 (b–c) are images of the repaired HIVE- and UPP-damaged H2mm samples, where cracking was more pronounced. In the HIVE-damaged sample no cracking was observed beyond the pre-existing crack discussed above for Figure 6.30 (b). The UPP-damaged sample had a wide network of relatively fine cracks, with some areas exhibiting higher levels of damage. The inset in Figure 6.31 (c) enlarges a section of the surface where parts of the coating around the crack had chipped out; other sections had lifted and become wedged elsewhere, as seen previously in Figure 5.21 (b) for the H2mm sample in HIVE.

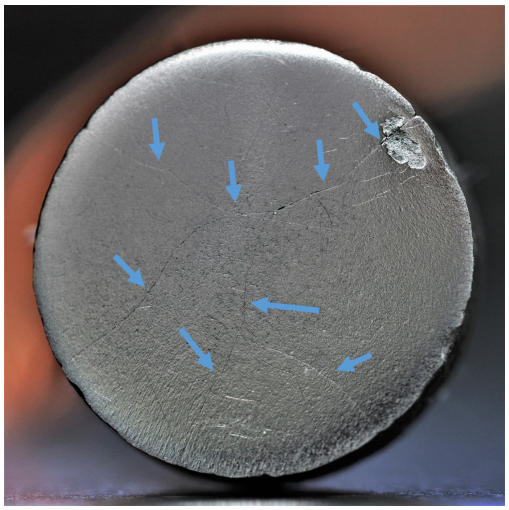
Figures 6.31 (d–e) show the repaired W substrate samples. No cracking was observed anywhere on the surfaces of these samples.



(a) Surface of the repaired reference H2mm sample following testing.

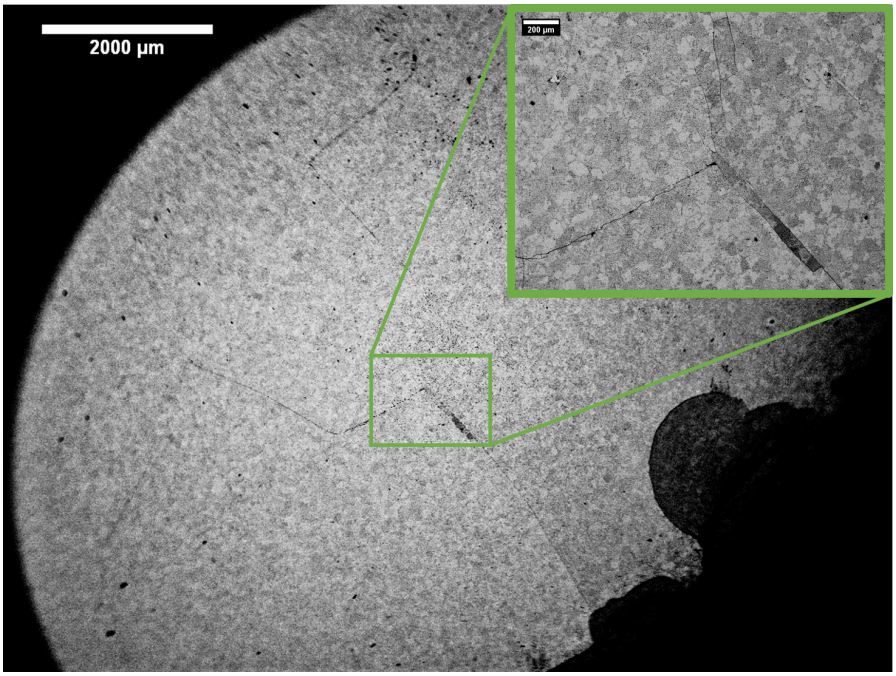


(b) Surface of the repaired, HIVE-damaged H2mm sample following testing.



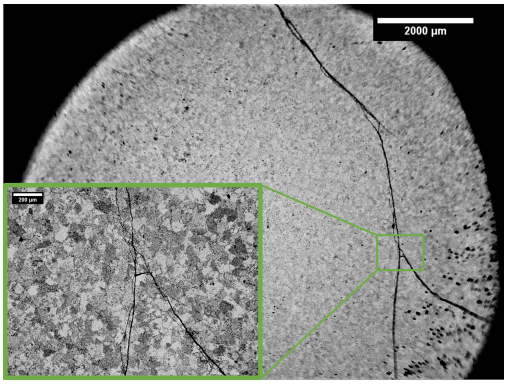
(c) Surface of the repaired, UPP-damaged H2mm sample following testing.

Figure 6.30: Photographs of the repaired H2mm samples after testing in HIVE. Arrows highlight crack locations.

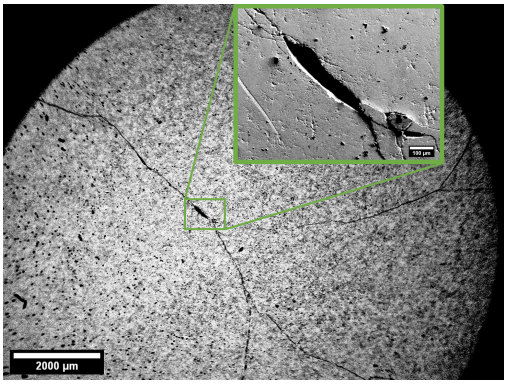


(a) Surface of the repaired reference H2mm sample following testing.

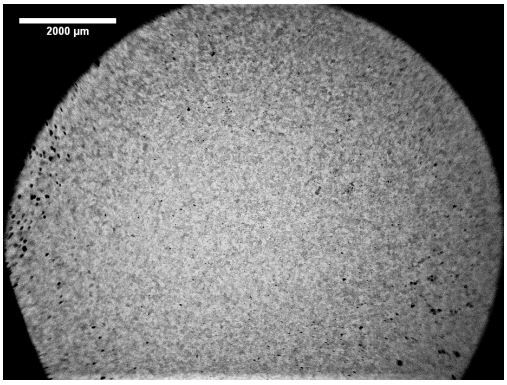
Figure 6.31: SEM images of the surface of the repaired samples after testing in HIVE.



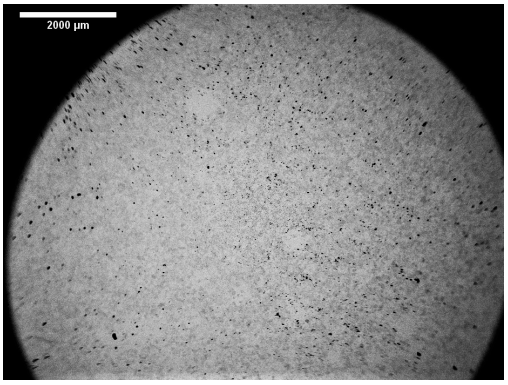
(b) Surface of the repaired, HIVE-damaged H2mm sample following testing.



(c) Surface of the repaired, UPP-damaged H2mm sample following testing.



(d) Surface of the repaired, HIVE-damaged W2mm sample following testing.



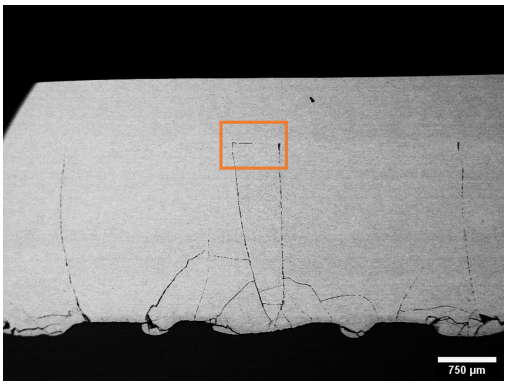
(e) Surface of the repaired, UPP-damaged W2mm sample following testing.

Figure 6.31: SEM images of the surface of the repaired samples after testing in HIVE.

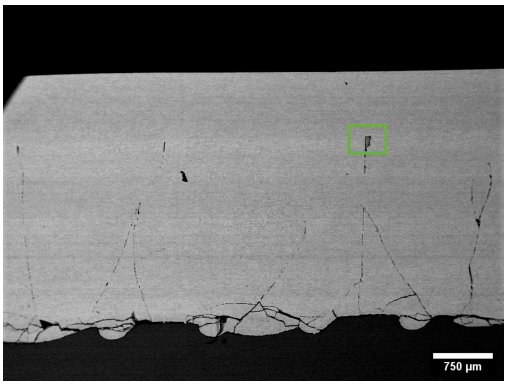
Cross-sectional examination of cracking

Figures 6.32–6.36 show cross-sectional SEM images of the repaired samples after testing in HIVE.

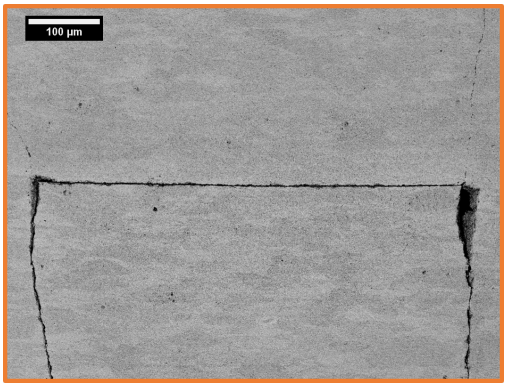
Figures 6.32 (a–b) are concentrated on the central part of the repaired reference sample. Cracking was prominent in the original W coating. It was considered that this cracking originated from the high stress applied during FAST manufacture of the repair coating, as cracking in this layer was also observed after repair, but before further damage, in Figure 6.20. Figures 6.32 (c–d) are higher magnification images from the corresponding orange and green boxes in Figures 6.32 (a–b). Figure 6.32 (c) shows an area of localised delamination in the form of a horizontal crack at the repair interface between two vertical cracks in the original W coating. The cracks in the original coating acted as stress concentrators which produced two fine vertical cracks in the repair coating. Figure 6.32 (d) shows a similar situation where a crack in the initial coating propagated into the new repair coating, although significantly thinner than the original cracks. Previous comparisons between the H2mm and H4mm indicated that thinner cracks resulted in less of the coating breaking off.



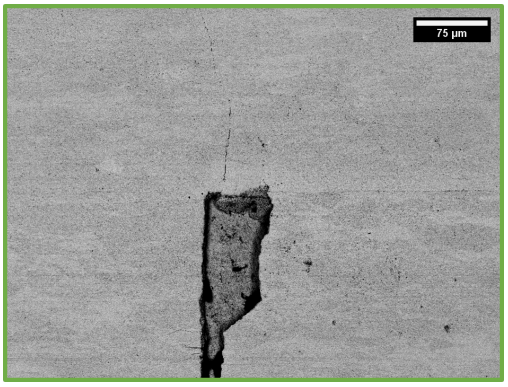
(a) BSE image of central part of repair reference sample. Orange box indicates location of Figure 6.32 (c).



(b) BSE image of central part of repair reference sample. Green box indicates location of Figure 6.32 (d).



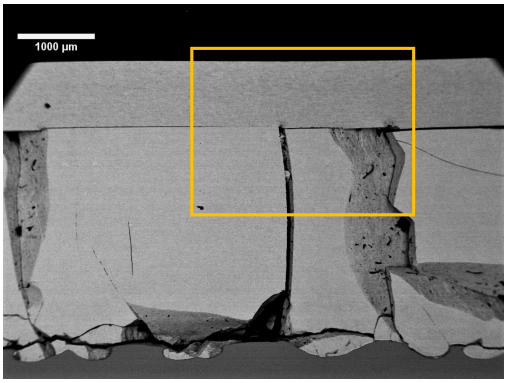
(c) Higher magnification BSE image of cracking in original W layer. Cracking led to localised delamination between the two original cracks, and to further vertical cracking into repair coating.



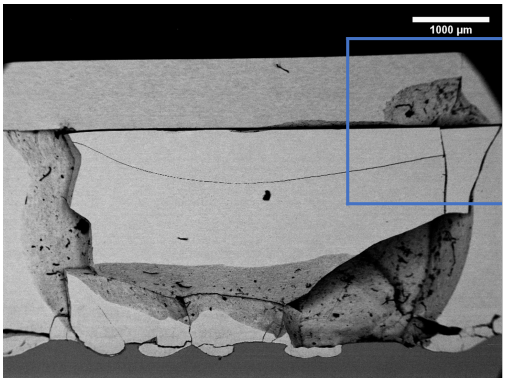
(d) Higher magnification BSE image of cracking in original W layer. Cracking led to a further vertical cracking in the repair coating.

Figure 6.32: Cross-sectional SEM images showing vertical cracking in the repaired reference H2mm sample following testing in HIVE.

Figures 6.33 (a–b) show significant damage in the original coating of the repaired HIVE-damaged H2mm sample after testing in HIVE. It was suspected that the pre-existing cracks produced in the first round of HIVE testing grew further when significant pressure was applied during the manufacture of the repair coating in the FAST. It was observed that the repair coating delaminated across almost the entire sample, as indicated previously in Figures 6.27 (c) & 6.28 (b) by the observed low temperature of the substrate. Figures 6.33 (c–d) are higher magnification images from the corresponding yellow and blue boxes in Figures 6.33 (a–b). Vertical steps in the original coating surface were visible throughout the sample. It was postulated that at least some of these displacements occurred during manufacture as the repair coating has filled some of the gaps. The two displacements highlighted in Figure 6.33 (c) had not produced any cracks into the new coating because the coating had delaminated at this point, so no stresses were transferred from the original coating. Conversely, in Figure 6.33 (d) a crack was observed to connect the leftmost crack in the original coating to the surface (through a chipped section of the new coating where material broke away when cross-sectioned).



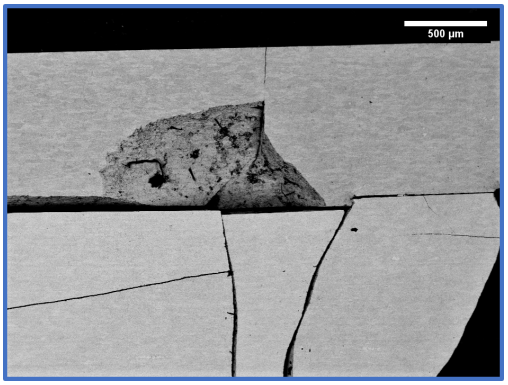
(a) BSE image of central part of repaired HIVE-damaged H2mm sample. Yellow box indicates location of Figure 6.33 (c).



(b) BSE image of central part of repaired HIVE-damaged H2mm sample. Blue box indicates location of Figure 6.33 (d).



(c) Higher magnification BSE image of cracking in original W layer. The repair coating had delaminated which resulted in hardly any cracks propagating into the repair coating.

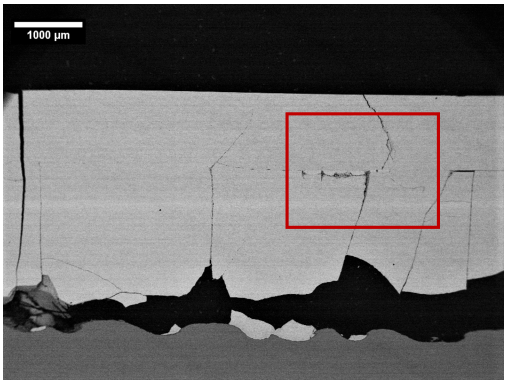


(d) Higher magnification BSE image of cracking in original W layer. Significant delamination and only one crack in the repair coating was observed.

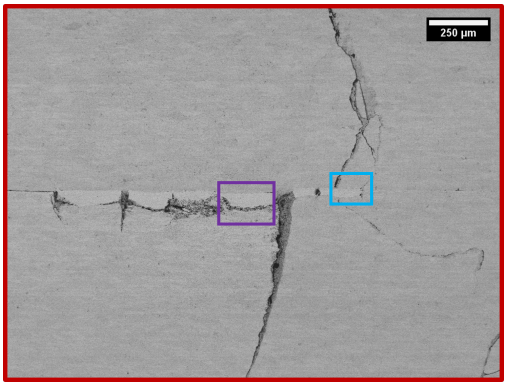
Figure 6.33: Cross-sectional SEM images showing vertical cracking in the repaired, HIVE-damaged H2mm sample following testing in HIVE.

Figure 6.34 shows images of the repaired UPP-damaged H2mm sample after testing in HIVE. Figure 6.34 (a) shows that vertical cracking from the original coating generally propagated through into the new coating, and the red box highlights the location of Figure 6.34 (b) and the area of original coating damaged by the transient heat flux applied by the Nd:YAG laser. As seen in all other UPP-damaged samples, the top layer of the laser-damaged area appeared brighter with BSE imaging because the W was more dense and had fewer impurities. Several cracks caused by the laser did not propagate very far into the original coating, and only one crack was observed propagating into the repair coating from the laser-damaged area. The locations of Figures 6.34 (c–d) correspond to the purple and light blue boxes in Figure 6.34 (b) respectively. In Figure 6.34 (c), the green circles at the top of the original W coating highlight previous blisters or other surface W defects caused by the laser; these were suppressed by the FAST process when consolidating the repair coating. The yellow oval depicts the highly-faceted growth regularly seen as the second closest thermally-affected region following laser damage (the closest being the densified W at the surface). Figure 6.34 (d) highlights a melted W particle that was redeposited on the surface of the W on the outer periphery of the laser spot. The area to the immediate left of this spot did not consolidate as well as the rest of the surrounding W and was visibly more porous.

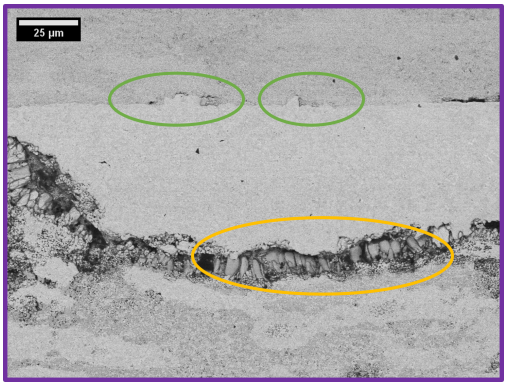
Figure 6.35 shows images of the repaired, HIVE-damaged W2mm sample. No cracking was observed at any point in the sample, as there was no coefficient of thermal expansion (CTE) mismatch between any layer and because no damage occurred when previously tested in HIVE.



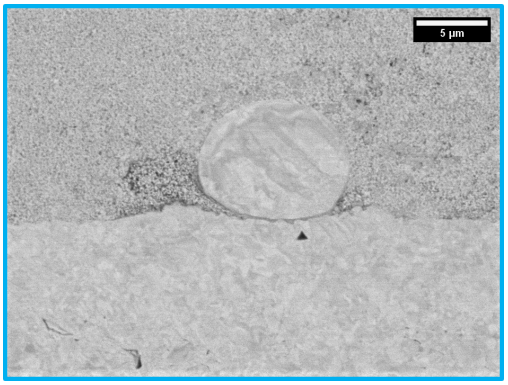
(a) BSE image of central part of repaired UPP-damaged H2mm sample. Red box indicates location of Figure 6.34 (b) and the laser-damaged area.



(b) Higher magnification BSE image highlighting the region exposed to transient heat loads. The purple and light blue boxes show the location of Figures 6.34 (c–d).

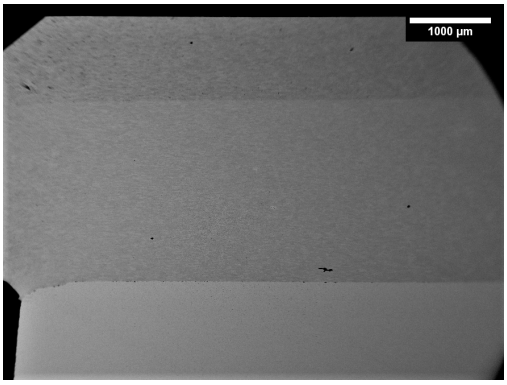


(c) Higher magnification BSE image which shows the original densified W surface and secondary faceted growth region directly underneath.

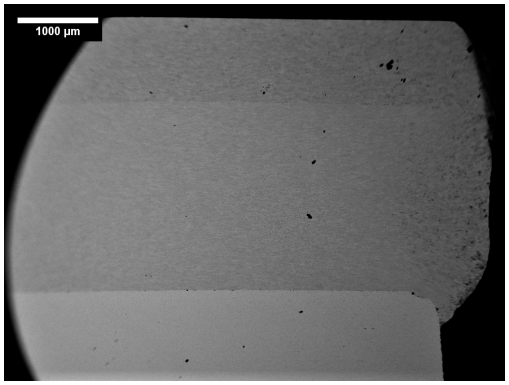


(d) High magnification BSE image that highlights a melted W deposit on the outer-edge of the transiently loaded area.

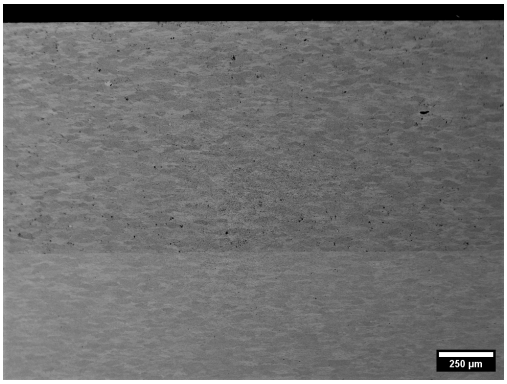
Figure 6.34: Cross-sectional SEM images showing vertical cracking in the repaired, UPP-damaged H2mm sample following testing in HIVE.



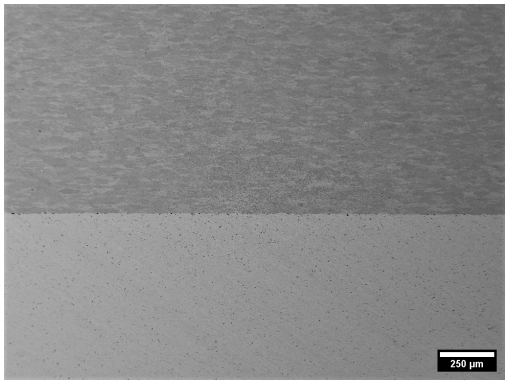
(a) BSE image of one end of repaired, HIVE-damaged W2mm sample.



(b) BSE image of other end of repaired, HIVE-damaged W2mm sample.



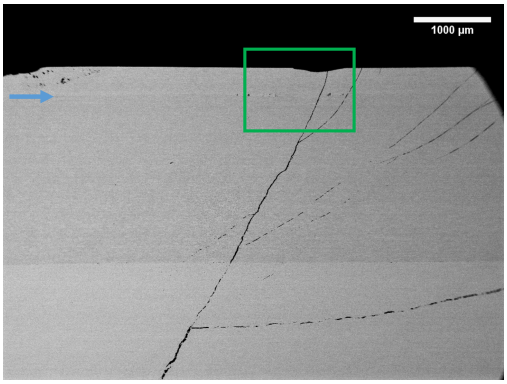
(c) Higher magnification BSE image which shows the interface between the original coating and the repair coating.



(d) Higher magnification BSE image which shows the interface between the original coating and the W substrate.

Figure 6.35: Cross-sectional SEM images which show no vertical cracking in the repaired, HIVE-damaged W2mm sample following testing in HIVE.

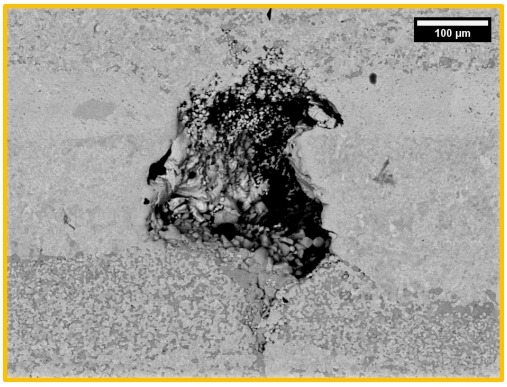
Figure 6.36 shows images of the repaired UPP-damaged W2mm sample. A crack network propagated in Figure 6.36 (a) throughout both coatings (repair and original) and the substrate as a result of an error during the mounting procedure; this was the thickest part of the sectioned sample and no cracking was observed anywhere else. The lines of the crack follow surface grooves left by the sectioning process. The blue arrow indicates the interface between the repair coating and the original coating; the green box highlights the location of Figure 6.36 (b) and the region that was damaged by the transient laser loading in UPP testing. Once again, the top of the laser-damaged area appeared brighter under BSE imaging due to the increased W composition as impurities were eliminated. The yellow and red boxes denote the locations of Figures 6.36 (c) & (d) respectively. Figure 6.36 (c) shows faceted growth at the edge of the densified W areas and provides a good comparison with finer, unexposed sintered material at the top of the pore where the powder did not completely fill the crack that formed during testing in UPP. Figure 6.36 (d) shows the crack at the edge of the laser-damaged region. The line of the crack appeared to deviate towards the edge of this area, potentially towards pre-existing damage caused by the laser. Aside from a few minor instances of porosity along the laser-damaged region (resulting from incomplete crack repair), as well as accidental cracks formed during the mounting process, this sample exhibited no discernible damage.



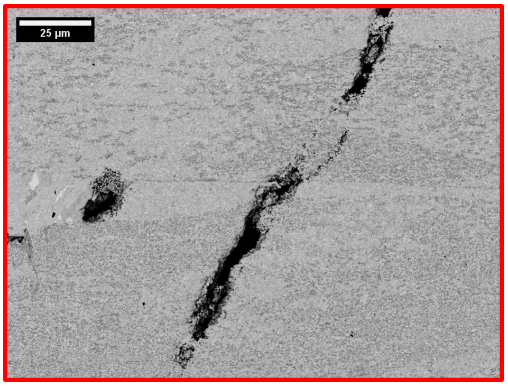
(a) BSE image of central part of repaired UPP-damaged W2mm sample. Green box denotes location of Figure 6.36 (b) and the laser-damaged area.



(b) Higher magnification BSE image of the laser-damaged area. Yellow and red boxes mark the location of Figure 6.36 (c–d).



(c) Higher magnification BSE image showing denser (brighter), damaged W layer with faceting seen at the edges in a pore.



(d) Higher magnification BSE image of crack angled towards the edge of the laser-damaged region, possibly due to pre-existing damage.

Figure 6.36: Cross-sectional SEM images showing little damage in the repaired, UPP-damaged W2mm sample following testing in HIVE.

6.4 Summary

Ensuring survival of PFCs under transient heat loads is a key step in verifying the suitability of a coating for use in a nuclear fusion reactor.

Steady-state thermal cycling tests (in Chapter 5) showed that W and hatched steel substrates with a 2 mm W coating were most likely to survive more advanced testing. Samples were exposed to an aggressive Ar plasma with additional transient heat loads using a high-powered Nd:YAG laser. This produced a base temperatures of up to 800 °C with a temperature change of 300–800 °C. Significant levels of cracking and surface modification were observed, but no samples catastrophically failed. More cracking occurred than observed in similar studies by Li and Morgan [124, 125], however the samples tested by Li and Morgan were of ITER-grade monoblock mock-ups. Upon sectioning, the reference sample used in this study failed at the laser-damaged spot, whereas FAST coatings generally survived.

Samples were then repaired, using the FAST, to apply a 1 mm thick coating on top of any pre-existing damage. The sintering process caused the coating of steel substrate samples to crack radially. It was suspected that this was due to powder infiltration into pre-existing cracks which then prevented the coating from returning to its stress-free state. Repairs to W substrate samples performed well, as no crack propagation occurred, and laser-damaged areas appeared to be near-fully healed. Repair coating quality was questionable, as the thinner coating meant that a higher concentration of C from the die was found closer to the substrate.

Repaired samples were also thermally cycled in HIVE to test their survival at fusion-relevant temperatures. W substrate samples performed as well as pristine samples in the first round of HIVE testing. The repaired reference and the UPP-damaged hatched steel substrate samples had similar temperature profiles and resulting microstructures as the 4 mm coating on hatched steel in the preliminary HIVE experiments in Section 5.3.2. The repair coating of the HIVE-damaged, hatched steel substrate sample failed and delaminated, which resulted in poor thermal testing performance during thermal cycling.

Repair work yielded novel promising results, particularly for W-W samples. W-steel samples may work with further development and careful monitoring to ensure that coating thickness is topped up only enough to maintain the thickness, rather than increase the thickness significantly as this is when large cracks and catastrophic failure are most likely to occur (as observed by comparing the H2mm and H4mm samples shown in Figures 5.24 & 5.32). FAST could be an appropriate technique for repair of PFC tiles with the implementation of some key improvements, such as swapping the die material from graphite to Mo to reduce C diffusion, or reducing the W powder with H_2 prior to manufacture (as shown by Choi et al. [69]). If component materials with closely-aligned thermal properties are selected (most importantly melting/operating temperature and CTE) then the FAST process could be developed to operate with for higher temperatures and pressures in order to produce higher density W coatings which should possess a higher thermal conductivity and performance.

7 Conclusions and further work

7.1 Conclusions

This thesis has investigated the manufacture, testing and repair of W coatings for use as PFCs in a nuclear fusion reactor. Work has focused on the optimisation of VPS coatings, modelling of residual stresses and strains from manufacture in FAST coatings and high heat flux testing of FAST coatings in fusion-relevant environments with the aim of reducing the manufacturing complexity and time to produce FW and divertor tiles. Steady-state and transient thermal cycling were important tests to provide comparisons with reference samples and with literature.

Objective 1

Produce an optimised, repeatable VPS recipe for spraying dense W coatings.

A full, improved VPS recipe was produced using a variety of optimisations for different stages of the VPS process. First the W powder feed mass flow rate to the gun was optimised, to ensure all powder was injected into the plasma successfully. Taguchi analysis was used to find near-optimum parameters related to the plasma 'flame': chamber pressure, Ar flow rate and H_2 flow rate. 'Wipe' tests and cycled spraying tests were used to measure the deposition density and W coating thickness and roughness to compare experiments. Finally, spray distance and gun traverse speed were optimised to increase coating deposition rate. The final recipe produced a 4 mm thick, W coating that was 90.7% dense and in comparison to the original group recipe was significantly less porous throughout. Further processing steps, such as thermomechanical heat treatments (e.g. rolling, HIPing, sintering under vacuum) could increase the density of these coatings with promising thickness for practical use in a fusion reactor.

Objective 2

Develop FE models of W coatings manufactured using the FAST, with the aim of understanding substrate texture and why it helps (or not) retain thick tungsten coatings.

FE models were created using the COMSOL Multiphysics® software and analytically validated to predict strains, stresses and stored elastic strain energy density accurately in bimetallic strips and discs cooled from the manufacturing temperature used in the FAST. These models were developed to explore crack propagation

(using calculated J-integral values) in the W coating, originating from both the W-steel interface and the surface of the W coating, for flat and 'hatched' substrate surface textures at various, user-selected, crack locations. Analysis of micrographs of relevant experiments revealed that crack formation was similar to that predicted by the models. It was concluded that cracking was most likely to occur at the coating-substrate interface and then to propagate vertically towards the coating surface into less compressively-stressed material. Hatched substrates were observed to induce angled cracks that then joined vertical cracks due to localised stresses caused by the substrate texturing. Deeper understanding of the effects of substrate texturing would enable the development of better techniques to produce stable W coatings (e.g. simpler design, cheaper/quicker machining, or targeted levels of vertical segmentation to increase adhesion further). Substrate-coating interfaces where regular vertical cracking could be induced would facilitate the bonding of dissimilar materials with a large CTE mismatch.

Objective 3

Understand and identify any compositional changes that occur at the W-steel interface of manufactured (FAST & VPS) samples.

As-manufactured FAST samples (with no substrate) had high impurity content (17.4 at% O and 8.8 at% C) in comparison with the VPS (0.22 at% O and 1.75 at% C). FAST and VPS samples were thermally aged for a variety of times and different temperatures to investigate the growth of new phases between the W coating and steel substrate. During manufacture of W coatings, the FAST process introduced further impurities from steel substrates. Thermal ageing led to the de-

velopment of a new phase that grew between powder 'splats' in the VPS samples and surrounded the finer W powder particles in the FAST samples. Cracking and failure occurred in regions with high levels of impurity. EDX and XRD data confirmed the composition of the new phases that formed: W_2C, Cr_3C_2 and WCr_2O_6 in VPS coatings and $FeCr_2O_4$, Fe_3O_4 and $Fe(WO_4)$ in FAST samples. Growth rate analysis of FAST samples by means of enhanced image contrast produced values for activation energy of 40 $kJ{\cdot}mol^{-1}$ and maximum growth rate coefficient of $5.3{\times}10^{-12}$ $m^2{\cdot}s^{-1}$. Both these values were significantly lower than those found by Reisner et al. [93], however both studies had a very limited number of data points to produce lines of best fit, so there was a large error margin on the calculated values. Higher growth rate coefficients were clearly observed in the present study, and it was postulated that this was due to the presence of smaller species such as C and O which diffuse faster than heavier metallic elements, which in turn may have reduced the activation energy. This thermal instability is undesirable in a fusion environment; significant development is required to produce purer and denser W coatings which may impede the growth of new phases between the W and steel.

Objective 4

Quantify the effect of substrate texture, material, and coating thickness on survival and crack response during steady-state thermal cycling of W coatings produced by FAST.

Four FAST sample types were thermally cycled in the Heating by Induction to Verify Extremes (HIVE) and Upgraded Pilot-PSI (UPP) facilities. The sample types were: 2 mm W coating on a flat steel substrate (F2mm), 2 mm W coating on a hatched steel substrate (H2mm), 4 mm W coating on a hatched steel substrate (H4mm) and 2 mm W coating on a flat W substrate (W2mm). HIVE testing consisted of leaving samples in the evacuated chamber overnight, before incremental thermal cycling (commissioning) up to 800 °C and then thermally cycling them 50 times between 300–800 °C. Samples were thermally cycled between 150–550 °C in UPP using a magnetised H_2 plasma. Samples responded to thermal cycling in similar ways: H2mm and H4mm samples both cracked early in the cycling process, with H4mm samples having fewer, but larger, cracks due to the increased stresses induced by the thicker coating. W2mm samples did not exhibit any signs of cracking or failure. The F2mm sample in HIVE delaminated (but stayed in place) during commissioning, significantly reducing the thermal conduction properties of the sample. Delamination meant that there were no interfacial strains, so cracking did not occur. The UPP F2mm sample was clamped, so did not delaminate, but cracking did occur; the coating delaminated at a later point. Once any sample had

cracked, no further cracking occurred. W substrate samples (W2mm) and thinner hatched steel samples (H2mm) were most promising for use in a fusion reactor, as damage was minimised and heat appeared to be fully transferred from the coating to substrate which would maximise the energy efficiency of the reactor.

Objective 5

Investigate the impact of substrate texture and material on coating survival and crack response during transient thermal cycling of W coatings produced by FAST.

Transient thermal cycling testing was undertaken in UPP, using an Ar plasma to produce a base temperature of up to 800 °C with a high-powered Nd:YAG laser providing transient pulses (25,000 at 20 Hz) that caused a temperature change of 300–800 °C. In comparison to results reported in literature, greater levels of cracking and surface modification were observed; it was noted however that the literature reports used ITER-grade monoblock 'mock-up' structures, which have been developed over the course of decades and therefore have better properties (e.g. higher purity, negligible porosity) than the preliminary research samples tested in this work. The reference W sample used for this thesis (rolled W) failed locally at the laser-damaged spot when sectioned (thereby limiting analysis); FAST coatings generally survived well enough for characterisation despite cracking significantly more during testing. Due to the pre-existing porosity in the FAST samples, powder particles were more thermally isolated than expected and faceted growth occurred

throughout the laser-damaged area. The surface of the damaged region was noticeably purer W, which indicated that impurity compounds were more volatile and had been ejected into the plasma which would lead to highly undesirable 'plasma poisoning' in a fusion reactor.

Objective 6

Investigate the feasibility of repairing W coatings using the FAST.

Samples were repaired using the FAST by applying a 1 mm thick W coating on top of HIVE- and UPP- damaged samples (and to a reference steel substrate sample). The original W coating cracked for all steel substrate samples, regardless of the level of pre-existing damage. It was postulated that this occurred due to powder particles filling the cracks that formed during cooling from manufacture or from thermal cycling testing, which then prevented the coating from returning to a stress-free state without producing further cracks. Cracking propagated into the new coating for steel substrate samples, but no cracking occurred for any tungsten substrate samples. This was a promising result as in-situ repair of PFCs has not been previously studied and reported for erosion damage and could significantly improve the economic viability of a fusion reactor in comparison to tile replacement, as the associated downtime would be much shorter.

Objective 7

Quantify the quality of repair, how this is affected by pre-existing damage and how this affects FAST-repaired coating survival.

Repaired samples were tested in HIVE for a further 50 cycles between 300–800 °C. The HIVE-damaged H2mm sample delaminated in a similar manner to the F2mm sample in HIVE, with noticeably degraded thermal properties. The reference repair and UPP-damaged H2mm samples both had a similar thermal response to the H4mm sample previously, due to the increased thickness of W coating. No failure occurred during testing for either tungsten substrate sample and laser-damaged spots in the tungsten substrate sample showed nearly no signs of former damage, as the repair W powder had filled in the cracks. Repaired fully-W samples performed as well as original coatings; a highly promising result for in-situ repair. Further development of the technique to reduce the impurities from manufacture should be undertaken. Pre-existing vertical cracks were not repaired and lead to a lower quality sample following sample repair.

7.2 Further work

VPS production

Further development of the VPS technique is required to build experience and confidence with the manufacture of W coatings for use in a nuclear fusion reactor. Delamination of W coatings on steel substrates was still a challenge even after a thorough optimisation process. This might be addressed by applying cooling to the steel substrate during spraying, to reduce the thermal contraction strain mismatch between substrate and coating (smaller ΔT for steel, to counter its larger CTE); however, this would require a different VPS 'recipe' to be developed. Similarly, a new recipe would be needed to apply W coatings on a W substrate, though this could lead to more promising results due to the lack of thermal expansion coefficient mismatch. Finally, the horizontal lamellae that are produced by the powder 'splats' encourage horizontal cracking. Directional heat treatment to encourage vertical recrystallisation (as observed by Kim et al. [108]) could be a simple additional processing step to address this issue. The VPS appeared to be a cleaner and more geometrically flexible manufacturing alternative to the FAST, and is already used for industrial scale operation and with further development could be a very promising candidate for use in initial manufacture or in-situ repair of PFCs.

FAST production

The FAST produced replicable original and repair coatings on a variety of substrates, but suffered from the drawback of high levels of introduced impurities; however, several future process refinements were identified during this work that could reduce this problem. Contamination from the air when moving samples between the glovebox and the FAST was recognised as a significant issue, so a means of improving the transport system between the glovebox and the FAST (such as a FAST within the glovebox system, as used by battery groups investigating highly air-sensitive materials) should be installed. The quality of the W nano-powder used for sample coatings can be increased by reducing it with H_2 as observed by Choi et al. [69]. Lastly, exchanging the graphite die set for Mo would prevent C diffusion into the sample.

Coating properties

In the course of this study, the focus primarily centred on coating manufacture and fusion-relevant high heat flux testing. It is important to note that certain aspects, such as mechanical and thermal properties, were not comprehensively assessed in this research. Ideally, there would have been time for bond strength and nanoindentation mapping tests for adhesion and phase growth studies respectively, and values of thermal diffusivity and conductivity would have been established for comparison with literature. Testing at elevated temperatures is highly desirable in order to ensure safe operation in the hostile environment of the reactor whilst maximising system efficiency. Therefore, future investigations should aim to incor-

porate a more comprehensive evaluation of these properties to provide a holistic understanding of the W coatings produced. Developing a better understanding on the effect of porosity on mechanical and thermal properties would provide targets to help focus further optimisation.

Fusion-relevant manufacture

The current monoblock design of divertor components is a W-clad CuCrZr pipe. The VPS is a proven technology for producing coatings on complex geometries, however the FAST requires matched, uniaxial geometries to ensure homogeneous densification. Therefore, the local geometry changes related to the pipe curvature is a challenge that must be overcome in order to sinter the W onto the pipe. Investigations should also be carried out into the repair of used tiles, either from JET or monoblock mock-ups, in order to establish the correct maintenance schedule, the optimal repair thickness to ensure coating survival, and also the repair method(s) suitable for alternative tile geometries. Further research into robotics for in-situ repair is also vital to minimise reactor downtime and reduce the need for manual intervention.

Finite element modelling

There are several areas for development following on from the research presented in this thesis. Crack modelling was relatively rudimentary, with user-defined crack location and propagation. A module is available in the COMSOL Multiphysics® software that allows the user to produce phase field models. These models can be used for fracture mechanics where the model will update the crack path itself

using user-set parameters. Combining this with modelling of the thermal cycling processes would improve our understanding of crack growth during testing. Modelling the behaviour of W powder particles during the initial and repair FAST processes was too complex and remained outside the scope of the project, but would be valuable in furthering the understanding of diffusion processes and of densification, and how they are affected by the FAST process relative to conventional sintering methods.

Bibliography

[1] Total Website. *Climate: our vision | Total.com*. URL: https://www.total.com/commitment/climate-change/climate-our-vision. Date accessed: 2020-04-25.

[2] Shell Website. *Our Response to Climate Change | Shell United Kingdom*. URL: https://www.shell.co.uk/a-cleaner-energy-future/our-response-to-climate-change.html. Date accessed: 2020-04-25.

[3] BP Website. *Reimagining energy | Who we are | Home*. URL: https://www.bp.com/en/global/corporate/who-we-are/reimagining-energy.html?gclid=EAIaIQobChMI1eD_j8qB6QIVD-h3Ch25sgRwEAAYASAAEgIpiPD_BwE. Date accessed: 2020-04-25.

[4] Frederick M. Mann and Edward T. Cheng. "Nuclear data for fusion: a view from two meetings". In: *Fusion Engineering and Design* 28.C (1995), pp. 446–448. ISSN: 09203796. DOI: 10.1016/0920-3796(95)90072-1.

[5] Richard Kembleton. "Nuclear fusion: What of the future?" In: *Managing Global Warming*. Academic Press, Jan. 2019, pp. 199–220. ISBN: 978-0-12-814104-5. DOI: 10.1016/B978-0-12-814104-5.00005-3. URL: https://www.sciencedirect.com/science/article/pii/B9780128141045000053%20https://linkinghub.elsevier.com/retrieve/pii/B9780128141045000053.

[6] Hannah Devlin. *Nuclear fusion on brink of being realised, say MIT scientists | Environment | The Guardian*. URL: https://www.theguardian.com/environment/2018/mar/09/nuclear-fusion-on-brink-of-being-realised-say-mit-scientists. Date accessed: 2018-11-29.

[7] CCFE. *Introduction to fusion energy*. URL: http://www.ccfe.ac.uk/introduction.aspx. Date accessed: 2018-11-29.

[8] Markus J. Aschwanden. "The Sun". In: *Encyclopedia of the Solar System*. Ed. by Tilman Spohn, Doris Breuer, and Torrence V. Johnson. 3rd ed. Elsevier, Jan. 2014. Chap. 11, pp. 235–259. ISBN: 9780124158450. DOI: 10.1016/b978-0-12-415845-0.00011-6.

[9] M.L Watkins and Jet Team. "Physics of high performance JET plasmas in DT". In: *Nuclear Fusion* 39.9Y (2002), pp. 1227–1244. ISSN: 0029-5515. DOI: 10.1088/0029-5515/39/9Y/302.

[10] A G Peeters. "The physics of fusion power". In: *Lecture Notes* (2009).

[11] Ursula Schneider. *Fusion: Energy of the Future | IAEA*. URL: https://www.iaea.org/newscenter/news/fusion-energy-future. Date accessed: 2018-12-13.

[12] Garry McCracken and P Stott. *Fusion: The Energy of the Universe*. 2013. ISBN: 9780123846563 (ISBN). DOI: 10.1007/s007690000247.

[13] ANS - Center for Nuclear Science and Technology Information. *Nuclear Fusion - ANS*. URL: http://www.nuclearconnect.org/know-nuclear/science/nuclear-fusion%20http://nuclearconnect.org/know-nuclear/science/nuclear-fusion. Date accessed: 2018-12-13.

[14] Wikipedia. *Helium-3*. URL: https://en.wikipedia.org/wiki/Helium-3. Date accessed: 2020-10-23.

[15] S. Möller et al. "HiperFer, a reduced activation ferritic steel tested for nuclear fusion applications". In: *Nuclear Materials and Energy* 17.June (2018), pp. 9–14. ISSN: 23521791. DOI: 10.1016/j.nme.2018.06.010. URL: https://doi.org/10.1016/j.nme.2018.06.010.

[16] S. Heuer et al. "Aiming at understanding thermo-mechanical loads in the first wall of DEMO: Stress–strain evolution in a Eurofer-tungsten test component featuring a functionally graded interlayer". In: *Fusion Engineering and Design* 135.June (2018), pp. 141–153. ISSN: 09203796. DOI: 10.1016/j.fusengdes.2018.07.011. URL: https://doi.org/10.1016/j.fusengdes.2018.07.011.

[17] U. Fischer et al. "The role of nuclear data for fusion nuclear technology". In: *Fusion Engineering and Design* 136.February (2018), pp. 162–167. ISSN: 09203796. DOI: 10.1016/j.fusengdes.2018.01.036. URL: https://doi.org/10.1016/j.fusengdes.2018.01.036.

[18] Youji Someya et al. "Fusion DEMO reactor design based on nuclear analysis". In: *Fusion Engineering and Design* 136.May (2018), pp. 1306–1312. ISSN: 09203796. DOI: 10.1016/j.fusengdes.2018.04.129. URL: https://doi.org/10.1016/j.fusengdes.2018.04.129.

[19] Jochen Linke. "High Heat Flux Performance of Plasma Facing Materials and Components under Service Conditions in Future Fusion Reactors". In: *Fusion Science and Technology* 49.2T (Feb. 2006), pp. 455–464. ISSN: 1536-1055. DOI: 10.13182/fst06-a1144.

[20] D. Zhu et al. "In situ melting phenomena on W plasma-facing components for lower divertor during long-pulse plasma operations in EAST". In: *Nuclear Fusion* 63.3 (Mar. 2023). ISSN: 17414326. DOI: 10.1088/1741-4326/acb3e1.

[21] J. H. You et al. "European DEMO divertor target: Operational requirements and material-design interface". In: *Nuclear Materials and Energy* 9 (Dec. 2016), pp. 171–176. ISSN: 23521791. DOI: 10.1016/j.nme.2016.02.005.

[22] Giacomo Dose et al. "Ultrasonic analysis of tungsten monoblock divertor mock-ups after high heat flux test". In: *Fusion Engineering and Design* 146.January (Sept. 2019), pp. 870–873. ISSN: 09203796. DOI: 10.1016/j.fusengdes.2019.01.102. URL: https://doi.org/10.1016/j.fusengdes.2019.01.102.

[23] Ch Linsmeier et al. "Development of advanced high heat flux and plasma-facing materials". In: *Nuclear Fusion* 57.9 (2017). ISSN: 17414326. DOI: 10.1088/1741-4326/aa6f71.

[24] International Atomic Energy Agency (IAEA). "21st IAEA Fusion Energy Conference". In: October. 2006.

[25] ITER. *ITER ... and then what? | ITER Mag 3*. URL: https://www.iter.org/mag/3/22. Date accessed: 2020-04-25.

[26] ITER Newsline. *Prototype | The hottest stuff in ITER*. URL: https://www.iter.org/newsline/-/3027. Date accessed: 2023-09-08.

[27] Forschungszentrum Jülich. *Plasma-facing Materials*. URL: https://www.fz-juelich.de/en/iek/iek-4/forschung/plasma-facing-materials. Date accessed: 2023-09-08.

[28] Muyuan Li and Jeong Ha You. "Interpretation of the deep cracking phenomenon of tungsten monoblock targets observed in high-heat-flux fatigue tests at 20 MW/m2". In: *Fusion Engineering and Design* 101 (Dec. 2015), pp. 1–8. ISSN: 09203796. DOI: 10.1016/j.fusengdes.2015.09.008. URL: http://dx.doi.org/10.1016/j.fusengdes.2015.09.008.

[29] G. Federici et al. "European DEMO design strategy and consequences for materials". In: *Nuclear Fusion* 57.9 (June 2017). ISSN: 17414326. DOI: 10.1088/1741-4326/57/9/092002.

[30] S. Brezinsek et al. "Beryllium migration in JET ITER-like wall plasmas". In: *Nuclear Fusion* 55.6 (June 2015). ISSN: 17414326. DOI: 10.1088/0029-5515/55/6/063021.

[31] R. V. Jensen et al. "Calculations of impurity radiation and its effects on tokamak experiments". In: *Nuclear Fusion* 17.6 (1977), pp. 1187–1196. ISSN: 17414326. DOI: 10.1088/0029-5515/17/6/007.

[32] Robert W. Conn, Russell P. Doerner, and Jongik Won. "Beryllium as the plasma-facing material in fusion energy systems - Experiments, evaluation, and comparison with alternative materials". In: *Fusion Engineering and Design* 37.4 (1997), pp. 481–513. ISSN: 09203796. DOI: 10.1016/S0920-3796(97)00092-6.

[33] R. V. Jensen, D. E. Post, and D. L. Jassby. "Critical Impurity Concentrations for Power Multiplication in Beam-Heated Toroidal Fusion Reactors". In: *Nuclear Science and Engineering* 65.2 (1978), pp. 282–289. ISSN: 00295639. DOI: 10.13182/NSE78-A27157.

[34] Oak Ridge National Laboratory. *Beryllium Toxicity Profile | Risk Assessment Information System (RAIS).* URL: https://rais.ornl.gov/tox/profiles/beryllium.html. Date accessed: 2020-11-13.

[35] L. L. Sneadb G. R. Longhursta and A. A. Abou-Sena. "The status of beryllium research for fusion in the United States". In: *Ineel/Con-03-00736* April 2017 (2003). URL: http://www.inl.gov/technicalpublications/Documents/2808477.pdf.

[36] Hiroshi Yoshida et al. "Safety handling of beryllium for fusion technology R and D". In: *International Nuclear Information System (INIS)* 24.3 (1992). URL: https://inis.iaea.org/search/search.aspx?orig_q=RN:24013676.

[37] ITER Newsline. *32nd ITER Council: A focus on updating the baseline.* URL: https://www.iter.org/newsline/-/3895. Date accessed: 2023-09-08.

[38] American Elements. *Silicon Carbide.* URL: https://www.americanelements.com/silicon-carbide-409-21-2. Date accessed: 2020-06-09.

[39] Wolfram Research Inc. *Melting Point for all the elements in the Periodic Table | periodictable.com.* URL: http://periodictable.com/Properties/A/MeltingPoint.html. Date accessed: 2018-12-13.

[40] International Atomic Energy Agency (IAEA). *What is Graphite*. URL: https://nucleus.iaea.org/sites/graphiteknowledgebase/wiki/Guide_to_Graphite/What%20is%20Graphite.aspx. Date accessed: 2020-06-09.

[41] Joachim Roth, Wolfgang Eckstein, and Maria Guseva. "Erosion of Be as plasma-facing material". In: *Fusion Engineering and Design* 37.4 (1997), pp. 465–480. ISSN: 09203796. DOI: 10.1016/S0920-3796(97)00091-4.

[42] Joachim Roth et al. "Tritium inventory in ITER plasma-facing materials and tritium removal procedures". In: *Plasma Physics and Controlled Fusion* 50.10 (Oct. 2008), p. 103001. ISSN: 0741-3335. DOI: 10.1088/0741-3335/50/10/103001. URL: https://iopscience.iop.org/article/10.1088/0741-3335/50/10/103001.

[43] Rion A. Causey and William R. Wampler. "The use of silicon carbide as a tritium permeation barrier". In: *Journal of Nuclear Materials* 220-222 (1995), pp. 823–826. ISSN: 00223115. DOI: 10.1016/0022-3115(94)00623-7.

[44] M. R. Gilbert et al. "Waste implications from minor impurities in European DEMO materials". In: *Nuclear Fusion* 59.7 (May 2019). ISSN: 17414326. DOI: 10.1088/1741-4326/ab154e.

[45] UK Radioactive Waste Inventory. *What are the main waste categories?* URL: https://ukinventory.nda.gov.uk/about-radioactive-waste/what-is-radioactivity/what-are-the-main-waste-categories/. Date accessed: 2020-11-13.

[46] J.N. Brooks et al. “Plasma-facing material alternatives to tungsten”. In: *Nuclear Fusion* 55.4 (Apr. 2015), p. 043002. ISSN: 0029-5515. DOI: 10.1088/0029-5515/55/4/043002. URL: https://iopscience.iop.org/article/10.1088/0029-5515/55/4/043002.

[47] R. G. Abernethy. “Predicting the performance of tungsten in a fusion environment: a literature review”. In: *Materials Science and Technology (United Kingdom)* 33.4 (2017), pp. 388–399. ISSN: 17432847. DOI: 10.1080/02670836.2016.1185260.

[48] John Campbell. *Complete Casting Handbook: Metal Casting Processes, Metallurgy, Techniques and Design: Second Edition*. 2015, pp. 1–1028. ISBN: 9780444635099. DOI: 10.1016/C2014-0-01548-1.

[49] A. Giannattasio et al. “Brittle-ductile transitions in polycrystalline tungsten”. In: *Philosophical Magazine* 90.30 (Oct. 2010), pp. 3947–3959. ISSN: 14786435. DOI: 10.1080/14786435.2010.502145.

[50] Xiazi Xiao et al. “High temperature nano-indentation of tungsten: Modelling and experimental validation”. In: *Materials Science and Engineering A* 743.October 2018 (Jan. 2019), pp. 106–113. ISSN: 09215093. DOI: 10.1016/j.msea.2018.11.079. URL: https://doi.org/10.1016/j.msea.2018.11.079.

[51] Chai Ren et al. “Methods for improving ductility of tungsten - A review”. In: *International Journal of Refractory Metals and Hard Materials* 75.January (Sept. 2018), pp. 170–183. ISSN: 22133917. DOI: 10.1016/j.ijrmhm.2018.04.012. URL: https://doi.org/10.1016/j.ijrmhm.2018.04.012.

[52] M. Rieth et al. “Recent progress in research on tungsten materials for nuclear fusion applications in Europe”. In: *Journal of Nuclear Materials* 432.1-3 (Jan. 2013), pp. 482–500. ISSN: 00223115. DOI: 10.1016/j.jnucmat.2012.08.018.

[53] MSE Supplies LLC. *List of Thermal Expansion Coefficients (CTE) for Natural and Engineered Materials*. URL: https://www.msesupplies.com/pages/list-of-thermal-expansion-coefficients-cte-for-natural-and-engineered-materials. Date accessed: 2020-06-11.

[54] B. Gludovatz et al. “Fracture toughness of polycrystalline tungsten alloys”. In: *International Journal of Refractory Metals and Hard Materials* 28.6 (Nov. 2010), pp. 674–678. ISSN: 02634368. DOI: 10.1016/j.ijrmhm.2010.04.007. URL: http://dx.doi.org/10.1016/j.ijrmhm.2010.04.007.

[55] TWI Global. *Diffusion Bonding - TWI*. URL: https://www.twi-global.com/what-we-do/our-processes/diffusion-bonding. Date accessed: 2024-02-20.

[56] W. W. Basuki and J. Aktaa. “Investigation of tungsten/EUROFER97 diffusion bonding using Nb interlayer”. In: *Fusion Engineering and Design* 86.9-11 (Oct. 2011), pp. 2585–2588. ISSN: 09203796. DOI: 10.1016/j.fusengdes.2011.03.017. URL: http://dx.doi.org/10.1016/j.fusengdes.2011.03.017.

[57] Widodo Widjaja Basuki and Jarir Aktaa. “Process optimization for diffusion bonding of tungsten with EUROFER97 using a vanadium interlayer”. In: *Journal of Nuclear Materials* 459 (2015), pp. 217–224. ISSN: 00223115. DOI: 10.1016/j.jnucmat.2015.01.033. URL: http://dx.doi.org/10.1016/j.jnucmat.2015.01.033.

[58] Qingshan Cai et al. “Rational design of composite interlayer for diffusion bonding of tungsten–steel joints”. In: *International Journal of Refractory Metals and Hard Materials* 70.September 2017 (Jan. 2018), pp. 155–161. ISSN: 22133917. DOI: 10.1016/j.ijrmhm.2017.10.002. URL: http://dx.doi.org/10.1016/j.ijrmhm.2017.10.002.

[59] Eliseo Visca et al. “Manufacturing and testing of ITER-like divertor plasma facing mock-ups for DEMO”. In: *Fusion Engineering and Design* 136.June (Nov. 2018), pp. 1593–1596. ISSN: 09203796. DOI: 10.1016/j.fusengdes.2018.05.064. URL: https://doi.org/10.1016/j.fusengdes.2018.05.064.

[60] J. Boscary et al. “Conceptual design of the next generation of W7-X divertor W-target elements”. In: *Fusion Engineering and Design* 192.September 2022 (July 2023), pp. 1–4. ISSN: 09203796. DOI: 10.1016/j.fusengdes.2023.113629.

[61] Q. Li et al. “Development and application of W/Cu flat-type plasma facing components at ASIPP”. In: *Physica Scripta* 2017.T170 (Sept. 2017), p. 14020. ISSN: 02811847. DOI: 10.1088/1402-4896/aa8921. URL: https://dx.doi.org/10.1088/1402-4896/aa8921.

[62] Youyun Lian et al. “Influence of surface morphology and microstructure on performance of CVD tungsten coating under fusion transient thermal loads”. In: *Applied Surface Science* 390 (Dec. 2016), pp. 167–174. ISSN: 01694332. DOI: 10.1016/j.apsusc.2016.08.060. URL: http://dx.doi.org/10.1016/j.apsusc.2016.08.060.

[63] Zhe Chen et al. “Recent research and development of thick CVD tungsten coatings for fusion application”. In: *Tungsten* 2.1 (Mar. 2020), pp. 83–93. ISSN: 2661-8028. DOI: 10.1007/s42864-020-00041-x. URL: https://doi.org/10.1007/s42864-020-00041-x.

[64] Youyun Lian et al. “Preparation and properties of CVD-W coated W/Cu FGM mock-ups”. In: *Fusion Engineering and Design* 88.9-10 (Oct. 2013), pp. 1694–1698. ISSN: 09203796. DOI: 10.1016/j.fusengdes.2013.02.155. URL: http://dx.doi.org/10.1016/j.fusengdes.2013.02.155.

[65] Donald M. Mattox. “Physical vapor deposition (PVD) processes”. In: *Metal Finishing* 98.1 (2000), pp. 410–423. ISSN: 00260576. DOI: 10.1016/S0026-0576(00)80350-5.

[66] Carmen García-Rosales et al. “High-heat-flux loading of tungsten coatings on graphite deposited by plasma spray and physical vapor deposition”. In: *Fusion Technology* 32.2 (1997), pp. 263–275. ISSN: 07481896. DOI: 10.13182/fst97-a19896.

[67] T. Weber et al. “Functionally graded vacuum plasma sprayed and magnetron sputtered tungsten / EUROFER97 interlayers for joints in helium-cooled divertor components”. In: *Journal of Nuclear Materials* 436.1-3 (2013), pp. 29–39. ISSN: 0022-3115. DOI: 10.1016/j.jnucmat.2013.01.286. URL: http://dx.doi.org/10.1016/j.jnucmat.2013.01.286.

[68] R. M. German, A. Bose, and S. S. Mani. “Sintering time and atmosphere influences on the microstructure and mechanical properties of tungsten heavy alloys”. In: *Metallurgical Transactions A* 23.1 (1992), pp. 211–219. ISSN: 03602133. DOI: 10.1007/BF02660866.

[69] Jonghyun Choi et al. “Fabrication of sintered tungsten by spark plasma sintering and investigation of thermal stability”. In: *International Journal of Refractory Metals and Hard Materials* 69.August (Dec. 2017), pp. 164–169. ISSN: 22133917. DOI: 10.1016/j.ijrmhm.2017.08.013. URL: http://dx.doi.org/10.1016/j.ijrmhm.2017.08.013.

[70] Frank Bergner et al. “Alternative Fabrication Routes toward Oxide-Dispersion-Strengthened Steels and Model Alloys”. In: *Metallurgical and Materials Transactions A: Physical Metallurgy and Materials Science* 47.11 (2016), pp. 5313–5324. ISSN: 10735623. DOI: 10.1007/s11661-016-3616-2.

[71] Jiří Matějíček et al. “On the structural and chemical homogeneity of spark plasma sintered tungsten”. In: *Metals* 9.8 (Aug. 2019). ISSN: 20754701. DOI: 10.3390/met9080879.

[72] Saša Novak et al. “Beneficial effects of a WC addition in FAST-densified tungsten”. In: *Materials Science and Engineering A* 772.September 2019 (Jan. 2020). ISSN: 09215093. DOI: 10.1016/j.msea.2019.138666.

[73] Jiří Matějíček et al. “Overview of processing technologies for tungsten-steel composites and FGMs for fusion applications”. In: *Nukleonika* 60.2 (2015), pp. 267–273. ISSN: 15085791. DOI: 10.1515/nuka-2015-0049.

[74] Wen Cui et al. “Joining and cycling performance of ultra-thick tungsten coatings on patterned steel substrates for fusion armour applications”. In: *Materials and Design* 212 (Dec. 2021), p. 110250. ISSN: 18734197. DOI: 10.1016/j.matdes.2021.110250. URL: https://doi.org/10.1016/j.matdes.2021.110250.

[75] François Raletz, Michel Vardelle, and Guillaume Ezo'o. "Critical particle velocity under cold spray conditions". In: *Surface and Coatings Technology* 201.5 (Oct. 2006), pp. 1942–1947. ISSN: 02578972. DOI: 10.1016/j.surfcoat.2006.04.061.

[76] Aaron Hall et al. "Deposition Behavior in Cold Sprayed Copper-Tungsten Metal Matrix Composites". In: (2015), pp. 2–5.

[77] P. Petrovskiy et al. "Analysis of copper-tungsten cold spray coating: Kinetics of coating formation and its thermal properties". In: *Surface and Coatings Technology* 385.October 2019 (Mar. 2020), p. 125376. ISSN: 02578972. DOI: 10.1016/j.surfcoat.2020.125376. URL: https://doi.org/10.1016/j.surfcoat.2020.125376.

[78] Hyun Ki Kang and Suk Bong Kang. "Tungsten/copper composite deposits produced by a cold spray". In: *Scripta Materialia* 49.12 (Dec. 2003), pp. 1169–1174. ISSN: 13596462. DOI: 10.1016/j.scriptamat.2003.08.023.

[79] Jan Cizek et al. "Cold sprayed tungsten armor for tokamak first wall". In: *Coatings* 9.12 (2019), pp. 1–15. ISSN: 20796412. DOI: 10.3390/coatings9120836.

[80] Fan Wang and Jianjun Huang. "Performance characterization and improvement of tungsten coating atmospheric plasma sprayed with submicron powder". In: *Surface and Coatings Technology* 254 (Sept. 2014), pp. 61–64. ISSN: 02578972. DOI: 10.1016/j.surfcoat.2014.05.063.

[81] Jiří Matějíček, Radek Mušálek, and Jakub Veverka. "Materials and processing factors influencing stress evolution and mechanical properties of plasma sprayed coatings". In: *Surface and Coatings Technology* 371.July 2018 (Aug. 2019), pp. 3–13. ISSN: 02578972. DOI: 10.1016/j.surfcoat.2019.01.105.

[82] Jiří Matějíček et al. "The Role of Laser Texturing in Improving the Adhesion of Plasma Sprayed Tungsten Coatings". In: *Journal of Thermal Spray Technology* 28.7 (Oct. 2019), pp. 1346–1362. ISSN: 15441016. DOI: 10.1007/s11666-019-00924-7.

[83] S. Heuer et al. "Atmospheric plasma spraying of functionally graded steel/tungsten layers for the first wall of future fusion reactors". In: *Surface and Coatings Technology* 366.March (May 2019), pp. 170–178. ISSN: 02578972. DOI: 10.1016/j.surfcoat.2019.03.017.

[84] Deyang Hu et al. "Effect of oxidation behavior on the mechanical and thermal properties of plasma sprayed tungsten coatings". In: *Journal of Thermal Spray Technology* 17.3 (2008), pp. 377–384. ISSN: 10599630. DOI: 10.1007/s11666-008-9190-4.

[85] Takashi Sakai et al. "Microstructural Investigation of CoNiCrAlY Coated Ni-Based Single Crystal Superalloy Prepared by LPPS". In: *Materials Transactions* 47.7 (2006), pp. 1665–1670. ISSN: 1345-9678. DOI: 10.2320/matertrans.47.1665. URL: http://joi.jlc.jst.go.jp/JST.JSTAGE/matertrans/47.1665?from=CrossRef.

[86] Joo L. Ong, David L. Carnes, and Kazuhisa Bessho. "Evaluation of titanium plasma-sprayed and plasma-sprayed hydroxyapatite implants in vivo". In: *Biomaterials* 25.19 (2004), pp. 4601–4606. ISSN: 01429612. DOI: 10.1016/j.biomaterials.2003.11.053.

[87] S. Tamura et al. “High-temperature properties of joint interface of VPS-tungsten coated CFC”. In: *Journal of Nuclear Materials*. Vol. 329-333. 1-3 PART A. Aug. 2004, pp. 711–716. DOI: 10.1016/j.jnucmat.2004.04.186.

[88] G. Thomas et al. “Interface topography and residual stress distributions in W coatings for fusion armour applications”. In: *Materials Science and Engineering A* 477.1-2 (2008), pp. 35–42. ISSN: 09215093. DOI: 10.1016/j.msea.2007.05.120.

[89] Jean Christophe Sublet, Michael Fleming, and Mark R. Gilbert. “From cutting-edge pointwise cross-section to groupwise reaction rate: A primer”. In: *EPJ Web of Conferences* 146 (Sept. 2017). ISSN: 2100014X. DOI: 10.1051/epjconf/201714602003.

[90] Richard J. Kurtz and G. Robert Odette. “Overview of reactor systems and operational environments for structural materials in fusion reactors”. In: *Structural Alloys for Nuclear Energy Applications*. Ed. by G. Robert Odette and Steven J. Zinkle. Elsevier Inc., Jan. 2019. Chap. 3, pp. 51–102. ISBN: 9780123970466. DOI: 10.1016/B978-0-12-397046-6.00003-4. URL: http://dx.doi.org/10.1016/B978-0-12-397046-6.00003-4.

[91] Ch Linsmeier et al. “Material testing facilities and programs for plasma-facing component testing”. In: *Nuclear Fusion* 57.9 (June 2017). ISSN: 17414326. DOI: 10.1088/1741-4326/aa4feb.

[92] Yuhong Xu. “A general comparison between tokamak and stellarator plasmas”. In: *Matter and Radiation at Extremes* 1.4 (July 2016), pp. 192–200. ISSN: 2468080X. DOI: 10.1016/j.mre.2016.07.001. URL: http://dx.doi.org/10.1016/j.mre.2016.07.001.

[93] Maximilian Reisner et al. “Interdiffusion and phase formation at iron-tungsten interfaces”. In: *Nuclear Materials and Energy* 19.March (May 2019), pp. 189–194. ISSN: 23521791. DOI: 10.1016/j.nme.2019.01.033. URL: https://doi.org/10.1016/j.nme.2019.01.033.

[94] S. Heuer et al. “Microstructural and micromechanical assessment of aged ultra-fast sintered functionally graded iron/tungsten composites”. In: *Materials and Design* 191 (June 2020). ISSN: 18734197. DOI: 10.1016/j.matdes.2020.108652.

[95] Yue Wang et al. “Microstructure, properties, and formation mechanisms of tungsten/steel hot isostatic pressing diffusion bonding joint utilizing a Ni-Si-B interlayer”. In: *Journal of Materials Processing Technology* 299.February 2021 (Jan. 2022). ISSN: 09240136. DOI: 10.1016/j.jmatprotec.2021.117303.

[96] Jonathan Pearl et al. “Cyclic medium heat flux testing of a WTa lattice structure on the HIVE facility”. In: *Fusion Engineering and Design* 194.February (Sept. 2023), p. 113699. ISSN: 09203796. DOI: 10.1016/j.fusengdes.2023.113699. URL: https://doi.org/10.1016/j.fusengdes.2023.113699.

[97] H. Greuner et al. “High heat flux facility GLADIS:. Operational characteristics and results of W7-X pre-series target tests”. In: *Journal of Nuclear Materials* 367-370 B.SPEC. ISS. (Aug. 2007), pp. 1444–1448. ISSN: 00223115. DOI: 10.1016/j.jnucmat.2007.04.004.

[98] D. Nicolai et al. “Upgrade of the material ion beam test facility MARION for enhanced requirements of JET and ITER”. In: *Fusion Engineering and Design* 86.9-11 (Oct. 2011), pp. 2791–2794. ISSN: 09203796. DOI: 10.1016/j.fusengdes.2011.05.005. URL: http://dx.doi.org/10.1016/j.fusengdes.2011.05.005.

[99] D. Nicolai et al. “New options for material testing at the material ion beam test facility MARION”. In: *Fusion Engineering and Design* 88.9-10 (Oct. 2013), pp. 2506–2509. ISSN: 09203796. DOI: 10.1016/j.fusengdes.2013.02.132. URL: http://dx.doi.org/10.1016/j.fusengdes.2013.02.132.

[100] Vishnu Ganesh et al. “High Heat Flux Testing of Graded W-Steel Joining Concepts for the First Wall”. In: *Energies* 16.9 (May 2023). ISSN: 19961073. DOI: 10.3390/en16093664.

[101] Patrick Majerus et al. “The new electron beam test facility JUDITH II for high heat flux experiments on plasma facing components”. In: *Fusion Engineering and Design* 75-79.SUPPL. (Nov. 2005), pp. 365–369. ISSN: 09203796. DOI: 10.1016/j.fusengdes.2005.06.058.

[102] K. Nakamura et al. “Disruption erosions of various kinds of tungsten”. In: *Fusion Engineering and Design* 39-40 (1998), pp. 295–301. ISSN: 09203796. DOI: 10.1016/S0920-3796(98)00241-5.

[103] Youyun Lian et al. “Thermal shock performance of CVD tungsten coating at elevated temperatures”. In: *Journal of Nuclear Materials* 455.1-3 (2014), pp. 371–375. ISSN: 00223115. DOI: 10.1016/j.jnucmat.2014.07.021. URL: http://dx.doi.org/10.1016/j.jnucmat.2014.07.021.

[104] S. Kanpara et al. “Fabrication of Tungsten & Tungsten Alloy and its High Heat Load Testing for Fusion Applications”. In: *Materials Today: Proceedings* 3.9 (2016), pp. 3055–3063. ISSN: 22147853. DOI: 10.1016/j.matpr.2016.09.020. URL: http://dx.doi.org/10.1016/j.matpr.2016.09.020%20www.sciencedirect.comwww.materialstoday.com/proceedings2214-7853.

[105] H. J.N. van Eck et al. “High-fluence and high-flux performance characteristics of the superconducting Magnum-PSI linear plasma facility”. In: *Fusion Engineering and Design* 142.April (May 2019), pp. 26–32. ISSN: 09203796. DOI: 10.1016/j.fusengdes.2019.04.020. URL: https://doi.org/10.1016/j.fusengdes.2019.04.020.

[106] V. P. Budaev et al. “The plasma device for the high-heat plasma testing of refractory metals and inventing of new highly porous materials”. In: *Journal of Physics: Conference Series* 891.1 (Oct. 2017), p. 12304. ISSN: 02023822. DOI: 10.1088/1742-6596/891/1/012304. URL: https://dx.doi.org/10.1088/1742-6596/891/1/012304.

[107] V. P. Budaev et al. “The PLM-2 plasma device for full-scale tests of fusion reactor materials with stationary plasma loads: Design parameters”. In: *Journal of Physics: Conference Series* 1383.1 (Nov. 2019), pp. 3–7. ISSN: 17426596. DOI: 10.1088/1742-6596/1383/1/012016.

[108] Hyun Su Kim et al. “Recrystallization of bulk and plasma-coated tungsten with accumulated thermal energy relevant to Type-I ELM in ITER H-mode operation”. In: *Journal of Nuclear Materials* 463 (July 2015), pp. 215–218. ISSN: 00223115. DOI: 10.1016/j.jnucmat.2014.12.002. URL: http://dx.doi.org/10.1016/j.jnucmat.2014.12.002.

[109] Hao Yin et al. “Recent studies of tungsten-based plasma-facing materials in the linear plasma device STEP”. In: *Tungsten* 1.2 (June 2019), pp. 132–140. ISSN: 26618036. DOI: 10.1007/s42864-019-00004-x. URL: https://doi.org/10.1007/s42864-019-00004-x.

[110] M. Wirtz et al. “Influence of high flux hydrogen-plasma exposure on the thermal shock induced crack formation in tungsten”. In: *Journal of Nuclear Materials* 420.1-3 (Jan. 2012), pp. 218–221. ISSN: 00223115. DOI: 10.1016/j.jnucmat.2011.09.035. URL: http://dx.doi.org/10.1016/j.jnucmat.2011.09.035.

[111] M. Wirtz et al. “Thermal shock behaviour of tungsten after high flux H-plasma loading”. In: *Journal of Nuclear Materials* 443.1-3 (2013), pp. 497–501. ISSN: 00223115. DOI: 10.1016/j.jnucmat.2013.08.002. URL: http://dx.doi.org/10.1016/j.jnucmat.2013.08.002.

[112] Frank Schoofs and Mike Gorley. “A route to standardised high heat flux testing: An example for tungsten”. In: *Fusion Engineering and Design* 139.January (Feb. 2019), pp. 132–136. ISSN: 09203796. DOI: 10.1016/j.fusengdes.2018.12.060. URL: https://doi.org/10.1016/j.fusengdes.2018.12.060.

[113] Narguess Nemati et al. “Microstructural evolution of tungsten under thermal loads: A comparative study between cyclic high heat flux loading and isochronous furnace heating”. In: *Nuclear Materials and Energy* 36.June (Sept. 2023), p. 101465. ISSN: 23521791. DOI: 10.1016/j.nme.2023.101465.

[114] R. Neu et al. “Investigations on cold spray tungsten/tantalum coatings for plasma facing applications”. In: *Nuclear Materials and Energy* 34.December 2022 (Mar. 2023). ISSN: 23521791. DOI: 10.1016/j.nme.2022.101343.

[115] C. M. Parish et al. “Effect of tungsten crystallographic orientation on He-ion-induced surface morphology changes”. In: *Acta Materialia* 62.1 (2014), pp. 173–181. ISSN: 13596454. DOI: 10.1016/j.actamat.2013.09.045. URL: http://dx.doi.org/10.1016/j.actamat.2013.09.045.

[116] S. Bardin et al. “Evolution of transiently melt damaged tungsten under ITER-relevant divertor plasma heat loading”. In: *Journal of Nuclear Materials* 463 (July 2015), pp. 193–197. ISSN: 00223115. DOI: 10.1016/j.jnucmat.2014.10.046. URL: http://dx.doi.org/10.1016/j.jnucmat.2014.10.046.

[117] Karl D. Hammond. “Helium, hydrogen, and fuzz in plasma-facing materials”. In: *Materials Research Express* 4.10 (Oct. 2017). ISSN: 20531591. DOI: 10.1088/2053-1591/aa8c22.

[118] Shin Kajita, Naoaki Yoshida, and Noriyasu Ohno. “Tungsten fuzz: Deposition effects and influence to fusion devices”. In: *Nuclear Materials and Energy* 25 (Dec. 2020), p. 100828. ISSN: 23521791. DOI: 10.1016/j.nme.2020.100828. URL: https://doi.org/10.1016/j.nme.2020.100828.

[119] Jacob A.R. Wright. “A review of late-stage tungsten fuzz growth”. In: *Tungsten* 4.3 (Sept. 2022), pp. 184–193. ISSN: 26618036. DOI: 10.1007/s42864-021-00133-2. URL: https://doi.org/10.1007/s42864-021-00133-2.

[120] V. P. Budaev et al. “High-heat flux tests of tungsten divertor mock-ups with steady-state plasma and e-beam”. In: *Nuclear Materials and Energy* 25 (Dec. 2020), p. 100816. ISSN: 23521791. DOI: 10.1016/j.nme.2020.100816. URL: https://doi.org/10.1016/j.nme.2020.100816.

[121] V. P. Budaev et al. “Erosion of Fuzz Layers Formed in Steady-State Plasma Discharge”. In: *Fusion Science and Technology* 79.4 (2023), pp. 407–412. ISSN: 19437641. DOI: 10.1080/15361055.2022.2118471. URL: https://doi.org/10.1080/15361055.2022.2118471.

[122] Y. Li et al. “Fracture behavior of tungsten-based composites exposed to steady-state/transient hydrogen plasma”. In: *Nuclear Fusion* 60.4 (2020). ISSN: 17414326. DOI: 10.1088/1741-4326/ab77e7.

[123] T. W. Morgan et al. “A high-repetition rate edge localised mode replication system for the Magnum-PSI and Pilot-PSI linear devices”. In: *Plasma Physics and Controlled Fusion* 56.9 (Sept. 2014). ISSN: 13616587. DOI: 10.1088/0741-3335/56/9/095004.

[124] Y. Li et al. “Influence of porosity and blistering on the thermal fatigue behavior of tungsten”. In: *Nuclear Fusion* 62.7 (July 2022). ISSN: 17414326. DOI: 10.1088/1741-4326/ac6a65.

[125] T. W. Morgan et al. “Combined high fluence and high cycle number transient loading of ITER-like monoblocks in Magnum-PSI”. In: *Nuclear Fusion* 61.11 (Nov. 2021). ISSN: 17414326. DOI: 10.1088/1741-4326/ac25c2.

[126] M. S. Tillack et al. “GAMBL – A dual-cooled fusion blanket using SiC-based structures”. In: *Fusion Engineering and Design* 180.May (July 2022), p. 113155. ISSN: 09203796. DOI: 10.1016/j.fusengdes.2022.113155. URL: https://doi.org/10.1016/j.fusengdes.2022.113155.

[127] Thomas R. Barrett et al. "CHIMERA Fusion Technology Facility: Testing and Virtual Qualification". In: *Fusion Science and Technology* 00.00 (2023), pp. 1–12. ISSN: 19437641. DOI: 10.1080/15361055.2022.2147766. URL: https://doi.org/10.1080/15361055.2022.2147766.

[128] S Mantry et al. "Tribo-performance of plasma-sprayed nanostructured yttria-stabilized zirconia coatings using Taguchi's experimental design". In: *Proceedings of the Institution of Mechanical Engineers, Part J: Journal of Engineering Tribology* 228.8 (Aug. 2014), pp. 872–880. ISSN: 1350-6501. DOI: 10.1177/1350650114535385. URL: http://journals.sagepub.com/doi/10.1177/1350650114535385.

[129] T J Steeper et al. "A design of experiment study of plasma-sprayed alumina-titania coatings". In: *Journal of Thermal Spray Technology* 2.3 (Sept. 1993), pp. 251–256. ISSN: 1544-1016. DOI: 10.1007/BF02650473. URL: https://doi.org/10.1007/BF02650473.

[130] D. J. Varacalle et al. "Fabrication of tungsten coatings and monoliths using the vacuum plasma spray process". In: *Surface and Coatings Technology* 61.1-3 (1993), pp. 79–85. ISSN: 02578972. DOI: 10.1016/0257-8972(93)90206-4.

[131] Christian Moreau et al. "Thermal diffusivity of plasma-sprayed tungsten coatings". In: *Surface and Coatings Technology* 61.1-3 (1993), pp. 67–71. ISSN: 02578972. DOI: 10.1016/0257-8972(93)90204-2.

[132] Srinivas Athreya and Y D Venkatesh. "Application Of Taguchi Method For Optimization Of Process Parameters In Improving The Surface Roughness Of Lathe Facing Operation". In: *International Refereed Journal of Engineering and Science* 1.3 (2012), pp. 13–19. DOI: 2319-1821.

[133] Vijay Ananth S. "Experimental and simulation analyses of superplastic forming of A16063/SiCp composites". PhD thesis. Anna University, 2013. URL: http://hdl.handle.net/10603/17747.

[134] Kyeong Ho Baik. "Spray/wind processing of hoop reinforced high temperaure composites". PhD thesis. University of Oxford, 1999.

[135] Sisir Mantry, Barada K. Mishra, and Madhusudan Chakraborty. "Parametric appraisal of process parameters for adhesion of plasma sprayed nanostructured YSZ coatings using taguchi experimental design". In: *The Scientific World Journal* 2013 (2013), pp. 1–9. ISSN: 1537744X. DOI: 10.1155/2013/527491.

[136] Gareth Thomas. "Advanced materials for plasma facing components in fusion devices". PhD thesis. Univeristy of Oxford, 2009. URL: https://ora.ox.ac.uk/objects/uuid:f8ba1ae1-f303-4c32-877e-dca421a3cb5c.

[137] H. R. Salimijazi et al. "Measuring substrate temperature variation during application of plasma-sprayed zirconia coatings". In: *Journal of Thermal Spray Technology* 16.4 (Dec. 2007), pp. 580–587. ISSN: 10599630. DOI: 10.1007/s11666-007-9050-7.

[138] Jiří Matějíček et al. "The influence of substrate temperature and spraying distance on the properties of plasma sprayed tungsten and steel coatings deposited in a shrouding chamber". In: *Surface and Coatings Technology* 318 (May 2017), pp. 217–223. ISSN: 02578972. DOI: 10.1016/j.surfcoat.2016.10.055.

[139] Lars Vanmunster et al. “Mechanical behavior of Ti6Al4V produced by laser powder bed fusion with engineered open porosity for dental applications”. In: *Journal of the Mechanical Behavior of Biomedical Materials* 126.November 2021 (Feb. 2022), p. 104974. ISSN: 18780180. DOI: 10.1016/j.jmbbm.2021.104974. URL: https://doi.org/10.1016/j.jmbbm.2021.104974.

[140] Ryan L. Payton, Domenico Chiarella, and Andrew Kingdon. “The upper percolation threshold and porosity–permeability relationship in sandstone reservoirs using digital image analysis”. In: *Scientific Reports* 12.1 (Dec. 2022), pp. 1–14. ISSN: 20452322. DOI: 10.1038/s41598-022-15651-3. URL: https://doi.org/10.1038/s41598-022-15651-3.

[141] Stephen Timoshenko. “Analysis of Bi-Metal Thermostats”. In: *Journal of the Optical Society of America* 11.3 (1925), p. 233. ISSN: 0030-3941. DOI: 10.1364/josa.11.000233.

[142] G.R. Odette et al. “W-Alloy and Composite Fracture test Method Development and Initial Exploration of Ductile Phase Toughening”. In: *Fusion Reactor Materials Program Semiannual Progress Report*. Ed. by FW Wiffen, R Godfrey, and B Waddell. Vol. DOE0313/52. June. 2012, pp. 89–102. ISBN: 9788578110796. DOI: 10.13140/RG.2.1.5159.4724.

[143] Bo-Shiuan Li. “Measuring Fracture Resistance Behaviour of Tungsten Using Chevron-Notched Micro-Cantilevers”. PhD thesis. University of Oxford, 2017.

[144] Byeong Seo Kong et al. “Measurement of fracture toughness of pure tungsten using a small-sized compact tension specimen”. In: *Materials* 13.1 (Jan. 2020), p. 244. ISSN: 19961944. DOI: 10.3390/ma13010244.

[145] W. Dahl and P. Langenberg. "Fracture Toughness Testing of Metallic Materials". In: *Encyclopedia of Materials: Science and Technology*. Ed. by K.H. Jürgen Buschow et al. 2nd ed. Elsevier, Jan. 2001, pp. 3336–3340. ISBN: 978-0-08-043152-9. DOI: 10.1016/b0-08-043152-6/00596-9.

[146] Alan T. Zehnder. *Fracture Mechanics*. 1st ed. Springer Science & Business Media, 2012, pp. 50–51. ISBN: 978-94-007-2595-9. DOI: 10.1007/978-94-007-2595-9.

[147] Hebei Metals Industrial Limited. *T91 / P91 Steel*. URL: http://www.metalspiping.com/t91-p91-steel.html. Date accessed: 2023-07-13.

[148] Gippeum J. Lim, Suk Jo Kang, and Ji Youn Lee. "Novel invasion indices quantify the feed-forward facilitation of tumor invasion by macrophages". In: *Scientific Reports* 10.1 (Dec. 2020), pp. 1–10. ISSN: 20452322. DOI: 10.1038/s41598-020-57517-6.

[149] Alo Francis Ireti et al. "Comparision of Imagej Analysis of Structure of Two Constructional Steel". In: *American Journal of Engineering and Applied Sciences* 11.1 (Jan. 2018), pp. 318–326. ISSN: 1941-7020. DOI: 10.3844/ajeassp.2018.318.326.

[150] ASM International. "Fe (Iron) Binary Alloy Phase Diagrams". In: *Alloy Phase Diagrams*. Ed. by H Okamoto, M E Schlesinger, and E M Mueller. Vol. 3. ASM International, Apr. 2016, p. 360. ISBN: 978-1-62708-163-4. DOI: 10.31399/asm.hb.v03.a0006162. URL: https://doi.org/10.31399/asm.hb.v03.a0006162.

[151] Dandan Qu et al. "Characterization of W/Fe functionally graded materials manufactured by resistance sintering under ultra-high pressure". In: *Fusion Engineering and Design* 91 (Feb. 2015), pp. 21–24. ISSN: 09203796. DOI: 10.1016/j.fusengdes.2014.12.014. URL: http://dx.doi.org/10.1016/j.fusengdes.2014.12.014.

[152] Widodo Widjaja Basuki and Jarir Aktaa. "Investigation on the diffusion bonding of tungsten and EUROFER97". In: *Journal of Nuclear Materials* 417.1-3 (Oct. 2011), pp. 524–527. ISSN: 00223115. DOI: 10.1016/j.jnucmat.2010.12.121. URL: http://dx.doi.org/10.1016/j.jnucmat.2010.12.121.

[153] Ta Siewert, Jc Madeni, and S Liu. "Formation and growth of intermetallics at the interface between lead-free solders and copper substrates". In: *Proceedings of the APEX ...* 1 (2003), pp. 2–8. URL: http://www.boulder.nist.gov/div853/Publication%20files/NIST_Apex94_Siewert.pdf.

[154] DIFFER. *Upgraded Pilot-PSI (UPP) | Dutch Institute for Fundamental Energy Research*. URL: https://www.differ.nl/facilities/upgraded-pilot-psi. Date accessed: 2023-09-07.

[155] Johannes Schindelin et al. "Fiji: An open-source platform for biological-image analysis". In: *Nature Methods* 9.7 (July 2012), pp. 676–682. ISSN: 15487091. DOI: 10.1038/nmeth.2019.

[156] Ralph A. Felice. "Expert System Spectropyrometer Results for Non-Black, Non-Grey, or Chaning Emissivity and Selectively Absorbing Environments". In: *ElectroTechno Exposition, Moscow*. 2003. URL: www.pyrometry.com%20http://pyrometry.com/farassociates_moscowpaper.pdf.

[157] Deena Titus, E. James Jebaseelan Samuel, and Selvaraj Mohana Roopan. "Nanoparticle characterization techniques". In: *Green Synthesis, Characterization and Applications of Nanoparticles*. Elsevier Inc., Jan. 2018. Chap. 12, pp. 303–319. ISBN: 9780081025796. DOI: 10.1016/B978-0-08-102579-6.00012-5. URL: https://doi.org/10.1016/B978-0-08-102579-6.00012-5.

[158] J. PiŇos et al. "About the information depth of backscattered electron imaging". In: *Journal of Microscopy* 266.3 (June 2017), pp. 335–342. ISSN: 13652818. DOI: 10.1111/jmi.12542.

[159] Y. A. Chang. "Phase investigations in the system zirconium-tungsten". In: *Journal of The Less-Common Metals* 17.3 (1969), pp. 325–328. ISSN: 00225088. DOI: 10.1016/0022-5088(69)90151-9.

[160] Musong Ko and Taiji Nishizawa. "Effect of magnetic transition on the solubility of alloying elements in alpha iron". In: *Nippon Kinzoku Gakkaishi* 43.2 (1979), pp. 118–126. DOI: 10.2320/jinstmet1952.43.2{_}118.

[161] A A Bolzan, B J Kennedy, and C J Howard. "Neutron Powder Diffraction Study of Molybdenum and Tungsten Dioxides". In: *Australian Journal of Chemistry* 48.8 (1995), pp. 1473–1477. DOI: 10.1071/CH9951473.

[162] D. Lenaz et al. "Structural changes and valence states in the MgCr2O4-FeCr2O4 solid solution series". In: *Physics and Chemistry of Minerals* 31.9 (Dec. 2004), pp. 633–642. ISSN: 03421791. DOI: 10.1007/s00269-004-0420-0.

[163] G. M. Santos et al. “Electron density distribution and electronic structure as tools to study the origin of ferroic states in ferroelectric and magnetic materials”. In: *Ferroelectrics* 500.1 (Aug. 2016), pp. 26–36. ISSN: 15635112. DOI: 10.1080/00150193.2016.1215754. URL: http://dx.doi.org/10.1080/00150193.2016.1215754.

[164] Dinçer Ülkü. “Untersuchungen zur Kristallstruktur und magnetischen Struktur des Ferberits FeWO4”. In: *Zeitschrift für Kristallographie* 124.3 (1967), pp. 192–219. DOI: doi:10.1524/zkri.1967.124.3.192. URL: https://doi.org/10.1524/zkri.1967.124.3.192.

[165] A. S. Kurlov and A. I. Gusev. “Neutron and x-ray diffraction study and symmetry analysis of phase transformations in lower tungsten carbide W2 C”. In: *Physical Review B - Condensed Matter and Materials Physics* 76.17 (Nov. 2007), pp. 1–16. ISSN: 10980121. DOI: 10.1103/PhysRevB.76.174115.

[166] W. Kunnmann et al. “Magnetic structures of the ordered trirutiles Cr2WO6, Cr2TeO6 and Fe2TeO6”. In: *Journal of Physics and Chemistry of Solids* 29.8 (1968), pp. 1359–1364. ISSN: 00223697. DOI: 10.1016/0022-3697(68)90187-X.

[167] Jochen Glaser, Ruth Schmitt, and H.-Jürgen Meyer. “Structure Refinement and Properties of Cr3C2”. In: *Zeitschrift für Naturforschung B* 58.9 (2003), pp. 929–933. ISSN: 0015-3230. DOI: 10.7868/s0015323016050053. URL: http://znaturforsch.com.

[168] Jantz Supply. *Steel Forging & Tempering Chart*. URL: https://knifemaking.com/pages/forging-steel-heat-color-chart. Date accessed: 2023-03-29.

[169] Ben Sampson. "On-Wing Innovation". In: *Aerospace Testing International* 2019.3 (Sept. 2019), pp. 76–82. ISSN: 1478-2774. DOI: 10.12968/S1478-2774(22)50233-1. URL: https://doi.org/10.12968/S1478-2774(22)50233-1.

[170] Dominic Perry. *PARIS: Rolls-Royce employs 'snakes on a plane' for engine repair*. URL: https://www.flightglobal.com/mro/paris-rolls-royce-employs-snakes-on-a-plane-for-engine-repair/133103.article. Flight Global.

[171] I. T. Chapman and A. W. Morris. "UKAEA capabilities to address the challenges on the path to delivering fusion power". In: *Philosophical Transactions of the Royal Society A: Mathematical, Physical and Engineering Sciences* 377.2141 (Mar. 2019). ISSN: 1364503X. DOI: 10.1098/rsta.2017.0436.

[172] M. Diez et al. "Tungsten coatings repair: An approach to increase the lifetime of plasma facing components". In: *Fusion Engineering and Design* 146.October 2018 (Sept. 2019), pp. 800–804. ISSN: 09203796. DOI: 10.1016/j.fusengdes.2019.01.084. URL: https://doi.org/10.1016/j.fusengdes.2019.01.084.

[173] Yu Li et al. "Laser repair of tungsten damaged by fusion-relevant plasmas". In: *Journal of Nuclear Materials* 580 (July 2023). ISSN: 00223115. DOI: 10.1016/j.jnucmat.2023.154426.

[174] G. De Temmerman et al. “Effect of high-flux H/He plasma exposure on tungsten damage due to transient heat loads”. In: *Journal of Nuclear Materials* 463 (2015), pp. 198–201. ISSN: 00223115. DOI: 10.1016/j.jnucmat.2014.09.075. URL: http://dx.doi.org/10.1016/j.jnucmat.2014.09.075.

[175] W Chapman. *Workshop Technology Part 1*. Fifth edit. Abingdon: CRC Press, 1972, p. 43. ISBN: 9781136898266. URL: https://books.google.co.uk/books?id=9O6yDwAAQBAJ.

[176] Cuncai Fan et al. “Helium radiation blistering mechanisms in tungsten: Ion channeling effects”. In: *Materialia* 27.October 2022 (Mar. 2023), p. 101664. ISSN: 25891529. DOI: 10.1016/j.mtla.2022.101664. URL: https://doi.org/10.1016/j.mtla.2022.101664.

[177] I. Smid et al. “Development of tungsten armor and bonding to copper for plasma-interactive components”. In: *Journal of Nuclear Materials* 258-263.PART 1 A (1998), pp. 160–172. ISSN: 00223115. DOI: 10.1016/S0022-3115(98)00358-4.

[178] A. Suslova et al. “Recrystallization and grain growth induced by ELMs-like transient heat loads in deformed tungsten samples”. In: *Scientific Reports* 4 (Nov. 2014), pp. 1–11. ISSN: 20452322. DOI: 10.1038/srep06845.

[179] Frances I. Allen, Peter Hosemann, and Mehdi Balooch. “Key mechanistic features of swelling and blistering of helium-ion-irradiated tungsten”. In: *Scripta Materialia* 178 (Mar. 2020), pp. 256–260. ISSN: 13596462. DOI: 10.1016/j.scriptamat.2019.11.039. URL: https://doi.org/10.1016/j.scriptamat.2019.11.039.

[180] Axel Forslund and Andrei Ruban. “Ab initio surface free energies of tungsten with full account of thermal excitations”. In: *Physical Review B* 105.4 (Jan. 2022). ISSN: 24699969. DOI: 10.1103/PhysRevB.105.045403.